AUSTENITIC STAINLESS STEELS FOR FUTURE NUCLEAR FUEL CLADDINGS

A Thesis Submitted to the College of
Graduate Studies and Research
In Partial Fulfillment of the Requirements
For the Degree of Doctor of Philosophy
In the Department of Mechanical Engineering
University of Saskatchewan
Saskatoon
Canada

By
Majid Nezakat

PERMISSION TO USE

In presenting this thesis in partial fulfillment of the requirements for a postgraduate degree from the University of Saskatchewan, I agree that the Libraries of this University may make it freely available for inspection. I further agree that permission for copying of this thesis in any manner, in whole or in part, for scholarly purposes may be granted by the professor who supervised my thesis work or, in their absence, by the Head of the Department or the Dean of the College in which my thesis work was done. It is understood that any copying or publication or use of this thesis or parts thereof for financial gain shall not be allowed without my written permission. It is also understood that due recognition shall be given to me and to the University of Saskatchewan in any scholarly use which may be made of any material in my thesis.

Requests for permission to copy or to make other use of material in this thesis in whole or part should be addressed to:

Head of the Department of Mechanical Engineering
57 Campus Dr.
University of Saskatchewan
Saskatoon, Saskatchewan (S7N 5A9)

ABSTRACT

Nuclear power systems have been under continuous development since the first nuclear power plant started operation in 1954. They are categorized into different generations, with each new generation having significant technological advances over the previous one. The worldwide effort to develop the next generation of nuclear reactors was defined at the Generation IV International Forum (GIF) in 2000. Six types of design were proposed, including supercritical water cooled reactor (SCWR). Materials in this reactor will be exposed to more severe environments than the current generation of reactors to assure higher efficiency in energy production and the current materials used for fuel cladding need to be improved or new materials should be developed. In this thesis, the behavior of two existing nuclear materials, stainless steels 310S and 316L was investigated, under conditions approximating the nuclear reactor environment.

An environment with dynamic loop of supercritical water (SCW) was used to test the performance of the alloys and the oxides formed were analyzed. Oxidation of the alloys in air was also performed for comparison. It was found that although both alloys showed good oxidation resistance in air at 600ºC, stainless steel 310S has better resistance in SCW environment compared to stainless steel 316L. A thin protective oxide layer of Mn_2CrO_4 spinel delays oxidation in alloy 310S.

In order to improve the oxidation resistance of 310S and 316L stainless steels, thermo-mechanical processing (TMP) was applied to modify their microstructures. The deformation and annealing texture of the as-received and processed samples were investigated by means of X-ray diffraction (XRD) and orientation imaging microscopy (OIM). Different rolling paths and different deformation levels before annealing were used to produce samples of different grain size with similar texture and samples of similar grain size with different textures. Subsequently, the oxidation resistance of thermo-mechanically processed 316L and 310S samples in SCW was studied. It was found that the oxidation resistance of stainless steels 316L and 310S can be improved up to four and five times, respectively, by decreasing the grain size below a critical value of 3 μm. It was demonstrated that samples with smaller grain size provided higher fraction of grain boundaries for fast diffusion of chromium to reach the surface and compensate losses due to dissolution of chromium in the oxidation media.

External oxide layers formed on as-received and thermo-mechanically processed stainless steel 316L samples was characterized to establish possible correlation between orientation of the substrate and oxide grains. Micro and macro textures of the substrate and the oxide layers were examined and the results showed that the texture of substrate did not affect the texture of magnetite (Fe_3O_4) in the upper oxide layer. In addition, the texture of magnetite did not affect the texture of hematite (Fe_2O_3) on samples where hematite was an additional oxide phase. The strong texture of both oxides was explained with surface free energy minimization and strain energy minimization theory. This means that the texture of both oxides is dictated by a competition between their surface and strain energies.

AKNOWLEDGEMENTS

This thesis would not have been possible without the help of many individuals. First and foremost, I would like to express my sincere gratitude to my distinguished supervisor, Professor Jerzy Szpunar for his continuous advice, support and encouragement throughout this research.

I am immensely grateful to my committee members, Dr. Qiaoqin Yang, Dr. Ikechukwuka Oguocha, Dr. Chary Rangacharyulu, and Dr. Huiqing Guo for the compassion and coaching they have given me throughout my doctorate program.

I wish to show my appreciation to my fellow graduate students and post-doctorate in the Advance Materials and Renewable Energy (AMRE) research group and Department of Mechanical Engineering, Dr. Nilesh Gurao, Dr. Salman Razavi, Dr. Ritwik Basu, Dr. Farhad Fathieh, Mohsen Sanayei, and Robert Peace for the countless hours of assistance, contributions and feedbacks.

Finally, I would like to acknowledge the VTT Technical Research Centre of Finland, Department of Mechanical Engineering at University of Saskatchewan, Natural Sciences and Engineering Research Council of Canada (NSERC), the Canada Research Chair programs, the Government of Saskatchewan's Innovative & Opportunity Scholarship, Toyota Automotive Engineering and Safety Scholarship for their financial and technical support.

DEDICATION

To my wife,

whose unconditional love and support made this work possible

To my mother,

although she left us too soon with a big empty space in our heart,

She never stopped believing in me

To my father,

who sacrificed his life to make a better life for his family.

TABLE OF CONTENTS

LIST OF TABLES

LIST OF FIGURES

ACRONYMS

BWR	Boiling Water Reactor
CANDU	CANada Deuterium Uranium
CO2e	Carbon Dioxide Equivalent
EDS	Energy Dispersive Spectroscopy
EBSD	Electron Backscattered Diffraction
FEG-SEM	Field Emission Gun Scanning Electron Microscope
GFR	Gas-Cooled Fast Reactor
GIF	Generation IV International Forum
IPF	Inverse Pole Figure
LFR	Lead-Cooled Fast Reactor
LWR	Light Water Reactor
MSR	Molten Salt Reactor
NRCan	Natural Resources Canada
ODF	Orientation Distribution Function
PWR	Pressurized water reactors
RBMK	Reactor Bolshoy Moshchnosty Kanalny (Russian) High power channel-type reactor
SCW	Super Critical Water
SCWR	Super Critical Water-Cooled Reactor
SEM	Scanning Electron Microscope
SFR	Sodium-Cooled Fast Reactor
TMP	Thermo-Mechanical Processing
VHTR	Very High Temperature Reactor
XRD	X-ray Diffraction

1 INTRODUCTION

1.1 Motivation

Nuclear power is one of the most reliable sources of energy in terms of the geological issues, the generated by-products by heat production reactions, the wastes managements, and the capacity of meeting huge demand for energy. Currently, many countries are using electrical energy provided by nuclear power plants which is almost 20 % of the total energy production by the end of 2015 [1,2]. This fraction will increase, although some nuclear power plants are being shut down or reaching their lifetime.

With improvements in safety, efficiency, and cost of the next generations of nuclear reactors, specifically generation IV, the number of nuclear plants will significantly increase worldwide in the years to come. Nine developed countries, including Canada, with the highest nuclear energy production both for domestic and industrial use established the Generation IV forum (GIF) in 2000 to incorporate the international effort in design and development of the future nuclear energy reactors [3]. The forum decided to select six nuclear systems among all the proposed designs with consideration of sustainability, safety and reliability, economics, and proliferation resistance and physical protection [4]. Being an active member since the beginning, Canada established a national program for Generation IV Energy Technologies in 2006 to support collaborative research and development of the two assigned candidate systems: supercritical water cooled reactor (SCWR) and very high temperature reactor (VHTR).

1.2 Knowledge gap

The accumulated knowledge and experience over the past four decades of designing and operating CANDU reactors is a great asset in the development of the SCWR technology for which the main focus is safety, thermohydraulics, chemistry and materials. Many designs of SCWR were studied to maximize thermodynamic efficiency, of which the temperature of the fluid can be as high as 625ºC at the outlet and approximately 325ºC at the inlet of the reactor. As a result, the type of materials that can withstand this elevated temperature regime together with high pressures (>22.1 MPa) is limited. Materials selection is even harder as no information is available about the behavior of materials in the aforementioned extreme conditions [5]. Therefore, the main concerns in selecting appropriate materials in the reactor core are prevention of stress corrosion cracking

(SCC), resistance to corrosion and resistance to neutron radiation damage. Among available materials, stainless steels and high nickel-chromium alloys have shown promising results [6–16]. These results are not only affected by the chemical composition of the studied alloys, but also their microstructure. Since microstructural effect are mainly related to changes in texture and grain size, thermo-mechanical processing (TMP) can be adopted to optimize the microstructure to improve the corrosion resistance. In this thesis, the focus will be on the effect of grain size and effect of texture on corrosion resistance in SCW environment.

1.3 Objectives of the thesis

The main goal of this thesis is to select a candidate material that will withstand the harsh environment of SCW during long time exposure. The hypothesis is that it is possible to select a material among the commercial alloys and improve its corrosion resistance in SCW with manipulating the microstructure. To achieve this goal, two microstructure variables of average grain size and texture should be separated so the effect each could be studied individually. This approach has not been reported elsewhere in the literature. It is believed that such a fundamental investigation would be beneficial for better understanding of the effect of microstructure on the corrosion resistance of reactor components. Stainless steels AISI 310S and 316L were selected for this study based on the available data in the literature and discussion with scholars at Natural Resources Canada (NRCan) and Atomic Energy of Canada Limited (AECL) who specifically work on development of the SCWRs. Considering the importance of fuel cladding in future nuclear reactors, this thesis addresses the corrosion resistance of the selected materials and the thermo-mechanical method to improve it by optimizing their microstructure. Therefore, the objectives of this Ph.D. study are defined as follows:

1. To evaluate the oxidation resistance of austenitic stainless steels 310S and 316L in SCW as well as in air for comparison.
2. To optimize the microstructure of austenitic stainless steels 310S and 316L thermo-mechanical processing to improve the corrosion resistance.
3. To evaluate the role of texture and grain size on improvement of the corrosion resistance of austenitic stainless steels 310S and 316L.
4. To recommend which of the investigated alloys and under what treatment conditions is expected to perform better in SCW.

1.4 Publications

The outcome of the current Ph.D. study has been presented in 6 peer-reviewed journal papers, 3 conference paper, and 1 poster presentation. Three of the journal papers have been published and three are under review.

1.4.1 Refereed Journal Papers

1. M. Nezakat, H. Akhiani, S. Penttilä, and J.A. Szpunar, “Oxidation Behavior of Austenitic Stainless Steel 316L and 310S in Air and Supercritical Water”, Nuclear Engineering and Radiation Science, 2 (2016) 021008.
2. M. Nezakat, H. Akhiani, M. Hoseini, and J.A. Szpunar, “Effect of thermo-mechanical processing on texture evolution in austenitic stainless steel 316L”, Materials Characterization, 98 (2014) 10-17.
3. M. Nezakat, H. Akhiani, S. Penttilä, S. M. Sabet, and J.A. Szpunar, “Effect of thermo-mechanical processing on oxidation of austenitic stainless steel 316L in supercritical water”, Corrosion Science, 94 (2015) 197-206.
4. M. Nezakat, H. Akhiani, S. Penttilä, and J.A. Szpunar, “Characterization of the oxide film on stainless steel 316L exposed to supercritical water environment”, Corrosion Science, Submitted.
5. M. Nezakat, H. Akhiani, and J.A. Szpunar, “Electron backscattered and x-ray diffractions study on deformation and annealing textures of austenitic stainless steel 310S”, Materials Characterization, Submitted.
6. M. Nezakat, S. Penttilä, and J.A. Szpunar, “Oxidation of thermo-mechanically processed austenitic stainless steel 310S in supercritical water”, Corrosion Science, Submitted.

1.4.2 Conference Papers and Posters

1. M. Nezakat, H. Akhiani, S. Penttilä, S. M. Sabet, J. Szpunar, “Oxidation of 800H/HT and AISI316L alloys in air and supercritical water”, The 7th International Symposium on Supercritical Water-Cooled Reactors (ISSCWR-7), Helsinki, Finland, 15-18 March 2015.
2. M. Nezakat, H. Akhiani, S. Penttilä, and J.A. Szpunar, “Characterization of oxide formed on thermo-mechanically processed austenitic stainless steel 316L in super-critical water”, The Nuclear Materials Conference, Hilton Clearwater, Florida, USA, 27-30 October 2014.

3. M. Nezakat, H. Akhiani, S. Penttilä, and J.A. Szpunar, “Oxidation resistance of thermo-mechanically processed austenitic stainless steel 316l in super critical water”, Pacific Basin Nuclear Conference, Vancouver, August 24-28, 2014.

4. M. Nezakat, H. Akhiani, and J.A. Szpunar, “Comparative study on the oxidation resistance of stainless steel 316L in air and super-critical water”, 26th Canadian Materials Science Conference, Saskatoon, June 1 - 4, 2014.

1.5 Thesis organization

The materials in the refereed journals listed in the previous section were used to write this thesis. As depicted in Figure 1.1,each chapter is comprised of a separate publication that addresses one or two of the thesis objectives. Manuscript are slightly modified to present the material in a logical sequence and to follow the thesis formatting. In order to avoid repetition, the overlap in introduction section of all papers are omitted and a general introduction is presented in chapter 2. In addition, the experimental methodology is only described in chapter 3. Figure 1.1 shows the outline of the thesis with the objectives addressed in each chapter. A brief overview of each chapter and the authors’ contributions to each paper are also given at the beginning of each chapter.

Chapter 4 addresses the first objective of the thesis, “to evaluate the oxidation resistance of austenitic stainless steels 310S and 316L in SCW as well as in air for comparison”. It reports a comparative study of corrosion of the as-received austenitic stainless steels 310S and 316L in air and SCW. The aim is to realize how the two alloys perform in SCW. Air oxidation was done to assess severity of oxidation in SCW environment.

In order to improve the corrosion resistance of stainless steels 316L in SCW, TMP is applied to optimize its microstructure. Evolution of the microstructure of stainless steel 316L during TMP is the subject of chapter 5. XRD and EBSD are used to measure the macro and micro textures that explains the deformation mechanisms and microstructural changes in stainless steel 316L. This chapter partially addresses the second objective of the thesis, “to optimize the microstructure of austenitic stainless steels 310S and 316L by thermo-mechanical processing to improve the corrosion resistance”.

Figure 1.1. Thesis outline with the objectives and manuscript title for each chapter.

The corrosion of the treated 316L samples in SCW is studied in chapter 6 to identify the corrosion mechanisms and the possible role of grain size and texture on the corrosion resistance of austenitic stainless steel 316L. For this purpose, EBSD technique coupled with EDS is implemented to collect the microstructural constituents' maps at the cross section of the oxide

layer. This chapter partially addresses the third and fourth objectives of the thesis, “to evaluate the role of texture and grain size on improvement of the corrosion resistance of austenitic stainless steels 310S and 316L”, and “to recommend which of the investigated alloys and under what treatment conditions is expected to perform better in SCW”.

The cross-section of the oxide layer is characterized with EBSD and XRD techniques in chapter 7 to provide a comprehensive understanding on whether there is a possible orientation relation between the substrate and oxide layer. This chapter partially addresses the third objective of the thesis, “to evaluate the role of texture and grain size on improvement of the corrosion resistance of austenitic stainless steels 310S and 316L”.

To improve the corrosion resistance of stainless steels 310S in SCW, TMP is applied to optimize the microstructure. Evolution of the microstructure of stainless steel 310S during TMP is the subject of chapter 8. XRD and EBSD are used to measure the macro and micro textures that explains the deformation mechanisms and microstructural changes in stainless steel 310S. This chapter partially addresses the second objective of the thesis, “to optimize the microstructure of austenitic stainless steels 310S and 316L by thermo-mechanical processing to improve the corrosion resistance”.

The corrosion resistance of the thermo-mechanically processed 310S samples in SCW is studied in chapter 9 to identify the corrosion mechanisms and the possible role of texture and grain size on the corrosion resistance. EBSD technique coupled with EDS is used to collect orientation and elemental maps at the cross section of the oxide layer. This chapter partially addresses the third and fourth objectives of the thesis, “to evaluate the role of texture and grain size on improvement of the corrosion resistance of austenitic stainless steels 310S and 316L”, and “to recommend which of the investigated alloys and under what treatment conditions is expected to perform better in SCW”.

Finally, the summary and conclusion of the thesis with some suggestions for future work are presented in chapter 10.

1.6 Contribution to original knowledge

The current Ph.D. thesis investigates the performance of two austenitic stainless steels in SCW before and after modification to their microstructures. It contributes to the current knowledge on the performance of candidates alloy for generation IV supercritical water-cooled reactors in three

categories. Firstly, this is the first time that a comprehensive study on the corrosion performance of two candidate alloy for generation IV supercritical water-cooled reactor (SCWR) in SCW and air is accomplished. The result of this study would be beneficial to select a proper material for use in SCWRs. Secondly, optimizing the microstructure of stainless steel 316L and 310S using thermo-mechanical treatment with the aim of improving their corrosion resistance in SCW is done for the first time. Efforts are made to separate the effect of average grain size and texture as to key parameters of microstructure. Quantitative and qualitative analyses of samples after corrosion test reveal the responsible mechanisms for improvement in corrosion resistance of the alloys after implementation of thermo-mechanical processing. Finally, micro and macro texture measurements on the cross-section and the surface of the oxide layer of as-received and processed samples for both alloys is performed for the first time. The surface morphology of oxide and the orientation relation between substrate and produced oxides was elucidated using XRD and insitu EBSD/EDS characterization techniques.

2 LITERATURE REVIEW

2.1 Overview

The role of nuclear power as a source of energy, and the challenges related to design and construction of the next generation of nuclear reactors will be discussed in this chapter. This chapter does not include a detailed literature review to avoid repetition and instead the introduction section of each chapters provides the detailed review on the related subject.

2.2 Nuclear energy

The implication of greenhouse gases emission to climate change has initiated a global awareness in realizing the value of the clean sources of energies. According to United Nations, intergovernmental panel on climate change, the entire world emits almost 27 gigatons of carbon dioxide equivalent (CO2e), a measure used to compare the emissions from various greenhouse gases based upon their global warming potential, annually from different sources of energies from which 37 percent belongs to electrical production industries. It is also stated that fifty to eighty percent reduction in greenhouse gas emissions is required to stabilize the present levels of carbon dioxide concentration in the atmosphere. As the result and also taking the increase of world demand for electricity in the near future into account, considerable attention to research and development in the field of non-greenhouse gas-emitting power sources is a necessity [17–20].

Considering the amount of carbon dioxide emission during the construction of a nuclear power plant, the mining and processing of fuel, routine operation, disposal of used fuel and the ultimate dismantling of the facility, make nuclear energy comparable to wind energy and geothermal energy. Nuclear energy production saves 2.4 billion tons of carbon dioxide emission annually which would otherwise be produced by fossil-fired power generation plants.

2.3 Current and future nuclear reactors

After commissioning of the first commercial nuclear power plant on June 27, 1954 in Obninsk Russia, nuclear reactors have been continuously under technological development. Each generation of nuclear reactors brought a significant technical advances in terms of cost, safety, and performance. Figure 2.1 shows the evolution of nuclear reactors in the past decades. The first generation was represented by various prototype designs including gas-cooled graphite-

moderated, or water-cooled water-moderated that were implemented during the period 1950 to 1970. The second generation are light water pressurized and boiling water reactors built from 1970 to the turn of the century, most of which are still in operation today. Third generation nuclear reactors, usually called Generation III/III+, are the current advanced reactors which are mainly light water reactor (LWR). They have extended lifetimes, better efficiency, and improved safety features in the event of core damage. At the beginning of the new millennium, the world demand and surveillance on nuclear energy has led to international collaboration agreement under the Generation IV International Forum (GIF) which was established to accomplish development of the next generation of nuclear reactors by 2040 [21].

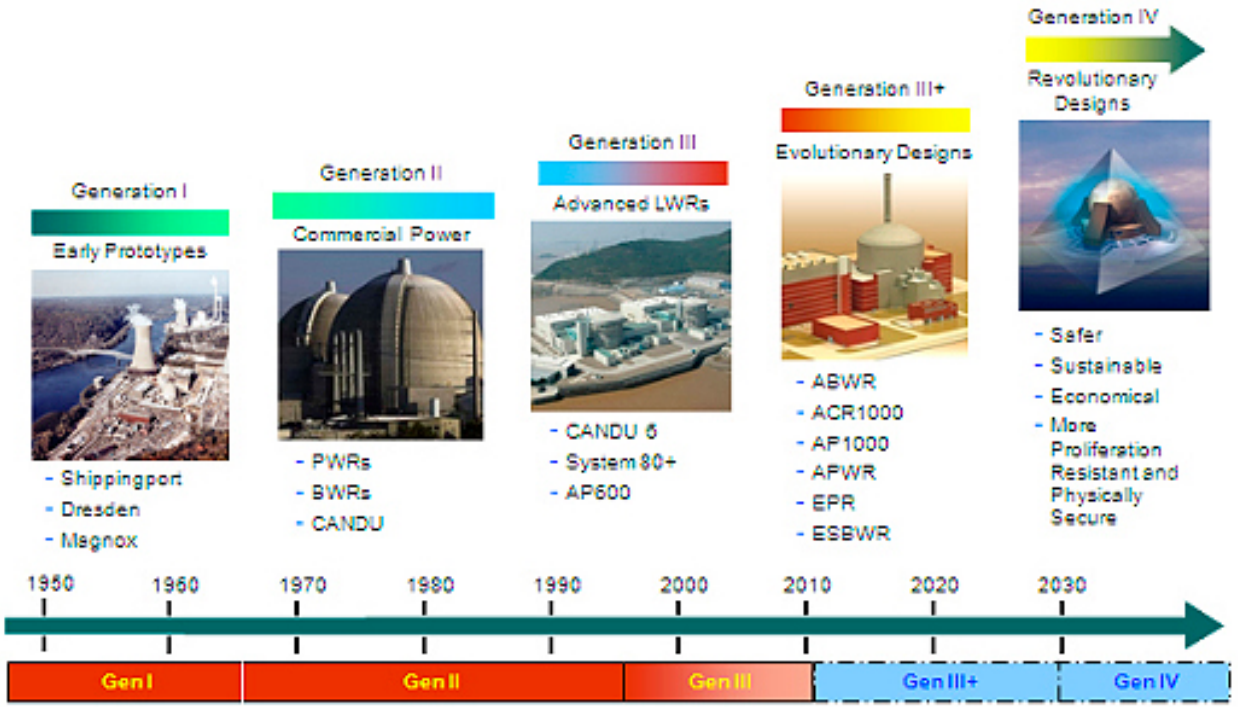

Figure 2.1. Evolution of nuclear energy reactors [21].

The currently operating nuclear reactors, so-called thermal reactors, need the high energy released neutrons in fission to be slowed down to thermal energies much less than 1 eV, so they can support fission process and maintain the chain reaction. Fast neutron reactors, on the other hand, are able to breed large amount of fissile material (Pu-239) from fertile material (U-238) which allows to extract at least fifty times more energy than the current thermal reactors from a given quantity of natural uranium. In addition, there is no need for a moderator and the core is

more compact compared to thermal reactors. Thus, as oppose to LWRs, the coolant does not serve as a moderator, and SCW or liquid metals are used to remove heat.

As of now, six different types of nuclear systems are under research and development globally. Among them, VHTR is a thermal neutron reactor, three others are fast neutron reactors including the gas-cooled fast reactor (GFR), Lead-cooled fast reactor (LFR), and Sodium-cooled fast reactor (SFR), and in addition molten salt reactor (MSR) and SCWR that can be operated as either a thermal or fast reactor. Table 2.1 listed the design specifications of these reactors. All of these concepts were selected from a wide range of possible designs and have potential to improve level of safety, increased sustainability, and have competitive economics [22]. Canada as a GIF member has undertaken the research and development in support of SCWR and VHTR systems. As SCWR is basically a developed version of the current CANDU reactors, SCWR was selected by NRCan as the main focus of research and development in collaboration with multilateral international organizations [23].

Table 2.1. Overview of the six Generation IV systems [22].

System	Neutron Spectrum	Coolant	Temperature (ºC)	Fuel Cycle	Size (MW)
SCWR	thermal/fast	Water	510-625	open/closed	300-700,1000-1500
VHTR	thermal	Helium	900-1000	open	250-300
SFR	fast	Sodium	550	closed	30-150,300-1500, 1000-2000
GFR	fast	Helium	850	closed	1200
LFR	fast	Lead	480-800	closed	20-180,300-1200,600-1000
MSR	fast/thermal	Fluoride salts	700-800	closed	1000

2.4 SCWR and material challenges

Figure 2.2 illustrates the operational temperature and pressure in BWR, PWR, and SCWR. In the current reactors, coolant temperature remains subcritical because of abrupt degradation in heat transfer at the surface of fuel rod covered by steam. The SCWR core, however, is operated above the critical point of water where no phase change is experienced and therefore the coolant temperature is able to exceed the pseudo-critical temperature (boiling temperature at subcritical pressure). As a result, SCWR has two important technical advantages over the conventional nuclear reactors. First, it has higher thermal efficiency due to high temperature and pressure of

turbine inlet steam. This means that SCWR would have 1.2 to 1.4 times higher thermal efficiency than current water cooled reactors. The second advantage is the simplification of the design with low capacity components. This could happen when there is no phase change and as a result the recirculation system and steam-water separation that is used in BWR, or steam generator and pressurizer used in PWR can be eliminated. On the other hand, the flow rate of the reactor coolant is much lower than in BWR and PWR as the enthalpy rise in the reactor core is much larger at supercritical state and therefore, low capacity components are needed. This simplification in design due to elimination of certain components will also result in significant drop in the capital cost [4,24].

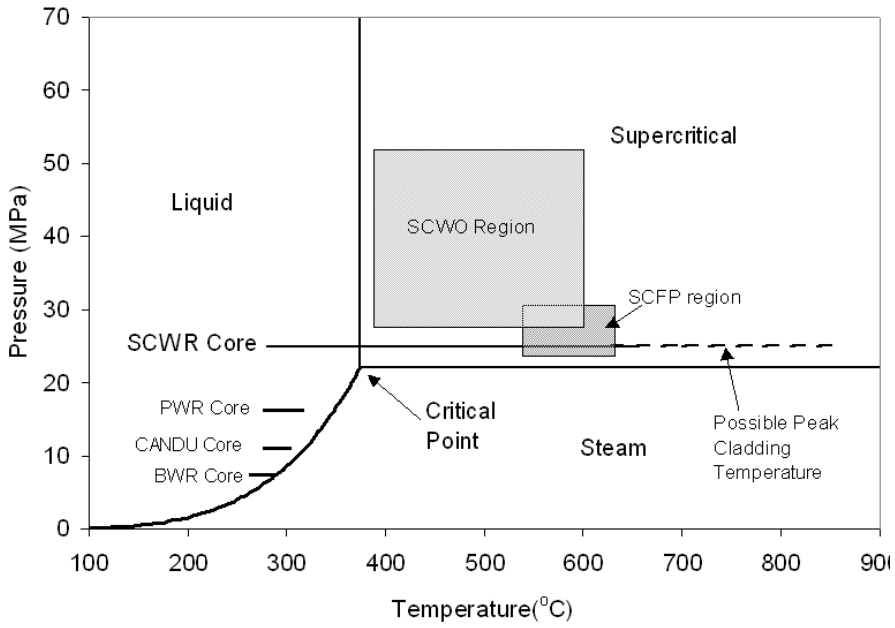

Figure 2.2. Phase diagram of water, showing the critical point and the relative operating regimes of SCWR, PWR, and BWR. The reference temperature shown is that of the US SCWR variant, while the Canadian SCWR outlet temperature is higher, at 625ºC [25].

Although there has not been any SCWR in operation as of now, using SCW as a coolant in a reactor was proposed in the 1960s [26,27]. Currently, two types of SCWR concepts have evolved from two existing reactor systems, as illustrated in Figure 2.3. The first concept, which is a large reactor pressure vessel, includes the reactor core heat source which is similar to conventional boiling water reactor (BWR) and pressurized water reactor (PWR) [28,29]. The second concept is

a design similar to CANDU and RBMK reactors and consists of number of pressure channels or tubes surrounding the fuel bundles [25].

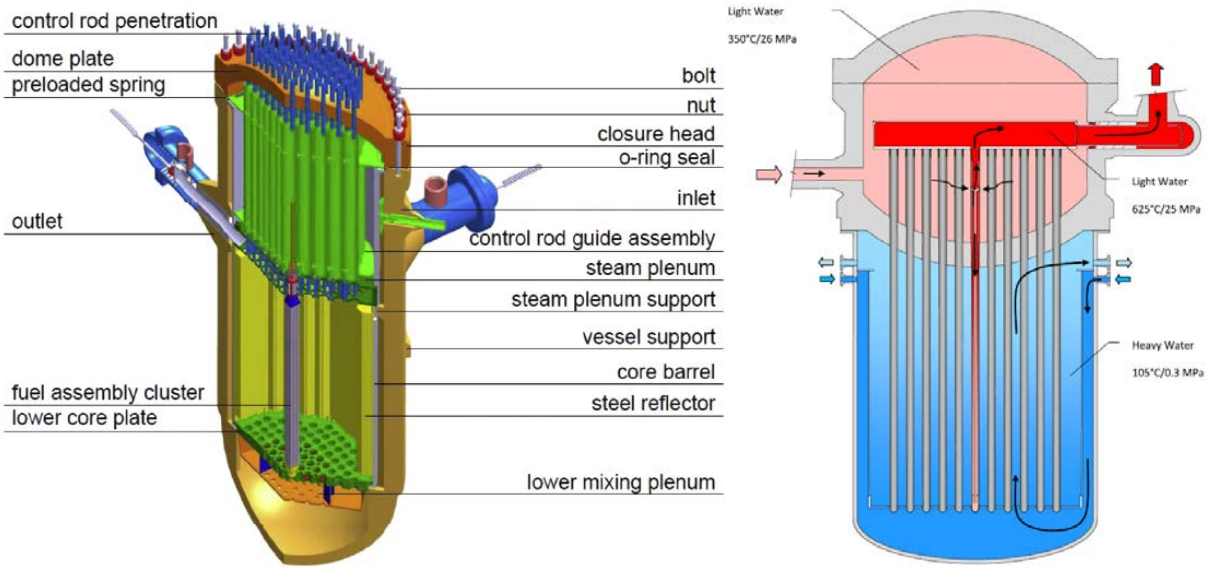

Figure 2.3. Schematic of (left) high performance light water reactor [29] and (right) Canadian SCWR [25].

Although SCWR has several advantages over the conventional nuclear reactors, there are technological challenges associated with its development. Demonstration of the passive safety system, the need for validation of transient heat transfer models, and finding materials for in and out of core components are the most important challenges to overcome ahead of exploitation of the SCWR. The candidate materials to be used inside the reactor are required to overcome the main concerns attributed to neutron irradiation damages, stress corrosion cracking (SCC), and corrosion at high temperatures and pressures. Up to now, several alloys including ferritic-martensitic steels (F-M steels), austenitic stainless steels, nickel-rich alloys, and titanium based alloys are candidates. Table 2.2 compares properties of these alloys [30].

As for radiation damage resistance, the candidate materials for in-core components required to have high neutron transparency. This is required to minimize neutron losses and to help sustaining the nuclear chain reactions. Table 2.3 lists the neutron absorption cross section of some of the elements used in the reactor core [31]. Cadmium and beryllium have respectively the highest and lowest absorption cross section. Cadmium is being used in control rods to stop the chain reaction in case of need or emergency. Beryllium on the other hand, was considered for fuel cladding

materials back in 1950s, but its brittleness, toxicity, and cost made it an inappropriate choice [31]. Zirconium alloys are being widely used as fuel cladding in the current generation of nuclear reactors including CANDU reactor. However, these alloys would not be suitable candidates for SCWR as good mechanical performance at higher temperatures and pressures is required. Therefore, alloys such as nickel based super alloys and austenitic stainless steels are more suitable. Nevertheless, as listed in Table 2.3, their neutron transparency are about 14 and 24 times lower than zirconium. In addition, considering the embrittlement and swelling issues attributed to formation of helium make nickel based super alloys less favorable in comparison to austenitic stainless steels.

Table 2.2. Corrosion resistance, radiation damage resistance and HT mechanical integrity comparison between candidates for fuel cladding materials [30].

Alloy Type	High Temperature Mechanical Integrity	Radiation Damage Resistance		Corrosion Resistance	
		Swelling[1]	Embrittlement[2]	General Corrosion	SCC[3]
F-M Steels	Low	High	High	Medium	High
Austenitic Stainless Steels (high Cr content)	High	High	Limited Data	High	Medium
Ni-Based	High	Low	Medium	High	Medium
Ti-Based	Medium	Limited Data	Limited Data	Medium	Limited Data

Table 2.3. Neutron absorption cross section of selected elements used inside the reactor core [31].

Element	Atomic Number	Neutron Absorption Cross Section (σa/barns)
Be	4	0.0092
Zr	40	0.184
Cr	24	3.05
Fe	26	2.56
Ni	28	4.49
U	92	7.57
Cd	48	2450

[1] Swelling is an increase in the alloy volume as a result of very strong radiation.

[2] Embrittlement means the loss of ductility due to presence of hydrogen and helium in SCW or neutron radiation.

[3] Stress corrosion cracking (SCC) is a result of simultaneous influence of stress and corrosive environment and characterizes susceptibility of material to form cracks.

2.5 Stainless steels

Having chromium content more than 11 weight percent and as a result having a surface protective layer of chromium oxide make stainless steels a suitable choice to be used in industry where good corrosion resistance is required. Stainless steels are classified by their predominant phase constituent as the ferritic, martensitic and austenitic stainless steels. The austenitic stainless steel family has the best high temperature corrosion resistance. They can be used at temperatures as high as 1000 ºC and maintain their good mechanical properties as well as oxidation resistance. This is because of higher chromium content and higher presence of nickel compared to the other two types of steel [32].

Since the start of global research aimed to select and improve alloys that are suitable for making various elements for the next generation of nuclear reactors, austenitic stainless steels have shown promising corrosion and irradiation resistance [6,33,34]. As shown in Table 2.3, high chromium content in austenitic stainless steels results in a good corrosion resistance and good resistance against stress corrosion cracking.

In this thesis, two types of stainless steels, 310S and 316L, will be tested for application in SCWR in details. We should note that this study is only on the corrosion resistance of these steels and their resistance to stress corrosion cracking deserves a separate research effort.

3 EXPERIMENTAL METHODOLOGY

3.1 Overview

In this chapter the selected alloys, the facility and experimental procedures for this study are described in detail. Austenitic stainless steels 316L and 310S are the two candidate alloys for this comparative study. Two conditions including SCW and air are applied to test these candidate materials. In addition, TMP is also utilized to optimize the microstructure of the as-received stainless steels with a goal to improve the oxidation resistance on the candidate alloys in oxidation conditions.

3.2 Materials

Chemical compositions of the candidate materials used in this study are listed in Table 3.1. They are hot rolled with an average grain size of 20μm. Stainless steel AISI 316L is the low carbon version of type 316 with addition of molybdenum to be especially used in severe corrosion environments due to the materials immunity from boundary carbide precipitation. The alloy main application is in heavy gauge welded components with low necessity for weld annealing for use in high stress environments. Owing to its high corrosion resistance, the material is also of great importance for marine application and oxidation at elevated temperature in atmospheric conditions [35,36]. Combining excellent high temperature oxidation resistance with good ductility and weldability, stainless steel AISI 310S is superior to 304 or 309 stainless steel in most environments due to its higher nickel and chromium content. This alloy can maintain good corrosion resistance and strength at elevated temperatures up to 1150ºC where sulphur gases are not present. This also applies for intermittent service up to 1040ºC. This grade has applications in food processing equipment, cryogenic structures, coal gasifier internal components, refractory anchor bolts, fluidized bed combustors, tube hangers for petroleum refining and steam boilers, burners and combustion chambers [35,36].

Table 3.1. Chemical composition of the as-received alloys.

Alloy	Element (wt %)										
	C	Mn	P	S	Si	Cr	Ni	Co	Cu	Mo	Fe
316L	0.016	1.33	0.03	0.001	0.54	17.32	10.07	0.21	0.35	2.02	bal.
310S	0.05	0.93	0.016	0.001	0.58	25.41	19.15	0.5	0.6	0.15	bal.

3.3 Thermo-mechanical processing

To prepare samples with different initial microstructures for oxidation test TMP was carried out. Strips of 50 mm × 50 mm × 6.25 mm (L×W×T) were cut from the as-received alloy and thermo-mechanically processed in two steps. First, they were cold rolled at room temperature with two different deformation modes: unidirectional rolling (UDR) and cross rolling (CR). Reduction in thickness achieved by cold rolling was up to 10, 30, 50, 70 and 90% with equal rolling inter-steps of 10% true strain. The small true strain was selected to avoid sample rupture due to strain hardening, especially at higher deformations. The implemented rolling processes and their differences are illustrated in Figure 3.1.

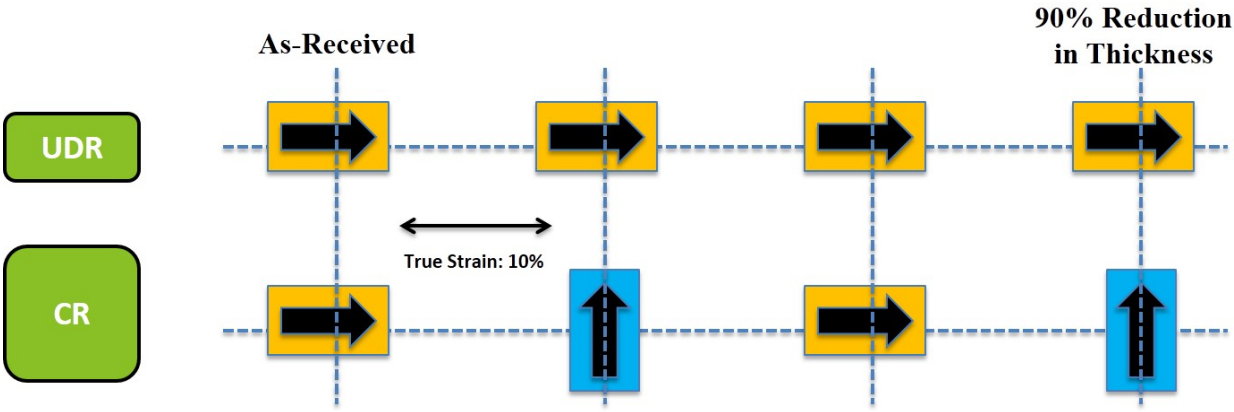

Figure 3.1. Schematic of TMP including unidirectional rolling and cross-rolling with equal inter-pass rolling steps of 10% true stain.

At the second step, to achieve a recrystallized microstructure with equiaxed grains, samples were annealed at 1050ºC for 5 minutes per millimeter thickness. Table 3.2 listed the detailed information of the as-received and thermo-mechanically processed samples used in this study. The sample name is comprised of deformation mode, value of the reduction in thickness, and post rolling treatment ("A" stands for annealing), respectively.

3.4 Samples preparation

Stainless steels 316L and 310S were supplied by manufacturer in plate form with thickness of 6.25 mm. A total of three samples of each as-received and thermo-mechanically processed materials were prepared to test in SCW for 100, 300, and 1000 hours. All samples were cut first

with precision cutter (Buehler Isomet 1000) to 25.0 mm × 15.0 mm × 0.6 mm (L×W×T) and a press driller was used to drill a hole of 2.5 mm diameter with the center located in the middle of the width and 5 mm form the top. Figure 3.2 depicts the schematic of a prepared sample with the position of the drilled hole. Samples were ground manually to 2000 grit (10μm SiC particles) with progressively done grinding process from 240, 320, 400, 600, 800, 1200, and 2000. They were cleaned in an ultrasonic bath in two solutions: water and detergent (1 drop/50 ml of distilled water) for 30 min and acetone for 10 min. Sample were handled with tweezers in every step after ultrasonic cleaning to avoid contamination. They were baked at 100ºC for an hour for moisture removal and then all of their dimensions were measured with a caliper and recorded. Samples were weighed three times using a scale to an accuracy of 10^{-5} g before and after oxidation tests.

Table 3.2. TMP conditions of stainless steel 316L and 310S.

Deformation mode	Reduction (%)	Post rolling treatment	Sample name	Average Grain Size (μm)	
				316L	310S
-	-	-	As-received	20	20
UDR	10	-	UDR10	-	-
		Annealed	UDR10A	20	20
	30	-	UDR30	-	-
		Annealed	UDR30A	15.1	12.5
	50	-	UDR50	-	-
		Annealed	UDR50A	6.7	6.2
	70	-	UDR70	-	-
		Annealed	UDR70A	3.2	2.9
	90	-	UDR90	-	-
		Annealed	UDR90A	1.1	1.3
CR	10	-	CR10	-	-
		Annealed	CR10A	20	20
	30	-	CR30	-	-
		Annealed	CR30A	8.6	8.3
	50	-	CR50	-	-
		Annealed	CR50A	6.0	5.9
	70	-	CR70	-	-
		Annealed	CR70A	2.4	2.3
	90	-	CR90	-	-
		Annealed	CR90A	1.1	1.5

Figure 3.2. Position of hole for samples.

3.5 Oxidation in air and supercritical water

Oxidation in air was carried out in a MTI Corporation GSL-1500X-50 tube furnace. To make sure oxygen concentration stays stable, a continuous airflow of 1 L/min was supplied through the tube furnace for the entire experiment. Figure 3.3 shows the tube furnace setup used for oxidation in air. Oxidation temperature was set at 600 ºC for 100, 300, and 1000h.

Figure 3.3. Tube furnace used for oxidation in air.

Testing for SCW condition was done in an autoclave at VTT Technical Research Center of Finland. Figure 3.4 depicts the schematic of the autoclave and sample holder rack used for conducting oxidation in SCW environment. Similar to oxidation in air, oxidation in SCW took place at 600ºC for 100, 300, and 1000h, except the pressure was 25 MPa. Details of the experiment conditions are listed in Table 3.3.

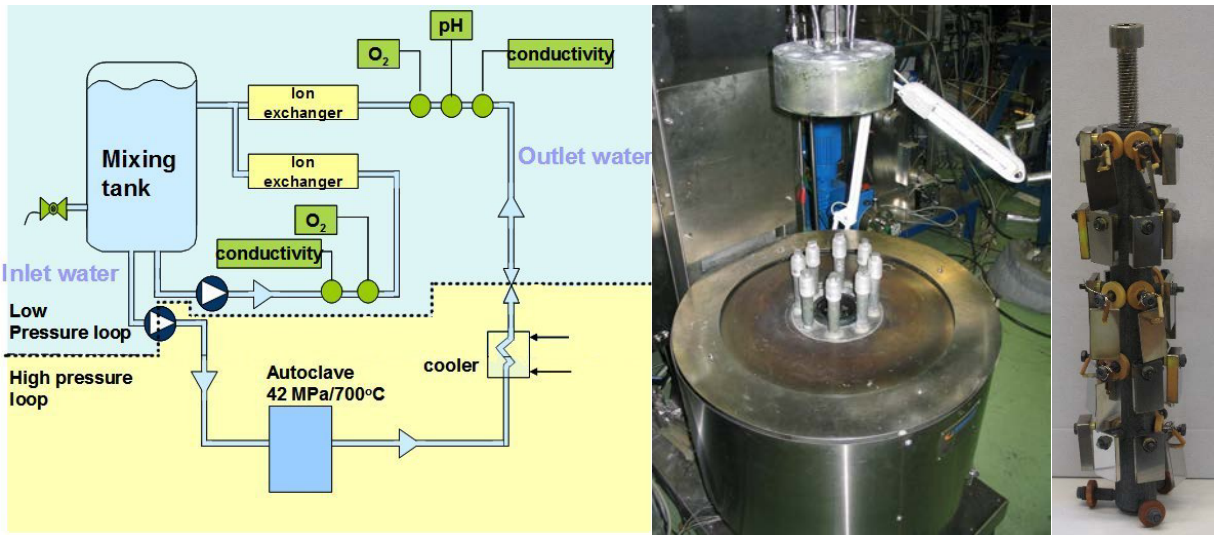

Figure 3.4. Schematic of the supercritical autoclave system and sample holder rack.

Table 3.3. Targeted and realized values for the SCW test environment

Quantity	Target value / range	Notes/realized values (mean ± SD)
Temperature	600ºC	Recorded mean 599 ± 1.0 ºC
Pressure	250 bar	Recorded mean 250 ± 0.9 bar
Inlet conductivity	0.1-0.5 µS/cm	Recorded mean 0.053 ± 0.001 µS/cm
Outlet conductivity	1.0-3.0µS/cm	Recorded mean 0.29 ± 0.11 µS/cm
Inlet dissolved O_2	150 ppb	Recorded mean 150 ± 0.5 ppb
pH of the inlet water	7.0	(Pure water)
Flow rate	~5 ml/min	Full renewal about every 2 h

3.6 Analysis of the samples

After oxidation experiments in the tube furnace and the autoclave, samples were cleaned and rinsed with acetone and distilled water. Inspection and analysis of the samples were carried out following the steps as described.

3.6.1 Visual inspection

All samples were handled with tweezers in all steps after removal from the furnace or autoclave.

Visual inspection was done right after to record all visible coloring changes, imperfections, exfoliation of oxide, excessive oxidation areas with digital camera. Samples were labeled with white paper to obtain a good contrast for a better inspection and identification. Photo of samples was captured with a Nikon 7100 DSLR camera after inspection.

3.6.2 Weight change

Weight changes in samples after oxidation is one of the easiest and most efficient ways to evaluate their resistance to conditions to which they were exposed. Samples were cleaned first and weighted five times using a OHSAUS AP110 digital scale. Figure 3.5 shows the digital scale used for weighing the samples. The results were recorded and the weight change per surface area were plotted to be used in following chapters.

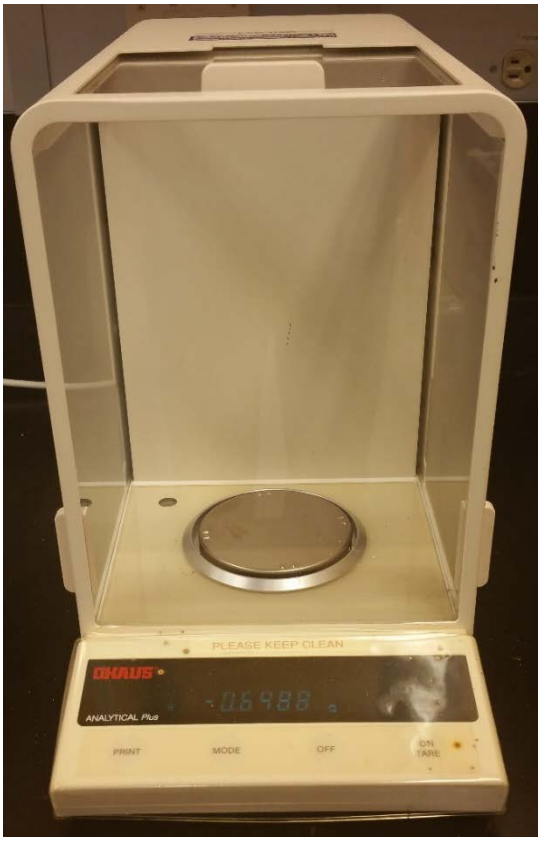

Figure 3.5. Digital scale OHAUS AP110.

3.6.3 X-ray diffraction and texture measurements

X-ray diffraction (XRD) technique with Cr Kα radiation was used to identify the present phases and compounds as well as the macro-texture of samples before oxidation (at the mid-section of deformed and recrystallized samples) and after oxidation (from top surface of the oxides). Cr Kα radiation was selected over Cu Kα to avoid fluorescence of iron atoms which appears in the background of the diffraction pattern. Figure 3.6 shows the Bruker D8 Discover XRD system used

in this experiment. Diffraction pattern was collected for 2θ between 20 to 120 degree to cover as much as possible peaks available in the range of detector geometrical limits. For macro-texture measurement, the incomplete pole figures of all samples were collected and the orientation distribution function (ODF) was constructed using Resmat® software. Reconstructed pole figures and inverse pole figures were obtained from the ODF if needed.

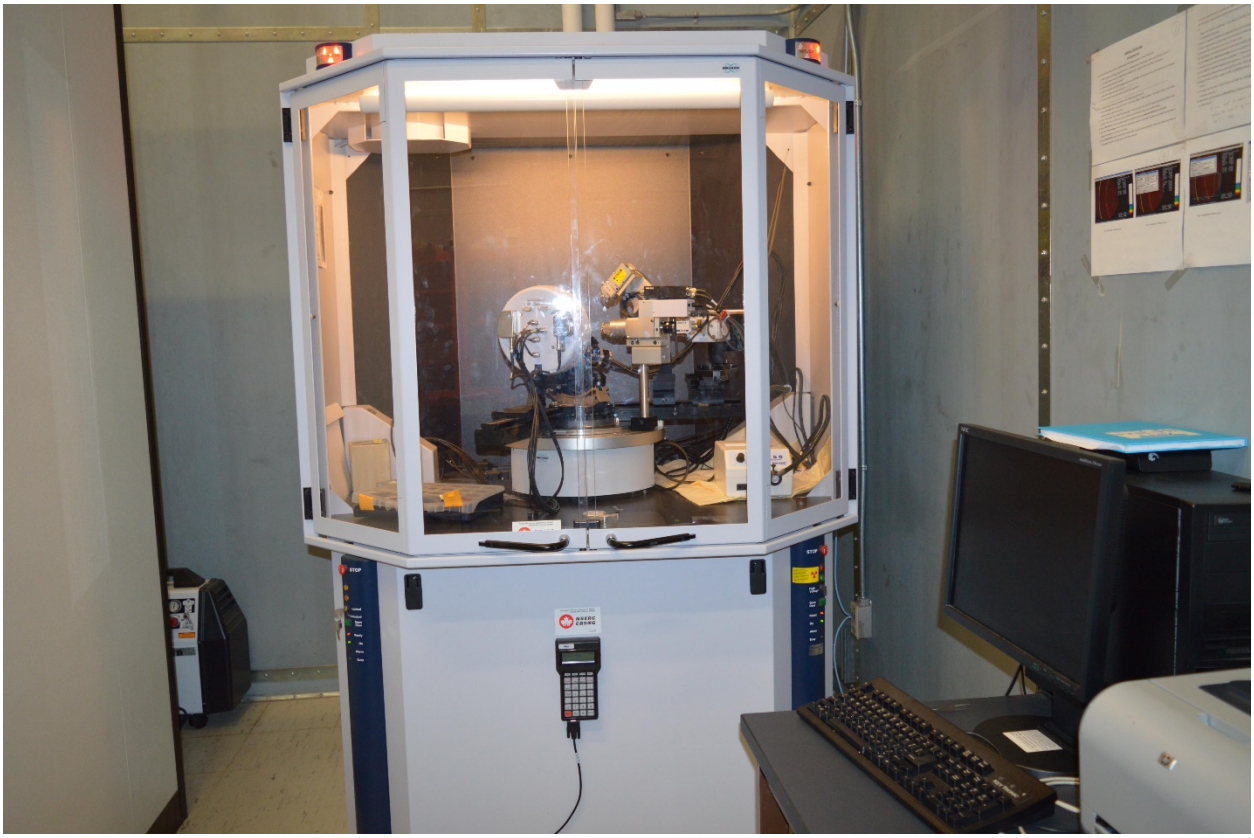

Figure 3.6. Bruker D8 Discover XRD system.

3.6.4 Scanning electron microscopy (SEM) and energy dispersive x-ray spectroscopy (EDS)

To examine the surface changes of the samples due to oxidation, SEM and EDS techniques were implemented. For this purpose, a Hitachi SU6600 SEM equipped with an Oxford X-Max Silicon Drift EDS were used (see Figure 3.7). The focus was mainly on changes of the surface morphology, microstructure, and composition. Secondary electron was detected to acquire good quality images for which SEM was set at 1 kV. To enable EDS to detect all the present elements in the samples, SEM was set at 15 kV. High resolution elemental map, line scans on top surface and at cross-section of oxides were collected to determine the composition of oxides.

Figure 3.7. Hitachi SU6600 SEM equipped with an Oxford X-Max Silicon Drift EDS and Oxford NordlysNano EBSD.

3.6.5 Electron backscatter diffraction system (EBSD)

Orientation imaging microscopy (OIM) is a surface analytical tool in SEM which is based on EBSD technique. To construct orientation maps or orientation imaging micrographs, scans of crystal orientation needs to be measured from a portion of the material surface. Details of microstructure such as grain orientation, shape, and size, grain boundary characteristics, texture, micro strain, and phase identification can be achieved from these maps [37–39]. In this study, SEM was set at 20 kV which was equipped with an electron backscatter diffraction system (Oxford NordlysNano EBSD). For data acquisition in EBSD technique, a near perfect polished sample surface is required. The samples were mounted at the cross section in a conductive and edge retention resin (Struers Polyfast®) and then grinded with abrasive paper up to grit number 2000 (10µm SiC particles). Polishing was performed using a water based diamond suspensions up to 1 µm diamond particle size (Struers DiaPro®) at polishing wheel speed lower than 150 rpm to avoid breakdown of the fragile oxide layer. Final stage of polishing was done using 0.04 µm colloidal silica suspension (Struers OP-S®) on a Vibratory Polisher (Buehler VibroMetTM 2) for 24 h.

4 OXIDATION BEHAVIOR OF AUSTENITIC STAINLESS STEEL 316L AND 310S IN AIR AND SUPERCRITICAL WATER

4.1 Overview

This chapter addresses the first objective of the thesis which is "to evaluate the oxidation resistance of austenitic stainless steels 310S and 316L in SCW as well as in air for comparison". It reports a comparative study of oxidation of the as-received austenitic stainless steels 310S and 316L in air and SCW. The aim is to evaluate how the two alloys perform in SCW and, for comparison they were oxidized in air at the same temperature as in SCW. In order to properly compare the performance of the both alloys, similar initial microstructures in terms of texture and grain size were selected. Both alloys were characterized using XRD, SEM and EDS techniques after oxidation in air and SCW to identify the oxides formed on their surfaces and to understand the mechanisms that decrease the oxidation in one case and increase it in another.

This manuscript was published in the Journal of Nuclear Engineering and Radiation Science[4] and slight changes have been applied to the original version to avoid repetition. To fulfill the objective addressed in this chapter, Dr. Hamed Akhiani[5] assisted the author of this Ph.D. thesis (Majid Nezakat) with preparation and processing of the samples as well as performing the data analysis. In addition, the corrosion tests in SCW were performed by Mr. Sami Pentillä[6]. Jerzy Szpunar, as the supervisor of this research, provided recommendation, consultation and discussion wherever it was needed. Except the entire or a portion of these parts, all the experiments, data acquisition, and data analysis were conducted by Majid Nezakat, the lead author of the paper. Majid Nezakat wrote the manuscript, integrated comments from the co-authors, and submitted it for review and publication.

4.2 Abstract

In this study, the oxidation resistance of austenitic stainless steels 316L and 310S in two different environments was evaluated; air at 600ºC and atmospheric pressure and SCW at 600ºC

[4] The copyright permission to use the manuscript in the thesis is obtained and provided in the appendix section. The references of this chapters are provided at the end of the thesis.

[5] Mitsubishi Hitachi Power Systems Canada, LTD., 826 58th Street East, Saskatoon, SK, S7K 5Z4, Canada

[6] VTT Technical Research Center of Finland, Materials for Power Engineering, P.O. Box 1000, FI-02044 VTT, Finland

and pressure of 25 MPa. Results indicated that both alloys showed good oxidation resistance in air by producing a protective oxide layer on their surface. In addition, alloy 310S exhibited lower weight gain during air oxidation compared to alloy 316L due to its higher content of chromium and nickel. Oxidation of alloy 310S in SCW was much lower than that of alloy 316L because of the formation of protective layer of Mn_2CrO_4 spinel on the surface. No protective scale was formed on the surface of the alloy 316L as magnetite (Fe_3O_4) and iron-chromium spinel ($FeCr_2O_4$) were the production of oxidation in SCW.

4.3 Introduction

Ever since the operation of the first commercialized nuclear power plant in the 1950s, nuclear reactors have been continuously under development. Each generation of the nuclear power plants brought new technical advances in safety, performance, and cost compared to the previous generation. Although the generation III nuclear reactors, as an evolution of current light water reactor (LWR) technology, made great improvements in performance, lifetime, and more desirable responses in the event of emergencies, there is room for more evolution especially in terms of better safety, more simplification in design, and efficiency. Therefore, Generation IV International Forum (GIF) as a joint international endeavor consisted of thirteen countries started the required research and developments to pursue the feasibility and performance challenges for establishment of the next generation of nuclear energy systems.

SCWR is one of the six concept designs on which the contributing members are working. In this design, SCW, as the cooling and heat transfer medium, provides higher thermal efficiency, and at the same time more severe environment for the structural materials used inside the reactor core [40,41]. As a result, one of the major challenges in design of generation IV nuclear power plants is to develop proper materials which are able to withstand the harsh medium inside the reactor. Among the proposed materials, Fe-Ni-Cr based alloys such as austenitic stainless steel 316L and 310S, which are used as structural materials in conventional nuclear reactors [42,43], drew a lot of attentions due to their superior properties including oxidation and creep resistance [4,5,44,45,13,46–50]. Few available literature on SCW oxidation of Fe-Ni-Cr based alloys reported that austenitic stainless steel 310S generally exhibit a lower oxidation rate and weight gain, compared to austenitic stainless steel 316L [51–54,15]. However, most of these studies have

been done using a static autoclave which often leads to lower oxidation and less spallation than dynamic/recirculating autoclaves.

The objective of this work is to evaluate the performance of stainless steels 316L and 310S in SCW using a dynamic/recirculating autoclave. For comparison, results from air oxidation at the same temperature and atmospheric pressure is also presented.

4.4 Materials and methods

Hot rolled stainless steels 316L and 310S billets with average grain size of 20μm were used in this study. The chemical composition of the alloys is shown in Table 3.1. A Bruker D8 Discover XRD system with Cr K_α radiation for macro-texture measurements was used. The incomplete pole figures at the mid-section of all specimens were collected and the orientation distribution function (ODF) was constructed using Resmat® software. Samples were cut from the as-received billets and mechanically abraded on all surfaces with abrasive paper up to grit number 2000 (10μm SiC particles). The final dimensions of samples were 24 mm × 14 mm × 0.6 mm (L×W×T) after mechanical grinding.

The samples were oxidized in SCW at 600ºC and 25 MPa for 100, 300 and 1000h in an autoclave connected to a recirculation water loop, as illustrated in Figure 3.4. The values of temperature, pressure, inlet and outlet water conductivity, oxygen content and flow rate, which were monitored and controlled, are listed in Table 3.3. Air oxidation was also conducted in a furnace with air flow at 600ºC and atmospheric pressure. The weight of each specimen was measured before and after 100, 300 and 1000h exposure and the weight changes were calculated per unit area. X-ray diffraction (XRD) technique with Cr Kα radiation was used once more to identify the present phases in the oxide scale. In addition, to characterize the oxide structure, the samples were mounted at the cross section in a conductive edge retention resin (Struers Polyfast®) and then grinded with abrasive paper up to grit number 2000 (10μm SiC particles). Polishing was performed using a water based diamond suspensions up to 1 μm diamond particle size (Struers DiaPro®) at polishing wheel speed lower than 150 rpm to avoid breakdown of the fragile oxide layer. Final stage of polishing was done using 0.04 μm colloidal silica suspension (Struers OP-S®) on a Vibratory Polisher (Buehler VibroMetTM 2) for 24 h. The cross section of the samples was then analyzed using field emission gun scanning electron microscope (FEG-SEM) at 20 kV

equipped with electron backscatter diffraction (EBSD) and energy dispersive spectroscopy (Oxford X-Max Silicon Drift EDS) detectors.

4.5 Results

To be able to compare the oxidation results of both alloys in air and SCW, they should have similar microstructure in terms of texture and grain size. Figure 4.1 and Figure 4.2 illustrate the ODF, and orientation imaging microscopy (OIM) map of the austenitic stainless steels, respectively. Common texture components of steels are also illustrated in Figure 4.3 as a reference. As it can be observed, four major texture components including Brass {110}<112>, S {123}<634>, Copper {112}<111>, and Cube {001}<100> are present in the ODF of both alloys. In addition, grain size measurements show that both alloys have almost similar average grain size of approximately 20µm.

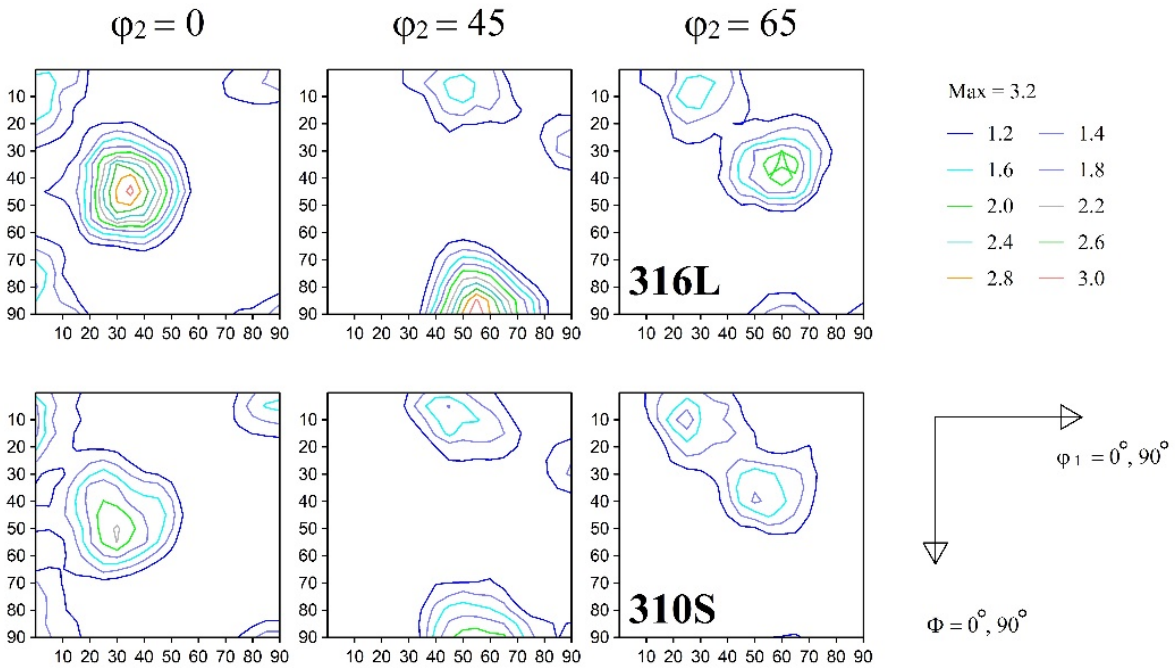

Figure 4.1. ϕ2= 0º, 45º, and 65º sections of the ODF of hot rolled stainless steels 316L and 310S.

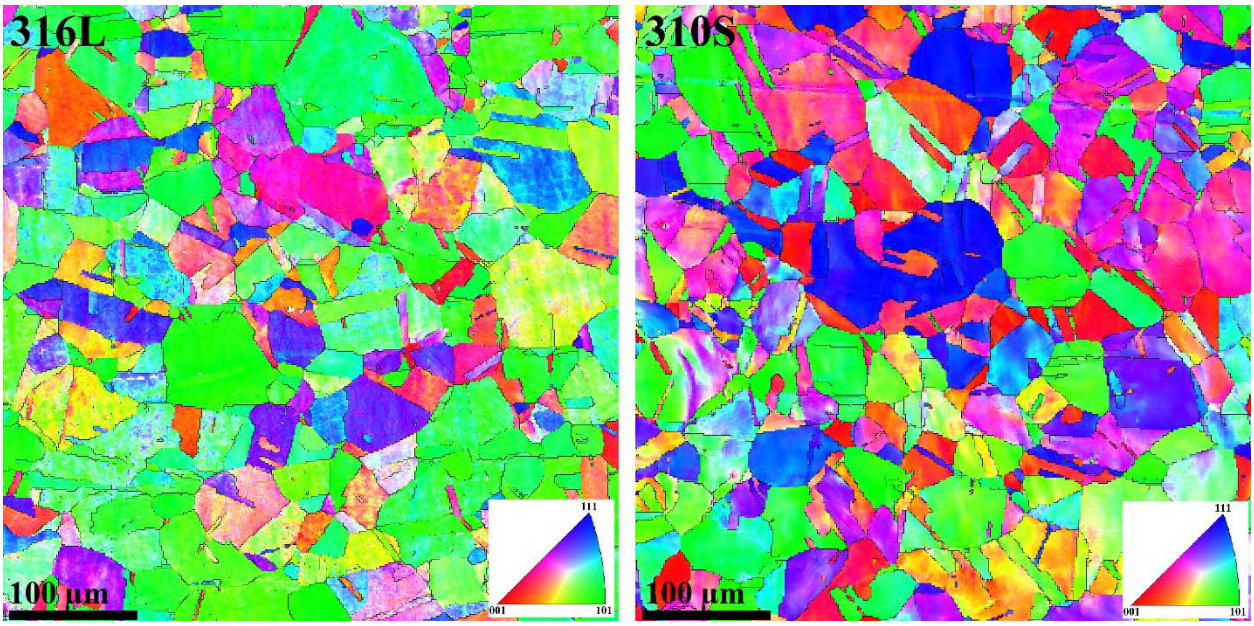

Figure 4.2. OIM map of hot rolled stainless steels 316L and 310S.

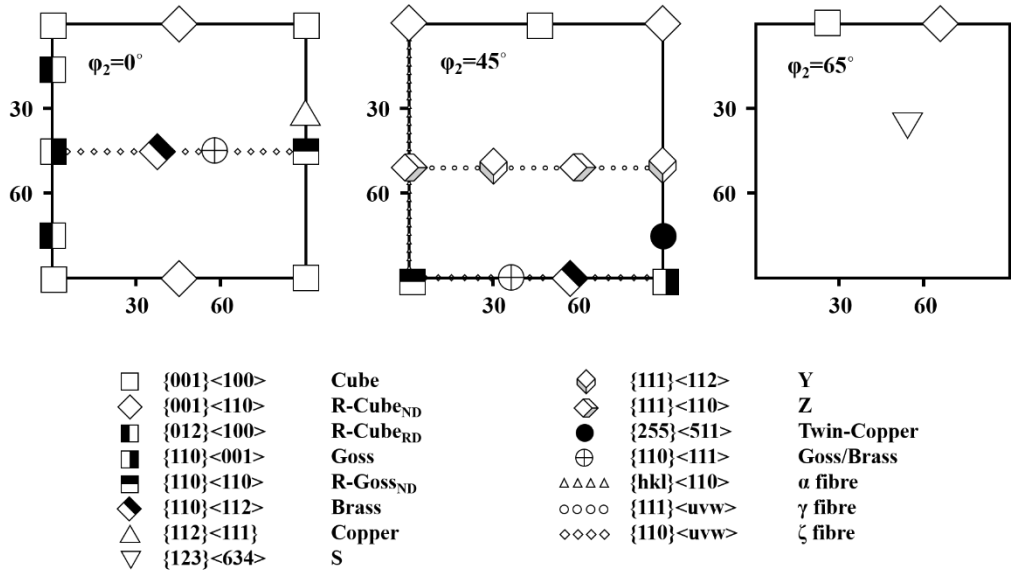

Figure 4.3. Main orientations and fibres observed in steels.

4.5.1 Weight Change

Figure 4.4 shows the weight change of stainless steels 316L and 310S after oxidation in air and SCW at 600ºC for 100, 300, and 1000h. In general, both alloys show a better oxidation resistance in air than that in SCW, however, the difference is more pronounced in case of stainless steel 316L. In addition, one can state that alloy 310S has a better performance in both air and SCW compared to alloy 316L.

As seen, after 100h of oxidation in air, stainless steel 316L has a weight gain about 0.2 mg/cm^2. This remains almost constant up to 1000h of oxidation. The weight change trend is different in SCW. As observed, the weight gain is about 0.6 mg/cm^2 after 100h of exposure to SCW and it increases to 1.8 mg/cm^2 after 300h of oxidation. It is obvious that the weight change is increasing by oxidation time in SCW, however, a weight loss is observed after 1000h.

As for stainless steel 310S, a weight gain is observed after 100h of air oxidation which is about 0.04 mg/cm^2. The weight gain increases to 0.05 mg/cm^2 after 300h and remains constant up to 1000h of oxidation. As oppose to 316L, stainless steel 310S does not experience weight loss during oxidation in SCW. The weight gain for alloy 310S in SCW starts at 0.02 mg/cm^2 after 100h of exposure time and it increases to 0.06 and 0.24 mg/cm^2 after 300 and 1000h, respectively.

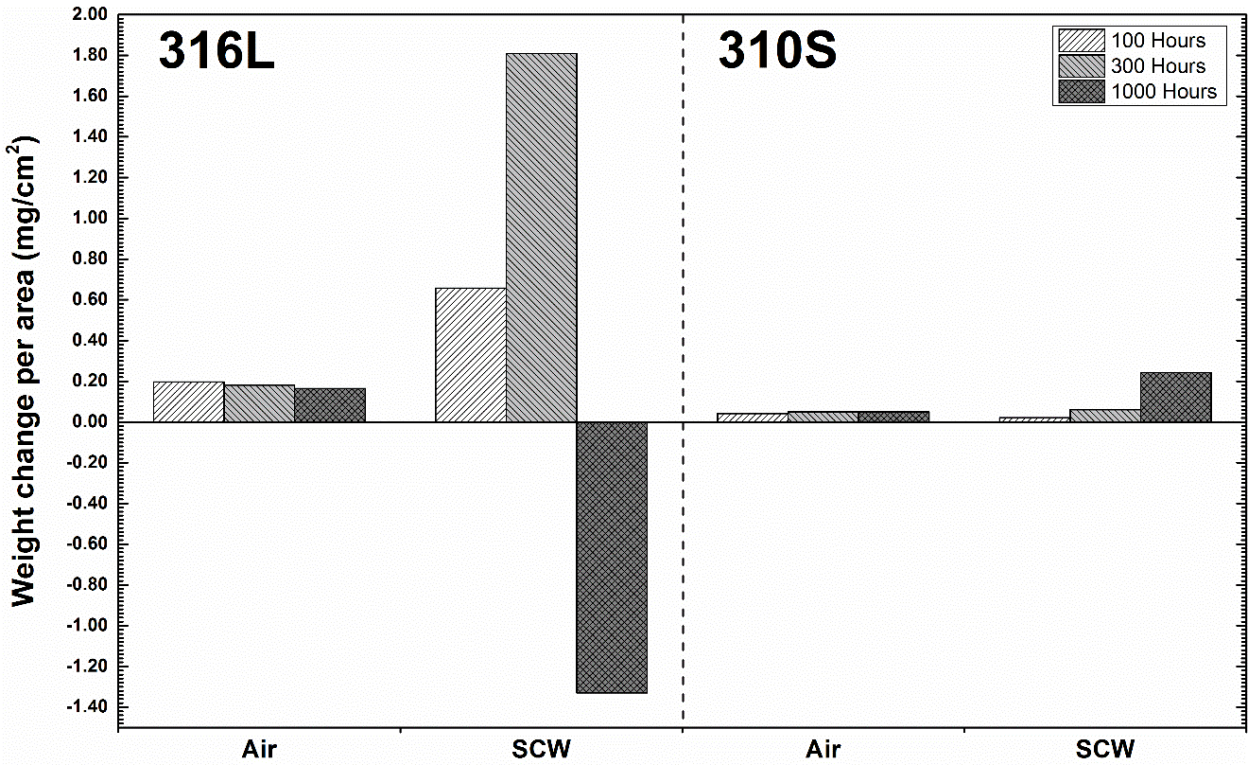

Figure 4.4. Weight change of stainless steels 316L and 310S in air and SCW.

4.6 Phase identification

Figure 4.5 illustrates the x-ray diffraction patterns of both alloys after oxidation in air and SCW. Since the weight change was constant during air oxidation up to 1000hours, only the oxidation patterns at 1000 hours are depicted. Three oxides including chromium oxide (Cr_2O_3),

iron-chromium spinel ($FeCr_2O_4$), and manganese-chromium spinel (Mn_2CrO_4) were detected on 316L sample after air oxidation. Similar oxides also formed on 310S sample during air oxidation. On the other hand, SCW exposure resulted in different oxides compared to those formed during air oxidation. It is noted that the intensity of the oxide peaks is much more pronounced for 316L sample compared to 310S sample. Hematite (Fe_2O_3), manganese-chromium spinel (Mn_2CrO_4), and nickel-iron spinel ($NiFe_2O_4$) are detected in XRD pattern of 310S sample after oxidation in SCW for 100 hours, while magnetite (Fe_3O_4) and iron-chromium spinel ($FeCr_2O_4$) are the oxide phases formed on alloy 316L. No oxide was formed or decomposed on both alloys until oxidation for 1000 hours.

Figure 4.6 shows the SEM micrograph, EDS elemental composition maps, and line scan of stainless steels 316L and 310S after 1000h of air oxidation at 600ºC. The SEM micrographs for both steels after oxidation show similar features including large and bright as well as dark and small oxide grains. The composition maps of the alloys show that the aforementioned oxide grains are manganese-chromium oxide and iron-chromium oxide, respectively. The iron-chromium oxide grain size is between 500 nm to 1 µm, while the average grain size of manganese-chromium oxides is about 100 nm. Line scan through both grains also confirms similar oxide compositions on the surface. Nevertheless, SEM and EDS techniques are not able to separate the chromium oxide from the other two spinel phases. Significantly higher intensities of the oxides' peaks in the XRD pattern of the alloy 316L after oxidation in SCW compared to that of air oxidation (see Figure 4.5) is an indication of much thicker oxide scale on this alloy. Therefore, the cross-section of the sample was observed by EBSD and EDS techniques.

Figure 4.7 depicts the EBSD band contrast and EDS elemental composition maps of the alloy 316L after 1000h exposure to SCW. The EDS maps were not normalized for better image contrast as concentration of chromium and nickel are very low compared to oxygen and iron. Three different regions are present in Figure 4.7 including external oxide, internal oxide, and substrate. Iron and oxygen are the only two elements present in the top layer (external oxide). The second layer (internal oxide), which is right beneath of the surface, is consisted of chromium, iron, and oxygen. The internal oxide layer has a similar thickness to that of the external one.

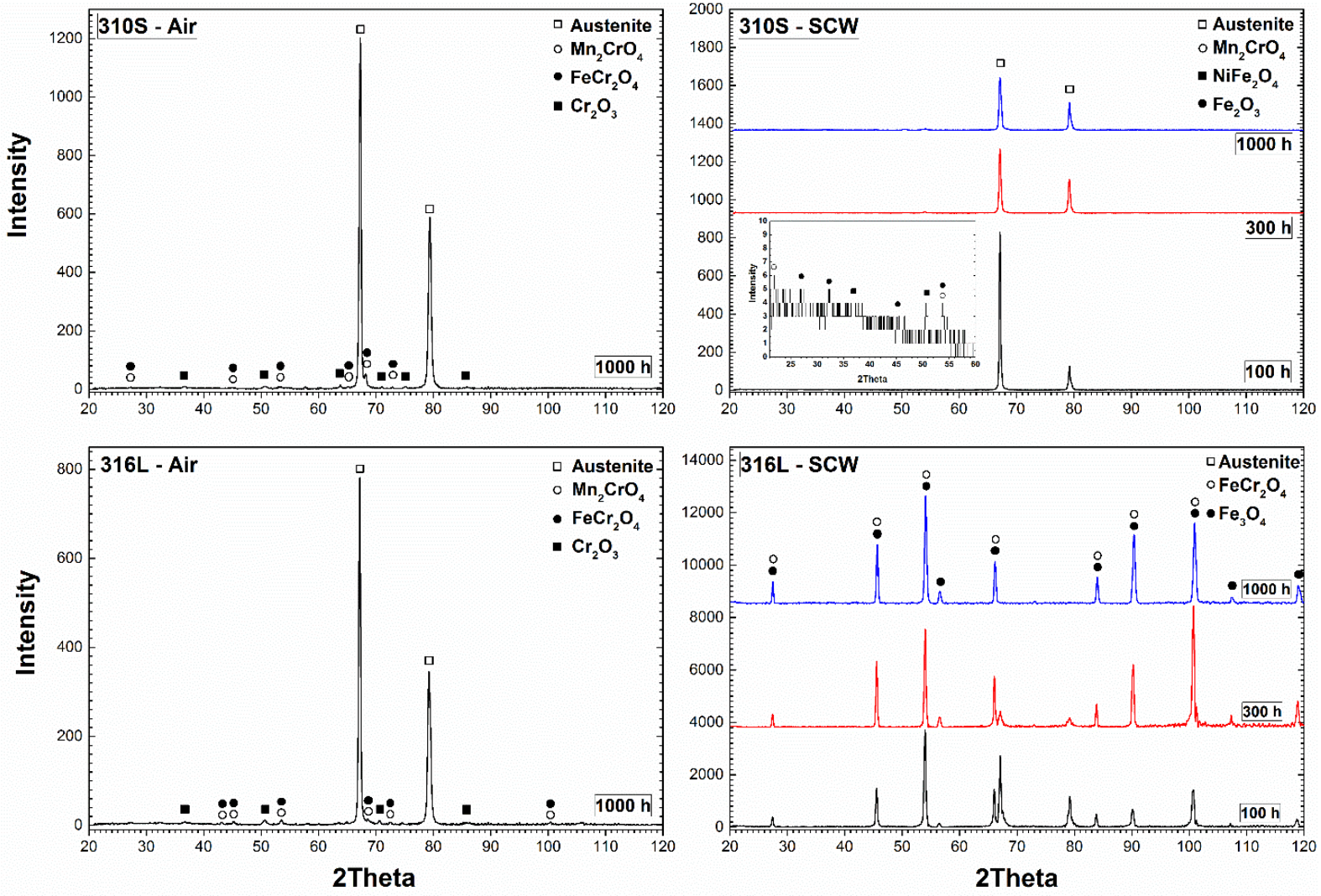

Figure 4.5. X-ray diffraction patterns of stainless steels 316L and 310S after oxidation in air at 600ºC and atmospheric pressure as well as SCW at 600ºC and 25 MPa.

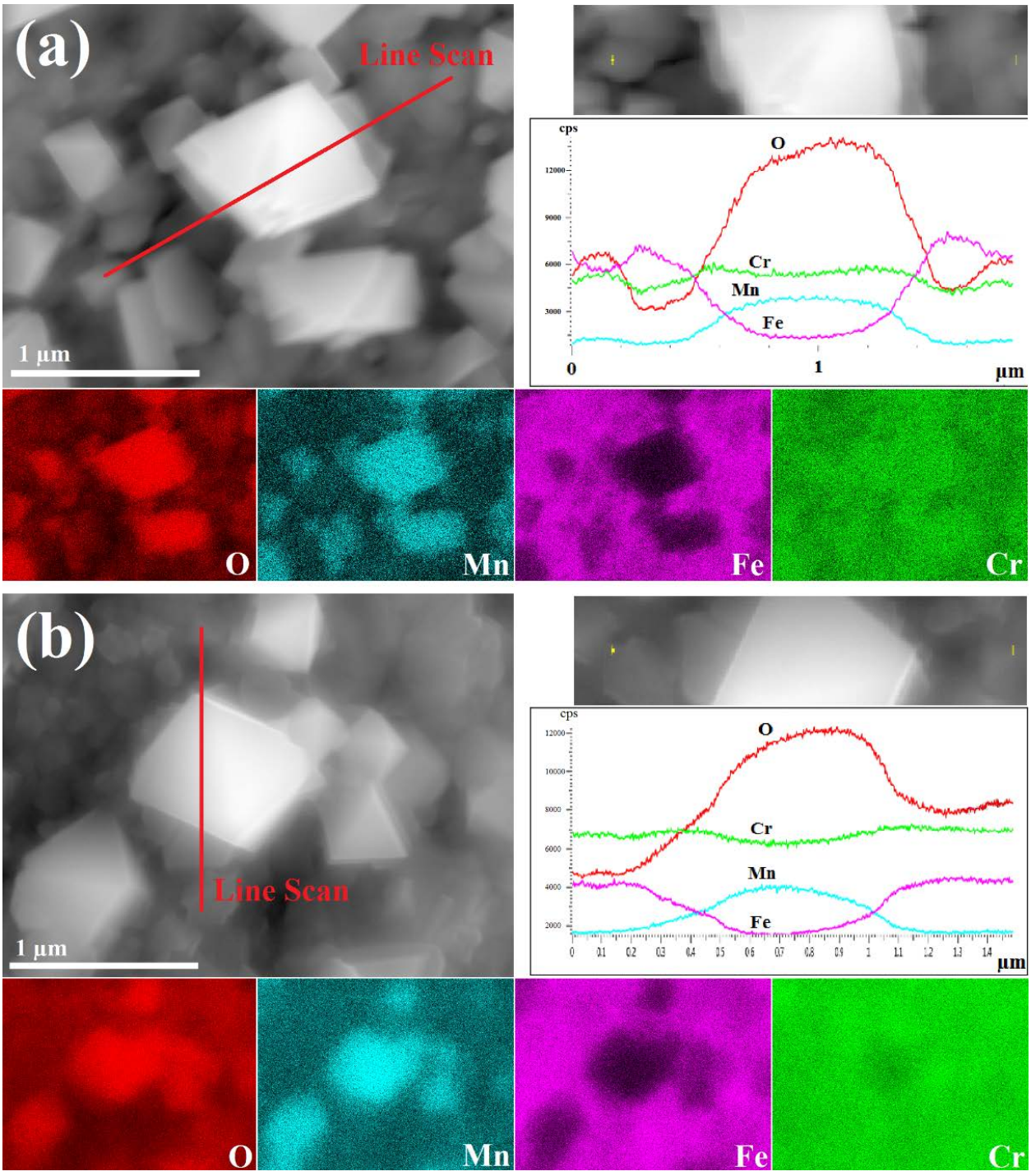

Figure 4.6. SEM micrograph, EDS elemental composition maps, and line scan of stainless steel (a) 316L, and (b) 310S after 1000h of oxidation in air at 600ºC and atmospheric pressure.

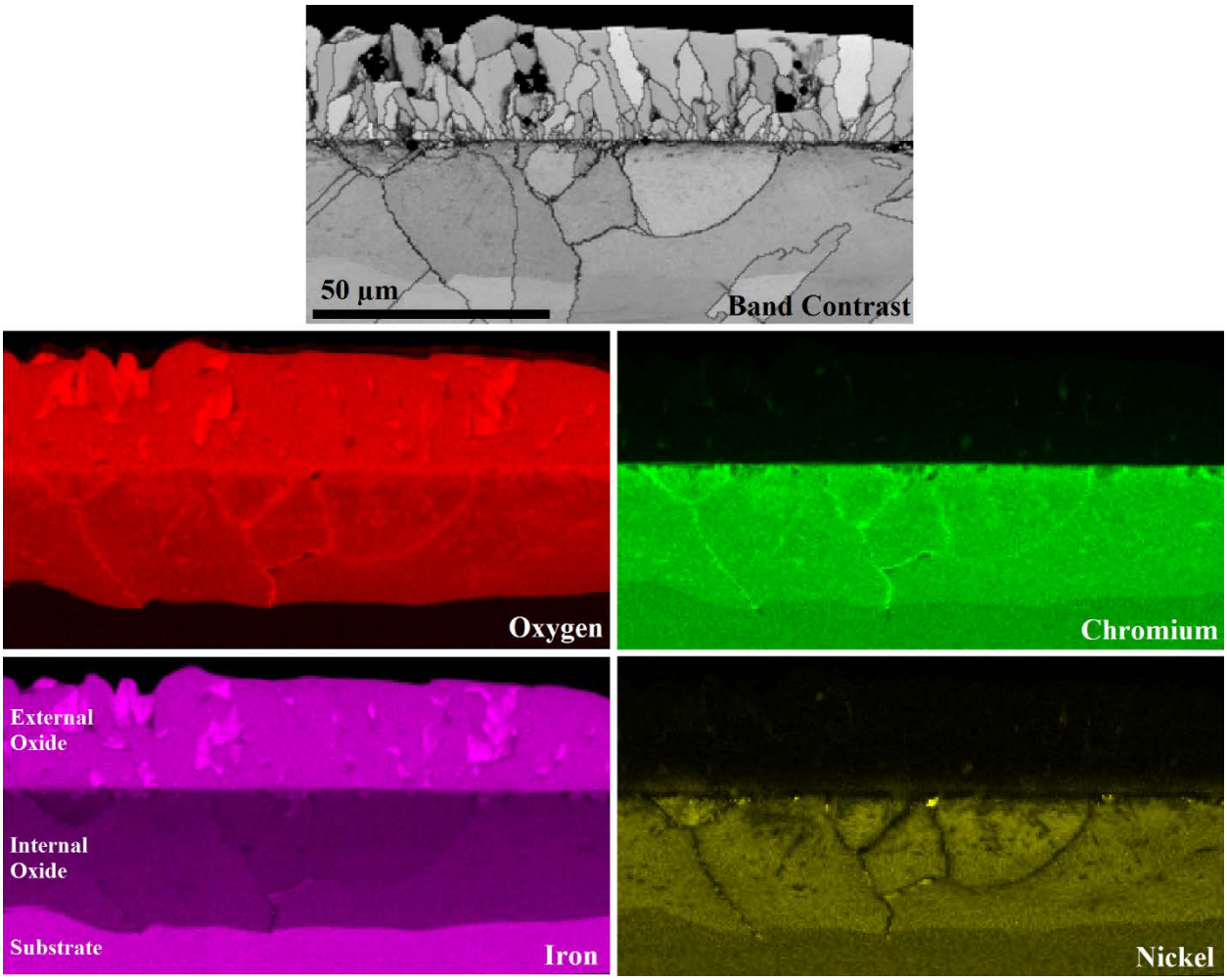

Figure 4.7. EBSD band contrast and EDS elemental composition of stainless steel 316L after exposure to SCW at 600ºC and 25 MPa for 1000h.

Figure 4.8 illustrates the SEM micrograph, EDS elemental maps, and composition line scan of the alloy 310S surface after 1000h exposure to SCW. It should be mention that the EDS maps are not normalized for better image contrast. As seen, three different regions are distinguishable. First is the matrix which is composed of oxygen, chromium, and manganese with average grain size of 100 nm; second region is consisted of oxygen, nickel, and iron that possesses oxide grains with average size of 500 nm; and finally the third zone is comprised of oxygen and iron with grains between 1 and 15 µm in size.

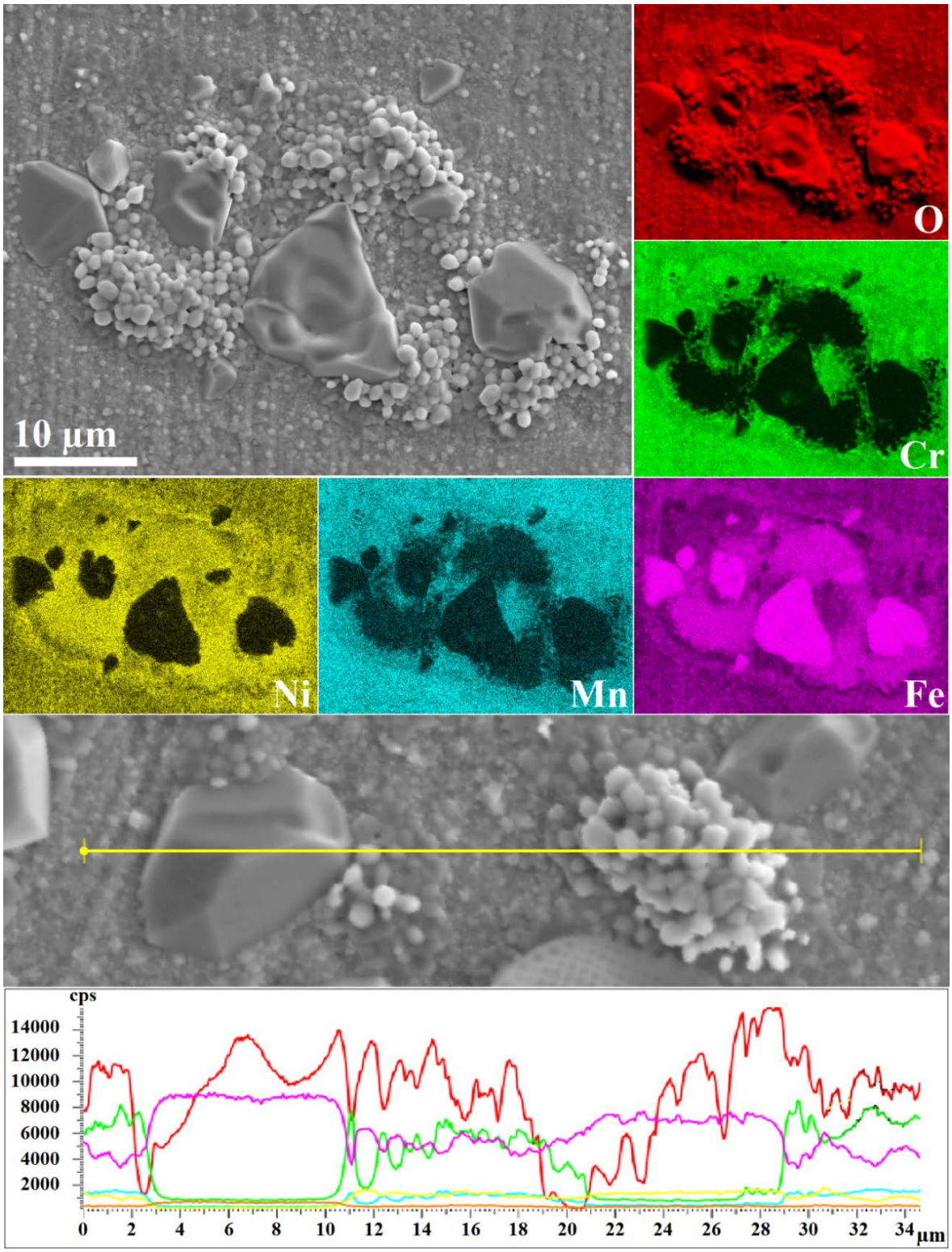

Figure 4.8. SEM micrograph, EDS elemental composition maps, and line scan of stainless steel 310S surface after exposure to SCW at 600ºC and 25 MPa for 1000h (color legends are similar for EDS map and line scan).

4.7 Discussion

4.7.1 Air oxidation

With respect to Fig. 5, the weight change of both 316L and 310S alloys after oxidation in air are almost constant. This indicates the formation of a protective layer on the surface of both alloys. Comparison of the EDS observation after oxidation (see Figure 4.6) with XRD patterns (see Figure 4.5) confirms the presence of manganese-chromium spinel (Mn_2CrO_4); however, chromium oxide (Cr_2O_3) is only detected in XRD patterns. Due to the protective nature of both oxide phases, i.e. very compact with good adhesion to the surface, oxidation would be retarded upon their formation on the surface. Therefore, after 100h of oxidation in air, the weight change is almost constant up to 1000h for both steels.

Comparing the weight change of both steels after oxidation shows that the alloy 310S has a better oxidation resistance compared to the alloy 316L before reaching constant weight change. As mentioned earlier, both samples have almost similar texture and average grain size (see Figure 4.1 and Figure 4.2). Moreover, they have produced the same oxide phases during air oxidation. Thus, difference in their chemical compositions is believed to be responsible for their different oxidation resistance. Based on Table 1, the major difference in the chemical compositional of the alloys is in the nickel and chromium content. It is known that steels with chromium content higher than 10% create a protective, adherent, and slow growing oxide layer during air oxidation in dry atmosphere [55–58]. This layer blocks the outward diffusion of other alloying elements and the inward diffusion of gaseous impurities [56]. Therefore, increasing the chromium content is one of the ways to improve the oxidation resistance in air. However, as chromium is a ferrite stabilizer in steels, the amount of nickel, as an austenite stabilizer, should be increased to be able to add more chromium to the alloy, so that sigma phase formation, as a brittle phase, is avoided, a better protection against oxidation is achieved and the alloy remains austenitic at room temperature for the best formability [55]. According to Table 1, since the alloy 310S possesses almost 100% and 50% more nickel and chromium compared to the alloy 316L, respectively, the former alloy could form the oxide layer more rapidly which is thick enough to protect the alloy from further oxidation.

4.7.2 Oxidation in SCW

Weight measurements before and after exposure to SCW show that the alloy 310S follows an increasing trend with oxidation time, yet the weight change is comparable to that of the alloy 316L

after air oxidation. This indicates that the 310S steel has a good performance in SCW. Accordingly, formation of a protective, adherent, and slow growing oxide layer on the surface of this alloy is expected [55–58]. Considering the XRD patterns in Figure 4.5 and EDS observation in Figure 4.8, the protective oxide layer that covers the entire surface of the alloy after 1000h of oxidation in SCW is manganese-chromium spinel (Mn_2CrO_4). Akhiani et al. [59] also observed this layer after exposure of Incoloy 800HT, with chemical composition comparable to that of the alloy 310S, to SCW at 600ºC and 25 MPa for 1000h. They reported that formation of manganese-chromium spinel (Mn_2CrO_4) hindered further oxidation of Incoloy 800HT. Beside the manganese-chromium spinel (Mn_2CrO_4), islands of hematite (Fe_2O_3), and nickel-iron spinel ($NiFe_2O_4$) are also visible in the SEM micrograph of the oxidized sample. Akhiani et al. also reported that hematite (Fe_2O_3) was formed on top of manganese-chromium spinel (Mn_2CrO_4) during oxidation of Incoloy 800HT in SCW. There are different proposed mechanisms about why and where on the surface these oxide islands are formed [60,61], nevertheless our observation shows that both of hematite (Fe_2O_3) and nickel-iron spinel ($NiFe_2O_4$) are located next to each other. This could imply that formation of one of the two oxides would facilitate the formation of the other. One possible explanation can be made based on the SEM micrograph (see Figure 4.8). Due to dissolution of the protective manganese-chromium spinel (Mn_2CrO_4) film at high temperature, more chromium is required on the surface to compensate the losses. This is not a problem on area close to grain boundaries, as chromium has higher diffusivity, however, the amount of chromium reach above the grain interior is not enough as it diffuses through the grain interior. As the result, the oxide layer above the grain interior is depleted of chromium and losses the protectiveness. On the other hand, iron and nickel diffuses through the non-protective layer and react with oxygen to form hematite (Fe_2O_3) and nickel-iron spinel ($NiFe_2O_4$).

The weight change of the alloy 316L during oxidation in SCW also shows an enhancing trend with oxidation time up to 300h; however, a weight loss happened after 1000h of oxidation due to spallation of the oxide scale. Figure 4.9 shows the images of the alloy 316L after exposure to SCW for 100, 300, and 1000h as well as the region that spallation happened after 1000h of oxidation. The main cause of oxide spallation is due to the stresses induced by a temperature drop. This drop in temperature can be due to fast cooling of the alloy after oxidation or thermal cycling of the alloy in service. Since no thermal cycling was involved in the experiment, the former cause led to the spallation of the oxide scale. Based on the XRD pattern and EDS observations (see Figure 4.5 and

Figure 4.7) of the alloy 316L, magnetite (Fe_3O_4) and iron-chromium spinel ($FeCr_2O_4$) are formed after 1000h of oxidation in SCW. Since the chromium content of this alloy is considerably lower than that of the alloy 310S, a mixture of iron-chromium spinel is produced at the beginning of the oxidation. Because the iron ions are much more mobile in this oxide scale than chromium ions (Cr^{3+}), quite pure iron oxide can be found at the outer surface of the scale at longer times [55]. This is not beneficial to corrosion resistance, because formation of magnetite leads to spalling of the non-protective oxide layer.

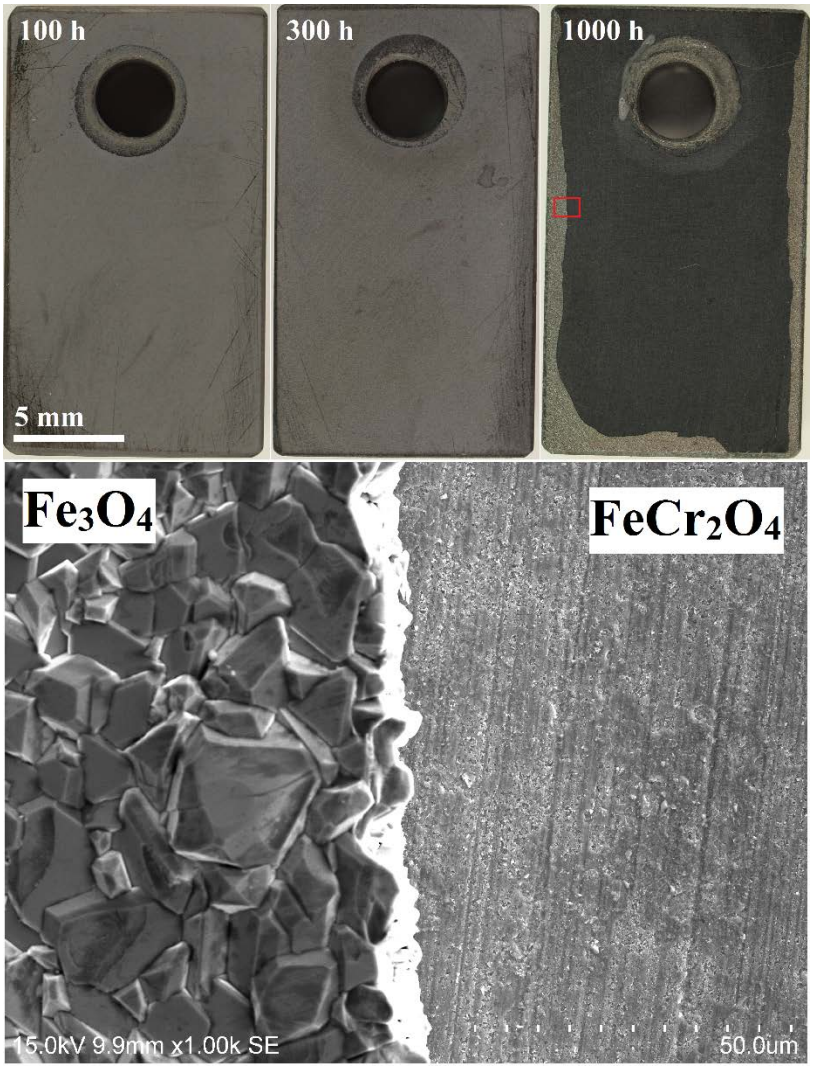

Figure 4.9. Stainless steel 316L after exposure to SCW at 600ºC and 25 MPa; top: oxide surface appearance of the samples after 100, 300, and 1000h of oxidation, bottom: SEM micrograph at spallation edge for the sample after 1000h of oxidation.

4.8 Conclusions

Oxidation of austenitic stainless steels 316L and 310S in air and SCW was studied and the followings were concluded:

1. Austenitic stainless steel 310S shows a better corrosion resistance in SCW compared to Austenitic stainless steel 316L.
2. Formation of Mn_2CrO_4 spinel on the entire surface of the alloy 310S is characterized as the protective layer against oxidation in SCW.
3. Fast cooling of the alloy 316L after 1000h of oxidation in SCW causes thermal shock in the thick oxide layer and results in spallation of oxide scale.
4. Formation of non-protective layers of magnetite (Fe_3O_4) and iron-chromium spinel ($FeCr_2O_4$) on the surface of the alloy 316L during oxidation in SCW results in more severe oxidation compared to the alloy 310S.

5 EFFECT OF THERMO-MECHANICAL PROCESSING ON TEXTURE EVOLUTION IN AUSTENITIC STAINLESS STEEL 316L

5.1 Overview

The results in chapter 4 revealed that although one of the selected alloys showed a good performance for corrosion test in SCW, there are microstructural factors to alter for increasing the corrosion resistance. It was hypothesized that this improvement in corrosion resistance can be achieved by decreasing the average grain size of the alloy or changing the texture in such a way that crystallographic planes with high atomic density form on the surface of the alloy. The aim of this chapter is to fulfill a part of the second objective of the thesis, "to optimize the microstructure of austenitic stainless steels 310S and 316L thermo-mechanical processing to improve the corrosion resistance", by selecting a thermo-mechanical processing procedure to produce samples with different grain sizes and different textures in austenitic stainless steel 316L. It should be noted that each of these two microstructural parameters (i.e. average grain size and texture) was set almost constant while changing the other one. For instance, one set of samples was produced with similar texture but different average grain sizes. In this chapter, the deformation and recrystallization mechanisms that led to change in the microstructure of each sample were studied systematically. Therefore, all the produced samples were characterized with EBSD and XRD techniques by which average grain size, micro-texture, and macro-texture were measured.

This manuscript was published in the Journal of Materials Characterization[7] and slight changes have been applied to the original version to avoid repetition. Dr. Hamed Akhiani[8] and Dr. Majid Hoseini[9] assisted the author of this Ph.D. thesis (Majid Nezakat) with preparation and processing of the samples and performing the data analysis. Jerzy Szpunar, as the supervisor of this research, provided recommendation, consultation and discussion wherever it was needed. Except the entire or a portion of these parts, all the experiments, data acquisition, and data analysis were conducted by Majid Nezakat, the lead author of the paper. Majid Nezakat wrote the manuscript, integrated comments from the co-authors, and submitted it for review and publication.

[7] The copyright permission to use the manuscript in the thesis is obtained and provided in the appendix section. The references of this chapters are provided at the end of the thesis.

[8] Mitsubishi Hitachi Power Systems Canada, LTD., 826 58th Street East, Saskatoon, SK, S7K 5Z4, Canada

[9] NOVA Chemicals, P.O. Box 5006, Red Deer, AB, T4N 6A1, Canada

5.2 Abstract

In this study we implemented two rolling modes to investigate the strain path effect on deformation and annealing textures of austenitic stainless steel 316L. We applied unidirectional rolling and cross rolling to achieve up to a 90% reduction in thickness. Results show that for deformed austenite, Brass, Goss and γ-fibre were the main texture components in the unidirectional rolled sample, while Brass was the dominant texture in the cross rolled sample. In addition, rotated copper and rotated cube were the main textures of martensite after 90% reduction for unidirectional rolled and cross rolled samples, respectively. Results also show that recrystallization texture has a direct correlation to that of deformed austenite since transformed martensite reversion was athermal. After recrystallization, Brass and a combination of Brass and Goss were the dominant textures for cross rolled and unidirectional rolled samples, respectively.

5.3 Introduction

Various industrial applications use austenitic stainless steels because of their favourable ductility and excellent overall corrosion resistance [62,63]. Therefore it is important to optimize their microstructure evolution to control significant physical and mechanical properties [64,65]. Industry creates a variety of products through different manufacturing processes, among which, rolling is considered the most important. Chowdhury et al. report that a combination of 80% cold deformation and subsequent annealing at 1050ºC in 316 steel produced the best resistance against sensitization [66]. During rolling, deformation mechanisms change with the alloy composition. The magnitude of stacking fault energy (SFE) controls the cross-slip, allowing different deformation mechanisms to be activated at different stages of deformation [67,68]. As the SFE decreases and the stacking faults become larger, cross-slip becomes more difficult and mechanical twinning is favoured. Most austenitic steels, such as austenitic stainless steels [69], nickel-based alloys [70], and high manganese Hadfield steels [71], have low-to-moderate SFE and therefore tend to form extended stacking faults, deformation twins and planar dislocation structures. These different lattice defects strongly influence the stress-strain response and the evolution of the texture during cold rolling.

It is well known that transformation of austenite into martensite can be induced by plastic deformation in these alloys [72–76]. During cold rolling, the austenite phase partially transforms to ά-martensite and the remaining austenite deforms by slip or deformation twinning [77,78].

Finally, martensite reverts to austenite grains during subsequent annealing, while recovery or recrystallization may occur during annealing within the remaining austenite depending on the heat treatment temperature [72]. Chowdhury et al. report that during annealing treatment a weak Brass {110}<112> texture component with spread towards the Goss {110}<100> was observed in recrystallized austenite [79]. The crystallographic orientation of new austenite grains formed by martensite reversion may be different from normal recrystallization. The orientation of remaining austenite grains after annealing depends on the plastic deformation mechanism upon cold rolling [80]. On the other hand, researchers expect formation of deformation-induced ά-martensite to affect the deformation behaviour of the remaining austenite, thereby influencing its final orientation. Kumar et al. report that ά-martensite is formed by selective transformation of the austenite phase having Brass {110}<112> orientation [81]. The reversion of martensite to the austenite phase during annealing happens upon two different mechanisms including athermal and diffusion-controlled transformation. Thus, depending on the reversion mechanism, the reverted austenite from ά-martensite may or may not have the same orientation as the remaining austenite. The athermal reversion of martensite involves coordinated movements of atoms and an atomic correspondence between the parent and product lattices. The reversion may not affect the orientation in this condition. However, in diffusional reversion, as the order of the atom arrangement in the product lattice is different from that of the parent lattice due to long-range movement of atoms during reversion [81,82], the atomic correspondence can no longer exist. Therefore, the orientation of the reverted austenite should change. The mechanism of martensite to austenite reversion may change based on the annealing temperature/time conditions. Thus, the annealing of cold-rolled metastable austenitic steels is of interest because of both the reversion of martensite to austenite and recovery/recrystallization in the remaining austenite. Several researchers have reported on the texture evolution of 316L stainless steel during cold rolling and annealing [80,81,83,84]. Chowdhury et al. [80] investigated the texture evolution of 316L stainless steel during cold rolling under ambient temperature, but observed no martensitic transformation in their work [77]. Our objective, in this work, is to address the texture evolution of cold rolled and annealed 316L stainless steel in depth, using Orientation Distribution Function (ODF).

5.4 Materials and methods

Hot rolled stainless steel 316L with a thickness of 6.25 mm and average grain size of 20µm was used as a starting billet for cold rolling. Table 3.1 shows the chemical composition of the alloy. strips of 50×50 mm^2 were cut from the as-received billet and then cold rolled them via unidirectional rolling (UDR) and cross-rolling (CR) up to 10, 30, 50, 70 and 90% reductions, with equal inter-pass rolling steps of 10% true stain. Figure 3.1 depicts the rolling processes implemented and the differences between them. All the cold rolled samples were annealed at 1050 ºC for 5 minutes per millimeter thickness. The sample name used in this study is comprised of deformation mode, value of the reduction in thickness, and post rolling treatment ("A" stands for annealing), respectively. Table 3.2 lists the sample preparation conditions that were used in this study. The macro-texture of specimens was measured using a Bruker D8 Discover diffractometer with a two-dimensional x-ray diffraction system (XRD^2) with Cr Kα radiation. Incomplete pole figures at the mid-section of all samples were collected including (111) and (200) for austenite phase and (110) and (200) for martensite phase. Then, the Orientation Distribution Function (ODF) was constructed using Resmat software and different textural fibres were extracted from ODFs for detailed discussions. In addition, Electron Backscattered Diffraction was utilized for micro-texture measurement using a Hitachi FEG-SEM SU6600 equipped with an Oxford EBSD system. The samples were tilted 70º to the horizontal plane using a pre-tilted sample holder and the SEM was operated at 20 kV. EBSD data was analyzed with HKL software. IPF maps extracted from EBSD data display grains' orientation relative to an axis, which was chosen to be the normal direction (ND) of the rolling plane.

5.5 Results

ODFs of samples were constructed from collected incomplete pole figures to compare deformation and annealing texture in stainless steel 316L. The first sample was cut from an as-received stainless steel 316L billet that was processed through hot rolling. For convenience, the major texture components and fibres are illustrated in Figure 4.3. Three important sections of the ODF at φ_2= 0º, 45º, and 65º show the common texture components in FCC steels. Figure 5.1 depicts the macro and micro texture of the as-received sample. Four major different components are visible, including Brass {110}<112>, S {123}<634>, Cube {001}<100>, and Copper

{112}<111>. EBSD image quality maps also confirm the presence of these components. As seen, Brass component has the highest volume fraction.

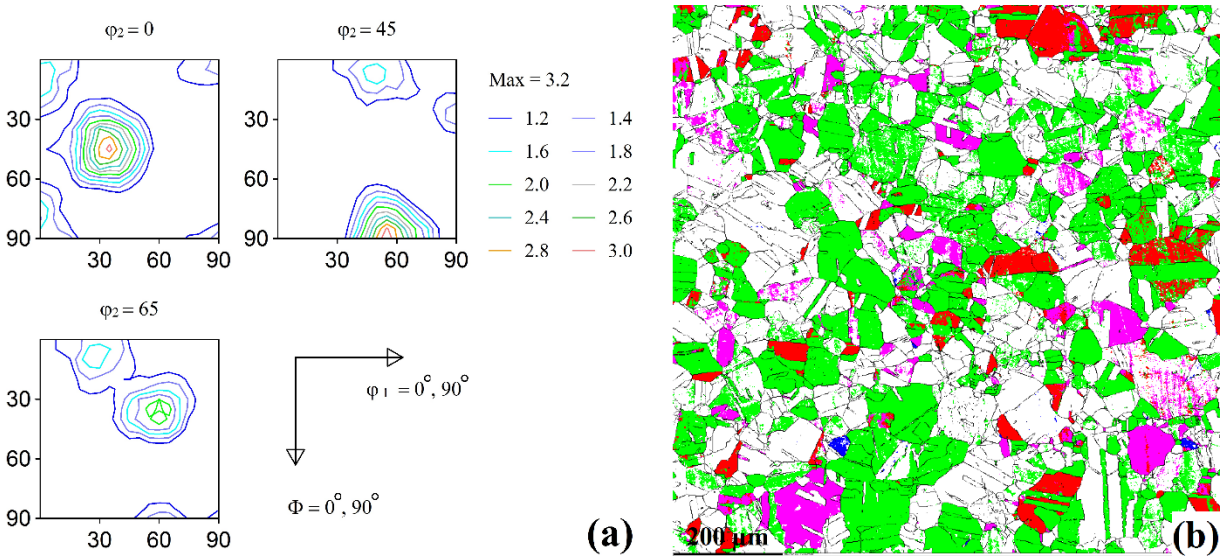

Figure 5.1. (a) IPF and important sections of the ODF; (b) OIM maps for Brass (green), S (pink), Cube (blue) and Copper (red) components of as-received stainless steel 316L.

5.5.1 Deformation Texture

After cold rolling, two phases, martensite and austenite, are present in 316L stainless steel. The transformation of the austenite phase formed the martensite phase at a very early stage of deformation (i.e. 10%). The volume fraction of martensite depends on the deformation percentage: the higher the deformation, the higher the martensite volume fraction [85]. The textures of each of these phases are discussed in the following sections.

5.5.1.1 Deformed Austenite

Figure 5.2 depicts important ODF sections of the remaining austenite for UDR and CR samples. After 10% reduction in thickness, both UDR10 and CR10 showed a slight decrease in Cube {100}<001> component compared to the as-received sample. In UDR10, the Brass {110}<112> component rotated around ND and spread towards Goss {110}<100> orientation.

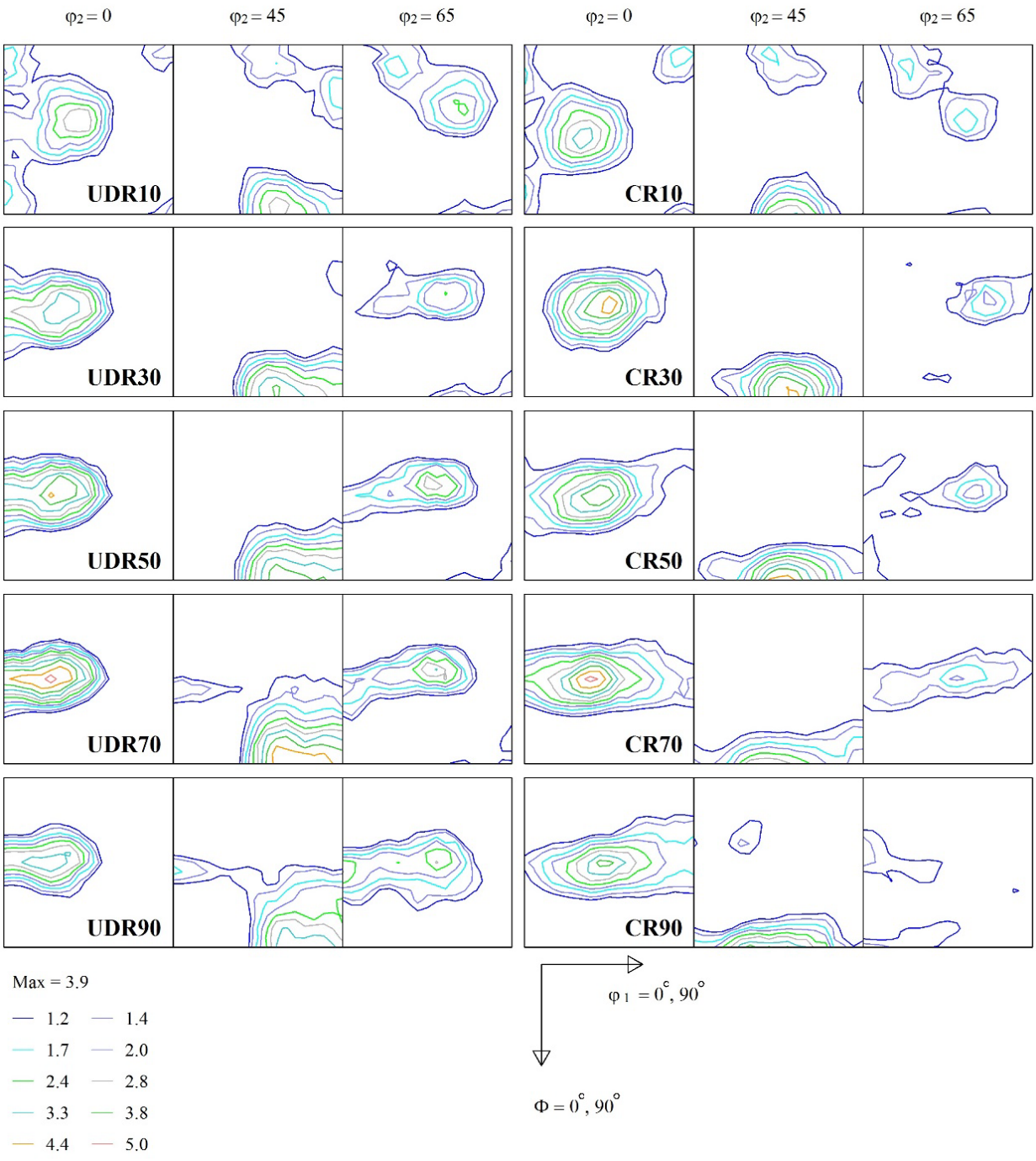

Figure 5.2. ϕ_2= 0º, 45º, and 65º sections of the orientation distribution function for austenite phase in stainless steel 316L after cold rolling up to 90% reduction in thickness.

In the CR10, Brass orientation remained the same but Copper {112}<111> component was eliminated. When deformation reduction reached 30%, Cube {100}<001> component disappeared and $(R\text{-}Cu)_{RD}$ {205}<uvw> was debilitated in UDR30, while eliminated in the CR30 samples. In

the UDR30, Brass component spread more towards Goss and Twin Copper (TC) {255}<511>, and at the same time S {123}<634> component spread towards (212)[1-20] and Copper component almost vanished. In CR30, Brass spread towards G/B {110}<111>, and S component spread toward (213)[-2-12]. After 50% reduction, Brass oscillated back from G/B in the CR50 while it was partially spread along ζ-fibre (zeta fibre), which means Goss and Brass were presented at this stage for UDR50. In UDR50, (TC) {255}<511> orientation was strengthened, R-Cu orientation completely disappeared and S component was strengthened in both UDR and CR samples. When deformation continued to 70%, γ-fibre appeared in the deformed austenite in the UDR70 by presenting (111)[1-10] and (111)[-1-12] orientations at the ODF section ϕ_2= 45º. Goss, Brass and TC components were intensified as well. On the other hand, in the CR70, {110} <uvw> fibre was intensified and spread back and S {123}<634> orientation was spread towards (213)[-2-12] and (212)[1-20] orientations. By 90% reduction, both Goss and Brass orientations were reduced in the UDR90 and γ-fibre was formed. The {110} <uvw> fibre was also reduced in CR90 at this deformation stage, and S {123}<634> orientation was eliminated, while (112)[3-72] orientation appeared.

5.5.1.2 Martensite

Figure 5.3 illustrates important ODF sections of deformation-induced ά-martensite. Martensite had been formed since the initial stages of deformation as it was attracted by a magnet. The texture of martensite for both samples, UDR10 and CR10, was R-C {100}<011> and (116)[1-10]. When deformation reached 30%, (223)[3-41] component, which is near (111)[3-41], was formed in both UDR30 and CR30. In addition, R-C orientation remained the same for CR30, while it spread towards R-Cu {112}<110> component in UDR30. By continuing the deformation to 50%, R-C {001}<110> was intensified in CR50, while it was reduced in UDR50 and at the same time spread towards R-Copper. Moreover, near (111)[3-41], orientation remained the same in UDR50, but it completely turned to (111)[3-41] and (111)[0-11] in the CR50.

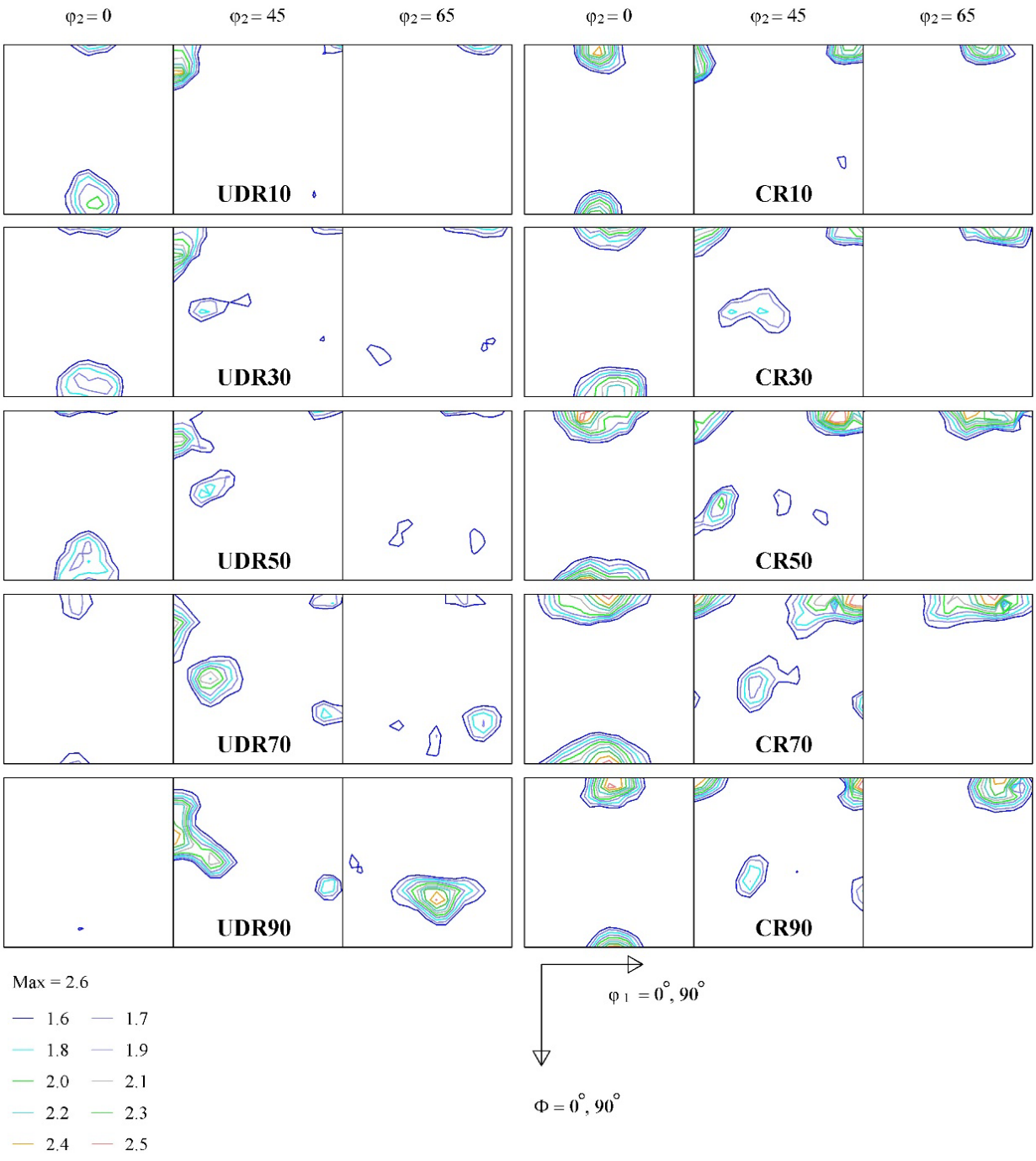

Figure 5.3. ϕ_2= 0º, 45º, and 65º sections of the orientation distribution function for martensite phase in stainless steel 316L after cold rolling up to 90% reduction in thickness.

After 70% reduction in thickness, R-C component reduced more and was about to disappear in UDR70, and R-Copper was more pronounced. In addition, (332)[-1-24] orientation that formed in the UDR70, (223)[3-41] spread to near (111)[2-31] with higher intensity. On the other hand, R-

C intensified in CR70 and spread along ζ-fibre. In this sample, (111) planes rotated in comparison to the CR50, and as a result Y {111}<121> and (111)[1-10] components appeared in ODF. With final reduction to 90%, R-C texture component was completely replaced by R-Copper in UDR90, while R-C intensified in CR90. Near (111)[2-31], orientation remained the same in UDR90 and (332) and [-1-24] orientation completely spread to (111)[-1-23]. In the CR90, (111)[1-10] was eliminated, but {111}<112> component remained at the end.

5.5.2 Annealing Texture

Figure 5.4 presents ODF sections of annealing texture for alloy 316L after cold rolling up to 90%. Since almost identical deformation textures for both martensite and austenite were formed after 10 % deformation in UDR10 and CR10, only UDR10 was annealed to avoid duplication of data. As shown, Brass {110}<112> and S {123}<634> were the major texture components in the UDR10A. There was also a minor {114}<uvw> component, which had a low intensity. In comparison to UDR10A, Goss {110}<001> appeared in UDR30A and S {123}<634> component was reduced, while {114}<uvw> component completely disappeared. The CR30A, however, showed a different trend. S component was reduced and Brass component started to spread along ζ-fibre. In UDR50A, Brass component was reduced and Goss was intensified in comparison to UDR30A. For CR50A, Brass component intensified and spread along ζ-fibre, while S component had nearly vanished. The Goss component was dominant in the UDR70A as Brass started to decline. Interestingly, a weak Copper {112}<111> appeared in this sample. On the other side, S component was completely eliminated in CR70A and Brass component intensified compared to CR50A. In the last two samples, UDR90A and CR90A, the intensity of major texture components decreased. Major components remained the same, and only (212)[1-20] and A {112}<011> orientations appeared in UDR90A and CR90A, respectively.

5.6 Discussion

5.6.1 Deformation Texture

5.6.1.1 Remaining Austenite

Figure 5.5 shows β-fibre and η-fibre evolution in UDR and CR samples. By comparing β-fibre and ODF sections in Figure 5.2 for both UDR and CR samples, one can observe three distinct stages in deformation. The first stage is elimination of Copper orientation. As depicted in Figure

5.2, Copper {112}<111> existed up to deformations of 30% for UDR samples and beyond that it was eliminated. Researchers report that the deformation mechanism is slip till this stage, which facilitates formation of grains with Copper {112}<111> orientation [78,80]. However, for our CR samples, Copper {112}<111> existed only up to the early stages of deformation and it was eliminated after 10% of deformation. The second stage of deformation is recognized by formation of twinnings and spread of Brass {110}<112> towards Goss {110}<001>. Goss component was strengthened from 30% reduction, which is believed to be facilitated by the formation of twinning.

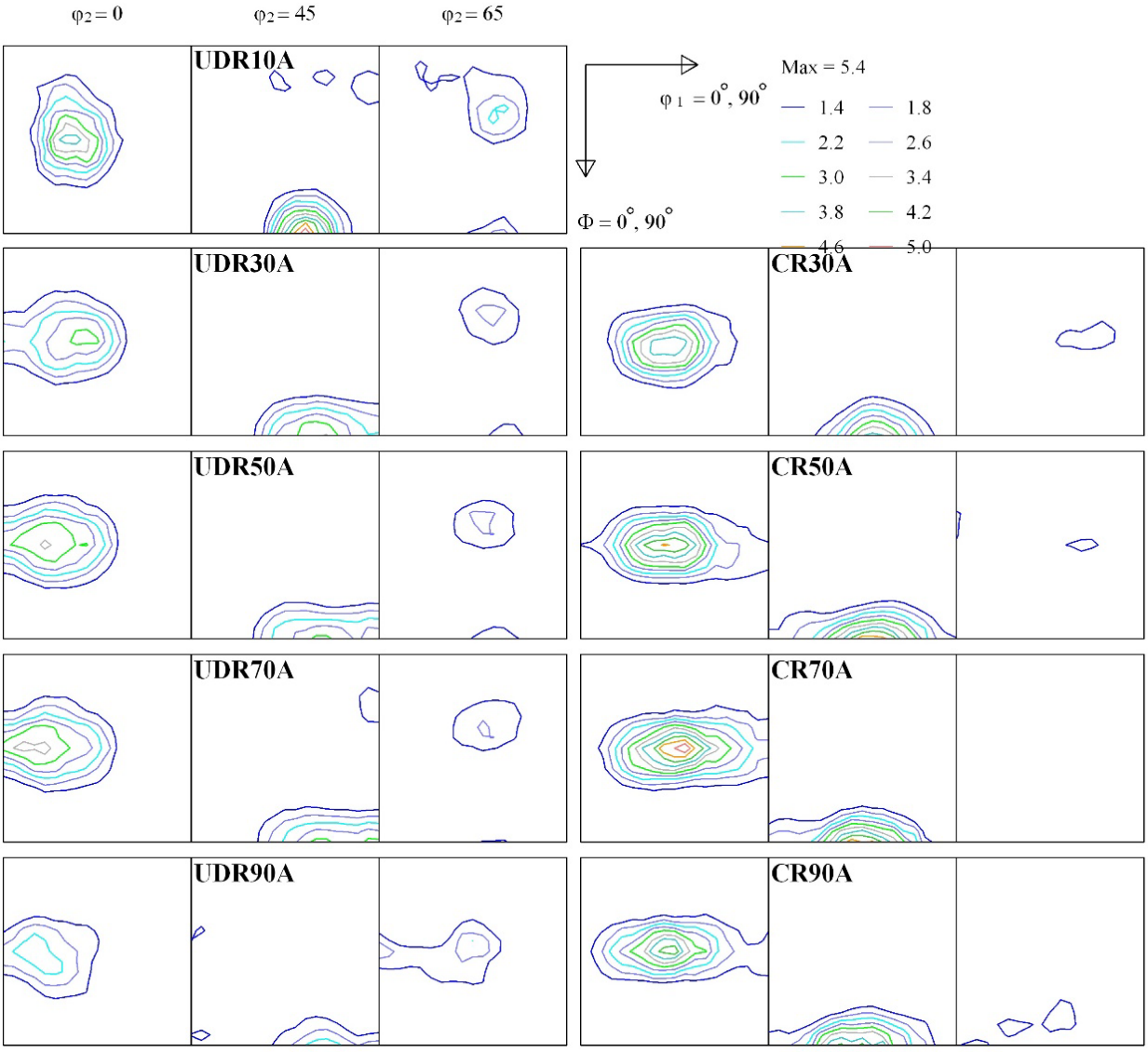

Figure 5.4. ϕ_2= 0º, 45º, and 65º sections of the orientation distribution function of annealed stainless steel 316L after cold rolling up to 90% reduction in thickness.

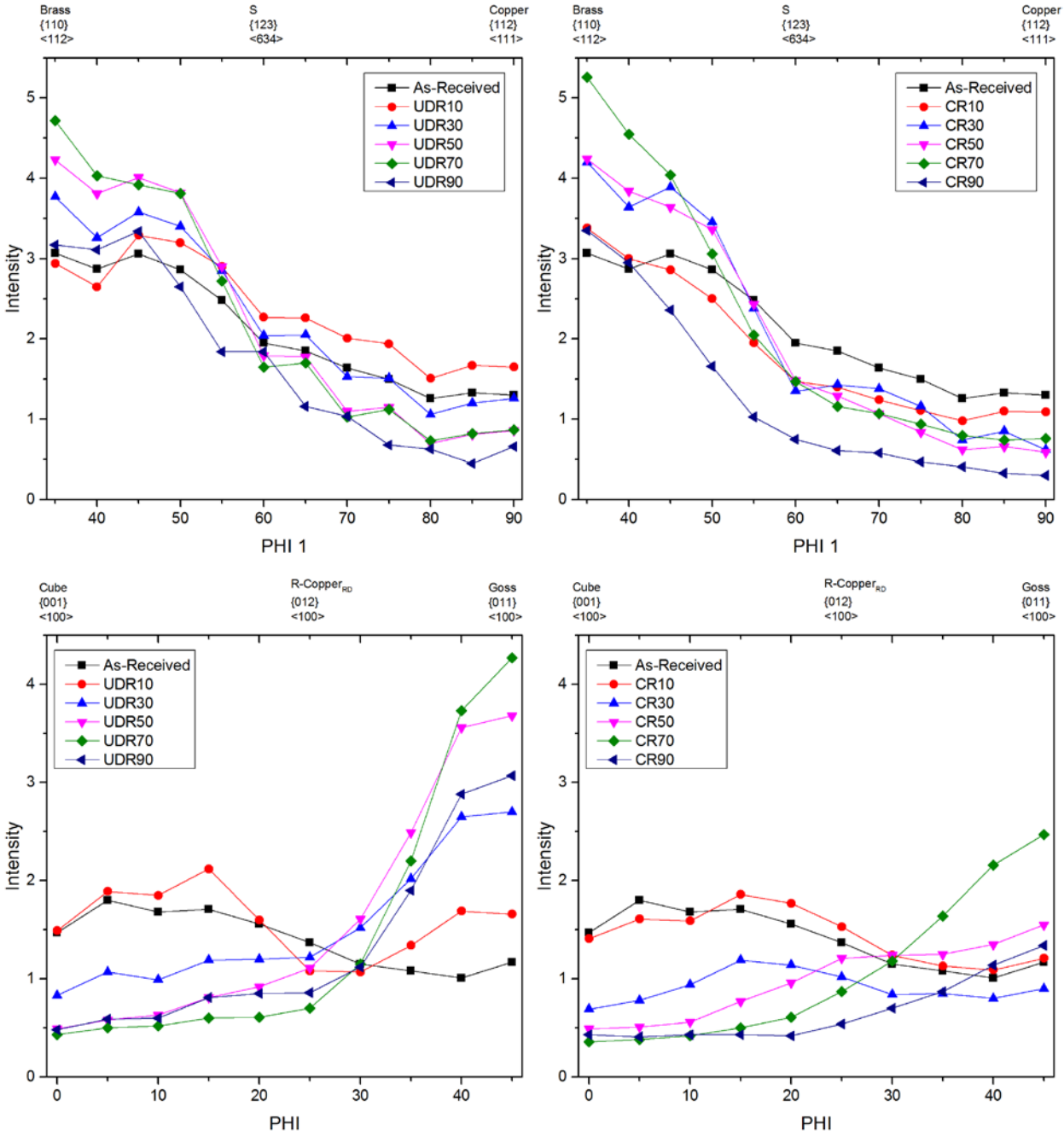

Figure 5.5. β-fibre and η-fibre for austenite phase in unidirectionally rolled and cross-rolled stainless steel 316L after deformation up to 90% reduction in thickness.

Figure 5.6 proves this by illustrating the formation of twinnings with Goss orientation. To elucidate the orientation relationship between the twins and the parent grains, a subset was prepared from a region of twinnings with Goss orientation. The (111) pole figure of the subset shows a common pole between the twins and the parent grains. The primary twin in the FCC

structure exhibits a 60º rotation around <111> crystal axis [86]. In order to consider a boundary as a coherent twin boundary, not only should the rotation be correct but also a boundary should coincide with the twinning plane. This will result in having a common pole in (111) PF on the subsets consisting of twins and parent grains. Similarly, this rotation resulted in 3 common poles in (110) PF. This phenomenon is reported in the work of Chowdhury et al. [80].

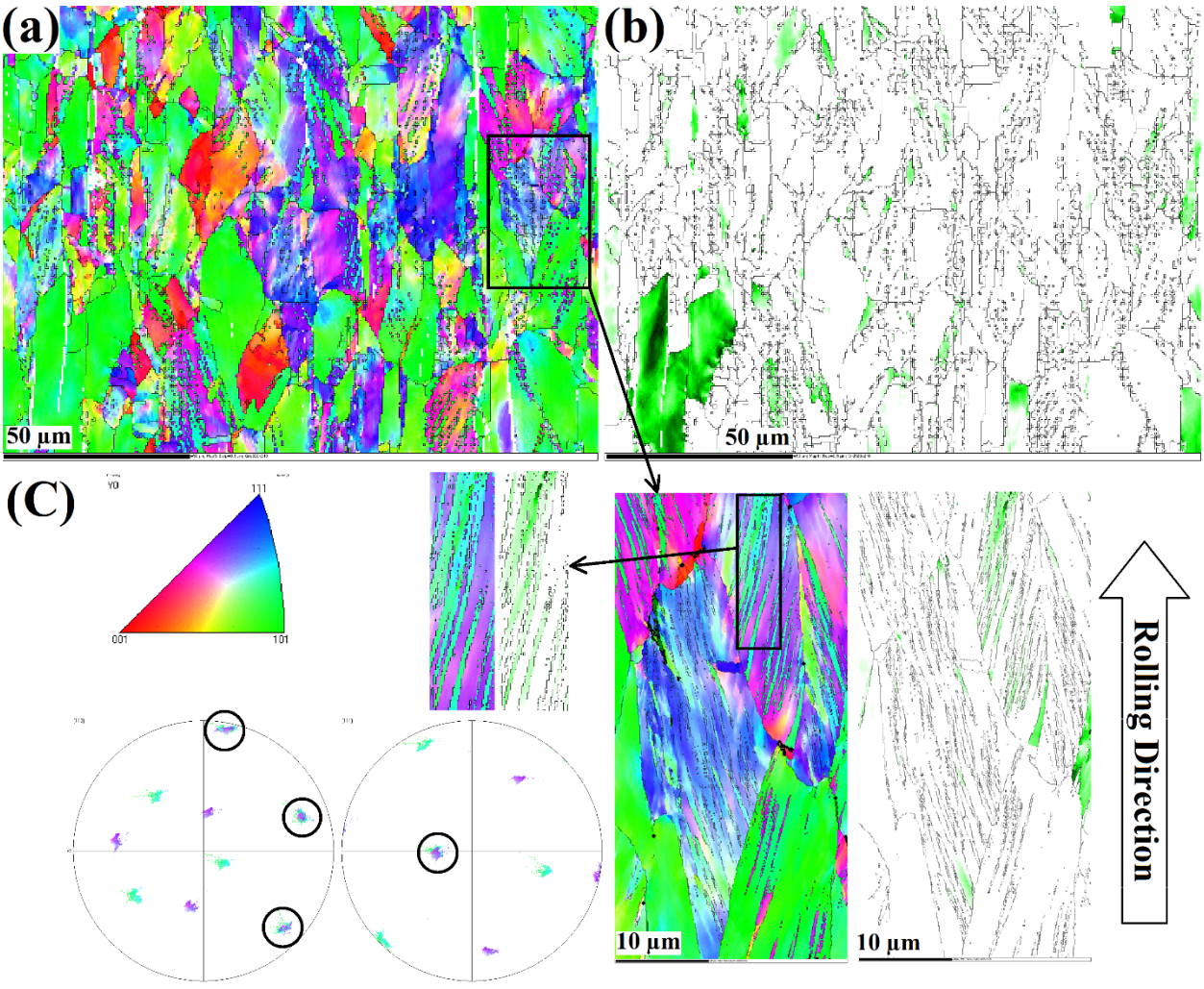

Figure 5.6. Orientation map of 30% deformed austenite showing; (a) IPF map, (b) Goss {110}<001> component, and (c) formation of twinning with Goss {110}<001> orientation.

On the other hand, as also reported in reference [68], when deformation reached 50% for UDR samples, the mechanism was changed by twinnings, which rotated grains with C {112}<111> and led to T-C orientation. Figure 5.7 depicts formation of grains with T-C orientation from those with Cu orientation. As seen, this process was somehow suppressed for CR samples, as it took until

70% of reduction. The reason is probably because of deformation mode, since a portion of the strain was released at each change of rolling direction in cross-rolling.

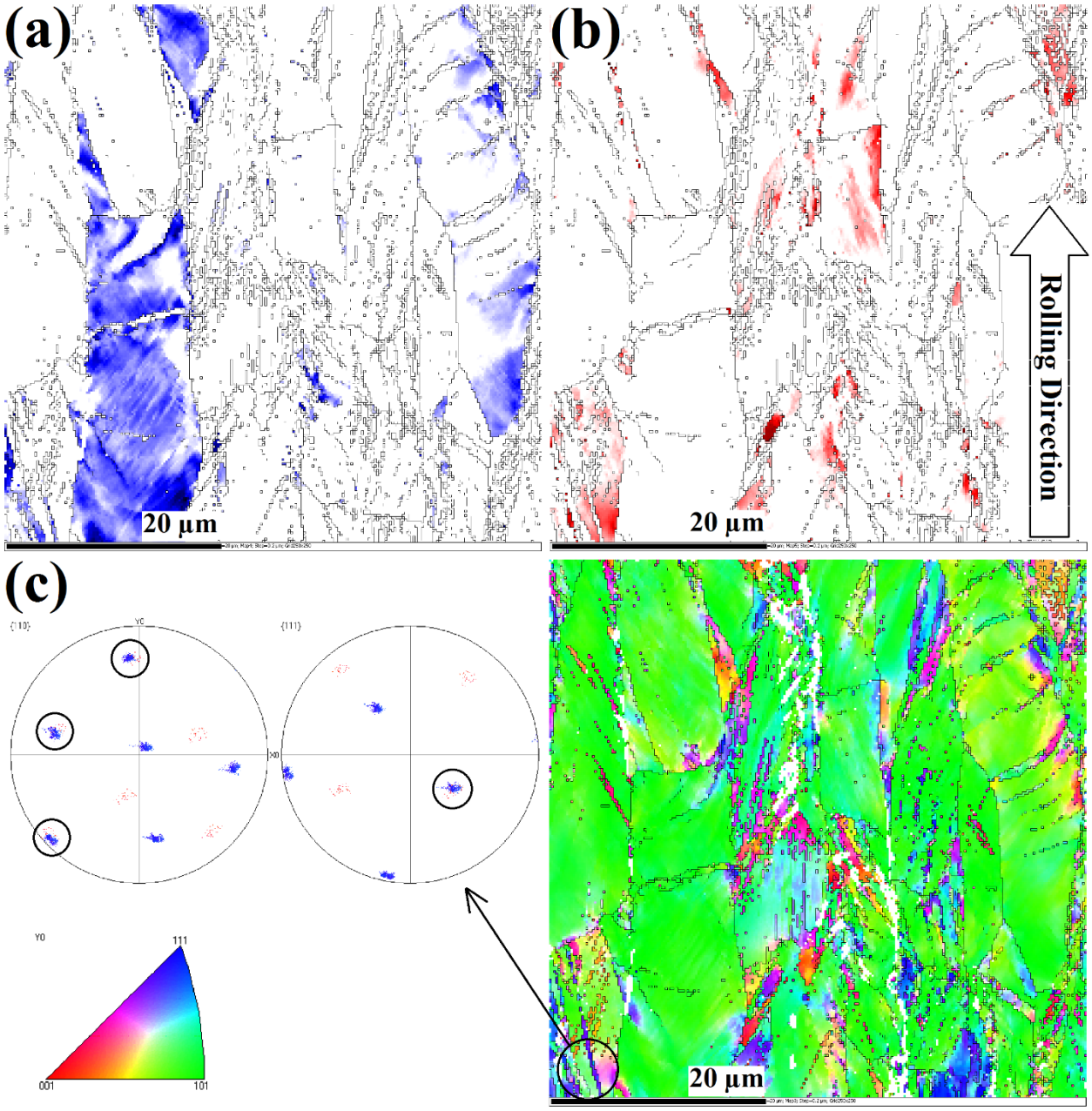

Figure 5.7. Orientation map of 50% deformed austenite showing; (a) TC {255}<511> component, (b) C {112}<111> component, (c) IPF map and pole figures near a deformation twinning.

The third stage of deformation happens by formation of γ-fibre {111}<uvw> due to saturation of Goss orientation [80]. As illustrated in Figure 5.8, by 70% reduction, γ-fibre was formed in

UDR70. As documented elsewhere [80] and seen in Figure 5.8, when Goss and Twin-Copper orientations are increased, {111} planes will form by alignment of twin lamellae parallel to the rolling plane. This process was yet to begin in our CR70. The reason could be due to the fact that Goss orientation was not completely saturated due to the difference in mode of deformation.

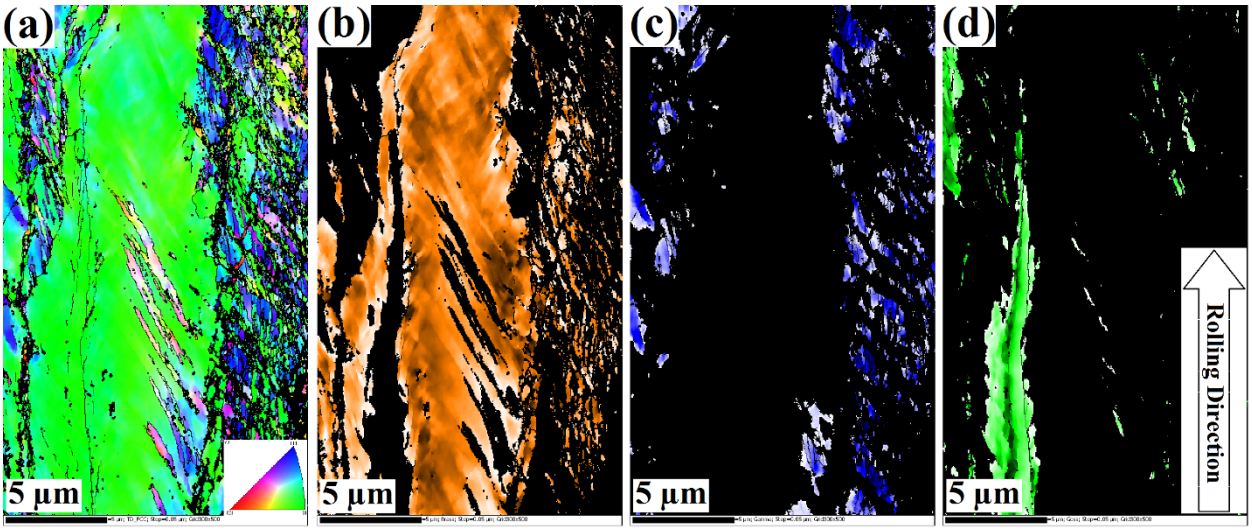

Figure 5.8. Orientation map of 70% deformed austenite showing; (a) IPF map, (b) Brass {110}<001> component, (c) γ-fibre, and (d) Goss {110}<001> component.

Upon further deformation to 90%, as expected, γ-fibre as well as T-C appeared and intensified in the ODF for the UDR90. On the other hand the Goss component was reduced in both UDR90 and CR90 in comparison to 70% samples. This trend was not expected as other researchers report an increase in Goss {110}<001> component [79–81]. Thus, OIM was used to investigate the reason for this phenomenon. As depicted in Figure 5.9, austenite grains were recovered in the UDR90, yet a deformed structure was still present. On the other hand, an unusual "undeformed" structure formed in the CR90, which led to relatively weak Brass texture. Therefore, Goss component was reduced less in the UDR90 because of recovery in comparison to the CR90 in which the undeformed structure happened. An example of how a highly deformed microstructure can be undeformed is reported by Farag et al. [87]. They found that the elongated grain structure produced in pure aluminium by a strain in torsion of 2.3 could be returned to an equiaxed grain structure if an equal and opposite strain was subsequently given.

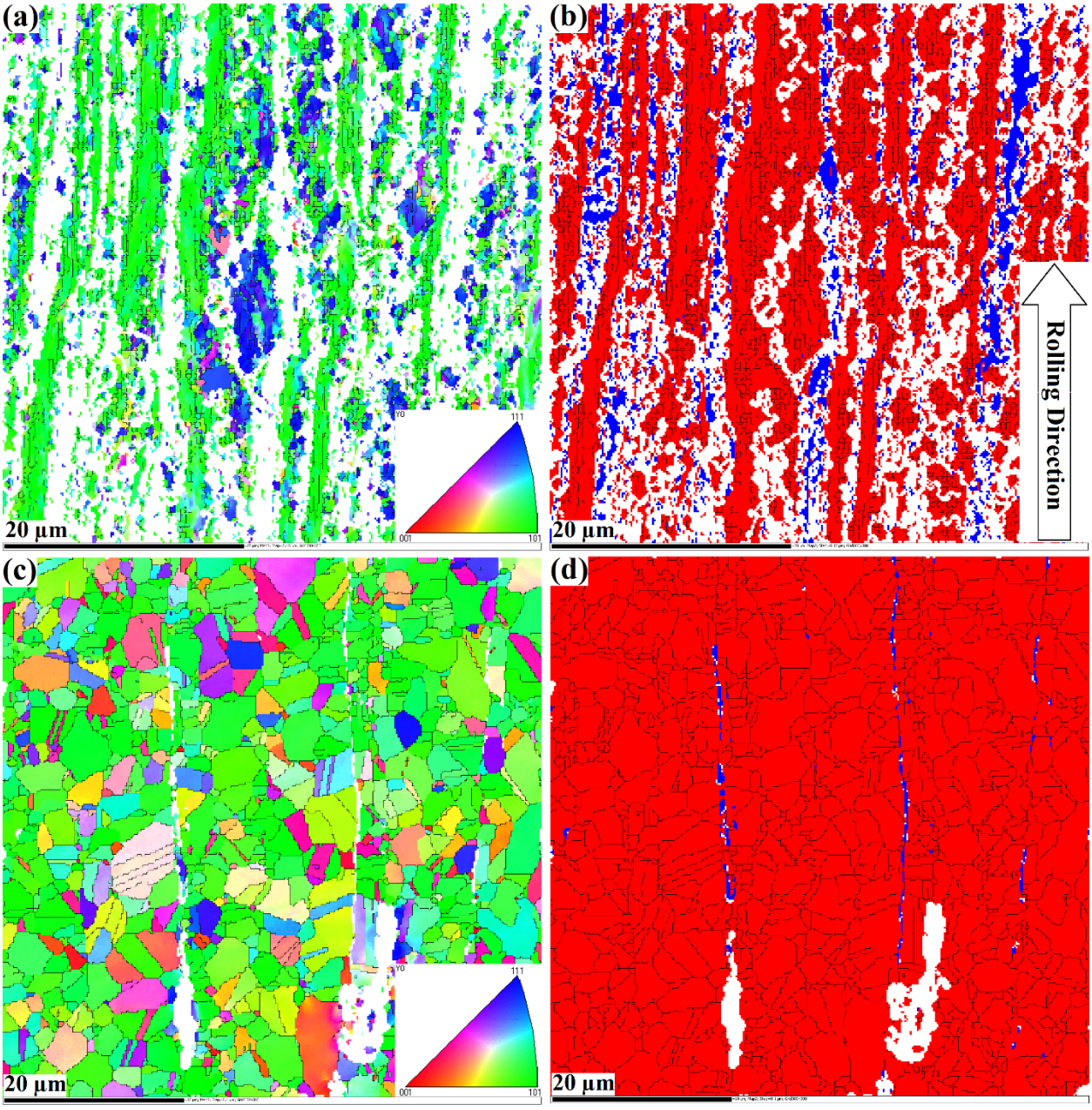

Figure 5.9. IPF map (a) UDR90, (c) CR90, and phase map (martensite: blue, austenite: red) of (b) UDR90 and (d) CR90.

5.6.1.2 Martensite

Figure 5.10 depicts α-fibre and ε-fibre evolution in martensite for UDR and CR samples. One can see from the previous section that C orientation was formed at initial stages of deformation in austenite and was eliminated after 30% reduction for both UDR and CR samples.

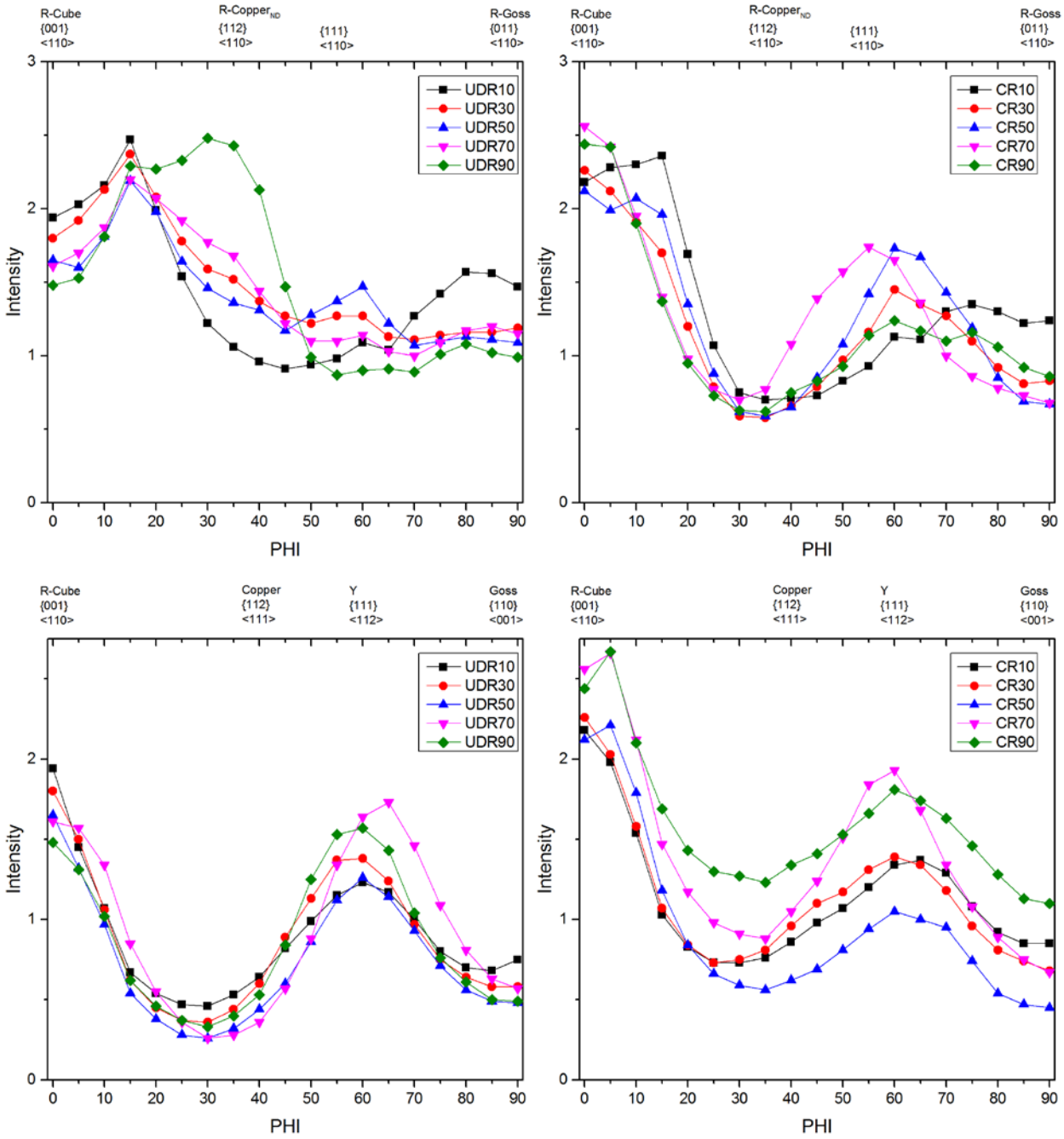

Figure 5.10. α-fibre and ε-fibre for martensite phase in unidirectionally rolled and cross-rolled stainless steel 316L after deformation up to 90% reduction in thickness.

At the same time (116)[1-10] orientation existed at 10% reduction in martensite and after 30% reduction it was eliminated. This implies that Cube orientation was facilitating the formation of (116)[1-10] orientation in martensite. As the deformation increased, depending on the strain path (mode of deformation), two different deformation textures were formed in martensite. After

deformation of 90% reduction in thickness, R-Cu {112}<110> along with a minor component of Y {111}<112> were formed in martensite for UDR90. As discussed in the previous sections, Brass and Goss were intensified with the increase in deformation in austenite and at the same time R-C component was debilitated while R-Cu {112}<110> in martensite was intensified. This implies that formation of Goss in deformed austenite facilitated formation of R-Copper in martensite for the UDR samples. Additionally, after 70% reduction in thickness, γ-fibre was formed in deformed austenite for the UDR samples and Y {111}<112> orientation was formed at the same time in martensite. Figure 5.11 illustrates γ-fibre for both transformed martensite and deformed austenite in UDR70. As depicted, γ-fibre grains of martensite formed along γ-fibre elongated grains of deformed austenite. This relates formation of Y {111}<112> orientation in martensite to formation of {111} fibre in austenite. On the other hand, R-C {001}<110> with minor orientation of Y {111}<112> were two texture components for deformed martensite in the CR90. As seen, R-C component was formed starting from the early stages of deformation in martensite and spread along ζ-fibre up to 70% deformation. Brass texture also spread along ζ-fibre up to 70% reduction in deformed austenite. The formation of R-C martensite grains along elongated deformed austenite Brass grains implies that the spread of R-C in martensite is attributed to the spread of Brass in austenite. In addition, the decrease in the intensity of R-C in martensite by formation of recrystallized Brass with weaker texture in austenite further supports this correlation.

5.6.2 Annealing Austenite

Figure 5.12 illustrates the evolution of β-fibre and η-fibre for annealed stainless steel 316L after cold rolling up to 90% reduction. Except at reduction of 90%, Brass {110}<112> was the main component with almost similar intensity for all CRA samples. For UDR samples, Brass {110}<112> intensity was reduced by increasing the deformation before annealing while at the same time, Goss {110}<001> intensity was increased. It is concluded that overall texture of the material was highly influenced by the deformation texture of deformed austenite. It means that reversion of ά-martensite happened through an athermal process, which resulted in annealing texture that was the same as the texture of the parent deformed austenite.

As observed, Brass texture strengthened when deformation increased in both the remaining and recrystallized austenite. It is concluded that orientation of deformed austenite affects the recrystallization texture of new grains after annealing. Additionally, S component, which was

reduced by increasing the deformation in the remaining austenite and was eliminated finally at 70% reduction for CR samples, experienced the same effect as the recrystallized Brass texture. Therefore, it is concluded that deformed grains with S {123}<634> orientation could facilitate the formation of new grains with S {123}<634> orientation. Besides, martensite had no major effect on the recrystallization texture of UDR and CR samples until 70% reduction in thickness before annealing, after which the martensite fraction was increased dramatically in all samples. Since martensite grain boundaries impede the movement of austenite grain boundaries during recrystallization, it is believed that formation of martensite increased the incubation time. This caused the incomplete recrystallization in the UDR90 sample following annealing.

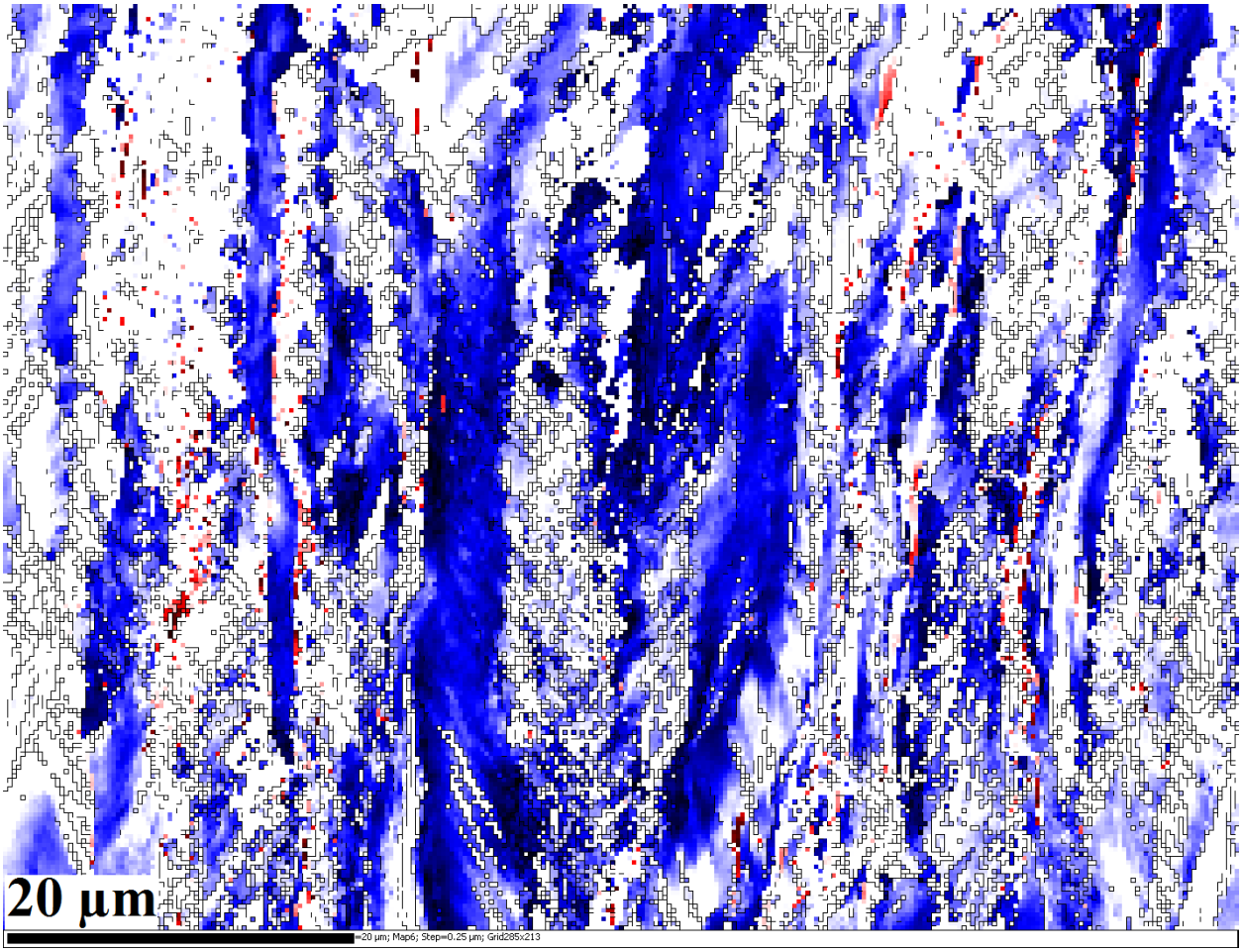

Figure 5.11. OIM map for γ-fibre fraction of austenite (blue) and martensite (red) in UDR70.

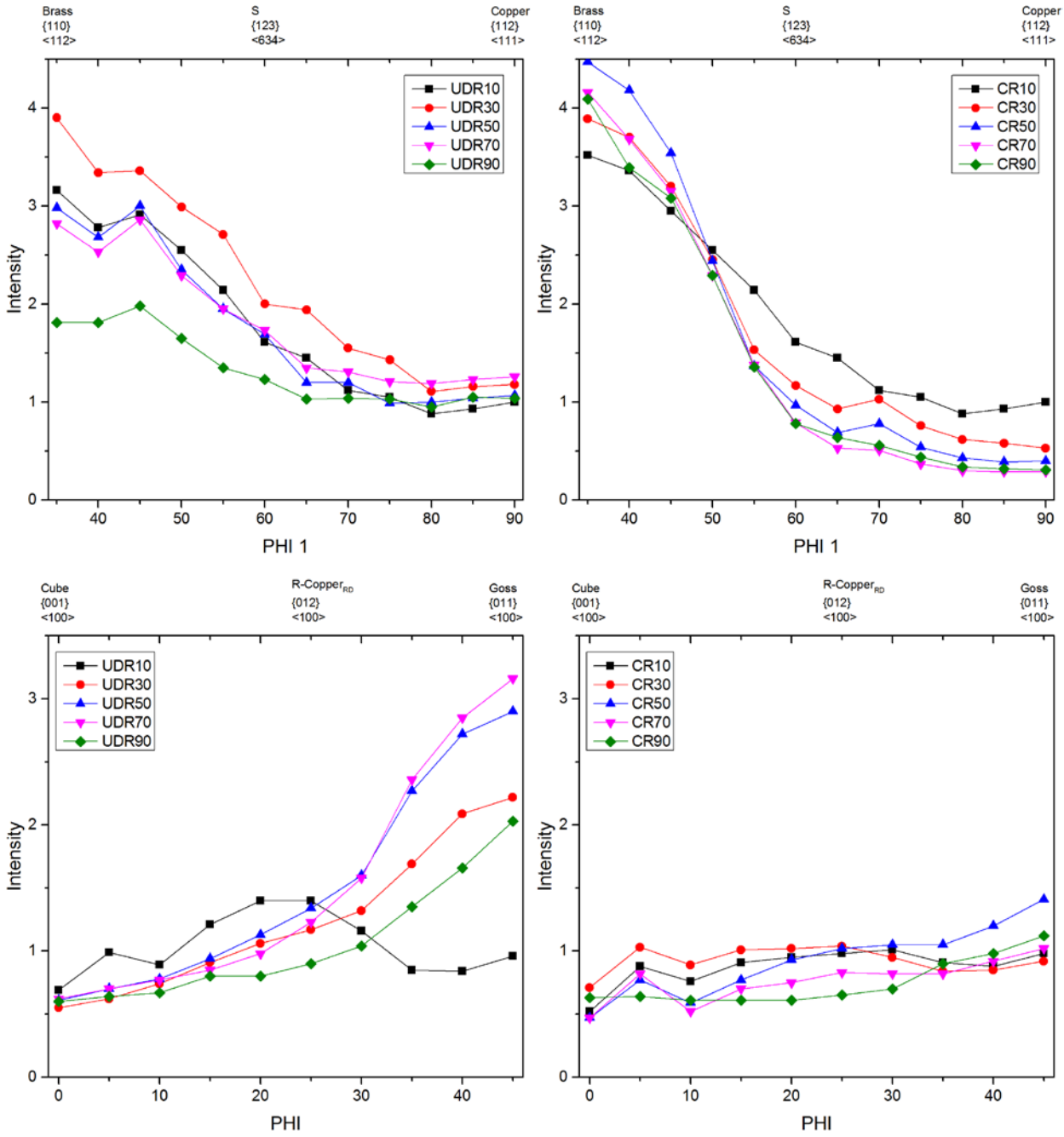

Figure 5.12. β-fibre and η-fibre of annealed stainless steel 316L after cold rolling up to 90% reduction in thickness.

5.7 Conclusions

A comprehensive study on evolution of deformation and recrystallization texture in austenitic stainless steel 316L was done. The following conclusions are made:

1. Rolling mode has a direct effect on the deformation texture of the remaining austenite. Unidirectional rolling results in Brass, Goss and γ-fibre textures, while cross-rolling forms mainly Brass texture for deformed austenite after 90% reduction in thickness.
2. Slip is the deformation mechanism at the early stages of deformation of austenite, while twinning plays the dominant role at higher levels of deformation.
3. An unusual phenomenon is observed after 90% of deformation in the cross-rolled sample in which a highly deformed microstructure transforms to an undeformed microstructure.
4. Strain path also has an important effect on the texture of transformed martensite during deformation. After 90% of deformation, R-Cu {112}<110>and R-C {001}<110> are the main texture components of transformed martensite for UDR and CR samples, respectively.
5. Recrystallization texture is affected mainly by the texture of deformed austenite since martensite reversion is athermal. At reductions higher than 70%, the incubation time for recrystallization of martensite increases, which results in incomplete recrystallization in the UDR sample.

6 EFFECT OF THERMO-MECHANICAL PROCESSING ON OXIDATION OF AUSTENITIC STAINLESS STEEL 316L IN SUPERCRITICAL WATER

6.1 Overview

The results from chapter 5 showed that the microstructure of austenitic stainless steel 316L was successfully optimized using thermo-mechanical processing. In accordance to chapter 5, the current chapter partially satisfies the third and fourth objectives of the thesis, "to evaluate the role of texture and grain size on improvement of the corrosion resistance of austenitic stainless steels 310S and 316L" and "to recommend which of the investigated alloys and under what treatment conditions is expected to perform better in SCW", by evaluating the corrosion resistance of the thermo-mechanically processed austenitic stainless steel 316L samples in SCW. Weight change as a factor of corrosion resistance was measured for all samples and results show that TMP successfully improved their corrosion resistance. Three characterization techniques including XRD, EDS, and EBSD were implemented to identify why TMP improved the corrosion resistance of austenitic stainless steel 316L. In this regard, the changes in the corrosion mechanisms are recognized and preferable microstructure to achieve better corrosion resistance for austenitic stainless steel 316L is proposed.

This manuscript was published in the Journal of Corrosion Science [10] and slight changes have been applied to the original version to avoid repetition. To fulfill the objectives addressed in this chapter, Dr. Hamed Akhiani[11] and Dr. Seyed Morteza Sabet[12] assisted the author of this Ph.D. thesis (Majid Nezakat) with preparation and processing of the samples as well as performing the data analysis. In addition, the corrosion tests in SCW were performed by Mr. Sami Pentillä[13]. Jerzy Szpunar, as the supervisor of this research, provided recommendation, consultation and discussion wherever it was needed. Except the entire or a portion of these parts, all the experiments, data acquisition, and data analysis were conducted by Majid Nezakat, the lead author of the paper.

[10] The copyright permission to use the manuscript in the thesis is obtained and provided in the appendix section. The references of this chapters are provided at the end of the thesis.

[11] Mitsubishi Hitachi Power Systems Canada, LTD., 826 58th Street East, Saskatoon, SK, S7K 5Z4, Canada

[12] Department of Ocean and Mechanical Engineering, Florida Atlantic University, Boca Raton, FL 33431, USA

[13] VTT Technical Research Center of Finland, Materials for Power Engineering, P.O. Box 1000, FI-02044 VTT, Finland

Majid Nezakat wrote the manuscript, integrated comments from the co-authors, and submitted it for review and possible publication.

6.2 Abstract

Oxidation resistance of thermo-mechanical processed stainless steel 316L was studied. The samples were oxidized in SCW with 150 ppb inlet-dissolved O_2 at 600ºC and 25 MPa. Results show that the proposed TMP improved the oxidation resistance by altering the microstructure of stainless steel 316L. It was observed that grain boundaries volume fraction and crystallographic orientation of austenite grains play an important role in oxidation resistance of the material. In addition, oxide exfoliation was completely prevented by applying 50% or more rolling reduction during the TMP.

6.3 Introduction

Over the past fifteen years, ongoing research and development of Generation IV nuclear reactor concepts has been conducted all over the world. The Gen-IV international forum has accepted six different concepts to improve the efficiency and safety of future nuclear power stations. Among them, SCWR has gained a lot of interest due to its simplified design, smaller volume, and higher thermal efficiency compared to light water reactors [88]. In the Canadian design of a SCWR, water enters the reactor core at ~350ºC and exits at 625ºC. It is worth noting that most commercial water-cooled reactors operating today have a coolant temperature barely exceeding 350ºC. Hence, the service environments expected for SCWRs pose significant challenges regarding materials selection [40,53,54,15,89,90,11,91]. The structural components will experience higher operating temperatures, higher neutron doses, and an extremely corrosive environment. Therefore, a systematic study on corrosion of candidate materials is required before they can be used in SCWRs. To date, austenitic stainless steels [45,13,46–49,51,52,92,93], Ni-base alloys [47–50,52,94–101], ferritic-martensitic steels [49,54,102–107], and oxide dispersion strengthened steels [108–111] are the main candidate materials for SCWRs. Among these materials, the austenitic stainless steels have the lowest cost. Several attempts have been made to improve the oxidation resistance of the selected materials using grain boundary engineering [46,98,112], surface modifications [92], and grain refinement [113,114,8]. Xu et al. [98] applied grain boundary engineering via TMP to alter the grain boundary character distribution of a nickel-

based alloy 690. They reported that grain boundary engineered samples have shown a better oxide adhesion compared to the As-received one. Tan et al. [112] performed TMP to improve the corrosion response of Incoloy 800H and Inconel 617. They observed that the fraction of low-Σ coincident site lattice boundaries has been significantly increased. After exposure to SCW, the oxidation of 800H and 617 samples was greatly mitigated as a result of the grain boundary engineering. In another study, Penttilä et al. [92] studied the effect of surface modification on the oxidation resistance of austenitic stainless steel 316L and found that machining the sample surface resulted in a fine-grained microstructure with high dislocation density in the subsurface zone. They showed that after oxidation at 650ºC and 25 MPa, a very thin chromium-rich oxide film, formed on the surface, may have suppressed the inward and outward diffusion of oxygen and iron, respectively. Elsewhere, Abe et al. [8] investigated the effect of grain refinement on oxidation behavior of austenitic stainless steels in superheated steam. They reported an improvement in oxidation resistance due to the formation of a grain refined layer on alloy surface. It is believed that the fine-grained structure was responsible for the formation of protective chromium oxide (Cr_2O_3) layer. Ren et al. [114] also observed an improvement in corrosion resistance of grain-refined ferritic-martensitic steels. It was stated that after exposure to SCW with 25 ppb oxygen at 500ºC for up to 3000h, the corrosion resistance of the grain-refined samples improved due to the enhanced diffusion of chromium to the surface, through a high density of grain boundaries. In our previous work, the microstructure and texture of thermo-mechanically processed austenitic stainless steel 316L were analyzed in detail [115]. The objective of this paper is to clarify how TMP improves the oxidation resistance of 316L steel in SCW. To our knowledge, this process has not previously been studied.

6.4 Materials and methods

Hot rolled stainless steel 316L with a thickness of 6.25 mm and average grain size of 20μm was used as a starting billet for cold rolling. Table 3.1 shows the chemical composition of the alloy. TMP was carried out to prepare samples with different initial microstructures for oxidation test. In the first step, strips of 50×50 mm^2 from the As-received billet were cut and then cold rolled via unidirectional rolling (UDR) and cross-rolling (CR) up to 10, 30, 50, 70 and 90% reductions in thickness, with equal inter-pass rolling steps of 10% true stain. A relatively small true strain was selected to avoid sample rupture due to strain hardening, especially at higher deformations. The

implemented rolling processes and their differences are illustrated in Figure 3.1. Specimens with length of 24 ± 0.01 mm, width of 14 ± 0.01 mm, and thickness of 0.6 ± 0.01 mm were cut from the cold rolled strips. Mechanical grinding of the specimen surfaces was performed using abrasive papers up to grit number 2000 (10µm SiC particles). In the second step, all the cold rolled specimens were annealed at 1050 ºC for 5 minutes per millimeter thickness. Since specimens were annealed at this stage, no stress concentration occurred on their surface [116,117]. Table 3.2 lists the samples and their TMP conditions. Sample name is comprised of cold rolling method (UDR or CR), deformation level (10, 30, 50, 70, and 90%), and post rolling treatment (A stands for annealing), respectively. In order to avoid duplication of data, CR10A was excluded in this study, since it has an almost identical structure to UDR10A [115]. Prior to oxidation, the macro-texture of specimens was measured using a Bruker D8 Discover diffractometer with a two-dimensional x-ray diffraction system (XRD^2) with Cr K_α radiation. The incomplete pole figures at the mid-section of all samples were collected and the orientation distribution function (ODF) was constructed using Resmat® software. Different textural components were extracted from ODFs for detailed discussions. An electron backscatter diffraction system (Oxford NordlysNano EBSD) installed on a Hitachi SU6600 field emission gun scanning electron microscope was used for phase identification and grain size measurement of thermo-mechanically processed material The Specimens were tilted 70º with respect to the horizontal plane using a pre-tilted sample holder and the scanning electron microscope was operated at 20 kV. Aztec HKL software was used to analyze the EBSD data and extracted Inverse pole figure maps from that data relative to an axis that was chosen to be the direction normal to the rolling plane. The specimens were oxidized in SCW at 600ºC and 25 MPa for 100, 300 and 1000h in an autoclave connected to a recirculation water loop, as illustrated in Figure 3.4. Table 3.3 shows values for temperature, pressure, inlet and outlet water conductivity, oxygen content and flow rate, which were monitored and controlled. To avoid leakage in the piping junctions, the water flow was kept low as the operating temperature was high (600ºC). The specimens were attached to a special sample holder where they were electrically insulated from the rack and from the autoclave body. The weight of each specimen was measured before and after 100, 300 and 1000h exposure and the weight changes were calculated per unit area. After the exposure test, the samples were mounted in a conductive edge retention resin (Struers Polyfast®). The cross-section of the samples was mechanically grinded up to abrasive paper grit number 2000 (10µm SiC particles) and then polished using water based diamond

suspensions up to 1 µm diamond particle size (Struers DiaPro®). At this stage, the polishing wheel speed was lower than 150 rpm to avoid breakdown of the fragile oxide layer. The polishing was continued using 0.04 µm colloidal silica suspension (Struers OP-S®) on a Vibratory Polisher (Buehler VibroMet^{TM} 2) for 24 h. Finally, the oxide layer structures were analyzed at the cross-sections of the samples using field emission gun scanning electron microscope at 20 kV. The microscope was equipped with EBSD and energy dispersive spectroscopy (EDS) detectors (Oxford X-Max Silicon Drift).

6.5 Results

6.5.1 Weight Change

Figure 6.1 depicts the weight changes of samples after exposure to SCW for 100 and 300 and 1000h. No oxide exfoliation was observed by visual inspection of the specimens after 100 and 300h of exposure. This was confirmed, since no decrease in weight was registered with increasing oxidation time up to 300h, as the weight of all samples increased. This shows that there was a good adhesion of oxide scale to the substrate up to 300h of oxidation for all samples. However, by 1000h of exposure time, As-received, UDR10A, UDR30A, and CR30A samples showed a decrease in weight, while the rest of the samples, which experienced more than 30% deformation during TMP, still showed weight gains. This demonstrates that at higher exposure times (i.e., more than 300h) samples are more susceptible to oxide exfoliation; however, TMP improved the adhesion of oxide scale to the substrate for the samples with deformation of more than 30%.

6.5.2 Phase identification & elemental composition

Figure 6.2 illustrates XRD patterns of thermo-mechanically processed samples after exposure to SCW at 600ºC and 25 MPa for 100, 300, and 1000h. After 100h of exposure time, all samples exhibited three different peaks corresponding to austenite, magnetite (Fe_3O_4) and spinel phase ($FeCr_2O_4$). By increasing the exposure time up to 300h, all phases were still present. However, with the increase of exposure time, the intensity of magnetite rose while the intensity of austenite was reduced. The same compounds were observed in all samples with increasing the exposure time to 1000h. Nevertheless, in the UDR70A, CR70A, UDR90A, and CR90A samples, hematite (Fe_2O_3) as well as chromium oxide were also detected. To complement the information obtained from XRD patterns, the cross-sections of As-received and UDR90A samples were studied.

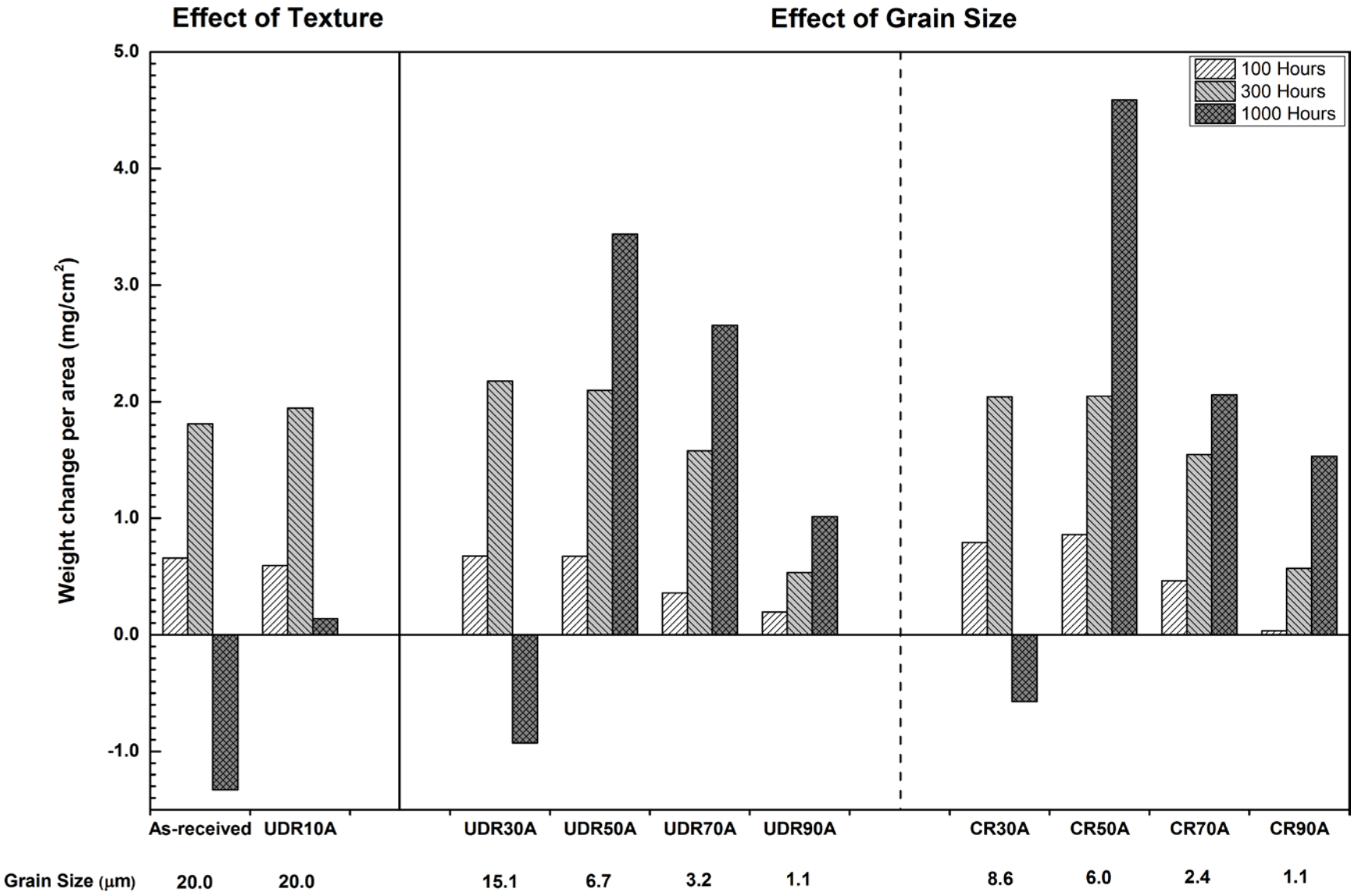

Figure 6.1. Weight change of thermo-mechanically processed stainless steel 316L samples after exposure to SCW at 600ºC and 25 MPa for 100, 300, and 1000h.

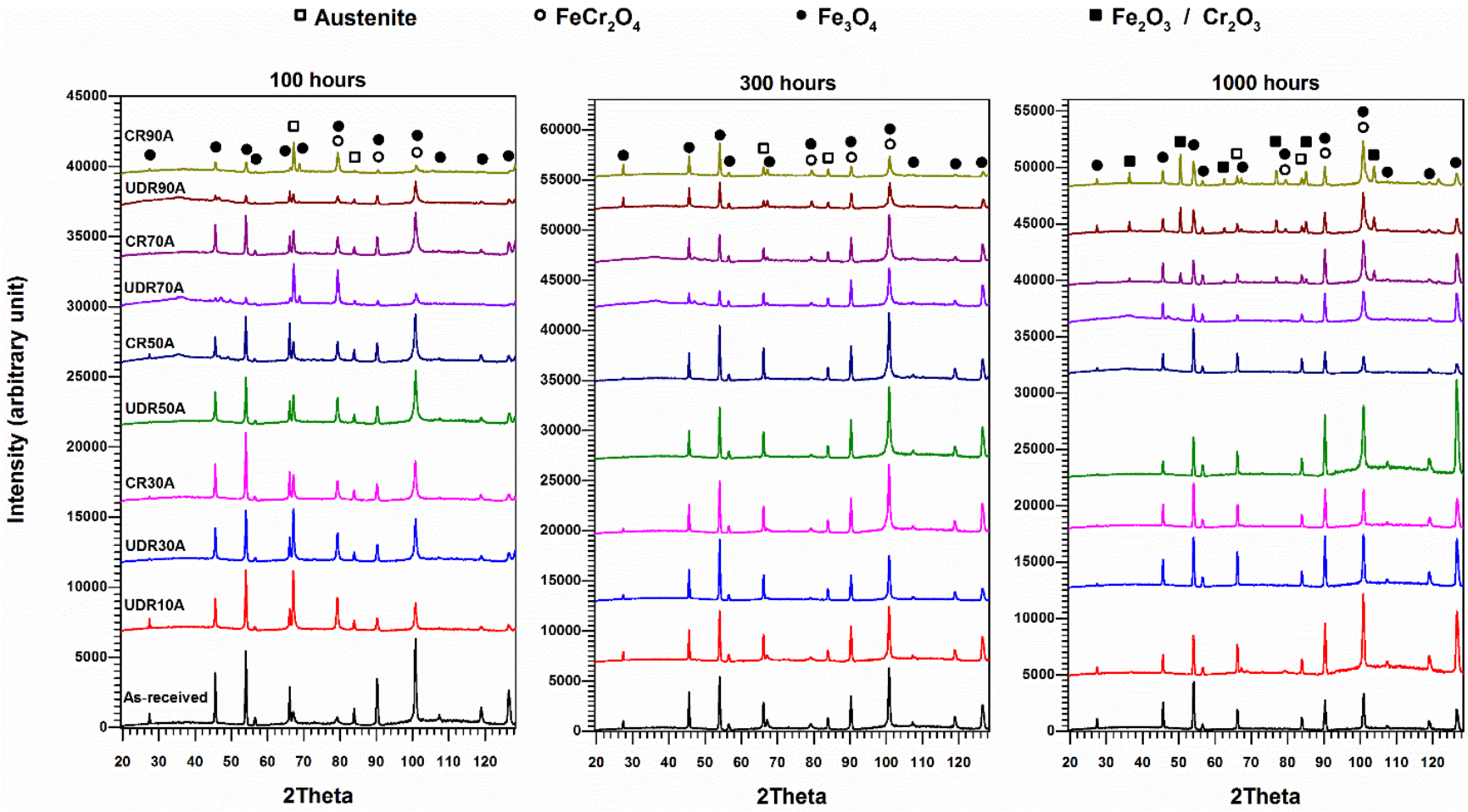

Figure 6.2. X-ray diffraction patterns of thermo-mechanically processed stainless steel 316L samples after exposure to SCW at 600ºC and 25 MPa for 100, 300, and 1000h.

Figure 6.3 depicts the EBSD band contrast and phase map as well as EDS maps of elemental composition on the cross-section of the As-received sample after an exposure time of 1000h. Due to very low concentration of chromium and nickel, compared to oxygen and iron, the EDS elemental maps were not normalized. Three different regions are present. The first region consists of iron and oxygen and, based on the EBSD phase map and XRD result, is composed of magnetite. As seen, initially small magnetite grains were formed on the substrate and some grains grew along the direction normal to the surface. The thickness of the external oxide layer (magnetite) was between 30-40µm. The second region, which had the same thickness as the first region, consists of chromium, iron, and oxygen. The XRD pattern identified this compound as spinel phase with a crystal structure similar to magnetite. It is notable that the EBSD phase map indexed the spinel phase the same as austenite since both have face-centred cubic structure. As well, the elemental distribution in this region shows that chromium concentration was higher at the grain boundaries than inside the grains. In addition, chromium oxide and nickel were observed at the grain boundaries; particularly, nickel exists near the oxide interface. However chromium oxide could not be detected by XRD because their quantities were too small.

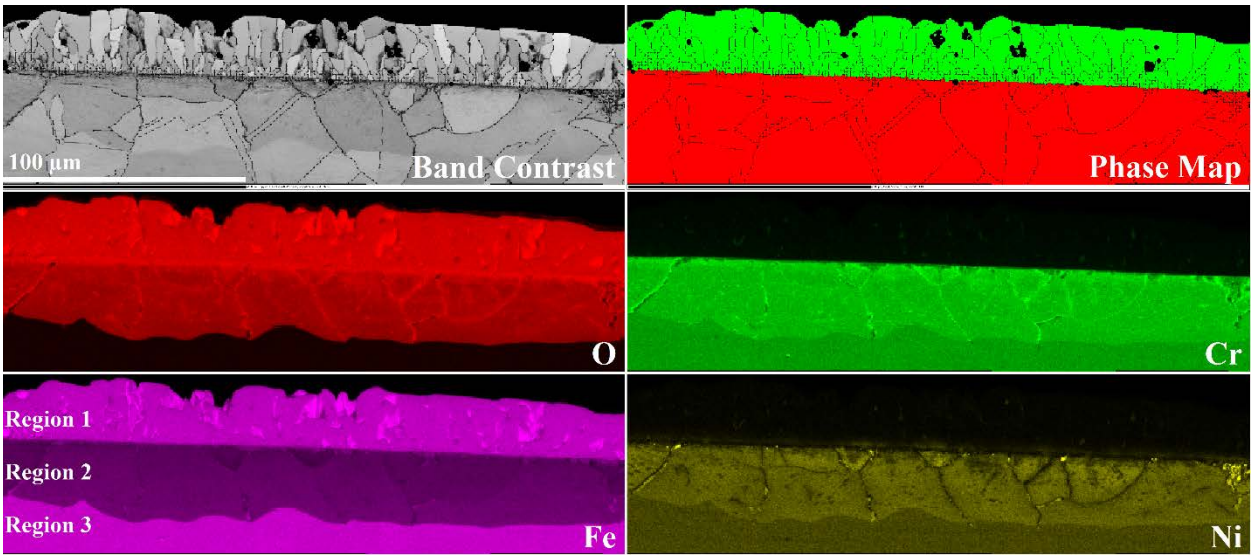

Figure 6.3. EBSD band contrast and phase map (red: austenite and spinel phase, green: magnetite) and EDS elemental composition of As-received stainless steel 316L after exposure to SCW at 600ºC and 25 MPa for 1000h.

Figure 6.4 illustrates the EBSD band contrast, phase, and EDS maps of the cross-section of the UDR90A sample after 1000h exposure time. Six distinguishable regions observed in this sample

were hematite, magnetite, spinel phase, chromium oxide, Ni-rich zone and austenite. The first two layers were composed of iron and oxygen, based on EDS maps. However, the EBSD phase map reveals that the upper layer was hematite with an average thickness of 3 µm. The hematite layer was elongated in the direction parallel to the oxidation surface with relatively large grains compared to the initial magnetite grains. In addition, the phase map indicates that the second layer consisted of magnetite with an average thickness of 10µm. This layer was formed at the interface between the external and internal oxide scales with small initial grains. By increasing the exposure time, some grains that exert less energy to the system grew larger in the direction normal to the surface. These grains were relatively larger in size compared with initially formed magnetite grains. The next two layers were the internally oxidized regions with an average thickness equal to the sum of the first two layers. The EDS elemental map reveals the presence of spinel phase in the third layer as chromium, iron, and oxygen were the main elements. In addition, the fourth region is consisted of chromium and oxygen which indicates the formation of chromium oxide. Presence of the spinel phase and the chromium oxide were also confirmed by XRD. The fifth and sixth regions are Ni-rich zone and austenite, respectively. Enrichment of nickel in the fifth region happened because of outward diffusion of chromium and iron. Some localized Ni-rich spots are also visible inside the spinel phase.

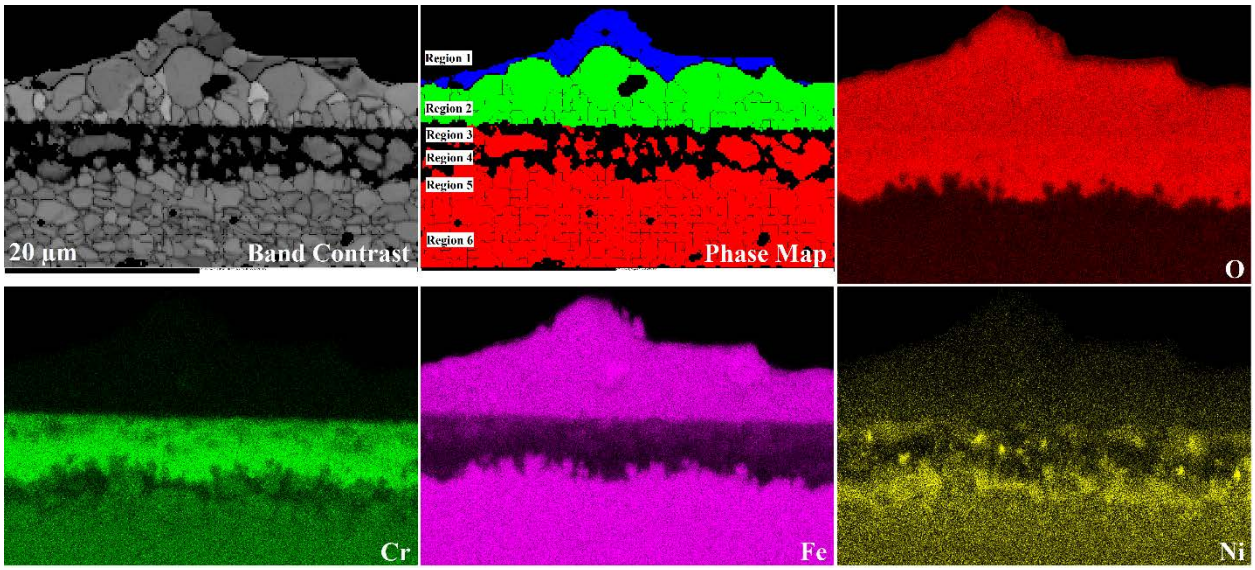

Figure 6.4. EBSD band contrast and phase map (red: austenite and spinel phase; green: magnetite; blue: hematite) and EDS elemental composition of thermo-mechanically processed (UDR90A) stainless steel 316L after exposure to SCW at 600ºC and 25 MPa for 1000h.

6.5.3 Surface morphology

Figure 6.5 illustrates surface morphologies of the As-received, UDR90A (corresponding to the highest oxidation resistance), and UDR30A (corresponding to the lowest oxidation resistance) samples after exposure to SCW at 600ºC and 25 MPa for 100, 300, and 1000h. After 100h of exposure time, magnetite was present on the surface of the As-received sample and it remained on the surface up to 1000h. Magnetite grains grew with increasing the exposure time from 3 µm to 20µm. The grains had a polyhedral shape up to 100h of oxidation, but turned to a flatter shape with sharper edges with increasing the exposure time. It was also seen that in the sample exposed for 1000h, a part of the magnetite grains spalled away and a sinuate pattern remained. UDR30A also showed the same trend, as magnetite was present at all exposure times and the grains grew from 3 µm to 20µm with increasing the oxidation time. The magnetite grains were also polyhedral in shape after 100h, and with increasing the oxidation time they grew into a flat shape; however, spallation was less and sinuate pattern was also observable.

Since the oxidation weight gain was lower in the UDR90A, magnetite did not completely cover the surface after 100h of exposure, and therefore spinel phase and chromium oxide that appeared as internal oxidation were exposed. At this stage, magnetite grains formed at the interface of internal/external oxidation regions so that it possessed a different range of grain sizes from sub-microns to 5 µm with polyhedral shape and round edges. Figure 6.6 shows the spinel phase as well as chromium oxide grains at higher resolution. Chromium oxide had tiny polyhedral shaped grains with sharp edges and an average grain size of 50 nm, while spinel phase consisted of flat grains with a larger grain size (~500 nm). By 300h of oxidation time, while a larger area of the surface was covered with magnetite, nucleation was still in progress and both chromium oxide and spinel phase were still observable. Nevertheless, the magnetite grains were larger in size with sharp edges and a flat shape. A clearly different oxide morphology was observed after 1000h of oxidation, which appeared to be hematite, based on XRD and EBSD results (Figure 6.3 and Figure 6.4). This would suggest that at some point between 300h and 1000h of exposure time, magnetite fully covered the surface and hematite started to nucleate on the top due to the lower concentration of iron on the surface. As seen, hematite grains were present from a few microns to 20µm with a wavy surface area. These grains squeezed together and completely covered the magnetite grains.

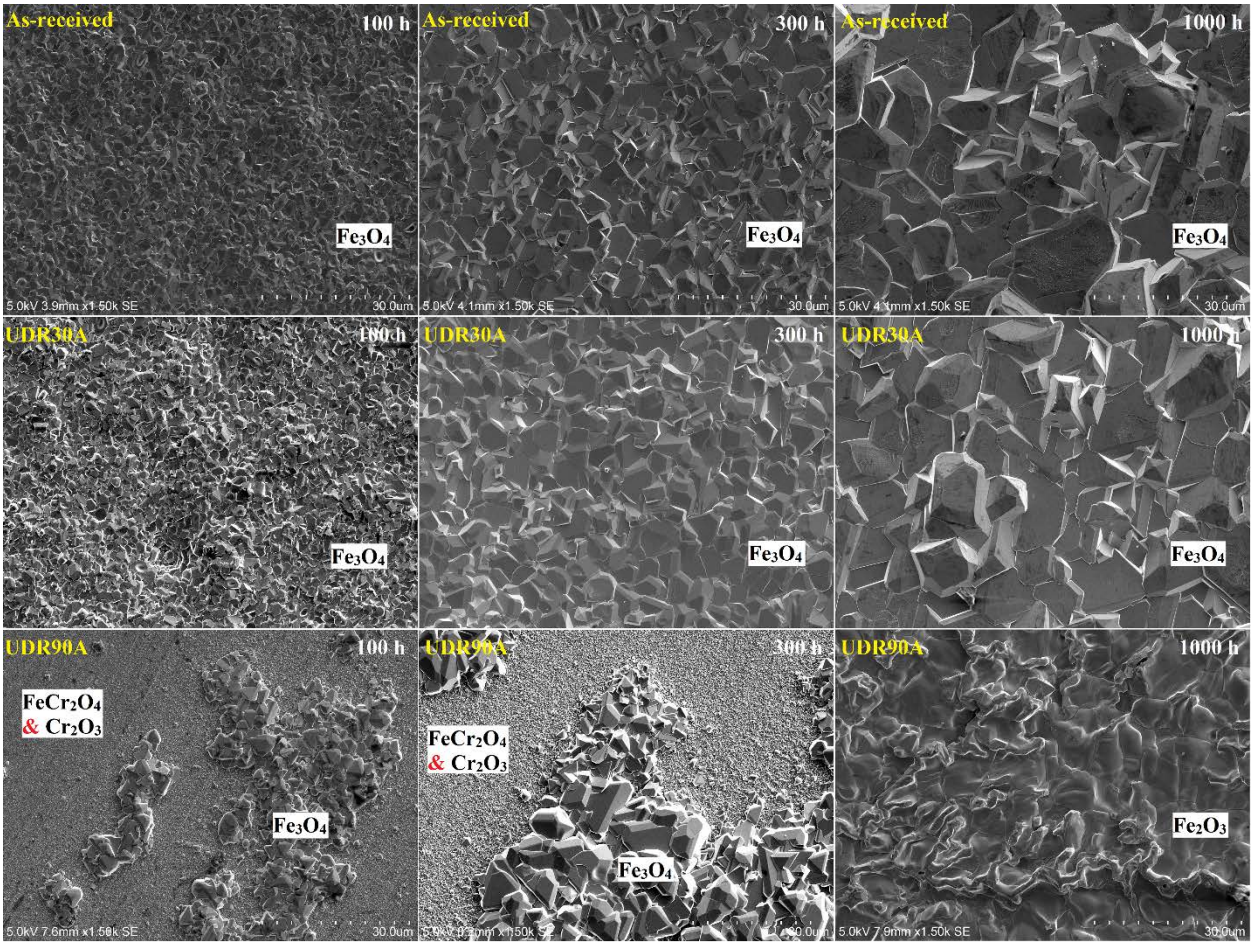

Figure 6.5. Surface morphologies of the oxide scales of As-received and thermo-mechanically processed (UDR30A and UDR90A) stainless steel 316L after exposure to SCW at 600ºC and 25 MPa for 100, 300, and 1000h.

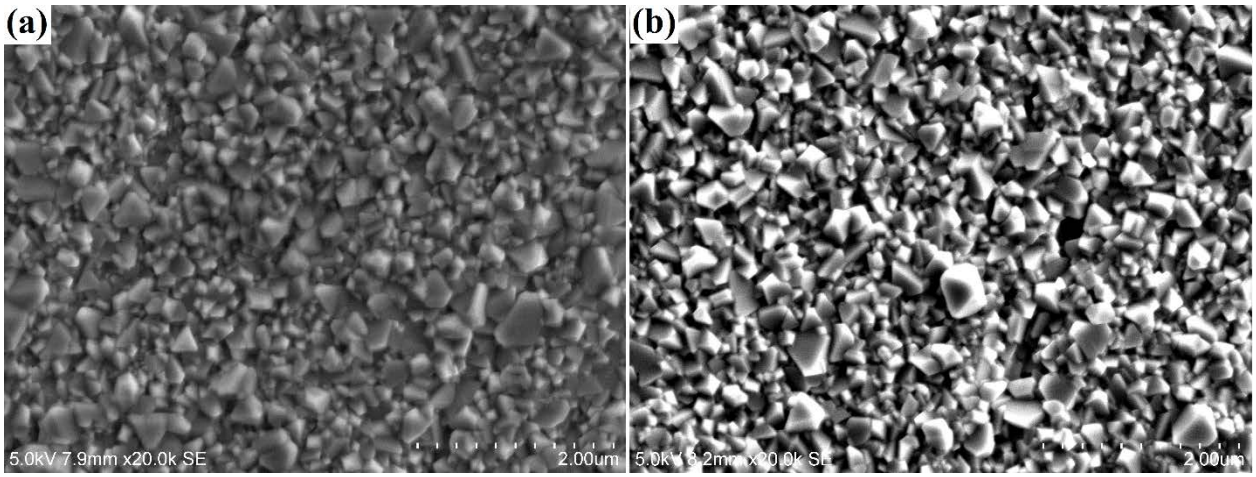

Figure 6.6. Surface morphologies of the spinel phase of thermo-mechanically processed (UDR90A) stainless steel 316L after exposure to SCW at 600ºC and 25 MPa for 100 and 300h.

6.6 Discussion

6.6.1 Oxidation Mechanism

The oxidation of stainless steel 316L exposed to SCW can be described through two mechanisms. Figure 6.7 (a) represents the oxidation mechanism for UDR70A, CR70A, UDR90A, and CR90A in SCW. The oxidation mechanism for the rest of the samples is displayed in Figure 6.7 (b).

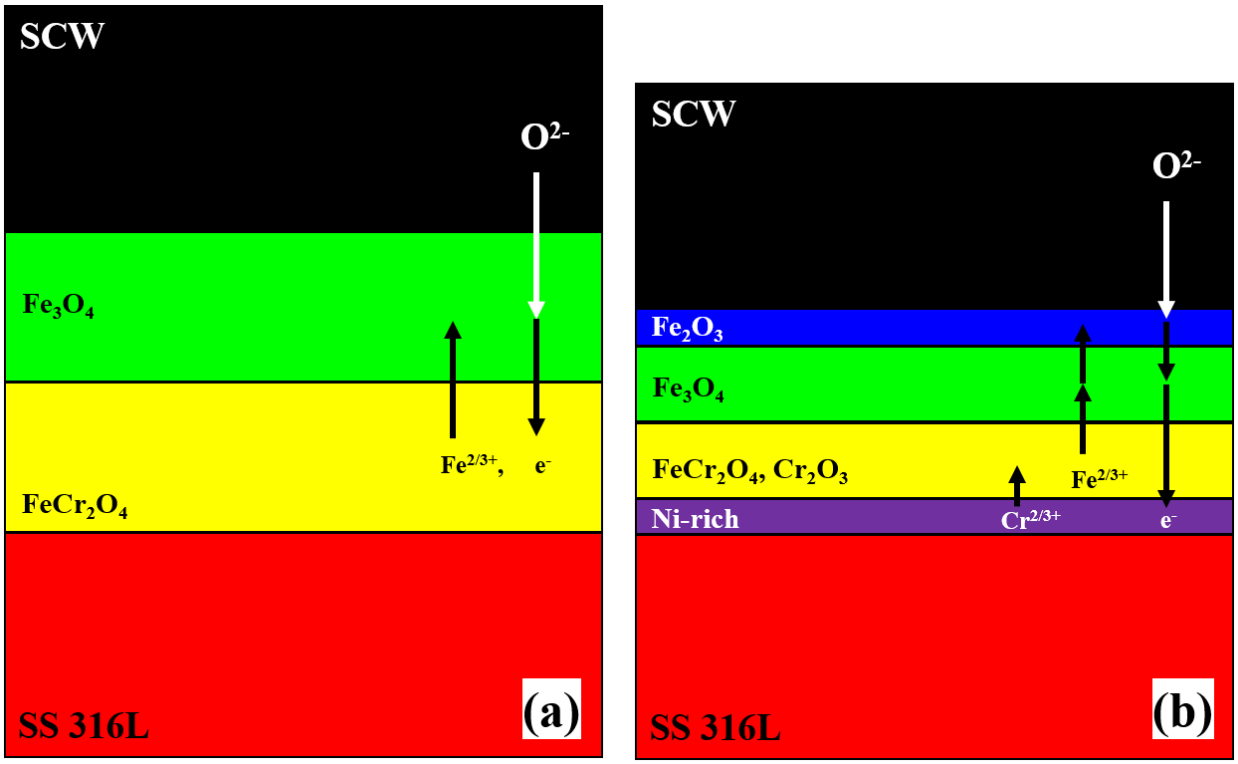

Figure 6.7. Oxidation mechanism for stainless steel 316L after exposure to SCW at 600ºC and 25 MPa (a) As-received, thermo-mechanically processed UDR10A, UDR30A, CR30A, UDR50A, and CR50A, and (b) thermo-mechanically processed UDR70A, CR70A, UDR90A, and CR90A.

The main difference between these mechanisms is the presence of Ni-rich zone, hematite and chromium oxide. Since iron ions must have a higher mobility than chromium ions in diffusing through the substrate to the surface, iron oxide (Fe_3O_4) started to form. Diffusion of iron ions can take place through both grain bodies and grain boundaries. However, grain boundaries have much higher diffusivity over the lattice, which allowed a higher fraction to diffuse [118]. Therefore, the diffusion of iron and chromium through grain boundaries is important in nanostructured materials. On the other hand, oxygen diffuses mostly through the grain boundaries into the substrate (see

Figure 6.3), where iron concentration was low enough to form spinel phase. Moreover, the lower concentration of iron and higher concentration of oxygen at the grain boundaries, compared with the grains bulk, led to the formation of chromium oxide. Oxygen does not interact with nickel since chromium has higher affinity [119]. Therefore, the formations of chromium oxide, which is thermodynamically possible, happened only at the grain boundaries.

The other possible oxidation mechanism happened in samples with smaller grain size including UDR70A, CR70A, UDR90A, and CR90A. The oxidation mechanism that was previously discussed applies here to some extent. However, with very small grains, below a critical grain size, the fraction of grain boundaries was high enough to cause the substrate to encounter a shortage of iron in a way that met the criteria for possible formation of chromium oxide inside the grains. Moreover, chromium diffused from beneath to the spinel phase region which led to depletion of chromium and enrichment of nickel. Chromium diffusion will provide enough material to form a continuous chromium oxide beneath the spinel phase. Now, the continuous chromium oxide acts as a protective barrier against further outward diffusion of iron ions as well as inward diffusion of oxygen ions. As a result, fewer iron ions were provided on the surface at the interface of iron oxide and SCW. After a certain amount of time, the condition for formation of hematite would have been provided.

These two mechanisms apply until oxide exfoliation start to begin. However, SEM and EDS observations at the cross-section and on the surface of the samples where exfoliation happened revealed that no further iron oxide was formed on top of the remained spinel phase with continuing the oxidation. This could be due to the shortage of iron in the substrate and slower diffusion of iron ions through the spinel phase. Nevertheless, longer exposure time (e.g. 3000h) is needed to reveal if a new oxide compound will form.

6.6.2 Surface Morphology

As shown in Figure 6.5, two different oxide morphologies are distinguishable. The first one happened in all samples except for UDR70A, CR70A, UDR90A, and CR90A. At the early stages of oxidation, a large number of magnetite grains with a polyhedral shape began to form on the substrate. The magnetite grains started to grow with increase in the oxidation time. Out of the whole surface covered by the magnetic grains, only those with preferable oriented grains would grow in the direction normal to the surface. Such preferential growth might be related to lower

surface energy of these grains. When oxide grains grow larger, they will have a rather flat surface. At higher oxidation times, flat shaped magnetite grains covered the entire surface of the samples. The second morphology occurred for UDR70A, CR70A, UDR90A, and CR90A samples. The difference between this morphology and the previous one is that when magnetite grains still had a polyhedral shape, hematite started to form on the top of these grains due to a deficiency of iron ions. Since the magnetite grains were not yet flat, the hematite first began to fill the gaps between magnetite grains. Consequently, the image of hematite grains shows a wavy pattern with higher internal stress, as the band contrast of hematite is darker than the freely elongated magnetite grains (see Figure 6.4). This is because the available nucleation sites were not on a flat surface and magnetite grains that acted as a substrate could also have permitted epitaxial growth for the hematite grains.

6.6.3 Oxidation Resistance

According to the weight change measurements and SEM observations, no oxide exfoliation was happened up to 300h of exposure time for any of the samples. As seen in Figure 6.1, the weight change trend for 300h of exposure time follows the similar trend to that of 100h. This trend is still similar after 1000h exposure for the sample in which exfoliation did not happen. Accordingly, it is believed that the samples that experienced oxide exfoliation after 1000h of exposure time would have followed the same trend in the absence of exfoliation. Therefore, the results of 300h oxidation of all samples are reasonable enough to compare their oxidation resistance in SCW.

It is known that TMP can alter the structure of materials including texture, grain size, and grain boundary character distribution, depending on deformation technique, deformation level, and heat treatment factors such as temperature and time. In this study, the texture of As-received stainless steel 316L was changed to some extent by TMP. This is possible by 10% of deformation that is followed by annealing. The average grain size of the thermo-mechanically processed specimen is remained the same as the As-received one. On the other hand, for each mode of deformation (i.e. UDR or CR), with increasing deformation during TMP up to 90%, the texture of samples remained almost the same, but their average grain size decreased. In this section, the influence of texture and microstructure will be discussed separately.

6.6.3.1 Effect of texture

Figure 6.8 presents the ODF sections of the As-received and UDR10A samples. Both samples had an average grain size of 20µm. Four major components with low intensity including Brass {110}<112>, S {123}<634>, Copper {112}<111>, and Cube {001}<100> were present in the As-received sample. All these components were also present in UDR10A except Cube {001}<100>. It should be noted that the Brass {110}<112> component had stronger intensity in UDR10A compared to the As-received sample. Although completely different textures were not generated, results show that TMP altered the texture of the As-received samples to some extent.

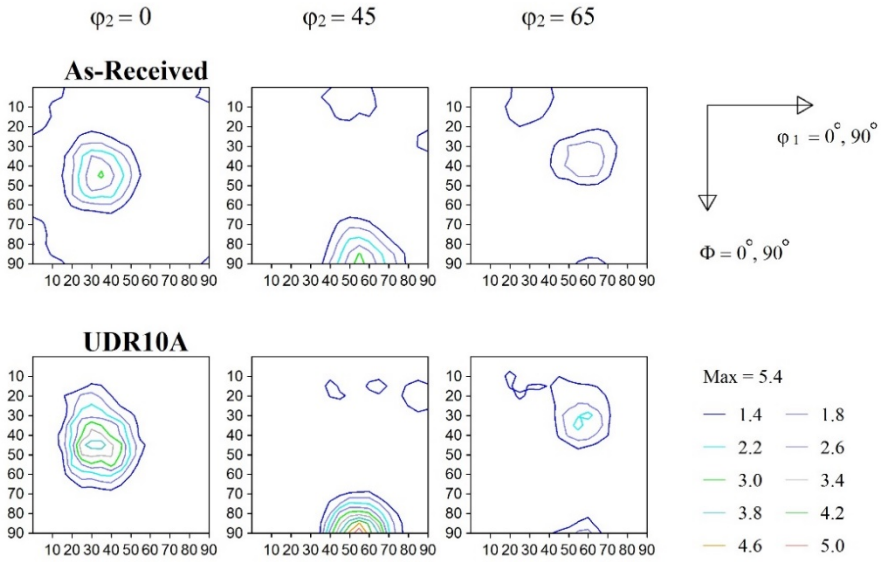

Figure 6.8. ODF sections at ϕ_2= 0º, 45º, and 65º for As-received and UDR10A samples.

Oxidation results showed no significant difference in the weight change of both samples after exposing to oxidative environment up to 100h; however, by increasing the oxidation time to 300h, a higher weight gain (~ 10%) was achieved for UDR10A sample, compared to the As-received sample (see Figure 6.1). In face-centred cubic materials, {001} planes have a higher atomic density than {110} planes. Considering the fact that the oxidation mechanism in the As-received and UDR10A samples was controlled by inward diffusion of oxygen and outward diffusion of iron, {001} planes with higher atomic density than {110} planes made the diffusion process harder in the samples textured this way. Therefore, although the differences in weight change are not significant, they could have been due to the presence of Cube {001}<100> component and a higher fraction of Brass {110}<112> component in the As-received and UDR10A samples, respectively.

The result for 1000h of oxidation is not comparable since oxide scale exfoliation was seen by visuals inspection of the both samples.

6.6.3.2 Effect of microstructure

Figure 6.9 depicts the ODF sections of thermo-mechanically processed stainless steel 316L in which a cold deformation from 30% up to 90% was applied. Clearly, Goss {110}<001> was the major texture component with almost the same intensity for all the UDR samples. Besides, Brass {110}<112> was the main texture component with almost the same intensity for CR samples.

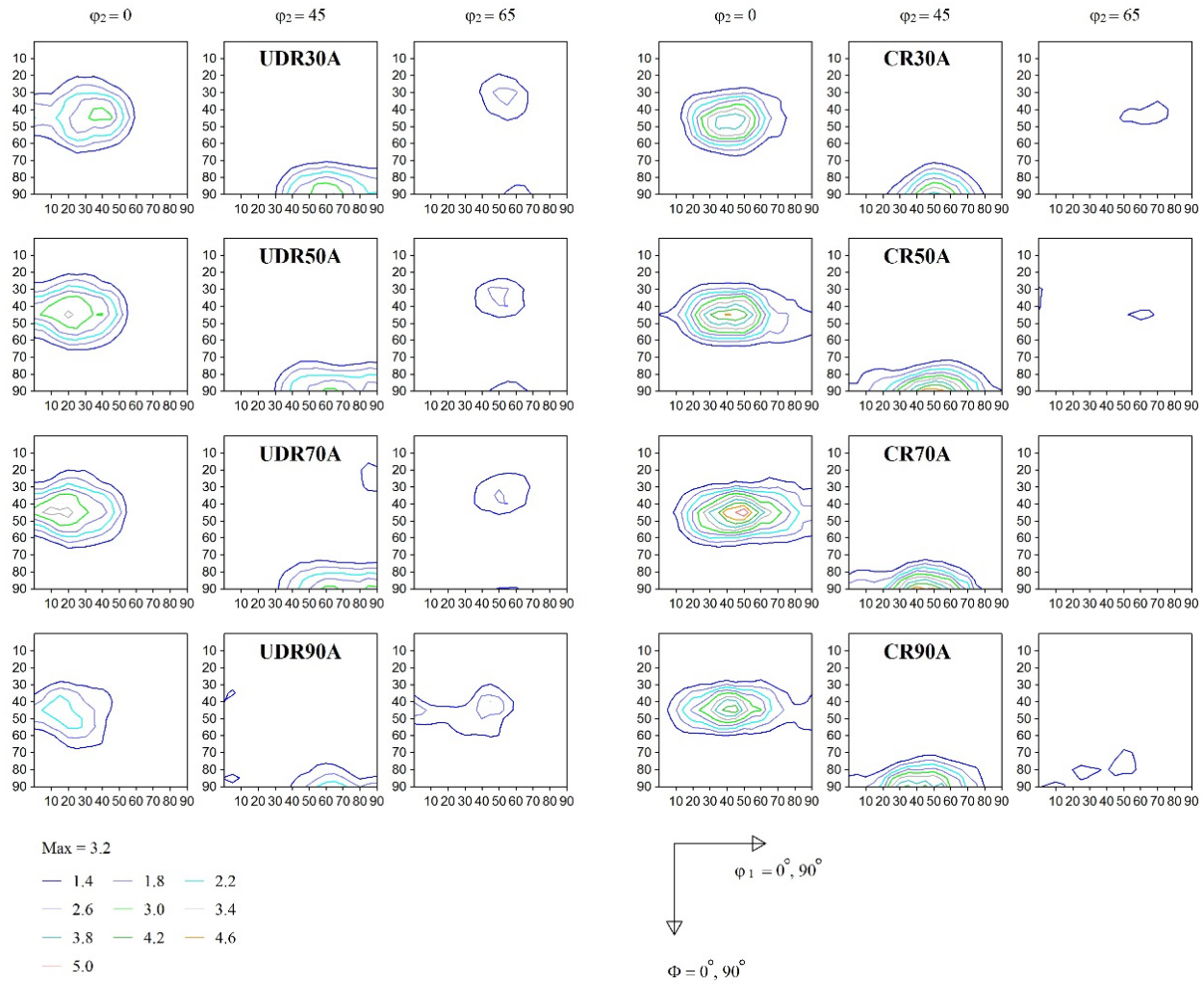

Figure 6.9. ODF sections at ϕ_2= 0º, 45º, and 65º for thermo-mechanically processed stainless steel 316L.

In other words, texture remained the same for the samples with the same deformation mode (i.e. UDR or CR). However, TMP changed the average grain size of the samples, as illustrated by Figure 6.10. The average grain size reduced with increasing the deformation during the treatment for both UDR and CR samples. However, CR samples show a slightly lower average grain size. In total, it appears that the TMP reduced the average grain size while {110}<uvw> texture does not change much.

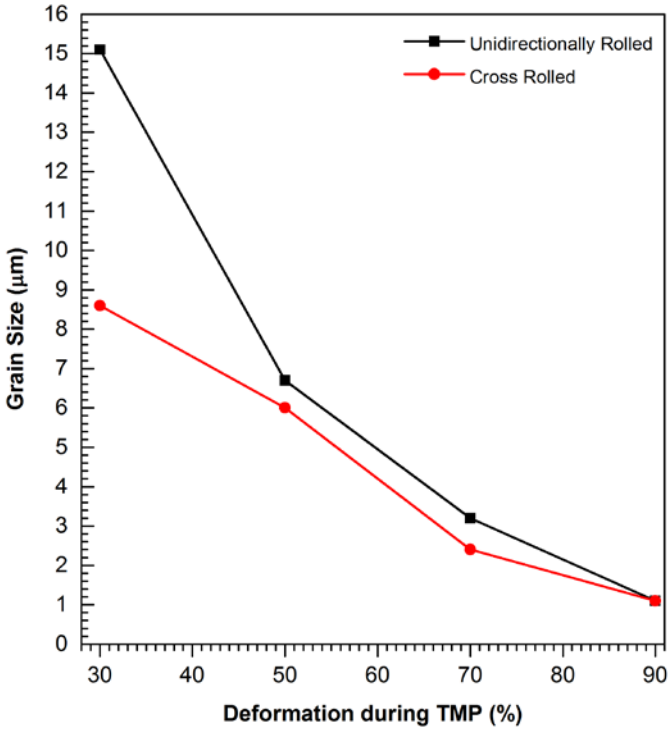

Figure 6.10. Effect of TMP on the grain size of stainless steel 316L.

It is well known that grain boundaries are fast diffusion pathways. Since diffusion is critical to oxide growth, one possible way to influence oxidation rates is to change the grain size. This has two potentially offsetting effects: Smaller grains allow oxide-forming elements, like iron, to quickly diffuse to the surface and form oxides, while a protective oxide layer like chromium oxide forms beneath. On the contrary, smaller grains can allow oxygen to rapidly enter the bulk metal and form an oxide, which is not desired [16]. Typically, the amounts of protective oxide-forming elements, like chromium, in the bulk metal determine whether smaller grains are beneficial to mitigating oxidation. According to the weight change, XRD, EBSD, and EDS results, below a critical average grain size, the protective oxide layer was thick and continual enough to decrease

the outward and inward diffusion rates of iron and oxygen ions, respectively. Consequently, the oxidation rate reduced drastically. The critical average grain size was found to be about 3 μm in this study (UDR70A and CR70A). Furthermore, decreasing the grain size also helped the formation of hematite, which showed a more compact morphology compared to magnetite. Therefore, it might also reduce the diffusion rate, although it has a minor effect.

6.7 Conclusions

The effect of TMP on austenitic stainless steel 316L after exposure to SCW were studied and the following are concluded:

1. TMP improvs the oxidation resistance of stainless steel 316L up to four times.
2. Oxide scale exfoliation is completely prevented by the TMP when the cold rolling thickness reduction is 50% and higher.
3. The average grain size of stainless steel 316L is successfully reduced from 20μm to 1 μm for almost the same {110}<uvw> texture via TMP. Oxidation resistance of the samples is enhanced with decrease in the grain size. It is found that below a critical average grain size, the higher fraction of grain boundaries causes the formation of a protective chromium oxide layer. The oxide layer is thick and continuous enough to decrease the diffusion rate of iron ions and oxygen ions and as a result the oxidation rate is reduced significantly. The critical average grain size is found to be about 3 μm.
4. Based on the average grain size, two oxidation mechanisms are identified. An attempt is made to explain existing surface morphologies that results from different oxidation mechanisms.
5. After the texture of the As-received sample is changed to some extent while keeping the grain size constant, it is observed that the presence of {001}<uvw> improved the oxidation resistance by 10%. However, some very different textures need to be generated to determine if texture is as important as grain size.

7 CHARACTERIZATION OF THE OXIDE FILM ON STAINLESS STEEL 316L EXPOSED TO SUPERCRITICAL WATER ENVIRONMENT

7.1 Overview

In chapter 6, it was shown that the thermo-mechanical processing can effectively increase the corrosion resistance of austenitic stainless steel 316L. This drastic change in the corrosion resistance of the alloy was explained based on the changes in the corrosion mechanisms. This chapter addresses a part of the third objective of the thesis, "to evaluate the role of texture and grain size on improvement of the corrosion resistance of austenitic stainless steels 310S and 316L", by investigating the orientation correlation between the alloy and the present oxides or the oxides themselves. The goal is to evaluate if the microstructural factors (i.e. average grain size and texture) of the substrate have any effect on the structure and orientation of the formed oxides. Therefore, XRD and EBSD techniques were utilized to characterized the oxide layer by measuring the micro and macro texture of each oxide present on the surface of the samples.

This manuscript is submitted to the Journal of Corrosion Science [14] for publication and slight changes have been applied to the original version to avoid repetition in the thesis. In order to satisfy the goals of this chapter, Dr. Hamed Akhiani[15] assisted the author of this Ph.D. thesis (Majid Nezakat) with preparation and processing of the samples as well as performing the data analysis. In addition, the corrosion tests in SCW were performed by Mr. Sami Pentillä[16]. Jerzy Szpunar, as the supervisor of this research, provided recommendation, consultation and discussion wherever it was needed. Except the entire or a portion of these parts, all the experiments, data acquisition, and data analysis were conducted by Majid Nezakat, the lead author of the paper. Majid Nezakat wrote the manuscript, integrated comments from the co-authors, and submitted it for review and possible publication.

[14] The copyright permission to use the manuscript in the thesis is obtained and provided in the appendix section. The references of this chapters are provided at the end of the thesis.

[15] Mitsubishi Hitachi Power Systems Canada, LTD., 826 58th Street East, Saskatoon, SK, S7K 5Z4, Canada

[16] VTT Technical Research Center of Finland, Materials for Power Engineering, P.O. Box 1000, FI-02044 VTT, Finland

7.2 Abstract

The formation of oxides structures on an austenitic stainless steel 316L after exposure to SCW at 600ºC and 25 MPa was studied. TMP was implemented to investigate the influence of texture and grain size of the substrate on the structure of the formed oxides. Results showed that magnetite develop a strong (111)<uvw> texture and hematite shows a strong near-(0001)<uvtw> texture. The texture of 316L substrate does not affect the texture of magnetite, and also the texture of magnetite does not influence the texture of hematite. However, the surface roughness of the magnetite could slightly alter the texture of hematite. The surface energy minimization and strain energy minimization models were used to explain the strong texture of magnetite and hematite.

7.3 Introduction

Thermal conductivity and reactivity of water significantly change at pressures and temperatures higher than 374.15ºC and 22.1 MPa. These changes can be adopted for a large number of applications such as destruction of hazardous chemicals by oxidation [51,52] and implementation as a cooling and heat transfer medium [40,41]. The latter application was employed to increase the thermal efficiency of future generation of nuclear reactors in the design of SCW reactor (SCWR) [4,21]. However, due to high corrosive environment of SCW on one hand and high fuel cladding peak temperature on the other, one of the major challenges upon bringing this concept reactor to a practical use is to find novel structural materials such as fuel cladding. As a result, members of Generation IV International Forum (GIF) initiated a search to develop the materials which can resist the harsh environment inside SCWR core [21]. Among the proposed materials, austenitic stainless steel AISI 316L, which is widely used as structural material in conventional nuclear reactors [42,43], drew a lot of attentions due to superior oxidation and creep resistance [45,13,46–49,92]. AISI 316L is a molybdenum-bearing austenitic stainless steel, which is also more resistant to general corrosion and pitting/crevice corrosion than the conventional chromium-nickel austenitic stainless steels such as AISI 304 [35,62,63]. Moreover, this alloy offers better creep resistance and higher tensile strength at elevated temperatures [35,62,63].

There are many studies in the literature about oxidation behavior of Fe-Cr-Ni based alloys in SCW in which weight change, oxidation mechanisms, and possible ways to improve the oxidation resistance are investigated [44,53,98,104,112,114,16,120–122]. However, there are only few

studies available on the structure of the oxide scale and the crystallographic relation between the oxide and the alloy [98,121]. In our previous study, we investigated the effect of TMP on oxidation of austenitic stainless steel AISI 316L in SCW at 600ºC and 25 MPa [44]. We suggested two possible oxidation mechanisms based on assumption of that average grain size plays an important role in oxidation resistance enhancement of AISI 316L. As a complimentary study to the previous work, we will analyze the microstructure of oxide formed on scale selected AISI 316L specimens to investigate an influence of the substrate microstructure on the structure of the oxide scale.

7.4 Materials and methods

As-received hot rolled stainless steel 316L billet with average grain size of 20μm and thickness of 6.25 mm was thermo-mechanically processed. The chemical composition of the alloy is shown in Table 3.1. First, strips of 50×50 mm^2 were cut from the As-received billet and cold rolled via unidirectional rolling (UDR) to 10% and 90% reduction in thickness, with equal rolling inter-steps of 10% true strain. A small true strain was selected to avoid sample rupture due to strain hardening, especially at higher deformations. Specimens with dimensions of 24 mm × 14 mm × 0.6 mm (L×W×T) were cut from the cold rolled strips. The surface of the specimens was mechanically abraded with abrasive paper up to grit number 2000 (10μm SiC particles). In the next step, both cold rolled specimens were annealed at 1050ºC for 5 minutes per millimeter thickness. Thermo-mechanically processed specimens will be referred as UDR10A and UDR90A from now on. The sample name was chosen to mark a type of cold rolling (UDR), deformation level (10 or 90%), and post rolling treatment (A stands for the annealing).

The macro-texture of specimens was measured using a Bruker D8 Discover X-ray diffraction (XRD) system with Cr K_α radiation. The incomplete pole figures at the mid-section of all specimens were collected and the orientation distribution function (ODF) was constructed using Resmat® software. In addition, a Hitachi SU6600 field emission gun scanning electron microscope (FEG-SEM) equipped with an electron backscatter diffraction system (Oxford NordlysNano EBSD) was used at 20 kV for phase identification and grain size measurement.

The specimens were oxidized in SCW at 600ºC and 25 MPa for 100, 300 and 1000h in an autoclave connected to a recirculation water loop, as illustrated in Figure 3.4. The values for temperature, pressure, inlet and outlet water conductivity, oxygen content and flow rate, which were monitored and controlled are listed in Table 3.3.

To characterize the oxide structure, the samples were mounted in a conductive edge retention resin (Struers Polyfast®) and then ground with abrasive papers up to 2000 grit (10µm SiC particles). Polishing was performed using a water based diamond suspensions up to 1 µm diamond particle size (Struers DiaPro®) at polishing wheel speed lower than 150 rpm to avoid breakdown of the fragile oxide scale. Final stage of polishing was done using 0.04 µm colloidal silica suspension (Struers OP-S®) on a Vibratory Polisher (Buehler VibroMetTM 2) for 24 h. Samples were then analyzed at the cross-section using FEG-SEM at 20 kV equipped with EBSD and energy dispersive spectroscopy (Oxford X-Max Silicon Drift EDS) detectors.

7.5 Results

7.5.1 Microstructure of samples

In order to separate the effect of grain size and texture of the alloy, the As-received, UDR10A and UDR90A samples were selected [44]. Figure 7.1 illustrates three important sections of the ODF at φ_2= 0º, 45º, and 65º for the samples.

For comparison, common texture components in face-centered cubic (FCC) steels are shown in Figure 4.3. The As-received and UDR10A samples have similar average grain size of 20µm, however rather different textures. As seen in Figure 7.1, four major texture components including Brass {110}<112>, S {123}<634>, Copper {112}<111>, and Cube {001}<100> are present in the As-received sample. The same components are present in the UDR10A sample except Cube {001}<100>. On the other hand, the UDR10A and UDR90A samples have similar texture components including Brass {110}<112>, S {123}<634>, and Copper {112}<111>, but UDR90A has an average grain size of 1 µm. Accordingly, by comparing the behaviour of these three samples during oxidation, the effect of grain size and texture of the substrate on the microstructure of the oxide can be analysed.

7.5.2 Identification of the oxide phases

XRD patterns of the As-received and thermo-mechanically processed stainless steel 316L samples after oxidation in SCW at 600ºC and 25 MPa for 100, 300, and 1000h are illustrated in Figure 6.2. The oxidation mechanisms of the samples were studied in our previous work [44]. As seen, after 100h of exposure, the peaks of three different phases including austenite, magnetite (Fe_3O_4) and $FeCr_2O_4$ spinel phase are present in all the samples. The same phases are still present

after 300h of exposure; however, the intensity of austenite is reduced while the intensity of magnetite is increased. With further increase in exposure time up to 1000h, the same peaks are still detectable in the As-received and UDR10A samples. Nevertheless, in the UDR90A sample, in addition to the austenite, magnetite and $FeCr_2O_4$ spinel phase, the peaks of hematite (Fe_2O_3) and chromium oxide (Cr_2O_3) are also observed. To complement the XRD results, the cross-section of samples were studied using EBSD. Since the same phases were detected by XRD for both As-received and UDR10A samples, only the results of EBSD observation of the As-received sample will be discussed here. EBSD band contrast map on the cross-section of the As-received sample after 100, 300, and 1000h of oxidation are illustrated in Figure 7.2.

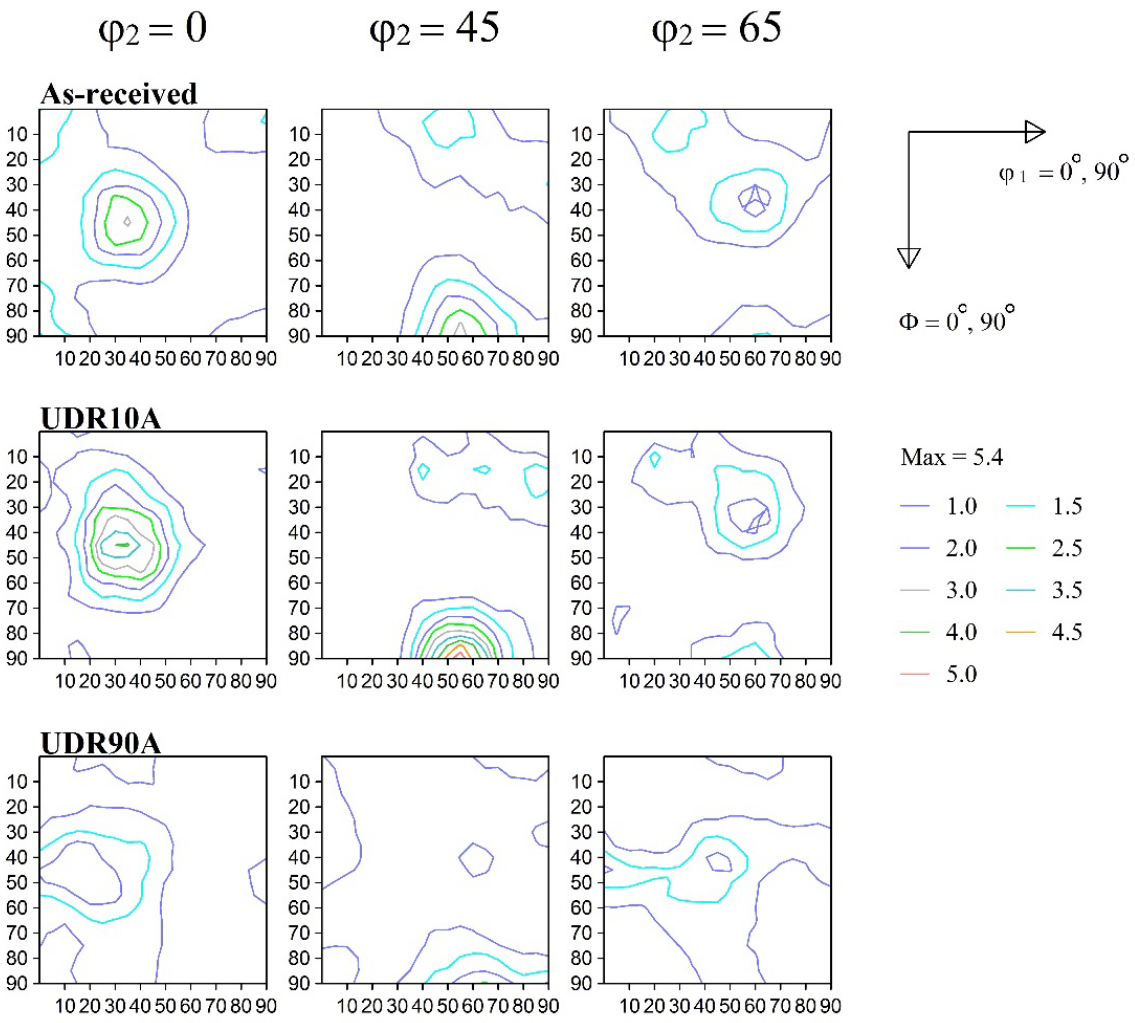

Figure 7.1. ϕ_2= 0º, 45º, and 65º ODF sections of As-received, UDR10A, and UDR90A austenitic stainless steel 316L samples.

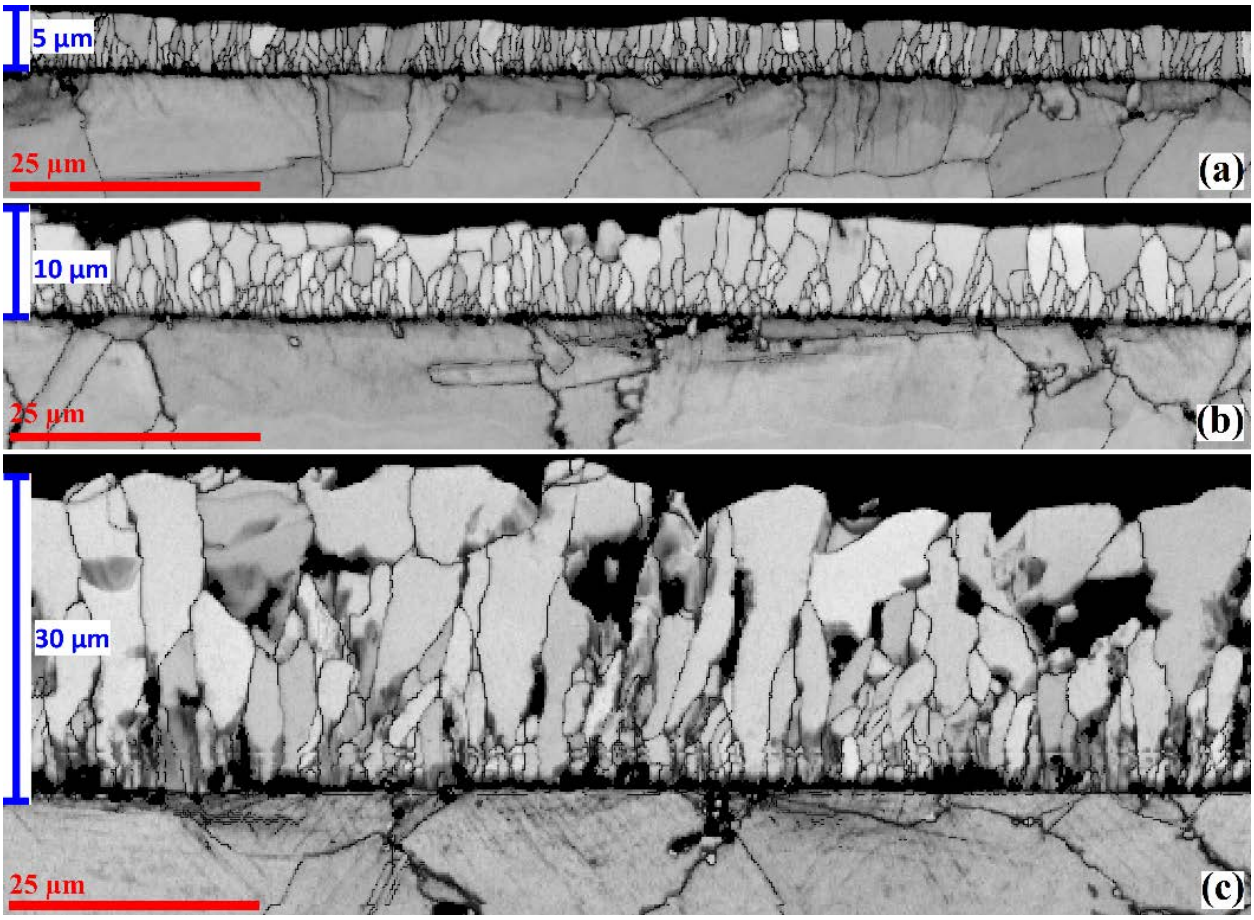

Figure 7.2. EBSD band contrast of the As-received stainless steel 316L after exposure to SCW at 600ºC and 25 MPa for (a) 100, (b) 300, and (c) 1000h.

After 100h of oxidation, an external oxide layer with a thickness of 5 µm was formed on top of the substrate. As shown, small oxide grains were formed initially at the interface of the oxide and the substrate and some grains grew larger with increase in oxidation time. This layer continued to thicken up to 10 and 30µm after 300h and 1000h of oxidation, respectively. This is in agreement with XRD results. It is worth mentioning that some of the oxide grains grew larger in both directions, normal and parallel to the oxidation surface. Figure 4.7 illustrates the EBSD band contrast and EDS elemental composition maps on the cross-section of the As-received sample after 1000h of oxidation. Due to very low concentration of chromium and nickel, compared to oxygen and iron, the EDS maps were not normalized. Three different regions can be distinguished here. Iron and oxygen are the only two elements present in the top layer (external oxide). The second layer (internal oxide), which is right beneath of the surface, is consisted of chromium, iron, and oxygen. The internal oxide layer has a similar thickness to that of the external one.

Since the XRD results show the formation of additional phases in the UDR90A sample compared to the other samples, EBSD observation was made on the cross-section of this sample. Figure 6.4 illustrates the EBSD band contrast, phase map, and EDS elemental composition maps of the UDR90A sample. According to the EDS, EBSD and XRD results, six distinct regions including hematite (Fe_2O_3), magnetite (Fe_3O_4), spinel phase of $(Fe,Cr)_xO_y$, chromium oxide, Ni-enriched zone and austenite are observable. The first two layers (external oxide) are composed of iron and oxygen according to EDS maps. EBSD phase map shows that the first layer is hematite and the second one is magnetite. The magnetite has a variable thickness along the oxide layer. The average minimum and maximum thickness of the magnetite layer is 4 µm and 8 µm, respectively. The thickness of hematite also differs from 2 µm to 6 µm, depending on the morphology of the magnetite layer. Small magnetite grains were formed at the interface of steel and oxide and some of them grew larger in the direction normal to the surface. Compared to magnetite, relatively large and flat hematite grains nucleated on top of magnetite and at 1000h of oxidation it completely covered the oxide surface. The EDS maps show that the next layer, which is the first layer of the internal oxide, is composed of chromium, iron and oxygen. However, beneath this layer, there is a lack of iron, which means that only chromium and oxygen are present. EDS maps show that at the interface of steel and internal oxide, there is a thin nickel-enriched layer with an average thickness of 1 µm.

7.5.3 Macro and micro texture of oxides

Due to low amount of chromium oxide and thick layers of iron oxides, it is possible to measure only the macro-texture of magnetite and hematite with XRD technique. Figure 7.3 shows the constructed inverse pole figure (IPF) of magnetite in direction normal to the specimen surface at different oxidation times. After 100h of oxidation, (111)<uvw> is the dominant oxide texture for all the samples. Furthermore, As-received and UDR10A samples have an additional (001)<uvw> as a minor texture component. Similar texture components are observed for magnetite with continuing the oxidation up to 300 and 1000h.

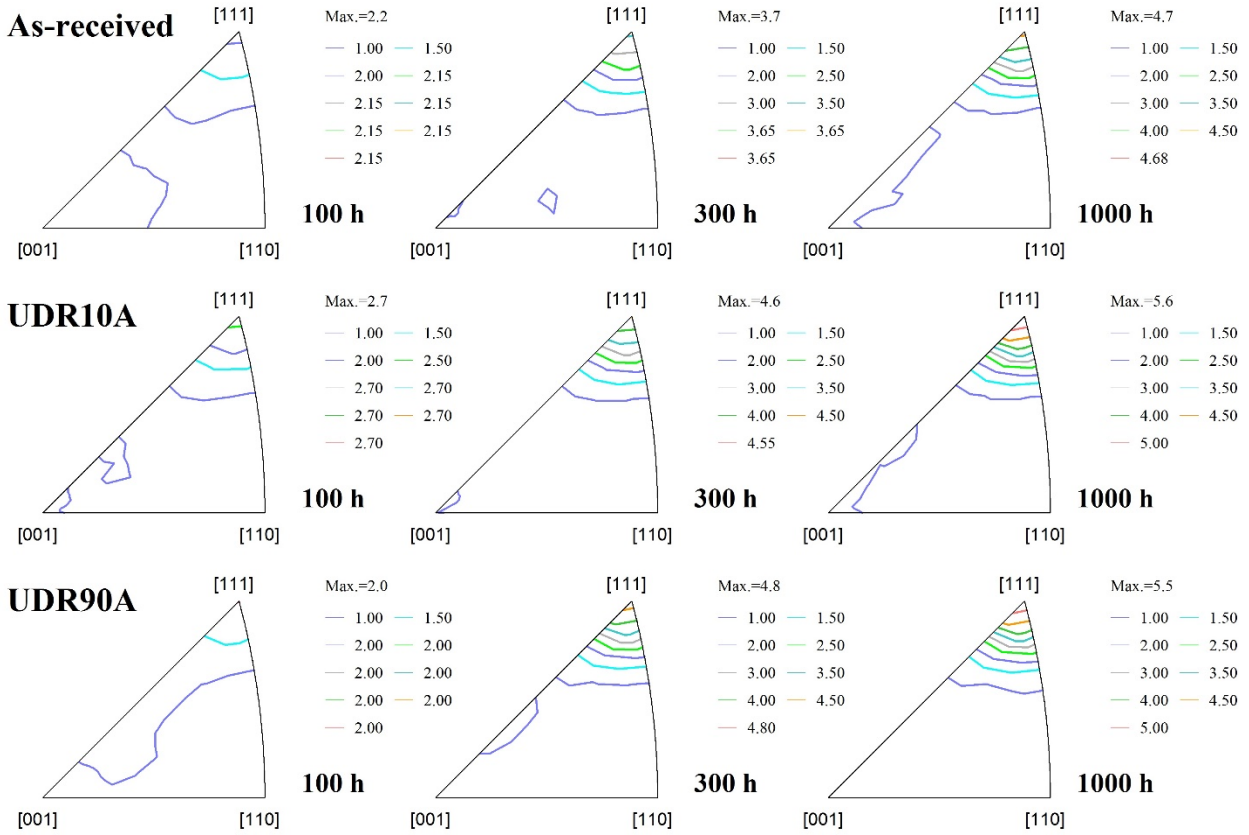

Figure 7.3. Inverse pole figure of magnetite in direction normal to the specimen surface for the As-received, UDR10A, and UDR90A samples after exposure to SCW at 600ºC and 25 MPa for 100, 300, and 1000h.

Figure 7.4 illustrates the IPF of hematite in direction normal to the specimen surface for the UDR90A sample after 1000h of oxidation. Two maxima including (11-25)<uvtw> and (10-13)<uvtw>, that are close to (0001)<uvtw>, are present in the IPF map.

To acquire a better understanding of the correlation between orientation of the oxides and substrate, EBSD method was used to analyze the micro-texture of both phases. Figure 7.5 depicts the orientation and IPF maps of the As-received sample at the cross-section after 1000h oxidation. As seen in the phase map, oxide scale is totally composed of magnetite. A subset of orientation map is magnified to show the orientation correlation between the grains of the substrate and magnetite. Due to the fact that Brass {110}<112> component is the dominant texture of the As-received sample, two grains with the same orientation are selected to represent the main texture. It can be observed that the first magnetite grains, which were formed at the interface of the substrate and oxide are small and equiaxed with average grain size of 2 µm. These grains are randomly oriented as they represent different colors in the orientation map with respect to IPF legend.

However, with further oxidation, the new magnetite grains with an average grain size of 10µm were formed on top of the first layer. Figure 7.5 (c) and (d) illustrate the orientation map and IPF of these grains. IPF maps show that the second layer of the magnetite grains has preferred orientation. It can be seen that (111)<uvw> is the dominant texture of the magnetite grains. This observation is more evident in the third layer, where oxidation was continued to 1000h. Figure 7.5 (e) depicts the IPF map of the third layer of magnetite grains. While (111)<uvw> is still the dominant texture, a minor texture component of (001)<uvw> is also present.

As discussed earlier, XRD results of the UDR90A sample showed hematite as an additional oxide phase after oxidation. EBSD technique was also implemented to validate the XRD results. Figure 7.6 shows the orientation and IPF maps of the UDR90A sample at the cross-section after 1000h of oxidation. As seen, hematite grains nucleated on top of the magnetite grains in such a way that there is minimal gap left in between. In addition, since the top surface of magnetite layer is not flat, more nuclei were formed on the magnetite grains at which the oxide scale was thicker. This resulted in a morphology with asperities and valleys which is also observed elsewhere [44]. IPF maps of hematite and magnetite are presented in Figure 7.6 (c) and (d), respectively. As illustrated, magnetite scale has a (111)<uvw> texture, while hematite has a near (0001)<uvtw> texture with a trigonal crystal structure.

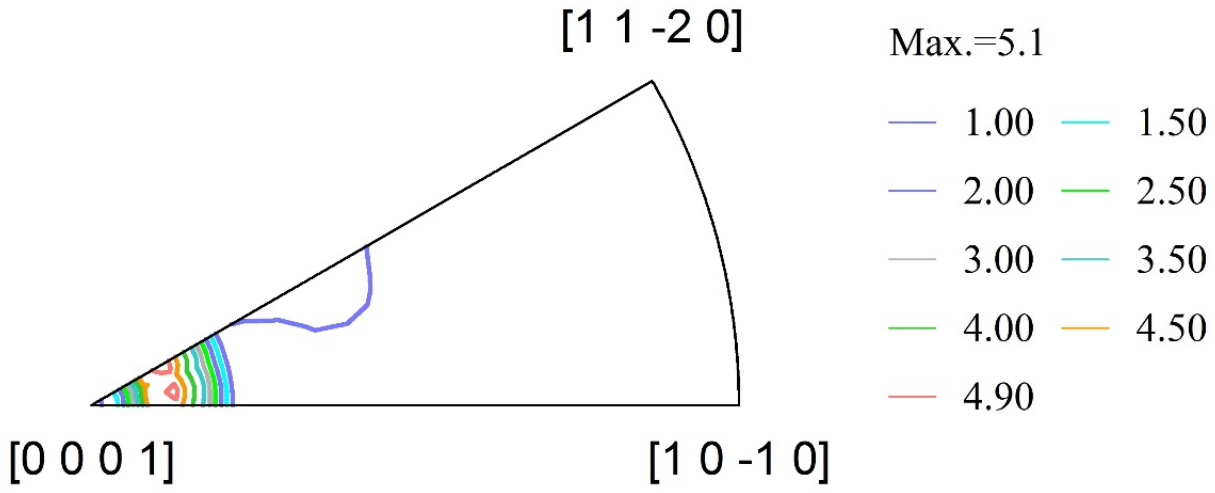

Figure 7.4. Inverse pole figure of hematite in direction normal to the specimen surface for the UDR90A sample after exposure to SCW at 600ºC and 25 MPa for 1000h.

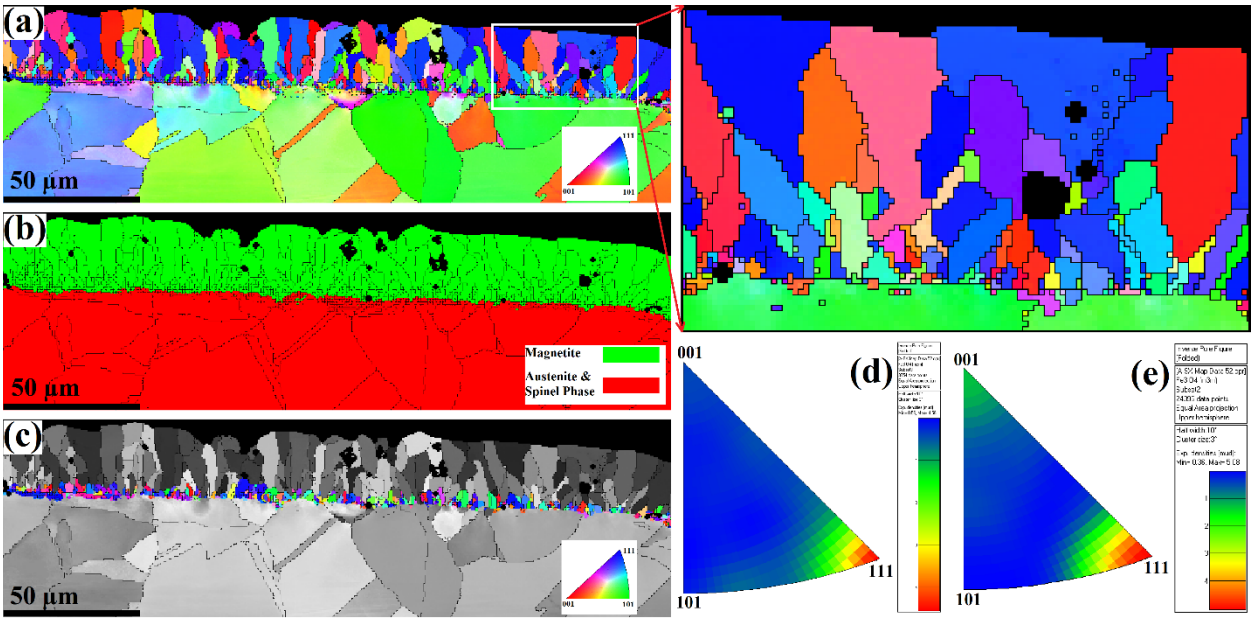

Figure 7.5. As-received stainless steel 316L after exposure to SCW at 600ºC and 25 MPa for 1000h; (a) orientation map, (b) phase map, (c) orientation map of the second layer of magnetite, (d) IPF of the second layer of magnetite, and (e) IPF of entire magnetite scale.

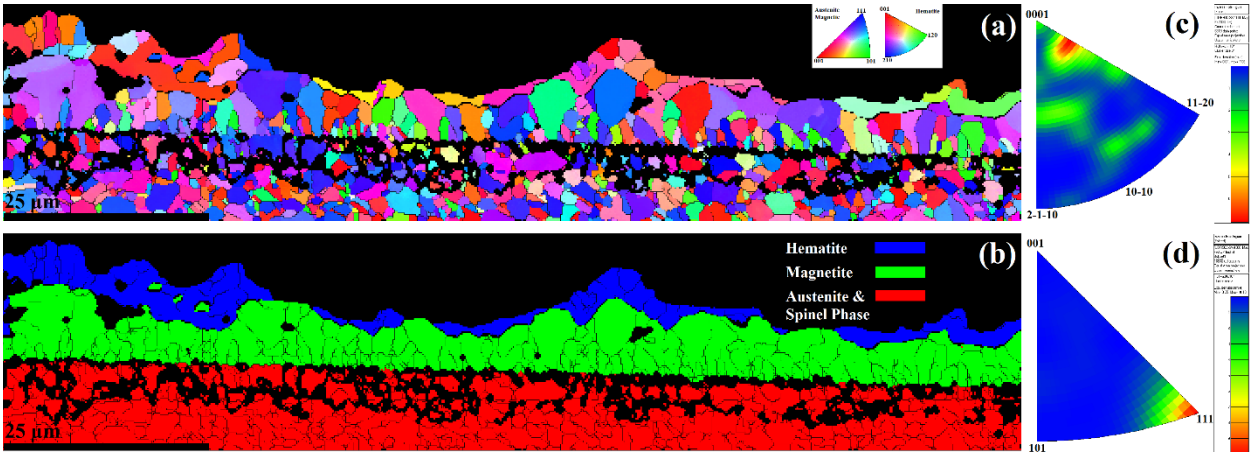

Figure 7.6. Thermo-mechanically processed (UDR90A) stainless steel 316L after exposure to SCW at 600ºC and 25 MPa for 1000h; (a) orientation map, (b) phase map, (c) hematite IPF, and (d) magnetite IPF.

7.6 Discussions

7.6.1 Oxide growth mechanism

XRD results (see Figure 6.2) showed that magnetite was formed on all the three samples. Figure 7.3 illustrates the IPF of magnetite in all the samples with increase in oxidation time. As mentioned, the texture of magnetite did not change with exposure time up to 1000h; however,

intensity of the maxima increased. This is attributed to thickening of the magnetite {111} planes as oxidation continues. EBSD observation clarified the growth mechanism. The growth of magnetite with increasing of oxidation time is illustrated in Figure 7.2, where the EBSD band contrast maps of the As-received sample for three different oxidation times are presented. The growth mechanism of magnetite phase is composed of three stages, all of which took place before 100h of oxidation time as observed in Figure 7.2 (a).

The first stage is characterized by formation of equiaxed grains with random orientation. The second stage is associated with formation and growth of new grains on top of the equiaxed grains which are formed at the first stage. The grain growth direction of magnetite at this stage is normal to the oxidation surface and as a result magnetite grains are columnar. Growing of magnetite grains in both normal and parallel directions to the oxidation surface is the third stage of growth. Growing in the normal direction is due to continuous formation of magnetite on top of the oxide surface which result in columnar shape of the grains. On the other hand, growing in the parallel direction is due to intake of neighbor grains to decrease the energy state of the oxide scale. This is the cause of significant drop in the number of oxide grains with increasing the oxidation time up to 1000h.

7.6.2 Orientation correlation of magnetite and substrate

In Figure 7.5, it can be observed that at the early stages of oxidation, randomly oriented small magnetite grains with an average grain size of 2 μm were formed at the interface of the steel and oxidation media. This indicates that the texture and the grain size of the substrate does not affect the orientation of the initially formed magnetite grains. However, the next layers of magnetite grains that were formed on top of the initial layer, have a preferred orientation. Figure 7.5 (c) and (d) demonstrate this orientation as (111)<uvw>. Moreover, by thickening of the magnetite scale with time, another texture component is formed in the As-received and UDR10A samples, which is not observed in the UDR90A sample. Figure 7.3 indicates that this texture component is (001)<uvw> and is present even after 100h of oxidation on the aforementioned samples. This is in agreement with EBSD observation as shown in Figure 7.5 (e) and Figure 7.6 (d). The difference between the texture of magnetite for the UDR90A sample and the other two, lies in the thickness of the magnetite scale. After 1000h of oxidation, the average thickness of the magnetite is 30μm for the As-received and UDR10A samples which is higher than that of the UDR90A sample (~ 4-8 μm). Thinner magnetite scale of UDR90A sample was correlated to the formation of a protective

chromium oxide (Cr_2O_3) layer beneath the substrate [44]. Thus, by increase in the magnetite thickness, formation of (001)<uvw> texture is being encouraged. This phenomenon can be explained on the basis of the surface and strain energies.

Although the nature of the texture changes as a result of variations in oxide thickness is not completely clear yet, many models and theories were suggested to elucidate these relations and changes [123–125]. Surface energy minimization and strain energy minimization is one of the most general models by which a competition and equilibrium between surface and strain energies is responsible to determine the texture. Based on this model, when oxide is thin, it shows an orientation corresponding to that with lowest surface energy and highest strain energy [123–125].

Even though the thickness of the oxide does not influence the surface energy, the strain energy of the oxide scale will increase by thickness [123,124]. This means that when the oxide scale is thin, the strain of the structure is very low and negligible and therefore, the surface energy is more important to be reduced. As a result, in order to compensate the deficiency of strain energy and make a balance between surface and strain energies, the texture of the oxide would be consist of planes with the lowest surface energy and the highest strain energy [123–125].

It is known that surface energy of crystallographic planes is inversely proportional to the atomic spacing [126], which means that {111} planes have the lowest surface energy in magnetite with FCC structure [32]. As a result, when the oxide thickness is small, {111} planes would increase and become the predominant texture component of the oxide. As the oxide thickness increases with oxidation time, the strain energy would be increased. At this point, the texture of the thick oxide tries to establish a balance between the surface and strain energies by decreasing the strain energy and increasing the surface energy [123–125]. Therefore, crystallographic planes with the second lowest level of surface energy and second highest level of strain energy, i.e. larger atomic spacing compared to {111} planes, would be nucleated with increasing the oxidation time. It is known that the second smallest atomic spacing in FCC structure belongs to {001} planes [32]. Therefore, with thickening of the magnetite layer, (001)<uvw> texture component would be encouraged to form beside (111)<uvw>.

7.6.3 Orientation correlation of hematite and magnetite

Previously we reported that when the average grain size of the stainless steel 316L is below a certain value, hematite would form on top of magnetite [44]. XRD and EBSD observation showed

that hematite was formed on the UDR90A sample after 1000h of oxidation. By investigating different local points at the interface of magnetite and hematite in this sample (see Figure 7.6) we can see that there are several examples in which hematite grains nucleated with different random orientations on a single magnetite grain, or on the contrary, one single hematite grain nucleated and grew on several magnetite grains with different orientations. This indicates that there is no orientation relation between magnetite and hematite grains.

Surface energy minimization and strain energy minimization model can be used to decipher the reason behind the strong near-(0001)<uvtw> texture of hematite oxide scale. Hematite has a trigonal crystallographic system in which {0001} planes have the highest atomic density, i.e. smallest atomic spacing, so that {0001} planes have the lowest surface energy [126]. Figure 7.6 (a) shows that the thickness of hematite layer is only between one to few grains. As explained earlier, at such a thin oxide layer, the texture of the oxide would be consisted of planes with lowest surface energy and highest strain energy in order to balance the energy levels. As a result, it is expected that hematite would have a (0001)<uvtw> texture with respect to normal direction to the oxidation surface. Figure 7.4 illustrates the IPF of hematite in direction normal to the specimen surface after 1000h of oxidation. According to Figure 7.4 and Figure 7.6 (c), (11-25)<uvtw> and (10-13)<uvtw>, that are near-(0001)<uvtw> components, are prominent texture components of hematite scale. This deviation from (0001)<uvtw> could be explained by morphology of the magnetite. As seen in Figure 7.6 (a), hematite grains were formed on top of magnetite scale with a asperities and valleys morphology, i.e. hematite scale has an uneven surface. In other words, the normal direction of the expected hematite {0001} planes are no longer ideally parallel to the normal direction of the oxidation surface. Therefore, some deviation would be expected from {0001}<uvtw>, depending on the angle between the normal of {0001} planes and that of the oxidation surface.

7.7 Conclusions

The structure of the oxide scale formed on austenitic stainless steel 316L after exposure to SCW at 600ºC and 25 MPa was studied and the followings are concluded:

1. The texture of stainless steel has no effect on the texture of magnetite. In addition, the texture of hematite is not affected by the texture of magnetite.

2. The magnetite grains grow larger in normal direction due to continuous formation of magnetite at the top of the oxide surface, as well as in parallel direction by consuming neighbor grains to decrease the energy state of the oxide scale. This results in less but larger magnetite grains after 1000h compared to 100h of oxidation.
3. Magnetite and hematite show strong (111)<uvw> and near-(0001)<uvtw> textures, respectively.
4. The strong texture of magnetite and hematite is explained based on the surface energy minimization and strain energy minimization model. In other words, the texture of magnetite and hematite is determined by a competition and balancing between their surface and strain energies.
5. The texture of hematite could be changed by variation of magnetite surface roughness.

8 ELECTRON BACKSCATTERED AND X-RAY DIFFRACTIONS STUDY ON DEFORMATION AND ANNEALING TEXTURES OF AUSTENITIC STAINLESS STEEL 310S

8.1 Overview

Chapter 8 completes the second objective of this research, "to optimize the microstructure of austenitic stainless steels 310S and 316L thermo-mechanical processing to improve the corrosion resistance". A similar hypothesis is proposed in this chapter to improve the corrosion resistance of austenitic stainless steel 310S in SCW by using the TMP procedure designed in chapter 5. The goal is to produce samples with different grain sizes and different textures in austenitic stainless steel 301S. as mentioned in the overview section of chapter 5, each of these two microstructural factors (i.e. average grain size and texture) should be set almost constant while changing the other one. A systematic study is approached in this chapter to identify the microstructural changes in each sample based on the deformation and recrystallization mechanisms. For this purpose, all the samples were characterized with EBSD and XRD techniques to measure their average grain size, micro and macro textures.

This manuscript was submitted to the Journal of Materials Characterization[17] and slight changes have been applied to the original version to avoid repetition. Dr. Hamed Akhiani[18] and assisted the author of this Ph.D. thesis (Majid Nezakat) with preparation and processing of the samples as well as performing the data analysis. Jerzy Szpunar, as the supervisor of this research, provided recommendation, consultation and discussion wherever it was needed. Except the entire or a portion of these parts, all the experiments, data acquisition, and data analysis were conducted by Majid Nezakat, the lead author of the paper. Majid Nezakat wrote the manuscript, integrated comments from the co-authors, and submitted it for review and possible publication.

8.2 Abstract

The texture evolution of deformed and annealed austenitic stain steel 310S was studied. The alloy was cold rolled up to 90% of reduction in thickness. Strain-induced martensite was formed

[17] The copyright permission to use the manuscript in the thesis is obtained and provided in the appendix section. The references of this chapters are provided at the end of the thesis.

[18] Mitsubishi Hitachi Power Systems Canada, LTD., 826 58th Street East, Saskatoon, SK, S7K 5Z4, Canada

from deformed austenite since the early stages of deformation. Slip mechanism was found to be insufficient to accommodate higher deformation strains. In fact, it was found that twinning plays an important role at higher deformation levels. In addition, two different rolling modes, unidirectional and cross rolling, resulted in Goss/Brass and Brass dominant textures in deformed samples, respectively. The same trend was also observed in annealed samples. The annealing texture was greatly affected by texture of the deformed parent phase and martensite did not contribute much as it showed an athermal reversion during annealing. Results also showed that when the fraction of martensite exceeds a critical point, especially at 90% of deformation, its grain boundaries impeded the movement of grain boundaries of austenite during annealing and as a result, recrystallization incubation time would increase. This caused incomplete recrystallization of highly deformed samples, which led to a rational drop in the intensity of the texture components.

8.3 Introduction

As a highly alloyed austenitic stainless steel, 310 is designed for elevated temperature applications. The low carbon version of this alloy, 310S, is less prone to embrittlement and sensitization in service. The high nickel and chromium contents provide this alloy with outstanding oxidation and creep resistance in continuous service at temperature up to 1200ºC [62,63]. However, utilizing wide range of manufacturing processes to produce various stainless steel parts can alter their oxidation resistance and mechanical properties [44,64,65,127,128]. Microstructural evolution in the face-centered cubic (FCC) metals during rolling, as one of the most conventional industrial processes, has always been an interesting topic in manufacturing [59,129–133]. There are several parameters that affect the microstructural evolution of the FCC alloys during rolling, among which stacking fault energy (SFE) [67,68], deformation mode (i.e. strain path) [44,59,70,115,134–138], and rolling temperature [82,139,140] have significant impacts.

The size of stacking fault depends on the chemical composition of the alloy and as it becomes larger, the cross-slip mechanism would be difficult during deformation. Thus, accommodating more deformation requires a secondary deformation mechanism; such as deformation twinning [141]. Stacking faults significantly affect stress-strain response and the evolution of the texture during rolling [86].

To date, a variety of deformation modes have been examined on austenitic stainless steels during the cold rolling process, including unidirectional rolling (UDR), two-step cross rolling

(TSCR), multi-step cross rolling (MSCR) and reverse rolling (RR). Gurao et al. [134] studied the effect of strain path during rolling on the texture evolution of two pure FCC metals. They reported that the cross rolled copper and nickel showed weaker texture components in contrast to the unidirectional and reverse rolled samples.

A key factor to the deformation and annealing texture of austenitic alloys is the formation of secondary phase [82,85,142,143]. It is known that austenite is thermodynamically metastable at room temperature in austenitic stainless steels. Generally, applying deformation below the martensitic deformation temperature (M_d) could result in the formation of strain-induced martensite, and further increase in deformation level is found to increase the fraction of martensite. Eskandari et al. [85] reported that amount of strain-induced martensite influences the degree of grain refinement in 316L austenitic stainless steel. In another study [82], Eskandari et al. found that increasing the initial grain size and strain, decreasing the rolling temperature, and using cross rolling lead to an increased volume fraction of martensite. They also reported that the impact of grain size before cold rolling is stronger than that of rolling reduction on grain refinement and as a result, the formation of a fine grain structure could be facilitated by using the smaller initial grain size accompanied by a high thickness reduction in a repetitive process. Shakhova et al. [76] studied the effect of annealing temperature on microstructure of deformed austenitic stainless steel S304H. They found that annealing below 700ºC results in an ultrafine-grained microstructure below 200 nm, while a remarkable grain growth takes place at higher annealing temperature.

Although the texture evolution has been studied in the past for austenitic stainless steels, there are limited studies on deformation and annealing texture of austenitic stainless steel 310S. Therefore, the purpose of this work is to find out the effect of different TMP parameters on the microstructure and texture evolution of this alloy. In this regard, we used a specific TMP strategy to elucidate the effect of deformation mode, level of deformation and subsequent annealing treatment.

8.4 Materials and methods

The chemical composition of austenitic stainless steel 310S, used for this study, is listed in Table 3.1. The As-received billet was hot rolled with a thickness of 6.25 mm and an average grain size of 20µm. Strips of 50 mm × 50 mm × 6.25 mm (L×W×T) were cut from the alloy and thermo-mechanically processed in two steps. First, they were cold rolled at room temperature with two

different deformation modes: unidirectional rolling (UDR) and cross rolling (CR). Reduction in thickness achieved by cold rolling was up to 10, 30, 50, 70 and 90% with equal rolling inter-steps of 10% true strain. The small true strain was selected to avoid sample rupture due to strain hardening, especially at higher deformations. At the second step, samples were annealed at 1050ºC for 5 minutes per millimeter thickness. The surface of the samples was mechanically abraded with abrasive paper up to grit number 2000 (10µm SiC particles). Polishing was performed using a water-based diamond suspension up to 1 µm diamond particle size (Struers DiaPro®). Final stage of polishing was done using 0.04 µm colloidal silica suspension (Struers OP-S®) on a Vibratory Polisher (Buehler VibroMetTM 2) for 12 h. Table 3.2 listed the thermo-mechanically processed samples used in this study. The sample name is comprised of deformation mode, value of the reduction in thickness, and post rolling treatment ("A" stands for annealing), respectively.

The micro and macro-texture of the samples were measured after the first and second steps of TMP using x-ray diffraction (XRD) and electron backscatter diffraction (EBSD) techniques, respectively. A Bruker D8 Discover XRD system with Cr K_α radiation was used for macro-texture measurements. The incomplete pole figures at the mid-section of all specimens were collected and the orientation distribution function (ODF) was constructed using Resmat® software. In addition, a Hitachi SU6600 field emission gun scanning electron microscope (FEG-SEM) equipped with an EBSD system (Oxford NordlysNano EBSD) operated at 20 kV was used for micro-texture, as well as phase identification and grain size measurements.

8.5 Results

To compare the deformation and annealing macro-texture of stainless steels, the constructed ODF at three important sections including $\varphi2$= 0º, 45º, and 65º are used. As a reference, Figure 4.3 illustrates the common texture components of steels. Figure 8.1 shows the ODF and orientation imaging microscopy (OIM) map of the As-received sample. Four major texture components including Brass {110}<112>, S {123}<634>, Copper {112}<111>, and Cube {001}<100> are present in the ODF of the As-received sample. The OIM map also reveals the same texture components. Based on both texture measurement techniques, Brass component is more prominent in the As-received sample.

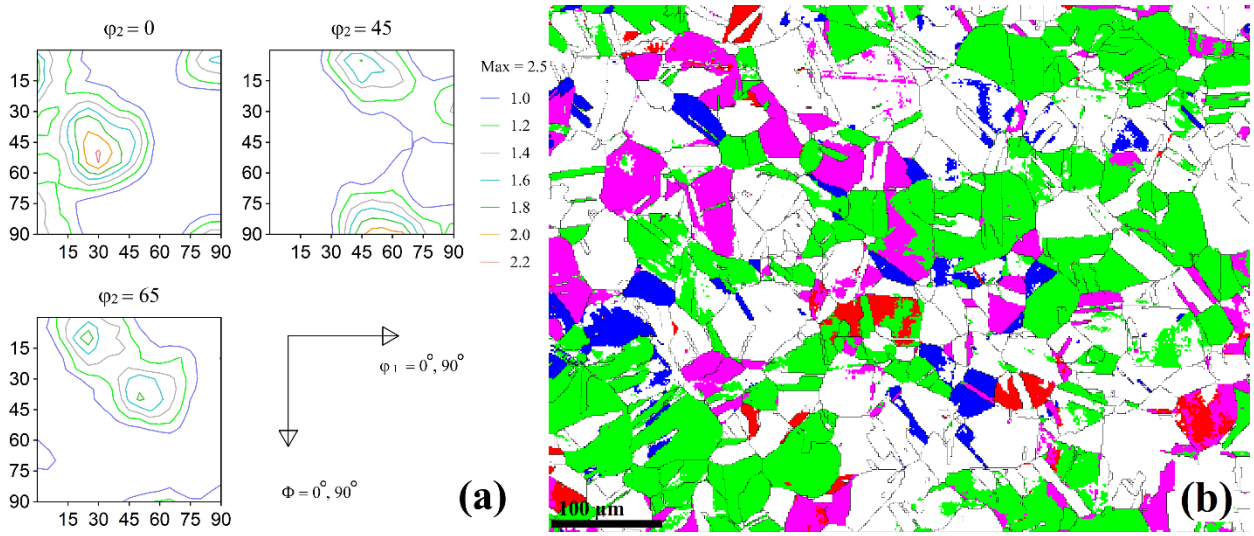

Figure 8.1. Hot rolled stainless steel 310S: (a) important sections of ODF, and (b) texture components; Brass (green), S (pink), Cube (blue) and Copper (red).

8.5.1 Deformation Texture

The microstructural investigations show that after cold deformation, in addition to deformed austenite, strain-induced martensite is also present in 310S stainless steel. As the volume fraction of martensite depends on the deformation level [80], one can expect higher amount of martensite at higher deformations. Hence, the texture of the two phases will be discussed separately.

8.5.1.1 Deformed Austenite

Figure 8.2 shows the deformation texture of austenite after cold rolling via UDR and CR. All of the texture components of the As-received sample are present in UDR10 sample. Brass component also undergo a shift towards Goss component. The same components are also present in CR10 sample with the exception of Copper {112}<111> which is eliminated during cold rolling.

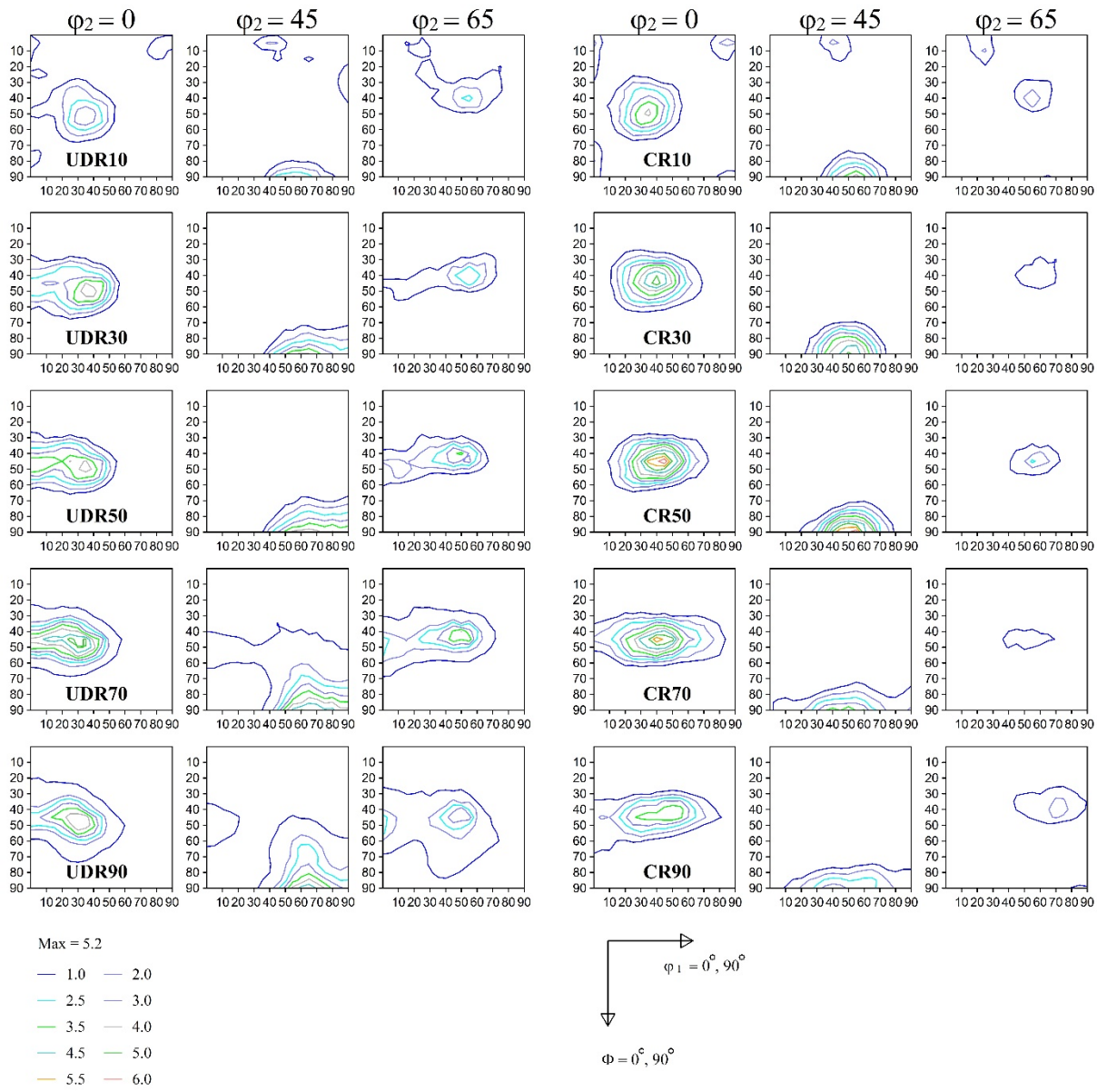

Figure 8.2. Deformation texture of stainless steel 310S; ϕ_2= 0º, 45º, and 65º ODF sections of the deformed austenite up to 90% reduction in thickness.

With respect to the As-received sample, Goss, Brass, and S components are all intensified in both UDR10 and CR10 samples. Increasing the deformation to 30% results in elimination of Cube {001}<100> and Copper {112}<111> in UDR30 sample. In addition, S component is spread towards (212)[1-20] and Brass component continues to shift towards Goss component and as a result intensity of Goss increases. It is notable that Twin-Copper (255)[5-1-1] component appeared with low intensity at this deformation level in UDR30 sample. In CR30 sample, Cube {001}<100>

component is also eliminated and Brass component is spread along ζ-fibre. Further increase in deformation to 50% introduces no new texture components in UDR50 and CR50 samples, however the intensity of all the existing components are intensified. As a result, Brass shifts more towards Goss, S component continues to spread towards (212)[1-20], and Twin-Copper (255)[5-1-1] component is intensified in UDR50 sample. On the other hand, Brass component continues to spread along ζ-fibre, especially towards ND-rotated Goss (R-Goss$_{ND}$). Higher deformation results in appearance of a new component since Gamma fibre {111}<uvw> is formed in UDR70 sample, with low intensity though. Intensity of Brass and Goss are increased and (212)[1-20] component is actually formed. Alternatively, Brass component almost covers the ζ-fibre in CR70 sample as it is spread completely towards R-Goss$_{ND}$, although the intensity is decreased slightly. At the final stage of the deformation, some reverse changes are observed. As seen, Gamma fibre {111}<uvw> is disconnected in UDR90 sample and the intensity of Brass and Goss components are reduced. The same trend is observed for CR90 as the intensity of Brass component decreased.

8.5.1.2 Martensite

As a simple practical method to prove the presence of martensite, one can use a magnet to see if the deformed sample is getting attracted or not. Using this method, we observed that martensite is formed at the lowest applied deformation (i.e. 10%). The texture of strain-induced ά-martensite at different steps of cold rolling is illustrated in Figure 8.3. As seen, the main texture component of UDR10 sample is rotated-cube (R-C) {100}<011>; however, (116)[1-10] component, which is a slight deviation from R-C {100}<011>, as well as rotated-copper (R-Cu) {112}<110> are present. CR10 sample also possesses R-C {100}<011> component with additional minor components including Y {111}<112>, and (223)[2-31], which is near to Y {111}<112>. When deformation increased to 30%, a new component, (223)[2-31], which is near to Y {111}<112>, is formed in UDR30 sample. In addition, in comparison to UDR10 sample, R-C {100}<011> and (116)[1-10] components are slightly reduced while R-Cu {112}<110> is intensified. As for CR30 sample, the same texture components are present at a slightly reduced intensity compared to CR10 sample. At 50% of deformation, further reduction in R-C {100}<011> and (116)[1-10] components are observed in UDR50 sample; however, (223)[2-31] component is intensified and Y {111}<112> is reduced. On the other hand, R-C {100}<011> is reduced in CR50 sample, while it spreads along ζ-fibre. (223)[2-31] component is also present with no change in the intensity.

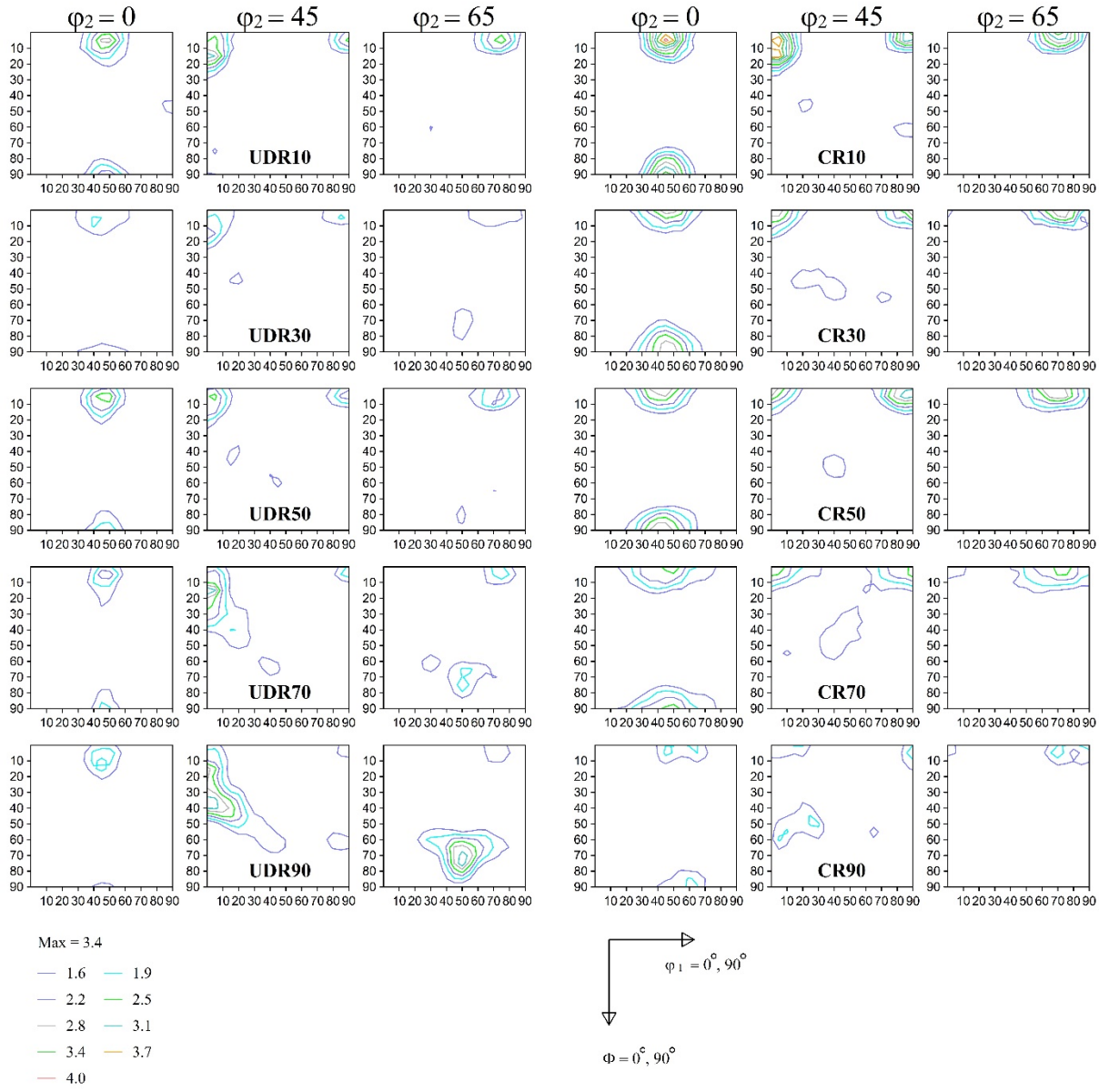

Figure 8.3. Deformation texture of stainless steel 310S; ϕ_2= 0º, 45º, and 65º ODF sections of the martensite up to 90% reduction in thickness.

Continuing the deformation to 70% results in reduction in R-C {100}<011> component and in the contrast, R-Cu {112}<110> and Y {111}<112> components are intensified. In CR70, the same trend is observed for R-Cu {112}<110> component as it is reduced while it continues to spread along ζ-fibre. At the maximum applied deformation, R-C {100}<011> shows further decline in intensity in UDR90 sample, while R-Cu {112}<110> and Y {111}<112> components are

strengthened. For CR90, R-C {100}<011> shows the same trend as it is reduced compared to CR70; however, (223)[2-31] is eliminated and Y {111}<112> is intensified.

8.5.2 Annealing Texture

The annealing textures of thermo-mechanically processed 310S samples are illustrated in Figure 8.4. Since the same deformation texture was achieved for both UDR10 and CR10 samples, only the former one (UDR10A) was annealed to avoid duplication of data. As it can be observed, texture components including Brass and S are present in UDR10A sample. There is also two minor (210)[1-25] and (113)[-3-32] components that have low intensities. These components are eliminated in UDR30A sample. In addition, Brass component is extended towards Goss and as a result, Brass shows a lower intensity. It is also worth to mention that S component is slightly reduced. For CR30A sample, Brass component is spread towards ND-rotated Brass (R-$Goss_{ND}$) {110}<110> and S component is shifted to (212)[-1-32]. Brass is reduced in UDR50A and Goss is increased with continuing spread of Brass towards Goss with increase in deformation during TMP. Additionally, in compare to UDR30A sample, the minor (210)[1-25] and (113)[-3-32] components are still present in this sample while S component is reduced. On the other hand, Brass component is spread along ζ-fibre for CR50A sample, from Goss to R-$Goss_{ND}$. It is also notable that the minor (212)[-1-32] component is weakened. Brass component does not shift anymore towards Goss in UDR70A sample, however, compared to UDR50A sample, the intensity of Goss and Brass components exhibits a counter swing. In addition, the minor (210)[1-25] component is also present in this sample and S component is also reduced. In comparison to CR50A sample, the ζ-fibre in CR70A sample was shrank from Goss and spread only towards R-$Goss_{ND}$. It has to be added that the (212)[-1-32] component is almost eliminated and the intensity of the Brass component is also upswing compared to CR50A sample. In UDR90A sample, as mentioned, although there is no more shift towards Goss, compared to UDR70A, the intensity of Goss and Brass are reduced and enhanced, respectively. In addition, the minor (210)[1-25] and (113)[-3-32] components are almost eliminated. It should be also noted that the intensity of S component is decaying with increase in deformation during TMP as UDR10A and UDR90A have the highest and lowest intensity for S component, respectively. In case of CR90A sample, both Brass and R-$Goss_{ND}$ are reduced compared to CR70A. Additionally, the minor (212)[-1-32] component is eliminated and (211)[0-11] component is formed.

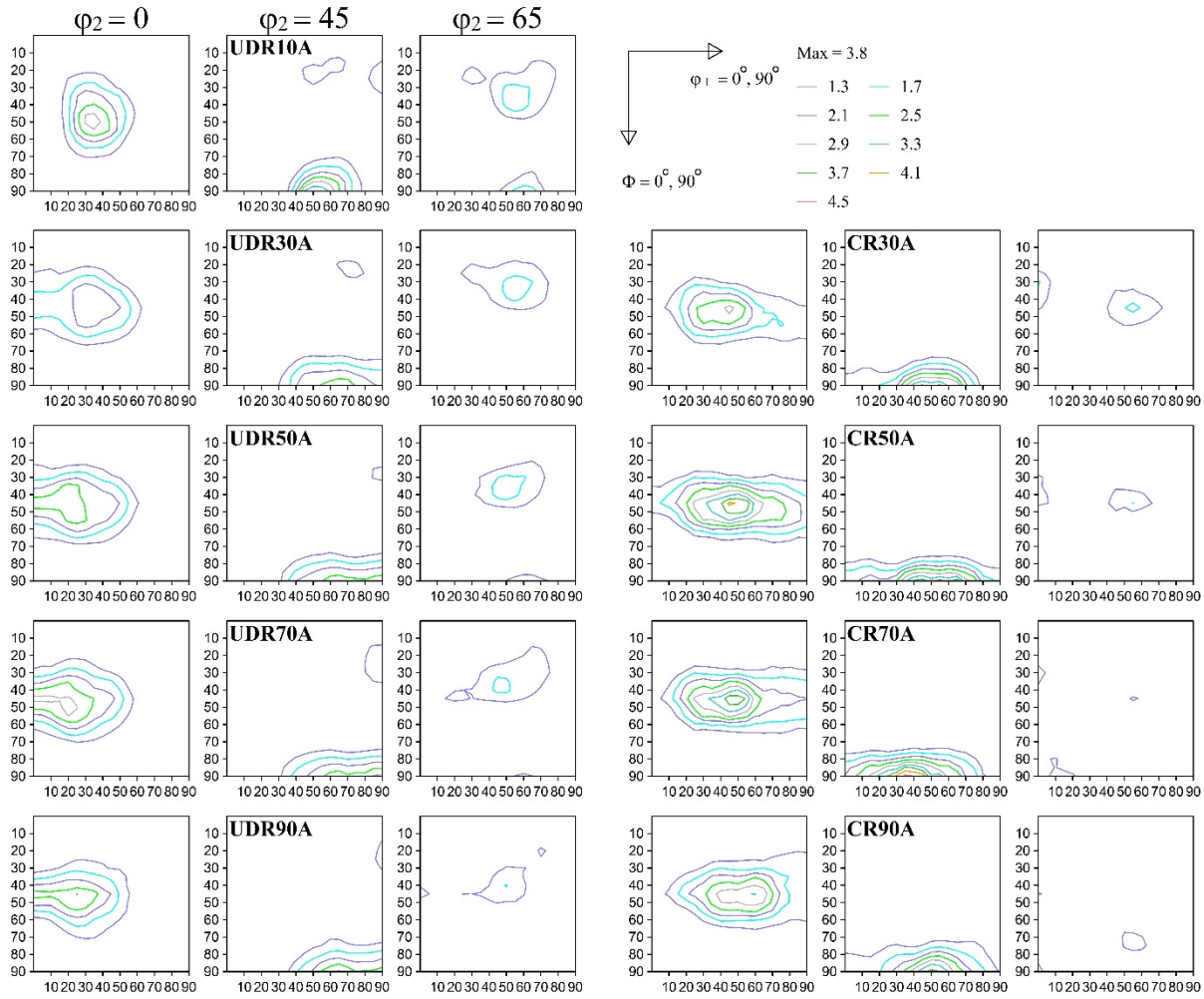

Figure 8.4. Annealing texture of stainless steel 310S; ϕ_2= 0º, 45º, and 65º ODF sections of the thermo-mechanically processed samples.

8.6 Discussions

8.6.1 Deformation Texture

8.6.1.1 Remaining Austenite

Our previous study has revealed that the deformation of austenitic stainless steel 316L consisted of three distinct stages including elimination of Copper {112}<111>, twinning, and formation of γ-fibre {111}<uvw> [115]. The evolution of β-fibre and η-fibre in the deformed austenitic stainless steel 310S are illustrated in Figure 8.5. By coupling the observations from the both fibres and ODF sections (see Figure 8.2), one can suggest that the aforementioned 3-stage deformation also occur in case of stainless steel 310S. Generally, elimination of Copper

{112}<111> is considered as the first stage of deformation in FCC austenitic steels [115,144]. However, Copper orientation increased after 10% of deformation in UDR samples. In our previous work [115], we reported that formation of Copper orientation is associated with slip mechanism.

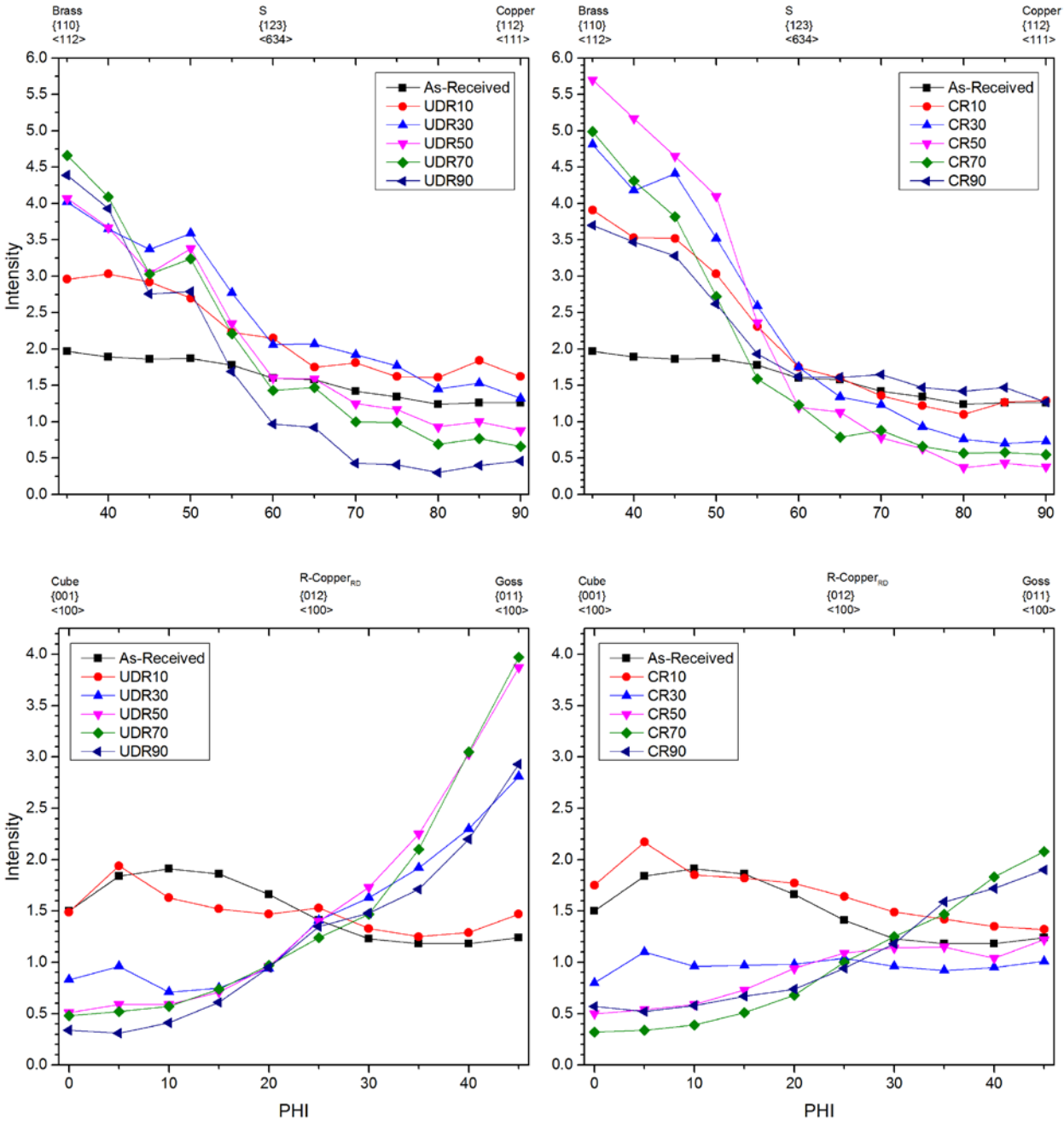

Figure 8.5. β-fibre (top) and η-fibre (bottom) for austenite phase in unidirectionally rolled and cross-rolled stainless steel 310S after deformation up to 90% reduction in thickness.

As deformation increased to 30%, Copper component is reduced since twinning is activated as the next deformation mechanism. After 50% of reduction in thickness, Copper component is eliminated. In comparison to UDR samples, twinning mechanism is activated at earlier stages of deformation for CR samples. As shown in Figure 8.5, increasing the deformation to 10% does not change the Copper component, while further increase of deformation to 30% eliminates the Copper {112}<111>. Activation of twinning mechanism would help the alloy to accommodate more strain after applying more reduction in thickness during cold rolling. The second stage of deformation is characterized by formation of twinning. Deformation twinning can contribute to spread the Brass {110}<112> component towards Goss {110}<001>. This means that further increase in deformation would increase the Goss {110}<112> intensity. Such an increase is observed as the deformation level increases (see Figure 8.5).

Figure 8.6 illustrates the orientation relation between the twins and parent grains from which a subset of Goss {110}<001> oriented grains with twinning was selected. A common pole between the twins and the parent grains in (111) pole figure of the subset is shown in Figure 8.6 (c). To take a boundary into account as a coherent twin boundary in FCC materials, a 60º rotation around <111> crystal axis as well as coincidence of a boundary with twinning plane should take place [86]. Therefore, this rotation would result in one and three common pole(s) in (111) and (110) pole figures of the subset including the twins and the parent grains, respectively [70,80,115].

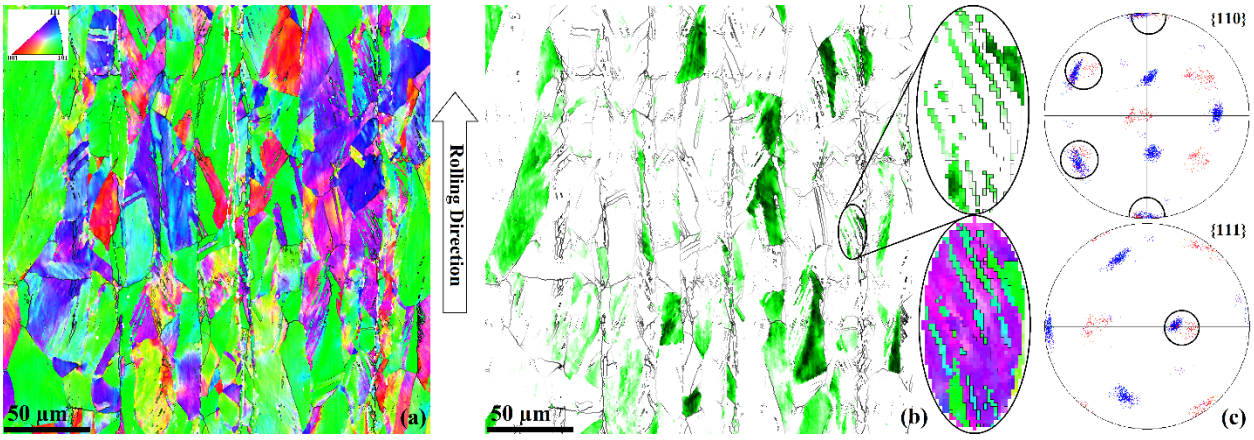

Figure 8.6. Orientation map of 30% deformed austenite in UDR sample showing; (a) IPF map, (b) Goss {110}<001> component, and (c) the presence of deformation twinnings with Goss {110}<001> orientation.

Continuing the deformation after this point would result in formation of Twin-Copper (255)[5-1-1] grains due to the rotation of the grains with Copper {112}<111> orientation. This rotation is accommodated by twining when deformation reaches 50% and 70% in UDR and CR samples, respectively [68,115]. Figure 8.7 shows how grains with Twin-Copper (255)[5-1-1] orientation are formed from those with Copper {112}<111> orientation. This delay in the formation of Twin-Copper (255)[5-1-1] grains in CR sample is expected as a fraction of strain would be released due to changing of deformation path at each inter-step of cold rolling.

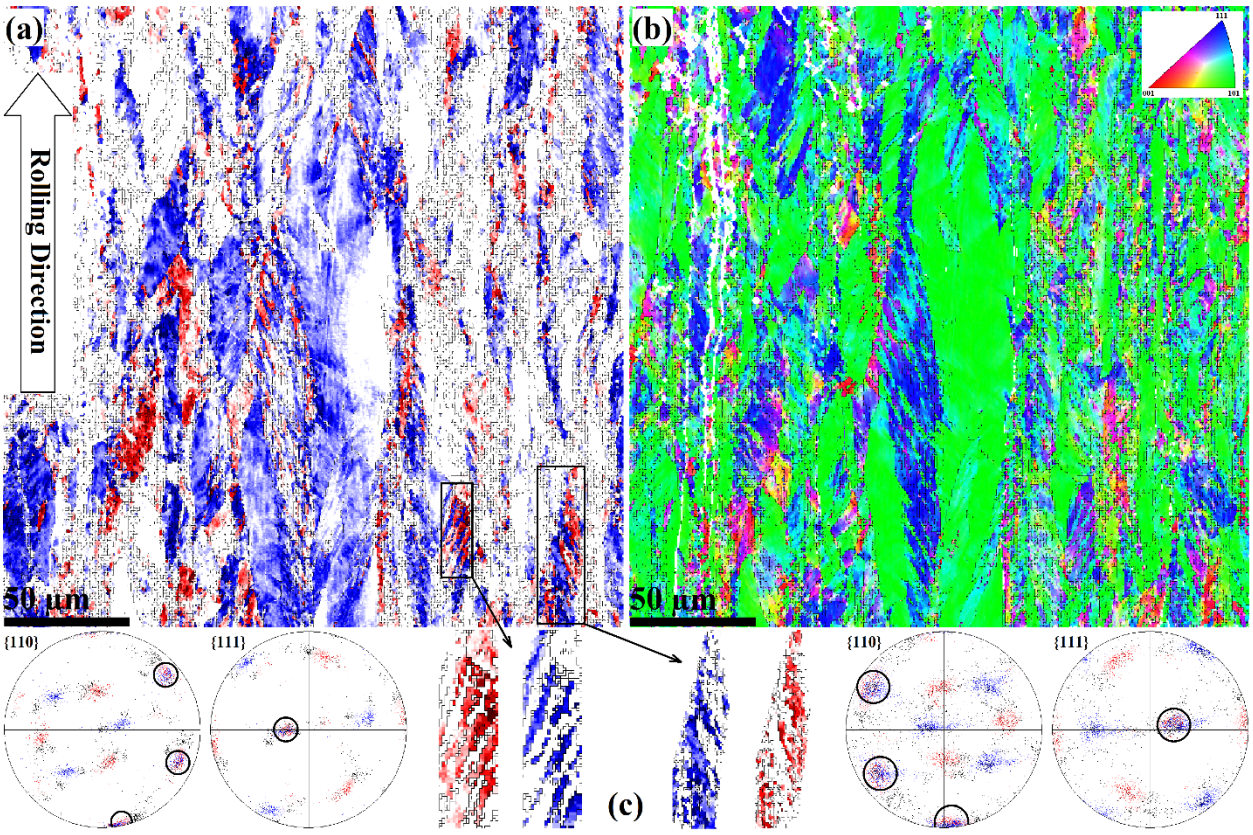

Figure 8.7. Orientation map of 50% deformed austenite in UDR sample showing; (a) TC {255}<511> and Copper {112}<111> component, (b) IPF map, and (c) pole figures near deformation twinnings.

Formation of γ-fibre {111}<uvw> as a result of saturation of Goss {110}<001> is the characteristic of third stage of deformation [80,115]. Nezakat et al. [115] and Chowdhury et al. [80] reported that γ-fibre {111}<uvw> grains nucleate by alignment of twin lamellae parallel to the rolling plane as a result of increase in Twin-Copper (255)[5-1-1] and Goss {110}<001> grains. This phenomenon is clearly visible in Figure 8.2 and Figure 8.8 as deformation reaches 70% in

UDR samples. The reason why this process is postponed in CR sample is because of the difference in the mode of deformation which resulted in incomplete saturation of Goss {110}<001> orientation.

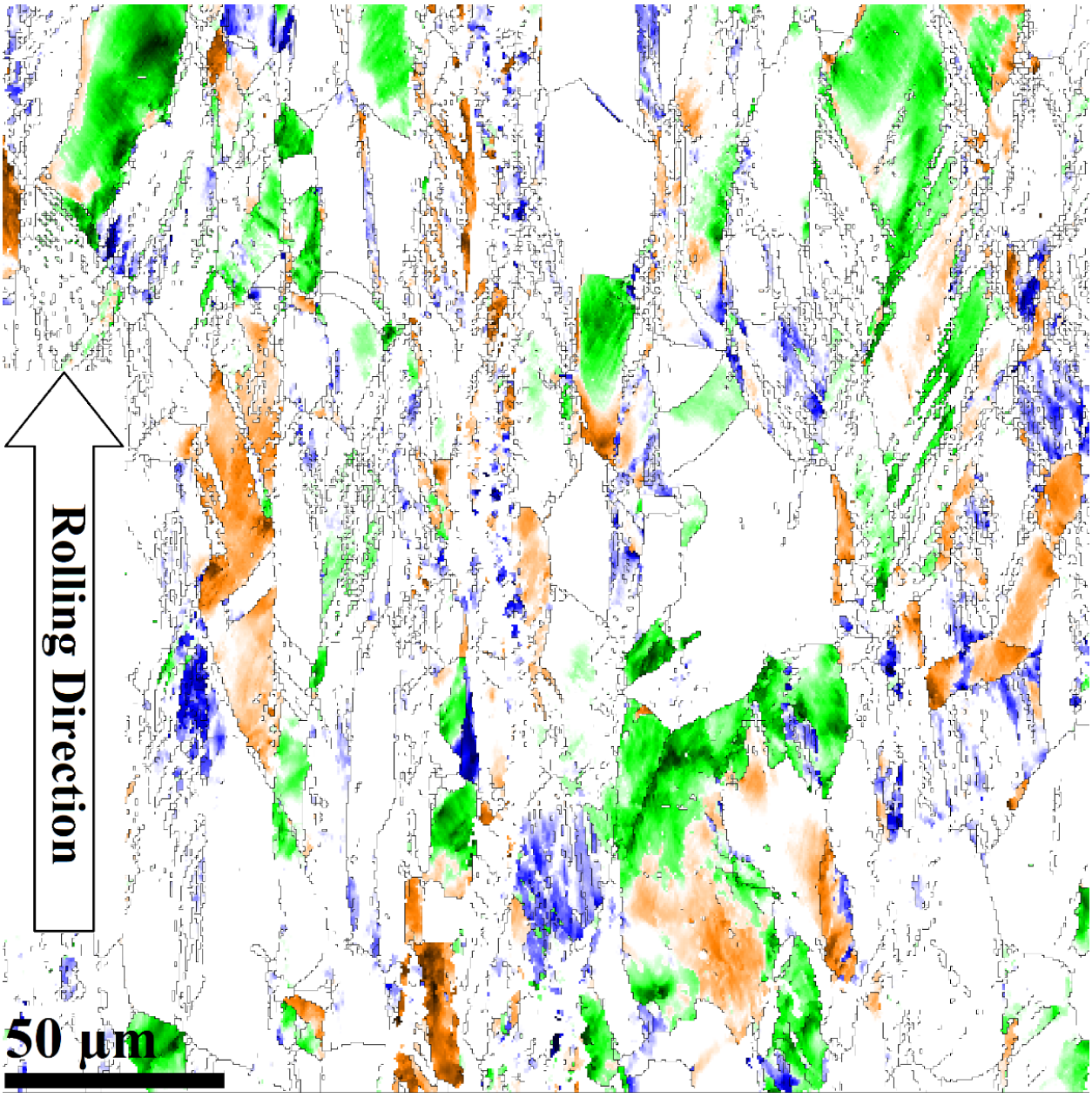

Figure 8.8. Orientation map of 70% deformed austenite in CR sample showing; (orange) Brass {110}<001> component, (blue) γ-fibre, and (green) Goss {110}<001> component.

Texture components are weakened as deformation increased to 90% in both UDR and CR samples. As a result, γ-fibre {111}<uvw> is not complete anymore and Twin-Copper (255)[5-1-

1], Goss {110}<001>, and Brass {110}<112> show lower intensities in UDR90 sample. Likewise, Brass {110}<112> component is reduced and shrunk to some extent in CR90 sample. To understand the cause of this drop in intensity, further investigation of 90% deformed samples is required. Figure 8.9 illustrates inverse pole figure (IPF) map, phase map and kernel average misorientation (KAM) map of 90% deformed austenite. For comparison, kernel average misorientation (KAM) map of 70% deformed austenite is also present.

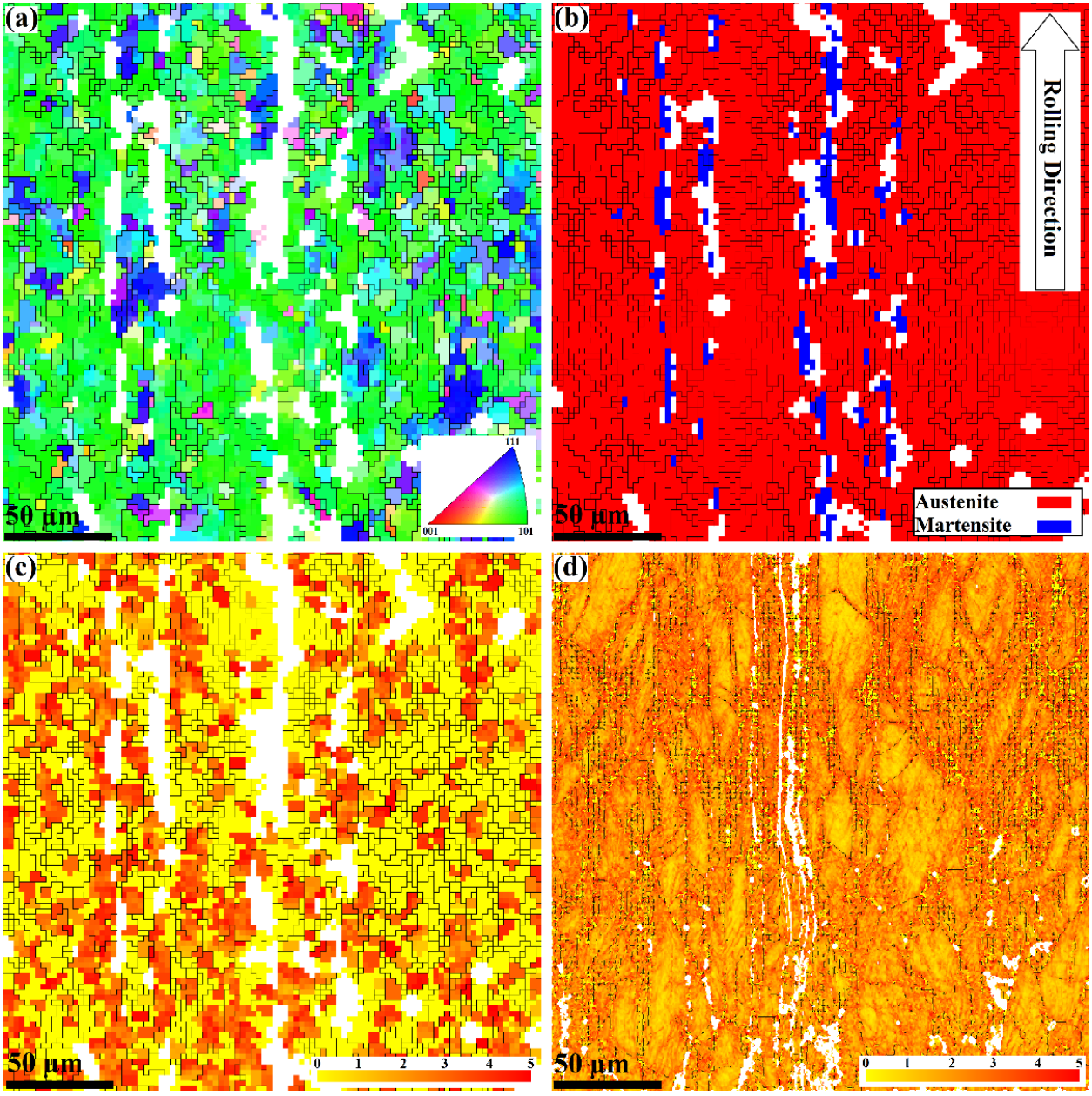

Figure 8.9. (a) IPF map, (b) phase map, (c) kernel average misorientation (KAM) map of 90% deformed austenite; (d) KAM map of 70% deformed austenite in CR sample.

As it can be observed, although a highly deformed structure is expected after 90% of deformation, a significant portion of the microstructure is covered with fine equiaxed austenite grains (Figure 8.9 (a)). Based on the KAM map, these grains are strain-free (Figure 8.9 (c)). In comparison, KAM map of 70% deformed austenite (Figure 8.9 (d)) shows that the entire structure is highly deformed. This can also be observed in Figure 8.10, where the kernel average misorientation versus relative frequency at the center of cross section of 70 and 90% deformed samples are illustrated. As seen, the relative frequency of low KAM values (less than 0.5º) in 90% deformed sample is about 10 times higher than that of 70% deformed one. On the other hand, the relative frequency of high KAM values (more than 0.5º) is higher in 70% deformed sample. This comparison suggests that the density of dislocations is lower in 90% deformed sample compared to 70% deformed one. Accordingly, one can conclude that recovery happened in 90% deformed structure presumably due to local increase in the temperature during the final stage of deformation. Therefore, a fraction of dislocations are omitted when opposite dislocations cancel out each other and the rest are aligned in a way to form new grain boundaries, which leads to a new fine-grain structure.

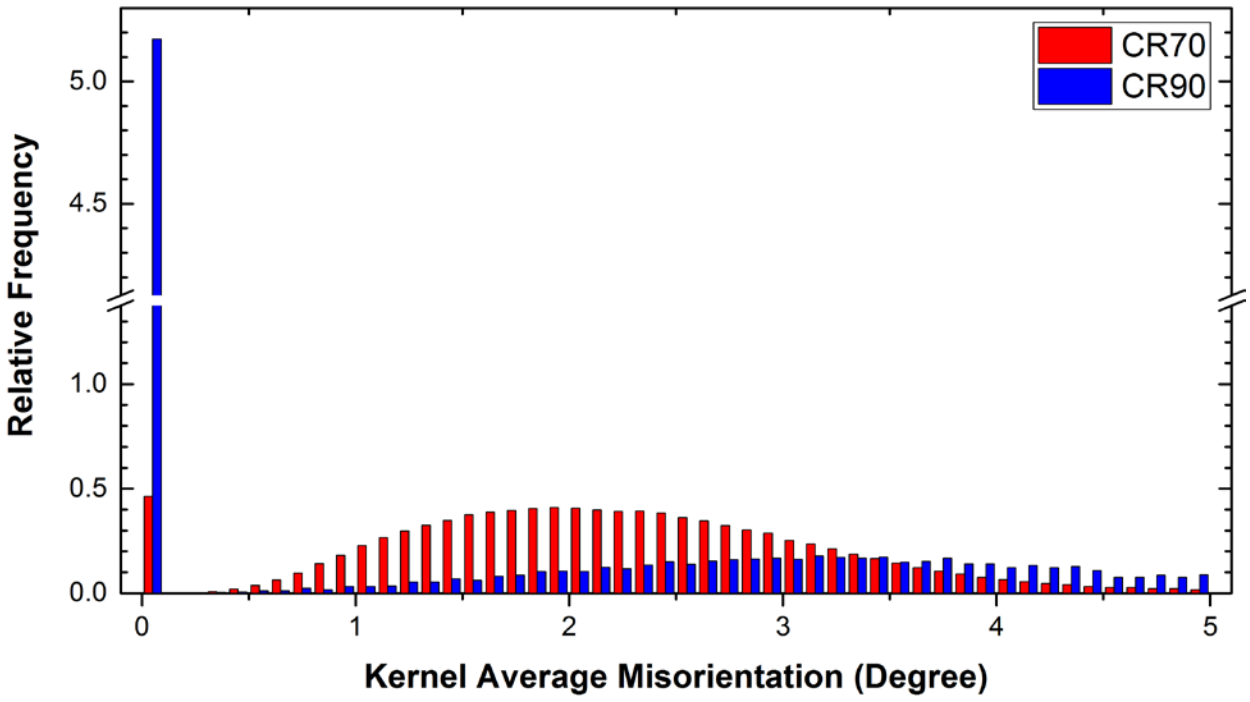

Figure 8.10. Kernel average misorientation vs. relative frequency for 70 and 90% deformed samples.

8.6.1.2 Martensite

Evolution of α-fibre and ε-fibre in martensite phase for both UDR and CR samples are depicted in Figure 8.11. As seen, for both UDR and CR samples, R-C {100}<011> component is formed in martensite at the early stages of deformation.

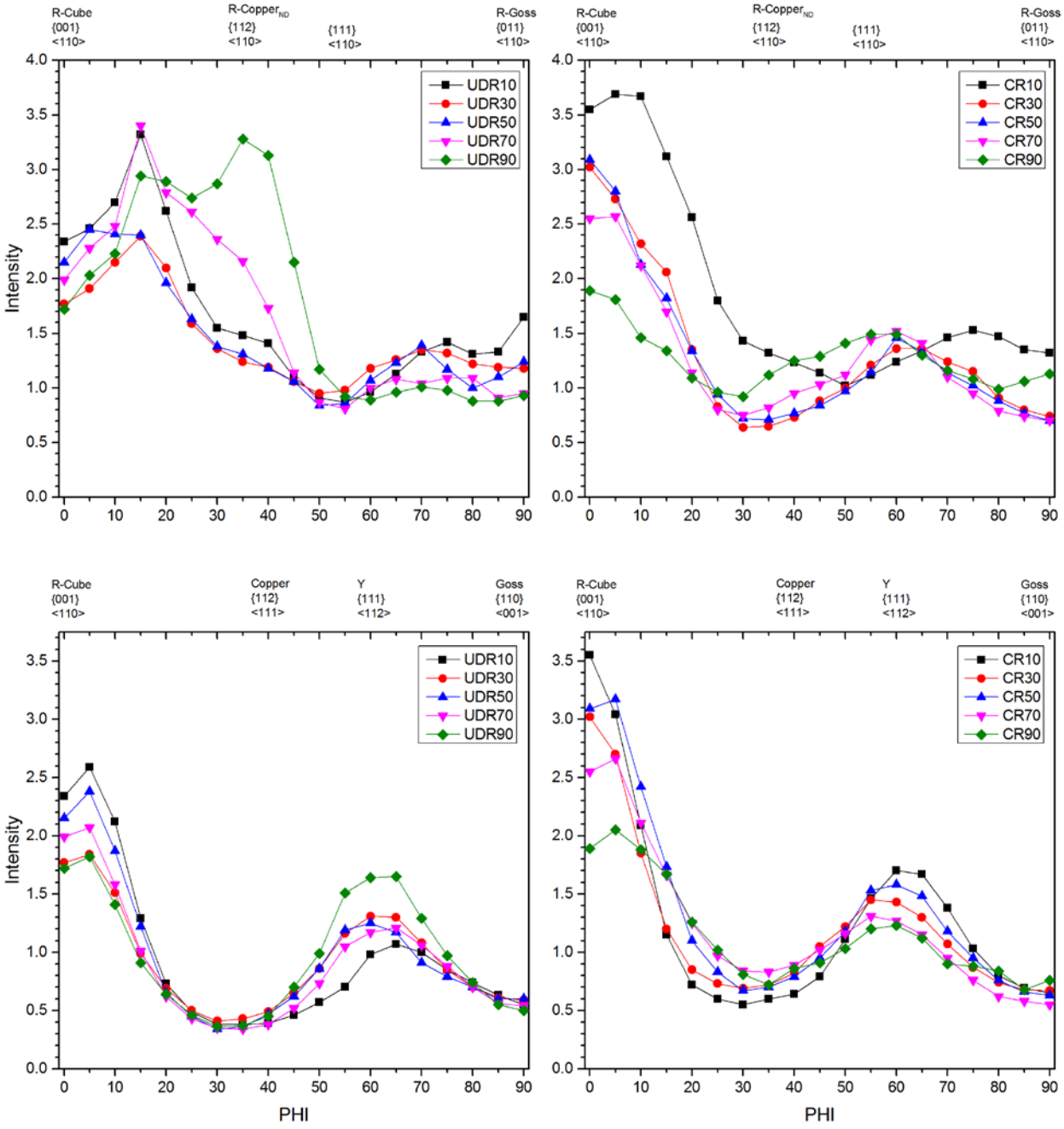

Figure 8.11. α-fibre and ε-fibre for martensite phase in unidirectionally rolled and cross-rolled stainless steel 316L after deformation up to 90% reduction in thickness.

In our previous work, we showed that formation of R-C {100}<011> component in martensite during cold deformation of stainless steel 316L is related to the presence of Copper orientation in deformed austenite [115]. As deformation increases, R-C {100}<011> orientation decreases in both UDR and CR samples. Additionally, R-C {100}<011> component is spread along the ζ-fibre with increase in deformation in CR samples. A similar spread is observed in deformed austenite in CR samples. On the other hand, Brass component is enhanced as deformation increases. Therefore, one can conclude that increase in the fraction of Brass component in deformed austenite would reduce the fraction of R-Cu in strain-induced martensite. Figure 8.12 illustrates the correlation between the aforementioned texture components in the corresponding phases.

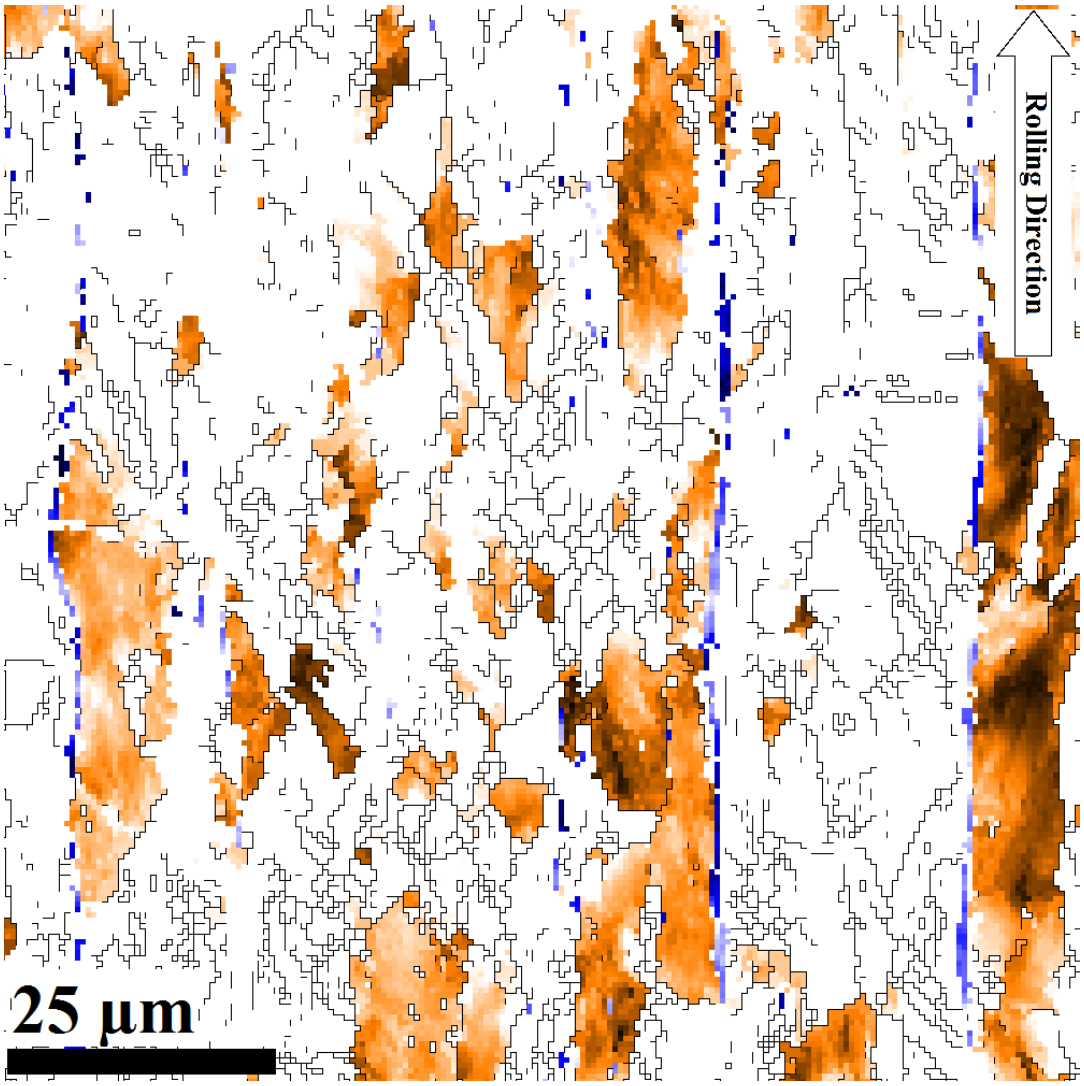

Figure 8.12. Orientation map of 50% deformed stainless steel 310S showing; (orange) Brass {110}<001> in deformed austenite, (blue) R-C {100}<011> in strain-induced martensite.

Another significant change in the texture of martensite is the formation of γ-fibre {111}<uvw> and R-Cu {112}<110>. Although R-Cu {112}<110> is a step ahead, both of the components are intensified at higher deformations, especially after 70% in UDR samples. This process is yet to begin in CR sample as the fraction of these two components starts to increase at 90% of deformation. One can correlate the formation of R-Cu {112}<110> in martensite to the formation of Goss component in deformed austenite. As mentioned earlier, with saturation of Goss component, γ-fibre {111}<uvw> is formed in deformed austenite. It is reported that formation of γ-fibre {111}<uvw> in martensite is related to formation of γ-fibre {111}<uvw> in austenite [115]. To verify this correlation, Figure 8.13 depicts the correlation of γ-fibre {111}<uvw> in both martensite and austenite in the 90% deformed stainless steel 310S. One can see that γ-fibre {111}<uvw> of martensite are formed adjacent to austenite phase with γ-fibre {111}<uvw> orientation. In other words, austenite phase with γ-fibre {111}<uvw> texture can facilitate the formation of strain-induced martensite with γ-fibre {111}<uvw> component.

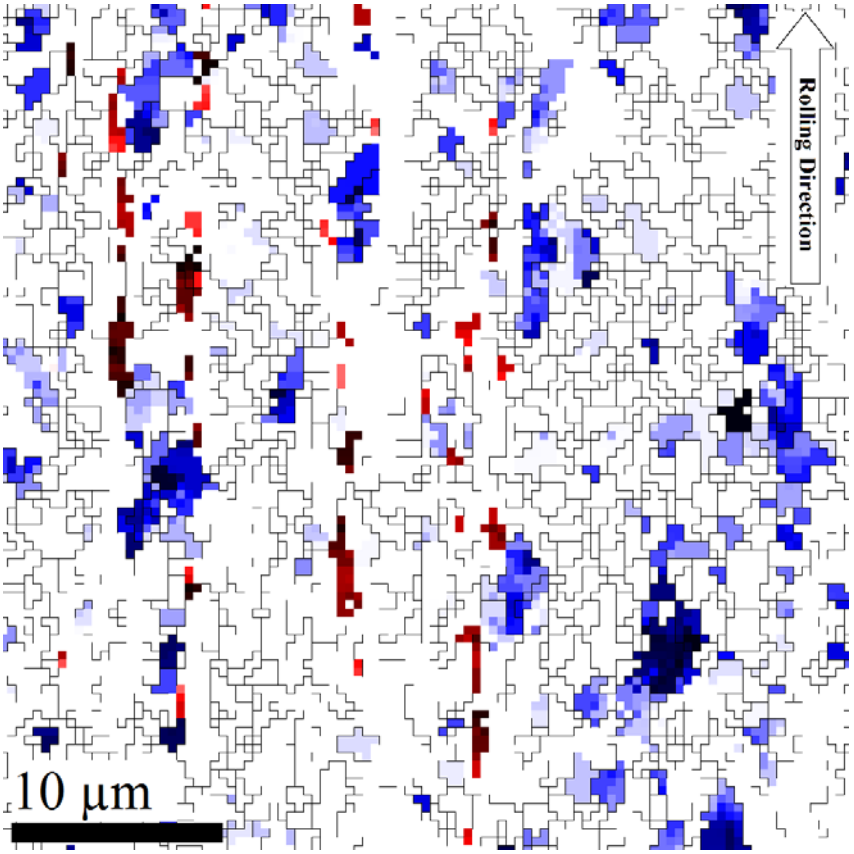

Figure 8.13. Orientation map of 90% deformed stainless steel 310S showing; (blue) γ-fibre {111}<uvw> in deformed austenite, (red) γ-fibre {111}<uvw> in strain-induced martensite.

8.6.2 Annealing Texture

Texture evolution of β-fibre and η-fibre in annealed stainless steel 301S after cold rolling up to 90% reduction is shown in Figure 8.14. Although there are some fluctuations, intensity of the Brass {110}<001> component for both UDR and CR samples is remained almost the same after annealing. Furthermore, intensity of the Goss {110}<001> component was increased by increasing the deformation prior to annealing in UDR samples, while it is slightly oscillated in CR samples. Thus, considering the texture components of deformed phases and their intensity, one can conclude that the final texture of the alloy after annealing is significantly affected by the deformation texture of deformed austenite. This implies that reversion of strain-induced martensite did not influence the annealing texture. In other words, reversion of ά-martensite took place via an athermal process. As a result, the texture of stainless steel 310S after annealing is the same as that of the parent deformed austenite. Moreover, as it is depicted in Figure 8.5 and Figure 8.14, S {123}<634> component is reduced in both samples by increase in deformation and the same trend applies after annealing. Therefore, it can be concluded that deformed grains with S {123}<634> orientation would facilitate the formation of new grains with the same orientation.

Another phenomenon that needs attention in annealing texture of 90% deformed UDR and CR samples is a drop in the intensity of Goss and Brass components after annealing compared to 70% deformed ones. One expects an increasing trend in the intensity of these two component up to the last stages of deformation. The cause of this drop in the intensity lies in the considerably higher fraction of strain-induced martensite compared to lower deformation levels. As reported elsewhere [115], martensite grain boundaries hinder the movement of those of austenite during recrystallization. As a result, this will increase the incubation time which cause incomplete recrystallization in 90% deformed samples after annealing. Thus, after annealing, texture components would have a lower intensity in 90% deformed samples compared to 70% deformed ones.

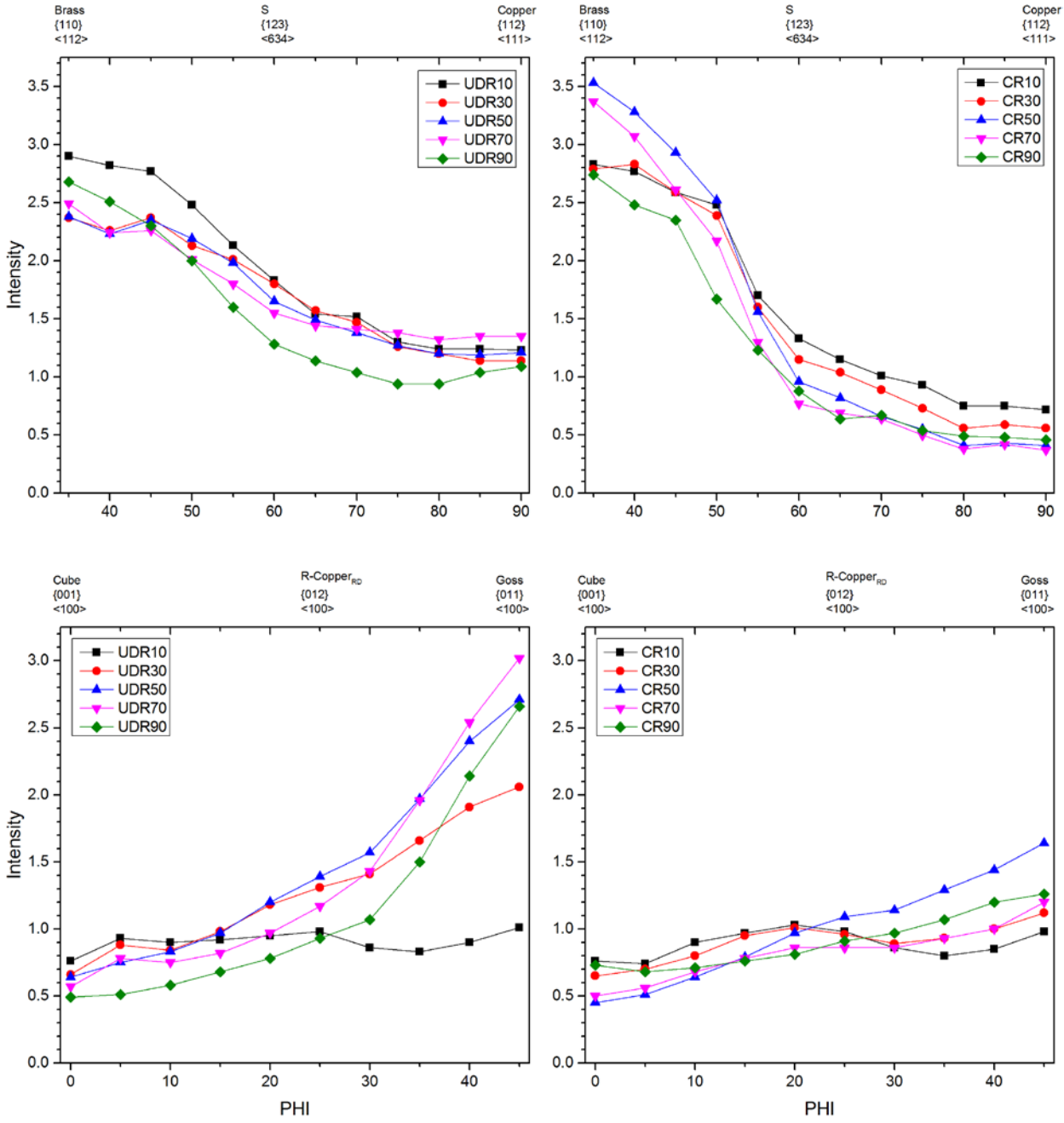

Figure 8.14. β-fibre and η-fibre of annealed stainless steel 316L after cold rolling up to 90% reduction in thickness.

8.7 Conclusions

Texture evolution of deformed and recrystallized austenitic stainless steel 310S was studied and these conclusions are made:

1. Strain-induced martensite is formed as a second phase from the early stages of cold rolling.

2. Texture of deformed austenite and strain-induced martensite are significantly influenced by deformation mode.
3. Deformation texture of austenite is a combination of Goss, Brass, and γ-fibre after 90% unidirectional cold rolling, while Brass is the dominant texture if cross rolling is implemented. Formation of γ-fibre in cross rolled samples is delayed due to incomplete saturation of Goss as a fraction of strain is released as a result of iterative changes in rolling direction.
4. Strain-induced martensite possesses rotated-copper {112}<110> and rotated-cube {100}<011> texture components if unidirectional and cross rolling are utilized, respectively.
5. Goss and Brass are the main texture components of unidirectionally rolled alloy after annealing. Furthermore, annealing texture of cross rolled alloy is consisted of Brass component.
6. Annealing texture of the alloy is found to be greatly affected by the texture of deformed austenite. Texture of strain-induced martensite has no major effect as the reversion of martensite during annealing process is athermal.
7. Regardless of the deformation mode, a rational drop in the intensity of annealing texture components is observed due to increase in incubation time. This is caused by higher fraction of martensite at 90% of deformation which significantly hinder the movement of austenite grain boundaries.

9 OXIDATION OF THERMO-MECHANICALLY PROCESSED AUSTENITIC STAINLESS STEEL 310S IN SUPERCRITICAL WATER

9.1 Overview

The results in chapter 8 demonstrated that the microstructure of austenitic stainless steel 310S was successfully engineered by producing desirable samples for corrosion test in SCW. This chapter completes the third and fourth objectives of the thesis, "to evaluate the role of texture and grain size on improvement of the corrosion resistance of austenitic stainless steels 310S and 316L" and "to recommend which of the investigated alloys and under what treatment conditions is expected to perform better in SCW", by assessment of the corrosion resistance of the thermo-mechanically processed austenitic stainless steel 310S samples in SCW. To do so, weigh change in the samples were measured before and after the corrosion test and it is realized that the thermo-mechanical processing was effective. XRD, EDS, and EBSD, as characterization technique, were implemented to identify why TMP improved the corrosion resistance of austenitic stainless steel 310S. As the result, the changes in the corrosion mechanisms are identified and preferable microstructure to achieve better corrosion resistance for austenitic stainless steel 310S is suggested. Moreover, the orientation correlation between the alloy and the present oxides or the oxides themselves were investigated. The goal is to understand if the microstructural factors (i.e. average grain size and texture) of the substrate have any effect on the structure and orientation of the formed oxides.

This manuscript is submitted to the Journal of Corrosion Science [19] for publication and slight changes have been applied to the original version to avoid repetition in the thesis. To fulfill the objectives addressed in this chapter, Mr. Sami Pentillä[20] assisted the author of this Ph.D. thesis (Majid Nezakat) by performing the corrosion tests in SCW. Jerzy Szpunar, as the supervisor of this research, provided recommendation, consultation and discussion wherever it was needed. Except the corrosion tests, all the experiments, data acquisition, and data analysis were conducted by Majid Nezakat, the lead author of the paper. Majid Nezakat wrote the manuscript, integrated comments from the co-authors, and submitted it for review and possible publication.

[19] The copyright permission to use the manuscript in the thesis is obtained and provided in the appendix section. The references of this chapters are provided at the end of the thesis.

[20] VTT Technical Research Center of Finland, Materials for Power Engineering, P.O. Box 1000, FI-02044 VTT, Finland

9.2 Abstract

Oxidation resistance of thermo-mechanically processed stainless steel 310S in SCW at 600ºC and 25 MPa for 100, 300 and 1000h was studied. The results indicated that TMP successfully improved the oxidation resistance due to smaller average grain size in the substrate. As the average grain size in the samples decreases oxide islands formed on the surface have more homogeneous distribution, were smaller in size and larger in numbers. The electron backscatter diffraction results demonstrated that there is no orientation relation between the oxide islands and the substrate.

9.3 Introduction

The world's demand for clean energy and environmental surveillance has led to development of more reliable power plants such as nuclear power systems that minimize production of carbon dioxide during operation. The generation IV international forum (GIF) was initiated in 2000 with the goal of creating safer and more efficient nuclear reactors. Canada, as one of GIF members, is focused on developing Canadian SCWR, which is an advanced version of the existing CANDU reactors [145–148].

It is expected that this design could achieve efficiencies of approximately 48% in comparison to the current CANDU reactors. However, due to elevated service temperatures and pressures, there are several key challenges, such as accelerated oxidation in SCW. Oxidation deteriorates the structural part of the reactor, especially the fuel cladding. This would result in production of hydrogen, oxide exfoliation, a drop in the heat transfer coefficient, and a reduction in the flow rate of the coolant as the result of decrease in clearance between fuel rods. Therefore, it is essential to select for cladding the material that is more resistant to deterioration under these conditions. In this regard, austenitic stainless steels have received attention for various applications in SCWR mainly due to their high corrosion and irradiation resistance [54,11,16,149,9,150]. They have been widely used in SCW fossil-fired plants, molten metal fast breeder reactors, various types of nuclear water-cooled reactors, and chemical plants. One grade of this alloy family, stainless steel 310S, has been short-listed as one of the candidate materials for the fuel cladding in the Canadian SCWR design [151]. This alloy exhibits relatively good general corrosion and good SCC resistance in SCW at 600ºC 25 MPa [152]. Despite of significant knowledge on the performance of these steels, there is a gap in understanding the effect of the initial microstructure of the alloy on the corrosion resistance in SCW. For the most part, studies reporting the corrosion resistance of austenitic

stainless steels exposed to SCW have been conducted using as-received (typically mill-annealed) material, without consideration of the influence of initial microstructure. Several attempts have been made to improve the oxidation resistance of stainless steel in SCW using surface modification [92] and grain boundary engineering [46,112,153,154]. However TMP [44,59,61,70,115,137,155] that seems to be a most promising technique, has not been implemented on stainless steel 310S. In this work, the influence of TMP is adopted to modify the microstructure and influence of texture and grain size on the oxidation resistance of 310S steel in SCW is studied.

9.4 Materials and methods

Hot rolled stainless steel 310S billet with the chemical composition listed in Table 3.1 used in this study. The initial thickness of the as-received billet was 6.25 mm and average grain size was 20μm. Samples with different initial microstructure for oxidation experiments were prepared in a two-step TMP. First, strips of 50×50 mm^2 from the as-received alloy were cold rolled via cross-rolling (CR) up to 50, 70 and 90% reductions in thickness. Inter-pass rolling steps of 10% true stain was selected to avoid fracture during rolling. Cold rolled specimens were cut to the dimensions of 24 ± 0.01 mm × 14 ± 0.01 mm × 0.6 ± 0.01 mm and then mechanically grinded to grit number 2000 (10μm SiC particles) using abrasive papers. In the next step all the cut samples were annealed at 1050ºC for 5 minutes per millimeter thickness to achieve stress free surface with the desired microstructure [116,117]. Samples were named in such a way that cold rolled is marked (CR), deformation reduction was 50, 70, and 90%, and A stands for post-rolling annealing.

Macro-texture of the thermo-mechanically processed samples was measured prior to oxidation using a Bruker D8 Discover diffractometer with a two-dimensional x-ray detector system (XRD^2) and Cr K_α radiation. The incomplete pole figures were collected at the mid-section of all samples to construct the orientation distribution function (ODF) with Resmat® software. For detailed discussions, various textural components were extracted from ODFs. For phase identification and grain size measurement of the thermo-mechanically processed samples, an electron backscatter diffraction system (Oxford NordlysNano EBSD) installed on a Hitachi SU6600 field emission gun scanning electron microscope was implemented. During the data acquisition, the scanning electron microscope was operating at 20 kV and samples were tilted 70º with respect to the horizontal plane using a pre-tilted sample holder. For EBSD data analysis, Aztec HKL® software was used and inverse pole figure maps were extracted relative to an axis normal to the rolling plane.

After microstructural analysis, all the samples were exposed to SCW at 600ºC and 25 MPa for 100, 300 and 1000h in an autoclave connected to a recirculation water loop. To avoid leakage in the pipes junctions, the water flow was kept low as the operating temperature was high. A special electrically insulated sample holder rack was used to mount the samples and avoid any electrical connection to the rack and autoclave body. After oxidation, the weight change were calculated per unit area by weighing each sample before and after exposure for 100, 300, and 1000h. For microstructural observation at the cross-section, samples were mounted in a conductive edge retention resin (Struers Polyfast®) and mechanically grinded up to abrasive paper grit number 2000 (10µm SiC particles) followed by polishing with a water based diamond suspensions up to 1 µm diamond particle size (Struers DiaPro®). To avoid breakdown of the fragile oxide layer, the polishing wheel speed was lower than 150 rpm. Final polishing continued up to 0.04 µm colloidal silica suspension (Struers OP-S®) on a vibratory polisher (Buehler VibroMet^{TM} 2) for 24 h. Oxide layer structure were then analyzed using Hitachi field emission gun scanning electron microscope at 20 kV. The microscope was equipped with EBSD and energy dispersive spectroscopy (EDS) detectors (Oxford X-Max Silicon Drift).

9.5 Results

9.5.1 Weight Change

Figure 9.1 illustrates the weight change of samples after exposure to SCW for 100, 300, and 1000h. Although there is a slight drop in weight change of CR50A and CR90A samples after 300h of oxidation compared to that of 100h, the graph shows an accumulative trend of weight gain with oxidation time for all samples. Additionally, visual inspection of samples did not reveal any sign of oxide exfoliation for all the three oxidation periods. This indicates good adhesion of oxide scale to substrate after oxidation up to 1000h. On the other hand, as a result of TMP, weight change diagram shows a descending trend with decreasing the average grain size of the samples. The reason can be a difference in the microstructure of stainless steel, which will be discussed later.

9.5.2 Phase Identification

The post-exposure x-ray diffraction patterns of thermo-mechanically processed samples are depicted in Figure 9.2. The first impression is that the picks of oxide phases are very weak compared to those of stainless steel gamma phase. This indicates that the alloy has a good oxidation

resistance. The pick intensity of oxide phases did not change with oxidation time up to 1000h. After careful characterization of oxide picks at different oxidation times, it was found that the same oxide phases, including hematite (Fe_2O_3), manganese-chromium spinel (Mn_2CrO_4), and nickel-iron spinel ($NiFe_2O_4$), are present in all samples. A part of x-ray diffraction pattern of as-received sample is magnified for better visual comparison of oxide phases. No oxide was formed or decomposed until 1000h of oxidation.

9.5.3 Surface morphology

The surface morphologies of the as-received and thermo-mechanically processed samples are illustrated in Figure 9.3. Two types of oxides, base film and oxide islands, grow on the surfaces of all samples. The surfaces are completely covered with the thin layer of oxide and some contamination from the autoclave material is observed. The oxide islands that are formed on the base film have different cluster sizes as marked with white arrows in Figure 9.3. As the average grain size of the substrate decreases, the oxide islands are distributed more homogeneously, with smaller cluster size and in higher numbers. The size of the oxide islands does not show a significant change with oxidation time, however, the number of islands is increased.

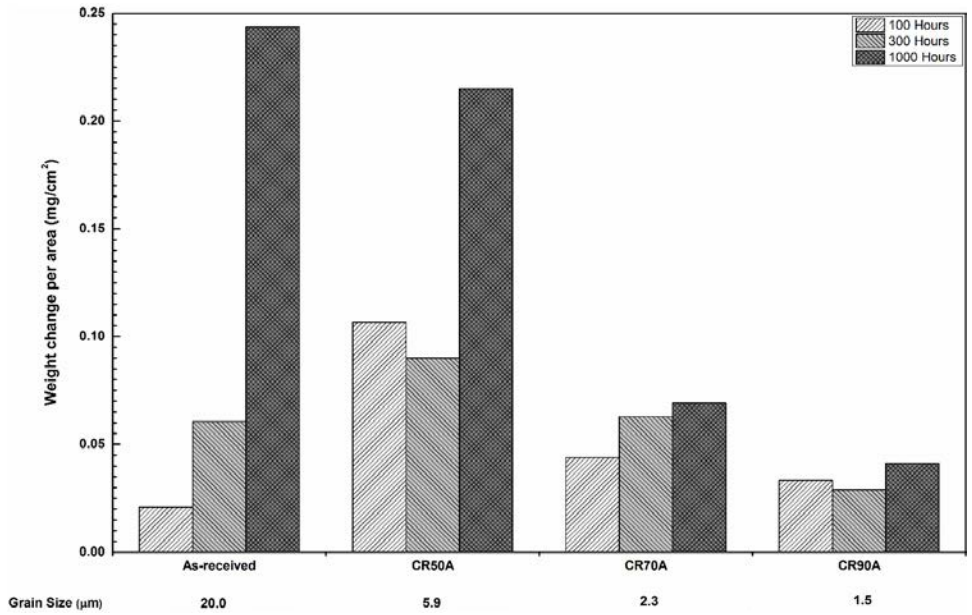

Figure 9.1. Weight change of as-received and thermo-mechanically processed stainless steel 310S samples after exposure to SCW at 600 ºC and 25 MPa for 100, 300, and 1000h.

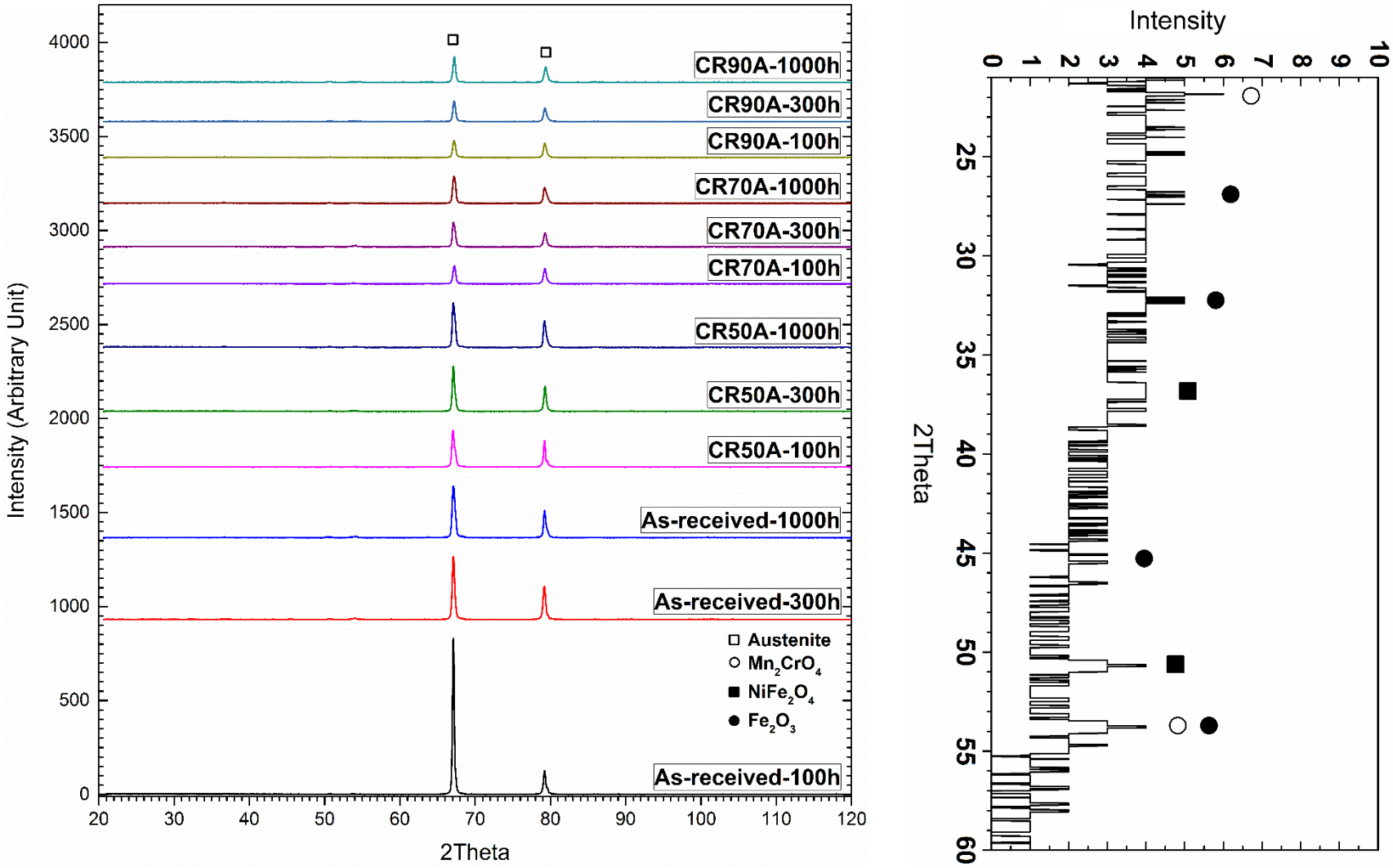

Figure 9.2. X-ray diffraction patterns of (left) as-received and thermo-mechanically processed, and (right) as-received stainless steel 310S samples after exposure to SCW at 600ºC and 25 MPa for 100, 300, and 1000h.

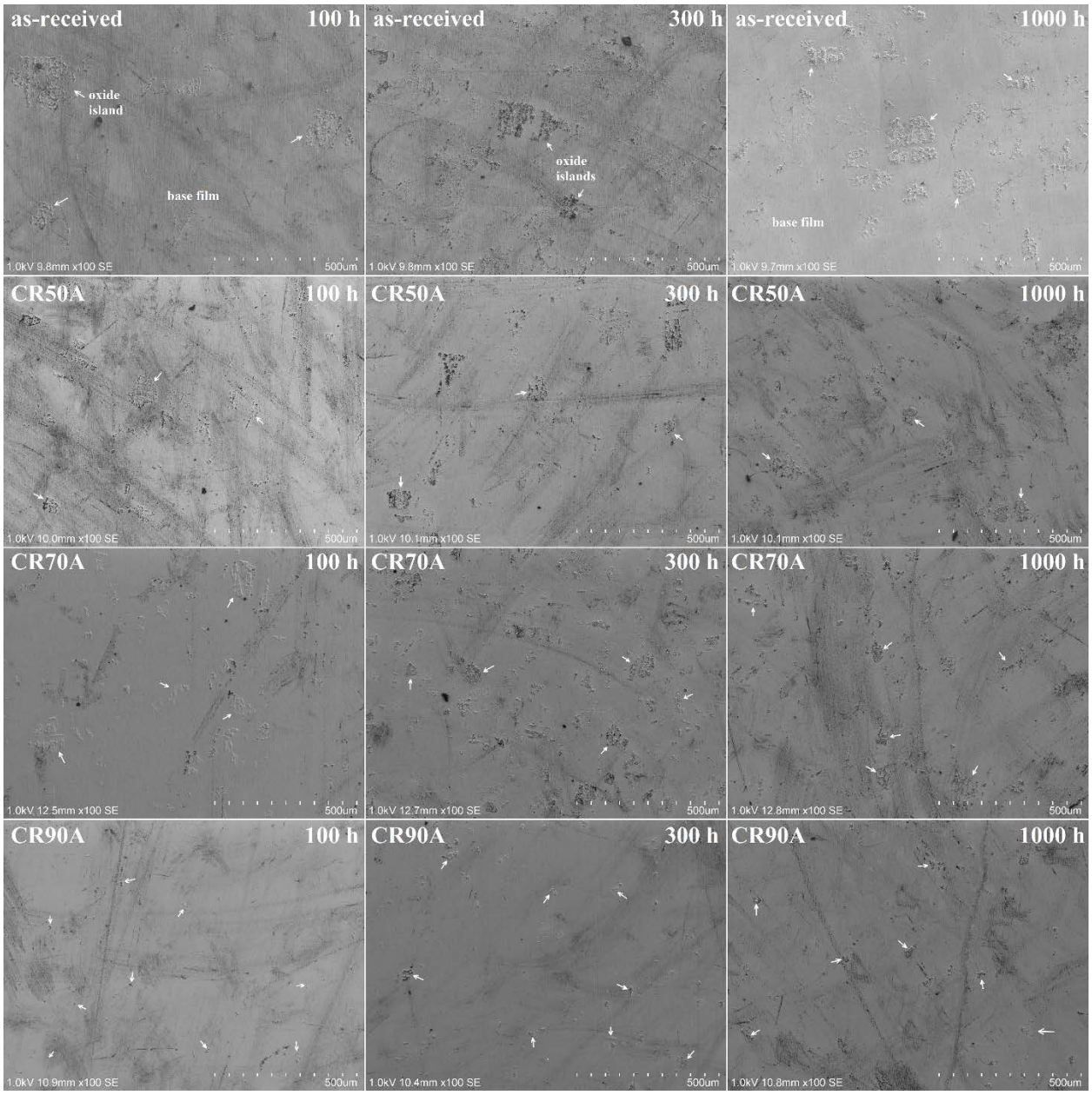

Figure 9.3. Surface morphologies of the oxide formed on the as-received and thermo-mechanically processed stainless steel 310S samples after exposure to SCW at 600ºC and 25 MPa for 100, 300, and 1000h.

9.6 Discussions

9.6.1 Oxidation mechanism

Figure 9.4 shows the elemental composition maps of the as-received alloy after 1000h exposure from two different angles. Five regions including substrate, nickel, internal oxide,

external oxide islands, and a thin oxide layer covering the rest of the surface are illustrated. Based on the elemental composition maps of iron, nickel and oxygen, the external oxide island has two different compositions. Some portion only consists of oxygen and iron, and the rest has also nickel. Comparing EDS data with XRD, and considering the fact that there is no iron or nickel oxide elsewhere in the map, the oxide island must made of hematite (Fe_2O_3) and nickel-iron spinel ($NiFe_2O_4$). The internal oxide, on the other hand, has only one composition and contains oxygen, manganese, and chromium. It has almost the same depth as the external oxide island. Considering the XRD result, the internal oxide is manganese-chromium spinel (Mn_2CrO_4). Using the same comparison, the thin oxide layer has structure of manganese-chromium spinel (Mn_2CrO_4). Small nickel-rich grains are also formed near to substrate, where oxide islands are present.

To decipher the oxidation mechanism of the alloy 310S in SCW, we can use the schematic representation shown in Figure 9.5. Upon exposure to SCW, a thin chromium-rich film forms on the surface due to the high concentration of chromium in stainless steel 310S. As it was already mentioned, this protective oxide layer is manganese-chromium spinel (Mn_2CrO_4). However, because of the dissolution of this film in SCW at elevated temperature, chromium reached the surface to compensate the losses. Considering the fact that chromium has a higher diffusivity along the grain boundaries in comparison to the grain interior, there will be more chromium supplied to the surface at areas above the grain boundaries to compensate the deficit. Therefore, the oxide layer above the grain interior is depleted of chromium and is less protected. In addition, iron and nickel diffuse through the non-protective layer and reacts with oxygen and form nickel-iron spinel ($NiFe_2O_4$) and iron oxide, but the amount of iron provided to the surface is enough only to form hematite (Fe_2O_3). On the other hand, the inward diffusion of oxygen through the non-protected layer results in formation of manganese-chromium spinel (Mn_2CrO_4) in the absence of iron.

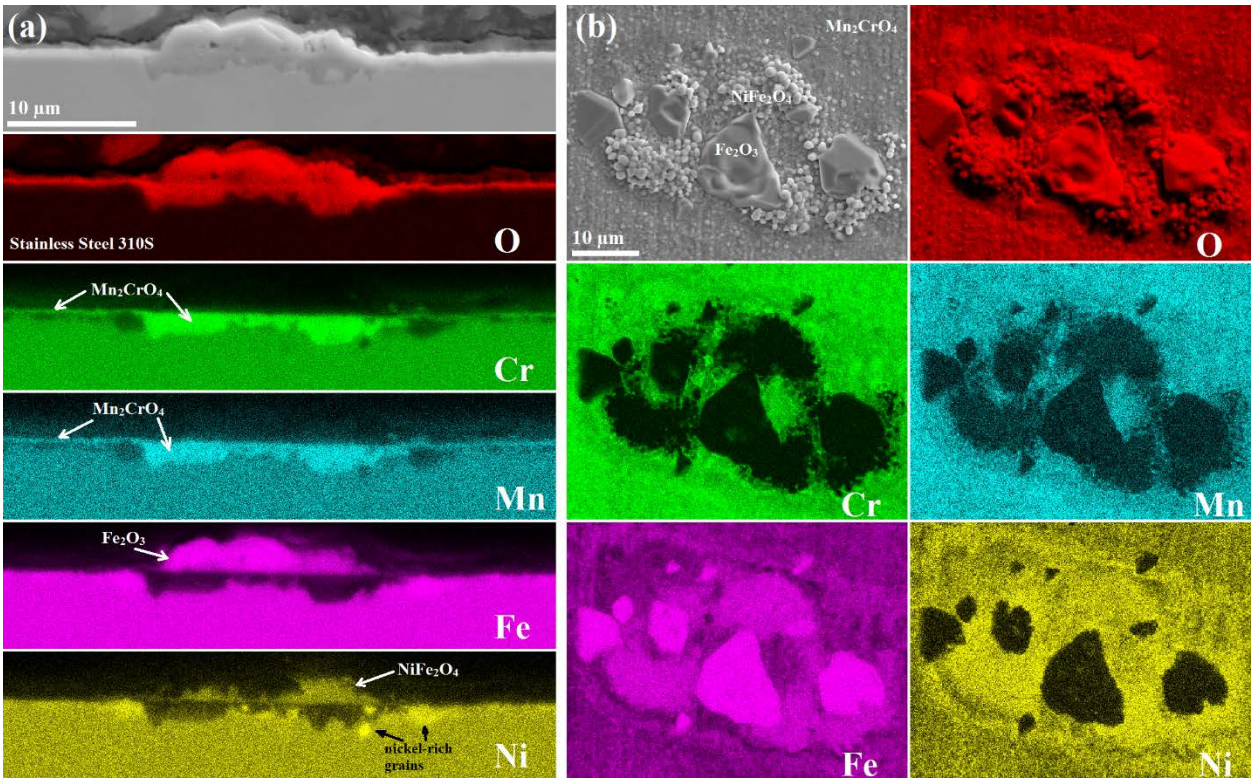

Figure 9.4. SEM micrograph and elemental composition maps of (a) cross-section, and (b) surface of as-received stainless steel 310S after exposure to SCW at 600ºC and 25 MPa for 1000h.

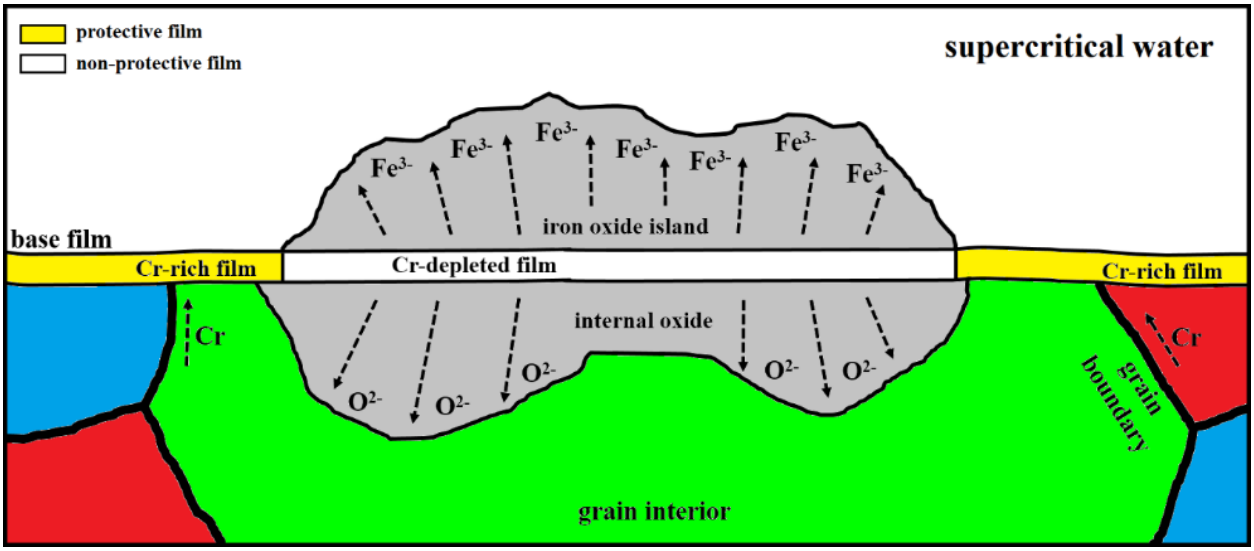

Figure 9.5. Oxidation mechanism of stainless steel 310S after exposure to SCW.

9.6.2 Oxidation resistance

Depending on the concentration of the alloying elements in stainless steels, especially chromium, or the density of grain boundaries in the microstructure, a number of oxides with different morphologies could form inside or on top of the alloy exposed to SCW [44,16,156,12]. In cases where there is not enough chromium in the alloy to compensate for the losses because of dissolution of the protective chromium-rich oxide layer, the exposed alloy will not be protected. On the other hand, high fraction of grain boundaries in the alloy could provide faster diffusion paths for chromium to reach the surface and to compensate for losses resulting from dissolution of the protective layer.

As stainless steel 310S has high percentage of chromium, reducing the average grain size via TMP to increase the grain boundaries volume fraction is expected to improve its oxidation resistance in SCW. Figure 9.6 shows the ODFs of the as-received and thermo-mechanically processed samples. The dominant texture of all samples is the same Brass {110}<112>, however the average grain size is decreased (see Figure 9.1) with rolling reduction during TMP. This observation is very important, as the effect of grain size must be separated from the effect of texture for the discussion of oxidation mechanism.

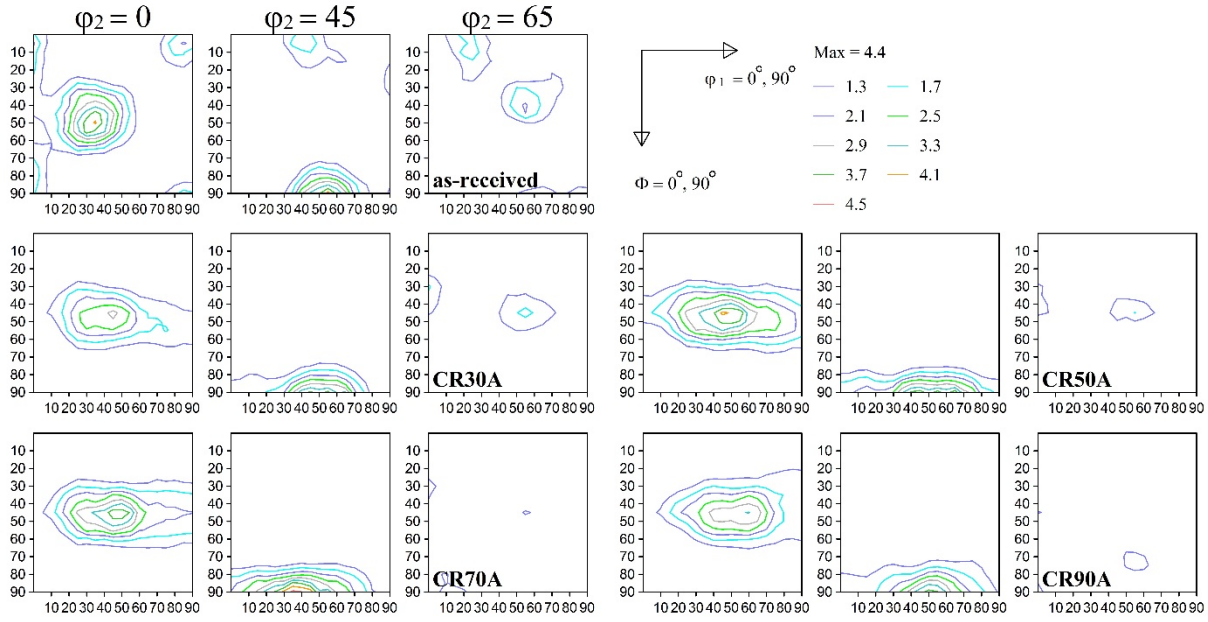

Figure 9.6. Annealing texture of stainless steel 310S; ϕ_2= 0º, 45º, and 65º ODF sections of the as-receive and thermo-mechanically processed samples.

Since all the samples have the same type of oxides, for comparison the elemental composition maps of the thermo-mechanically processed CR90A sample at the cross-section and top surface are depicted in Figure 9.7. This sample has an average grain size of 1.5 µm which is smaller than that of as-received alloy (20µm). The same oxide compositions with the similar morphology are observed in the CR90A sample and in the as-received one. This implies that the oxidation mechanism does not change with decrease in the average grain size, however, the size of the oxide island decreases. This was also confirmed by observation of surface morphology as presented in the Figure 9.3. We observed that reduction of grain size increases the density of grain boundaries and as a result, the fraction of grain interior area is lower. This would create smaller oxide islands.

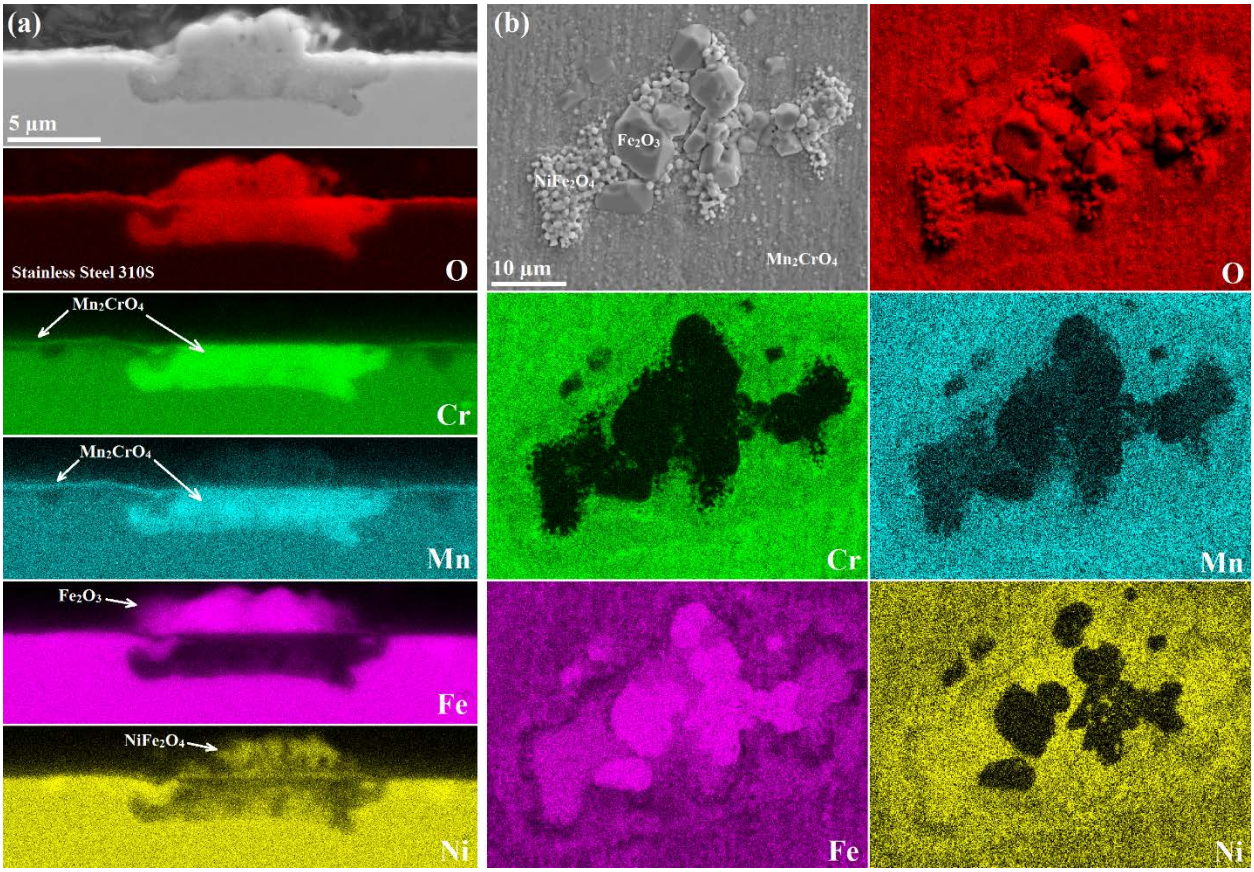

Figure 9.7. SEM micrograph and elemental composition maps of (a) cross-section, and (b) surface of thermo-mechanically processed stainless steel 310S after exposure to SCW at 600ºC and 25 MPa for 1000h.

9.6.3 Oxide texture

Depending on the oxidation regime, the orientation of the oxide grains could change during the nucleation and growth processes. Figure 9.8 illustrates the band contrast, phase map, and inverse pole figure map of the as-received sample and CR90A samples after exposure.

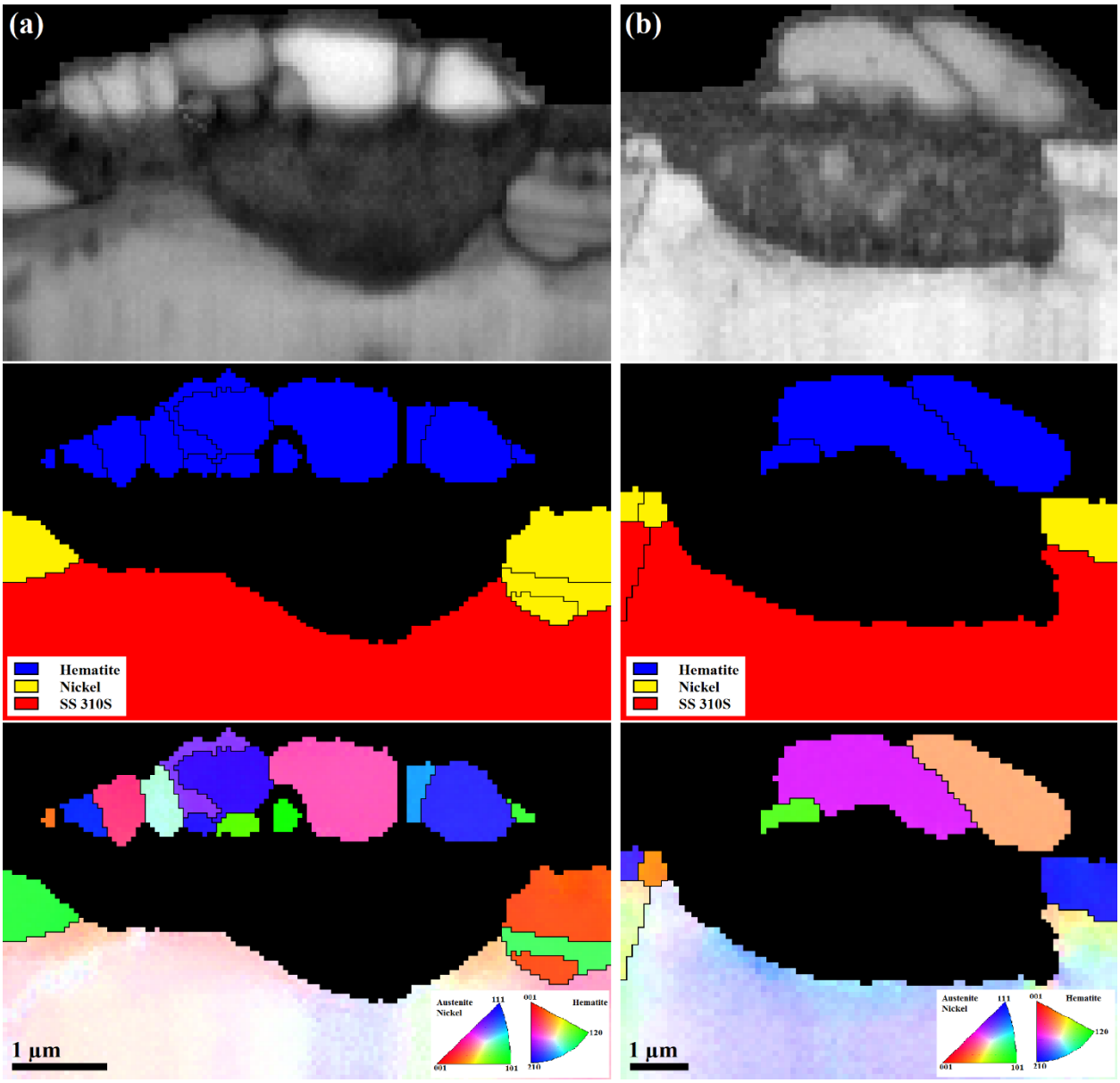

Figure 9.8. Band contrast, phase map, and inverse pole figure map of (a) as-received, and (b) thermo-mechanically processed (CR90A) stainless steel 310S samples after exposure to SCW at 600ºC and 25 MPa for 1000h.

Due to very small grains size of the manganese-chromium spinel (Mn_2CrO_4) and nickel-iron spinel ($NiFe_2O_4$), EBSD was not able to index these phases. In order to make a comparison, two oxide islands were selected from each sample where the substrate grain has similar orientation. One can observe that hematite (Fe_2O_3) grains are smaller for the as-received sample compared to those of CR90A sample. This could be related to higher number of nucleation sites for hematite (Fe_2O_3) due to higher interior grain area for the as-received sample. One the other hand, regardless of the orientation of the substrate in both samples, hematite (Fe_2O_3) grains nucleate and form rather random orientation on the surface. This was also observed for stainless steel 316L exposed to SCW [44,157]. According to this study, the orientation of hematite (Fe_2O_3) grains is dictated by the surface energy and strain energy. Therefore, after formation of the first layer of randomly oriented oxide grains on the surface, the next layers of oxide will choose the orientation with the lowest surface energy and highest strain energy. Thus, it is expected that if oxidation continues for stainless steel 310S for more than 1000h, the hematite (Fe_2O_3) would have (0001)<uvtw> texture with trigonal crystallographic structure.

9.7 Conclusions

TMP was implemented to improve the oxidation resistance of stainless steel 310S. The followings can be concluded from this study:

1. Weight change measurements indicates that TMP successfully improves the oxidation resistance of stainless steel 310S. Higher fraction of grain boundaries due to smaller average grain size of the thermo-mechanically processed samples is found to be the reason as they provide much faster diffusion paths for chromium to reach the surface.
2. Oxide Islands formed on the surface are distributed more homogeneously, and have smaller size and are higher in number, as the average grain size of the oxidized samples decreases.
3. Texture of hematite (Fe_2O_3) oxide is not affected by the texture of the substrate in all samples. The random orientation of single-layer hematite oxide islands is attributed to random nucleation of hematite grains on the surface.
4. The smaller average grain size of hematite grains on the as-received sample is related to larger nucleation sites provided on the as-received sample due to higher fraction of interior grain area exposed to the oxidation media.

10 SUMMARY, CONCLUSIONS, AND RECOMMENDATIONS FOR FUTURE WORK

This Ph.D. thesis investigates the performance of two candidate alloys in super critical water for generation IV Canadian Super Critical Water-cooled Reactor. The main hypothesis is that the corrosion resistance of the alloys can be improved by altering the microstructural parameters including average grain size and texture (dominant orientation of the grains). To test the hypothesis, the thesis selects and validates a thermo-mechanical processing to investigate the effects of average grain size and texture on the corrosion resistance of both alloys. The results in the thesis reveal that the hypothesis is valid if certain microstructural factors are met. In this chapter, a brief summary of the thesis, and notable conclusions are presented. In addition, the promising topics for future work and further studies are provided.

10.1 Summary

The Canadian Super Critical Water-cooled Reactor (SCWR) is a promising advanced nuclear system that is under development due to its higher thermal efficiency and simpler design compared to the current generation of operating nuclear reactors. To endure the extreme conditions (core outlet temperature of up to 625 ^{o}C and Pressure above 25 MPa), materials selection to be used in the reactor is a challenge. This Ph.D. research focuses on the feasibility of improving the corrosion resistance of the currently available materials in the market by using a thermo-mechanical treatment to be used inside the SCWR.

In chapter 1, the motivation of this research was clarified. The current knowledge gap in developing the future generation of nuclear reactors was described and based on that the objectives of the thesis were provided. In addition, thesis organization with the list of published article in refereed journals and conferences and the extent of contribution of this dissertation to the knowledge were elaborated.

A general literature review was provided in chapter 2, as each manuscript of the thesis contains detailed review of literature relevant to the subject.

Although each manuscript has a section for materials and methods, Chapter 3 delivered a detailed experimental methodology of the research for a comprehensive understanding of the whole experimental procedure.

Chapter 4 focused on performance of the selected alloys for this study. The supercritical water condition in Canadian SCWR was replicated in an autoclave working at 25 MPa of pressure and 600 ºC of temperature. Austenitic stainless steels 316L and 310S were tested in this autoclave for 100, 300, and 1000h to assess their long term corrosion resistance. For comparison air oxidation at similar temperature and atmospheric pressure was done for a better understanding of their resistance to extreme environments. The existing corrosion mechanisms were identified and correlated to the performance of both alloys. Studying the performance of these two alloys in SCW, this chapter covered the first objective of the thesis, "to evaluate the oxidation resistance of austenitic stainless steels 310S and 316L in SCW as well as in air for comparison".

In chapter 5, the microstructure of stainless steel 316L was modified using a thermo-mechanical treatment. The idea was to change the average grain size and texture of the alloy separately and test the engineered microstructure in SCW condition for improvement in corrosion resistance. The deformation and recrystallization mechanisms led to the microstructural changes of the alloy were studied in detail. This chapter addressed a part of the second objective of the thesis, "to optimize the microstructure of austenitic stainless steels 310S and 316L thermo-mechanical processing to improve the corrosion resistance".

In chapter 6, the thermo-mechanically processed samples of austenitic stainless steel 316L were tested in SCW. It was realized that changes to grain size has a stronger effect compared to changes to the texture of the alloy. A critical average grain size was identified, below which the corrosion resistance of the alloy would improve significantly. The changes in corrosion mechanisms explained the significant improvement of corrosion resistance of the steel. This chapter partially fulfilled the third and the fourth objectives of the thesis, "to evaluate the role of texture and grain size on improvement of the corrosion resistance of austenitic stainless steels 310S and 316L", and "to recommend which of the investigated alloys and under what treatment conditions is expected to perform better in SCW".

Chapter 7 focuses on the crystallographic relation of austenitic stainless steel 316L and the oxide formed after the corrosion test. The goal was to realize if the crystallographic orientation of the substrate grains played any role on the orientation of the oxides or stress concentration in the oxide layer. It was comprehended that the strong texture of the formed oxides can be explained based on the surface energy minimization and strain energy minimization model and the substrate texture has no effect on the orientation of the oxide grains. This chapter partially addressed the

third objectives of the thesis “to evaluate the role of texture and grain size on improvement of the corrosion resistance of austenitic stainless steels 310S and 316L”.

In chapter 8, the effect of the thermo-mechanical treatment, that is proposed in chapter 5, on the microstructure of the austenitic stainless steel 310S was investigated. Similar idea of chapter 5 was also behind this treatment to change the microstructural parameters (i.e. average grain size and texture of the alloy) separately before corrosion test in SCW. This chapter focuses on going into detail of the deformation and recrystallization mechanisms causes the microstructural changes of the steel. The second objective of the this, “to optimize the microstructure of austenitic stainless steels 310S and 316L thermo-mechanical processing to improve the corrosion resistance”, was completed in this chapter.

The main goal of chapter 9 was to assess the corrosion resistance of the thermo-mechanically processed samples of austenitic stainless steel 310S in SCW. Similar to the results of alloy 316L, it was shown that the average grain size of the alloy 310S has a greater effect on the corrosion resistance compared to the effect of the texture. It was realized that below a certain average grain size, the corrosion resistance of the alloy considerably improves. Studying the changes in the corrosion mechanisms explained this improvement. Additionally, the crystallographic correlation of the substrate and the oxides formed on the surface was studied. It was comprehended that the random orientation of oxide islands is attributed to random nucleation of oxide grains on the surface. This chapter completed the third and fourth objectives of the thesis, “to evaluate the role of texture and grain size on improvement of the corrosion resistance of austenitic stainless steels 310S and 316L”, and “to recommend which of the investigated alloys and under what treatment conditions is expected to perform better in SCW”.

10.2 Conclusions

The following are the major conclusions and outcomes achieved through this Ph.D. research:

1. Austenitic stainless steel 310S is a better candidate material for application in generation IV Canadian supercritical water-cooled reactor (SCWR) compared to Austenitic stainless steel 316L. Corrosion tests at 600 ºC indicated that alloy 310S shows a better corrosion resistance in SCW. A thin protective layer of Cr_2O_3 and Mn_2CrO_4 spinel that form on the surface of alloy 310S, hinders the corrosion. Better corrosion resistance of alloy 310S in comparison to alloy 316L was attributed to higher chromium content of the 310S alloy. The non-protective oxide

layer formed on alloy 316L was consisted of magnetite (Fe_3O_4) and iron-chromium spinel ($FeCr_2O_4$). The magnetite was formed externally with thick and porous structure that exfoliated from the surface during cooling to room temperature.

2. In order to optimize the microstructure to improve the corrosion resistance in SCW, austenitic stainless steel 316L samples with different average grain size and texture is produced successfully using TMP. Evolution of deformation and recrystallization texture of the alloy demonstrates that rolling path has a meaningful impact on the texture. At highest degree of cold deformation, 90% reduction in thickness, UDR produces a combination of Goss {110}<100>, Brass {110}<112>, and γ-fibre {111}<uvw> orientations, while CR mainly results in Brass {110}<112>. Deformation mechanism at early stages of cold rolling is slip, but twinning is the dominant mechanism at higher deformation level. For deformation induced martensite, UDR and CR rolling path results in rotated-copper {112}<110> and rotated-cube {100}<011>, respectively. Although texture of deformation induced martensite is also affected by cold rolling path, recrystallization texture is determined by the texture of the deformed austenite. As a result, the annealing texture of samples with UDR history during TMP is a combination of Goss {110}<100> and Brass {110}<112> while Brass {110}<112> is the dominant orientation in specimens with CR history.
3. Thermo-mechanical processing can improve the corrosion resistance of Austenitic stainless steel 316L up to four times that could be achieved by reducing the average grain size below 3 µm. Two corrosion mechanisms were identified to explain this statement. It is understood that higher fraction of grain boundaries in samples with average grain size below the 3 µm caused formation of a protective layer of chromium oxide (Cr_2O_3) on their surface. The layer is found to be thick and continuous enough to decrease the corrosion resistance significantly.
4. Substrate orientation in austenitic stainless steel 316L has no effect on the orientation of magnetite (Fe_3O_4) formed after corrosion test in SCW. Magnetite grains has strong (111)<uvw> texture and as corrosion test continues they consume neighbor grains that results in larger grains at longer corrosion periods. With changes in the corrosion mechanisms in samples with average grain size below 3 µm, hematite (Fe_2O_3) forms on magnetite with a near-(0001)<uvtw> texture. The strong texture of both oxides is dictated by a competition between their surface free energy and strain energy.

5. To optimize the microstructure of austenitic stainless steel 310S for improving the corrosion resistance in SCW, thermo-mechanical processing can successfully produce samples with different average grain size and texture. Texture of deformed austenite and deformation induced martensite is greatly influenced by the deformation path in austenitic stainless steel 310S. UDR results in a combination of Goss {110}<100>, Brass {110}<112>, and γ-fibre {111}<uvw> in deformed austenite, while Brass {110}<112> texture is dominant if CR is implemented. In addition, UDR and CR produce {112}<110> and rotated-cube {100}<011> in martensite, respectively. As the reversion of martensite during annealing process is athermal, the texture of deformation induced martensite has no effect on annealing texture of the 310S alloy and it is determined by the texture of deformed austenite. Therefore, Goss {110}<100> and Brass {110}<112> were found to be the major texture components of the annealed samples with UDR history during TMP, while the samples with CR history had Brass {110}<112> texture after TMP.
6. Improving the corrosion resistance of austenitic stainless steel 310S in SCW is possible by means of TMP. It is comprehended that the higher fraction of grain boundaries in the processed samples provide much faster diffusion paths for chromium to reach the surface and compensated for losses due to dissolution of chromium in the oxidation media. Results also indicated that the oxide islands formed on the surface have smaller size and are higher in number as the average grain size of the oxidized 310S samples decreases. Micro texture of hematite (Fe_2O_3) was not influenced by the texture of the substrate in all investigated samples. Random orientation of single-layer hematite oxide islands was attributed to random nucleation of hematite grains on the surface.

10.3 Future work

10.3.1 Study the oxidation in occurrence of a failure

In chapter 4, oxidation of stainless steel 316L and 310S in air and SCW were studied. It will be beneficial to study the air oxidation of these alloys at more elevated temperatures to evaluate their performance in case of cooling system failure in reactor that leads to temperatures above 1000 ºC.

10.3.2 Design process to achieve significantly different alloy texture

In chapter 5 and chapter 8, the effect of TMP on microstructural evolution of stainless steel 316L and 310S was studied. These two chapters were focused on preparation of samples with different average grain size and similar texture. It would be of great interest to produce samples via a different process that results in a significantly different textures and similar average grain size to have a better understanding of the texture effect on the corrosion in SCW.

10.3.3 Introducing other parameters into the test condition

In chapter 6 and chapter 9, corrosion of thermo-mechanically processed stainless steel 316L and 310S were assessed. Evaluating stress corrosion cracking, irradiation, and creep resistance of these alloys in SCW environment might help to design TMP treatment to improve these properties.

REFERENCES

[1] Nuclear Energy Data 2015, 2015.

[2] Key World Energy Statistics 2015, 2015.

[3] Gen IV International Forum, in: GIF Symp. Proc. 2012 Annu. Rep., Nuclear Energy Agency, Organisation for Economic Co-Operation and Development, San Diego, 2013.

[4] OECD Nuclear Energy Agency, Technology Roadmap Update for Generation IV Nuclear Energy Systems, (2014) 1–66.

[5] S. Penttilä, A. Toivonen, J. Li, W. Zheng, R. Novotny, Effect of surface modification on the corrosion resistance of austenitic stainless steel 316L in supercritical water conditions, J. Supercrit. Fluids. 81 (2013) 157–163.

[6] P. Yvon, F. Carré, Structural materials challenges for advanced reactor systems, J. Nucl. Mater. 385 (2009) 217–222.

[7] L. Zhang, Y. Bao, R. Tang, Selection and corrosion evaluation tests of candidate SCWR fuel cladding materials, Nucl. Eng. Des. 249 (2012) 180–187.

[8] H. Abe, S.M. Hong, Y. Watanabe, Oxidation behavior of austenitic stainless steels as fuel cladding candidate materials for SCWR in superheated steam, Nucl. Eng. Des. 280 (2014) 652–660.

[9] L. ZHANG, Z. SHEN, R. TANG, Q. ZHANG, SCC susceptibility of candidate cladding materials for SCWR, in: 7th Int. Symp. Supercrit. Water-Cooled React., Helsinki, Finland, n.d.: pp. 306–317.

[10] T.R. Allen, Y. Chen, X. Ren, K. Sridharan, L. Tan, G.S. Was, et al., Comprehensive Nuclear Materials, Elsevier, 2012.

[11] T.R. Allen, Y. Chen, L. Tan, X. Ren, K. Sridharan, Corrosion of Candidate Materials for Supercritical Water-Cooled Reactors, in: 12th Int. Conf. Environ. Degrad. ofMaterials Nucl. Power Syst., 2005: pp. 1397–1407.

[12] L. Zhang, F. Zhu, R. Tang, Corrosion mechanisms of candidate structural materials for supercritical water-cooled reactor, Front. Energy Power Eng. China. 3 (2009) 233–240.

[13] M. Sun, X. Wu, Z. Zhang, E. Han, Oxidation of 316 stainless steel in supercritical water, Corros. Sci. 51 (2009) 1069–1072.

[14] C. Sun, R. Hui, W. Qu, S. Yick, Progress in corrosion resistant materials for supercritical water reactors, Corros. Sci. 51 (2009) 2508–2523.

[15] S. Baindur, Materials challenges for the supercritical water-cooled reactor (SCWR), Bull. Can. Nucl. Soc. 29 (2008) 32–38.

[16] T. Allen, Y. Chen, X. Ren, K. Sridharan, L. Tan, Material performance in supercritical water, in: Compr. Nucl. Mater., Elsevier Inc., 2012: pp. 279–326.

[17] Comparison of Lifecycle Greenhouse Gas Emissions of Various Electricity Generation Sources, London, 2011.

[18] D. Weisser, W. Strasse, A guide to life-cycle greenhouse gas (GHG) emissions from electric supply technologies, 2007.

[19] P.J. Meier, Life-cycle assessment of electricity generation systems and applications for climate change policy analysis, University of Wisconsin - Madison, 2002.

[20] Externalities and Energy Policy: The Life Cycle Analysis Approach, in: Nucl. Dev., Nuclear Energy Agency, Paris, 2001: p. 240.

[21] A technology roadmap for generation IV nuclear energy systems, 2002.

[22] GIF Portal - Generation IV Systems, (n.d.).

[23] N.S. and E.R.C. of C.C.D. Government of Canada, NSERC - Canada's National Program on Generation IV Energy Technologies – Research and Development Priorities for 2012–16, (2009).

[24] T. Schulenberg, L.K.H. Leung, D. Brady, Y. Oka, K. Yamada, Y. Bae, et al., Supercritical water-cooled reactor (SCWR) development through GIF collaboration, 2009.

[25] M. Yetisir, M. Gaudet, D. Rhodes, Development and integration of Canadian SCWR concept with counter-flow fuel assembly, in: 6th Int. Symp. Supercrit. Water-Cooled React., Guangdong, 2013.

[26] N.A. Dollezhal, I.Y. Emel'yanov, P.I. Aleshchenkov, Development of superheating power reactors of beloyarsk nuclear power station type, in: Third Int. Conf. Peac. Uses At. Energy, Geneva, 1964: pp. 256–265.

[27] J.H. Wright, J.F. Patterson, Status and application of supercritical-water reactor coolant, in: Am. Power Conf., 1966: pp. 139–149.

[28] Y. Oka, S.I. Koshizuka, Concept and design of a supercritical-pressure, direct-cycle light water reactor, Nucl. Technol. 103 (1993) 295–302.

[29] T. Schulenberg, J. Starflinger, European research project on the high performance light water reactor, in: 4th Int. Symp. Supercrit. Water-Cooled React., Heidelberg, 2009.

[30] L. Heikenhiemo, D. Guzonas, C. Fazio, GEN IV Materials and Chemistry Research – Common Issues with the SCWR Concept, in: 5th Int. Symp. Supercrit. Water-Cooled React., Heidelberg, 2009.

[31] C.R.F. Azevedo, Selection of fuel cladding material for nuclear fission reactors, Eng. Fail. Anal. 18 (2011) 1943–1962.

[32] W.D. Callister, D.G. Rethwisch, Materials Science and Engineering: An Introduction, 9th ed., John Wiley & Sons, Inc, 2013.

[33] Y. Chen, K. Sridharan, T.R. Allen, Corrosion of Candidate Austenitic Stainless Steels for Supercritical Water Reactors, Corros. 2007. (2007).

[34] X. Ren, K. Sridharan, T.R. Allen, Corrosion of ferritic–martensitic steel HT9 in supercritical water, J. Nucl. Mater. 358 (2006) 227–234.

[35] J.R. Davis, ASM International, Stainless steels, ASM International, 1994.

[36] K.H. Lo, C.H. Shek, J.K.L. Lai, Recent developments in stainless steels, Mater. Sci. Eng. R Reports. 65 (2009) 39–104.

[37] B.L. Adams, S.I. Wright, K. Kunze, Orientation imaging: The emergence of a new microscopy, Metall. Trans. A. 24 (1993) 819–831.

[38] S.I. Wright, B.L. Adams, K. Kunze, Application of a new automatic lattice orientation

measurement technique to polycrystalline aluminum, Mater. Sci. Eng. A. 160 (1993) 229–240.

[39] A.J. Schwartz, M. Kumar, B.L. Adams, D.P. Field, eds., Electron Backscatter Diffraction in Materials Science, Second, Springer US, 2009.

[40] C. Sun, R. Hui, W. Qu, S. Yick, Progress in corrosion resistant materials for supercritical water reactors, Corros. Sci. 51 (2009) 2508–2523.

[41] P. Kritzer, Corrosion in high-temperature and supercritical water and aqueous solutions: a review, J. Supercrit. Fluids. 29 (2004) 1–29.

[42] T.R. Allen, F. Balbaud-Celerier, T. Asayama, M. Pouchon, J.T. Busby, S. Maloy, et al., Status Report on Structural Materialsfor Advanced Nuclear Systems, 2013.

[43] X. Luo, R. Tang, C. Long, Z. Miao, Q. Peng, C. Li, Corrosion behavior of austenitic and ferritic steels in supercritical water, Nucl. Eng. Technol. 40 (2007) 147–154.

[44] M. Nezakat, H. Akhiani, S. Penttilä, M. Sabet, J. Szpunar, Effect of thermo-mechanical processing on oxidation of austenitic stainless steel 316L in supercritical water, Corros. Sci. 94 (2015) 197–206.

[45] T.M. Hayward, I.M. Svishchev, R.C. Makhija, Stainless steel flow reactor for supercritical water oxidation: corrosion tests, J. Supercrit. Fluids. 27 (2003) 275–281.

[46] M. Sekine, N. Sakaguchi, M. Endo, H. Kinoshita, S. Watanabe, H. Kokawa, et al., Grain boundary engineering of austenitic steel PNC316 for use in nuclear reactors, J. Nucl. Mater. 414 (2011) 232–236.

[47] M. Fulger, M. Mihalache, D. Ohai, S. Fulger, S.C. Valeca, Analyses of oxide films grown on AISI 304L stainless steel and Incoloy 800HT exposed to supercritical water environment, J. Nucl. Mater. 415 (2011) 147–157.

[48] I. Betova, M. Bojinov, P. Kinnunen, S. Penttilä, T. Saario, Surface film electrochemistry of austenitic stainless steel and its main constituents in supercritical water, J. Supercrit. Fluids. 43 (2007) 333–340.

[49] D. Gómez-Briceño, F. Blázquez, a. Sáez-Maderuelo, Oxidation of austenitic and ferritic/martensitic alloys in supercritical water, J. Supercrit. Fluids. 78 (2013) 103–113.

[50] L. Tan, T.R. Allen, Y. Yang, Corrosion behavior of alloy 800H (Fe–21Cr–32Ni) in supercritical water, Corros. Sci. 53 (2011) 703–711.

[51] X. Gao, X. Wu, Z. Zhang, H. Guan, E. Han, Characterization of oxide films grown on 316L stainless steel exposed to H2O2-containing supercritical water, J. Supercrit. Fluids. 42 (2007) 157–163.

[52] E. Asselin, A. Alfantazi, S. Rogak, Corrosion of nickel–chromium alloys, stainless steel and niobium at supercritical water oxidation conditions, Corros. Sci. 52 (2010) 118–124.

[53] G.S. Was, P. Ampornrat, G. Gupta, S. Teysseyre, E.A. West, T.R. Allen, et al., Corrosion and stress corrosion cracking in supercritical water, J. Nucl. Mater. 371 (2007) 176–201.

[54] J. Kaneda, S. Kasahara, F. Kano, N. Saito, T. Shikama, H. Matsui, Material Development for Supercritical Water-cooled Reactor, in: 5th Int. Sym. SCWR, Canadian Nuclear Society, Vancouver, 2011.

[55] N. Birks, G. H.Meier, F.S. Pettit, High-Temprature Oxidation of Metals, 2nd ed., Cambridge University Press, 2006.

[56] D. Young, High Temperature Oxidation and Corrosion of Metals, 1st ed., Elsevier Ltd, Oxford, 2008.

[57] R. Guillamet, J. Lopitaux, B. Hannoyer, M. Lenglet, Oxidation of stainless steels (AISI 304 and 316) at high temperature. Influence on the metallic substratum, Le J. Phys. IV. 03 (1993) 349–356.

[58] R. Peraldi, B. Pint, Effect of Cr and Ni contents on the oxidation behavior of ferritic and austenitic model alloys in air with water vapor, Oxid. Met. 61 (2004) 463–483.

[59] H. Akhiani, M. Nezakat, S. Penttilä, J. Szpunar, The oxidation resistance of thermo-mechanically processed Incoloy 800HT in supercritical water, J. Supercrit. Fluids. 101 (2015) 150–160.

[60] S. Mahboubi, G.A. Button, J. Kish, Oxide scales formed on austinitic Fe-Cr-Ni alloys exposed to supercritical water: role of alloying elements, in: 19th Pacific Basin Nucl. Conf., Canadian Nuclear Society, Vancouver, 2014.

[61] H. Akhiani, M. Nezakat, S. Penttila, J.A. Szpunar, H.Akhiani, M. Nezakat, et al., The effect of thermo-mechanical processing on the oxidation behaviour of Incoloy 800H/HT in Supercritical water, J. Supercrit. Fluids. 101 (2015) 150–160.

[62] M. McGuire, Stainless steels for design engineers, ASM International, 2008.

[63] J. Beddoes, J.G. Parr, Introduction to Stainless Steels, ASM International, 1999.

[64] H. Hu, Texture of Metals, Texture. 1 (1974) 233–258.

[65] H.-R. Wenk, P. Van Houtte, Texture and anisotropy, Reports Prog. Phys. 67 (2004) 1367–1428.

[66] S.G.S. Chowdhury, R. Singh, The influence of recrystallized structure and texture on the sensitization behaviour of a stable austenitic stainless steel (AISI 316L), Scr. Mater. 58 (2008) 1102–1105.

[67] J. Venables, The electron microscopy of deformation twinning, J. Phys. Chem. Solids. 25 (1964) 685–692.

[68] J. Christian, S. Mahajan, Deformation twinning, Prog. Mater. Sci. 39 (1995) 1–157.

[69] C. Donadille, R. Valle, P. Dervin, R. Penelle, Development of texture and microstructure during cold-rolling and annealing of FCC alloys: Example of an austenitic stainless steel, Acta Metall. 37 (1989) 1547–1571.

[70] H. Akhiani, M. Nezakat, J.A. Szpunar, Evolution of deformation and annealing textures in Incoloy 800H/HT via different rolling paths and strains, Mater. Sci. Eng. A. 614 (2014) 250–263.

[71] P. Adler, G. Olson, W. Owen, Strain hardening of Hadfield manganese steel, Metall. Mater. Trans. …. 17 (1986).

[72] I. Tamura, Deformation-induced martensitic transformation and transformation-induced plasticity in steels, Met. Sci. 16 (1982) 245–253.

[73] M. Botshekan, S. Degallaix, Y. Desplanques, Influence of martensitic transformation on

the low-cycle fatigue behaviour of 316LN stainless steel at 77 K, Mater. Sci. …. 234-236 (1997) 463–466.

[74] D. Ye, S. Matsuoka, N. Nagashima, N. Suzuki, The low-cycle fatigue, deformation and final fracture behaviour of an austenitic stainless steel, Mater. Sci. Eng. A. 415 (2006) 104–117.

[75] B.R. Kumar, a. K. Singh, B. Mahato, P.K. De, N.R. Bandyopadhyay, D.K. Bhattacharya, Deformation-induced transformation textures in metastable austenitic stainless steel, Mater. Sci. Eng. A. 429 (2006) 205–211.

[76] I. Shakhova, V. Dudko, a. Belyakov, K. Tsuzaki, R. Kaibyshev, Effect of large strain cold rolling and subsequent annealing on microstructure and mechanical properties of an austenitic stainless steel, Mater. Sci. Eng. A. 545 (2012) 176–186.

[77] N. Solomon, I. Solomon, Deformation induced martensite in AISI 316 stainless steel, Rev. Metal. 46 (2010) 121–128.

[78] S. Vercammen, B. Blanpain, B.C. De Cooman, P. Wollants, Cold rolling behaviour of an austenitic Fe–30Mn–3Al–3Si TWIP-steel: the importance of deformation twinning, Acta Mater. 52 (2004) 2005–2012.

[79] S.G. Chowdhury, S. Das, B. Ravikumar, S. Kumar, G. Gottstein, Textural Development in AISI 316 Stainless Steel during Cold Rolling and Annealing, Mater. Sci. Forum. 408-412 (2002) 1371–1376.

[80] S.G. Chowdhury, S. Das, P.K. De, Cold rolling behaviour and textural evolution in AISI 316L austenitic stainless steel, Acta Mater. 53 (2005) 3951–3959.

[81] B. Kumar, B. Mahato, Influence of strain-induced phase transformation on the surface crystallographic texture in cold-rolled-and-aged austenitic stainless steel, … Mater. Trans. A. 36 (2005) 3165–3174.

[82] M. Eskandari, a. Kermanpur, a. Najafizadeh, Formation of Nanocrystalline Structure in 301 Stainless Steel Produced by Martensite Treatment, Metall. Mater. Trans. A. 40 (2009) 2241–2249.

[83] B. Ravi Kumar, B. Mahato, N.R. Bandyopadhyay, D.K. Bhattacharya, Comparison of rolling texture in low and medium stacking fault energy austenitic stainless steels, Mater. Sci. Eng. A. 394 (2005) 296–301.

[84] A. Kurc-Lisiecka, Forming of the texture, structure and mechanical properties of cold-rolled AISI 304 steel, Bulletin.is.gliwice.pl. (2013) 23–29.

[85] M. Eskandari, a. Najafizadeh, a. Kermanpur, Effect of strain-induced martensite on the formation of nanocrystalline 316L stainless steel after cold rolling and annealing, Mater. Sci. Eng. A. 519 (2009) 46–50.

[86] A. Rollett, F.. Humphreys, G. Rohrer, M. Hatherly, Recrystallization and related annealing phenomena, Pergamon, 2004.

[87] J. Jonas, H. McQueen, W. Wong, Deformation under hot working conditions, Iron Steel Inst. Publ. (1968) 103.

[88] J. Buongiorno, P. MacDonald, Supercritical water reactor (SCWR), 2003.

[89] S. Penttilä, A. Toivonen, L. Rissanen, L. Heikinheimo, Generation IV Material Issues -

Case SCWR, J. Disaster Res. 5 (2010) 469–478.

[90] K.L. Murty, I. Charit, Structural materials for Gen-IV nuclear reactors: Challenges and opportunities, J. Nucl. Mater. 383 (2008) 189–195.

[91] X. Ru, R.W. Staehle, Predicting corrosion and stress corrosion cracking of Fe-Cr-Ni alloys in supercritical water based on historical experience, in: Tech. Meet. Mater. Chem. Supercrit. Water Cool. React., Netherlands, n.d.: pp. 1–87.

[92] S. Penttilä, A. Toivonen, J. Li, Effect of surface modification on the corrosion resistance of austenitic stainless steel 316L in supercritical water conditions, … J. Supercrit. …. 81 (2013) 157–163.

[93] I.M. Svishchev, R.A. Carvajal-Ortiz, K.I. Choudhry, D.A. Guzonas, Corrosion behavior of stainless steel 316 in sub- and supercritical aqueous environments: Effect of LiOH additions, Corros. Sci. 72 (2013) 20–25.

[94] L. Tan, X. Ren, K. Sridharan, T.R. Allen, Corrosion behavior of Ni-base alloys for advanced high temperature water-cooled nuclear plants, Corros. Sci. 50 (2008) 3056–3062.

[95] K.-H. Chang, S.-M. Chen, T.-K. Yeh, J.-J. Kai, Effect of dissolved oxygen content on the oxide structure of Alloy 625 in supercritical water environments at 700ºC, Corros. Sci. 81 (2014) 21–26.

[96] D.B. Mitton, J.-H. Yoon, J. a. Cline, H.-S. Kim, N. Eliaz, R.M. Latanision, Corrosion Behavior of Nickel-Based Alloys in Supercritical Water Oxidation Systems, Ind. Eng. Chem. Res. 39 (2000) 4689–4696.

[97] Q. Zhang, R. Tang, C. Li, X. Luo, Corrosion behavior of Ni-base alloys in supercritical water, Nucl. Eng. …. 41 (2009) 107–112.

[98] P. Xu, L.Y. Zhao, K. Sridharan, T.R. Allen, Oxidation behavior of grain boundary engineered alloy 690 in supercritical water environment, J. Nucl. Mater. 422 (2012) 143–151.

[99] Q. Zhang, R. Tang, K. Yin, X. Luo, L. Zhang, Corrosion behavior of Hastelloy C-276 in supercritical water, Corros. Sci. 51 (2009) 2092–2097.

[100] X. Zhong, E.-H. Han, X. Wu, Corrosion behavior of Alloy 690 in aerated supercritical water, Corros. Sci. 66 (2013) 369–379.

[101] L. Tan, X. Ren, K. Sridharan, T.R. Allen, Effect of shot-peening on the oxidation of alloy 800H exposed to supercritical water and cyclic oxidation, Corros. Sci. 50 (2008) 2040–2046.

[102] R. Klueh, Elevated temperature ferritic and martensitic steels and their application to future nuclear reactors, 2005.

[103] X. Zhong, X. Wu, E.-H. Han, Effects of exposure temperature and time on corrosion behavior of a ferritic–martensitic steel P92 in aerated supercritical water, Corros. Sci. 90 (2015) 511–521.

[104] Y. Chen, K. Sridharan, T. Allen, Corrosion behavior of ferritic–martensitic steel T91 in supercritical water, Corros. Sci. 48 (2006) 2843–2854.

[105] N. Zhang, H. Xu, B. Li, Y. Bai, D. Liu, Influence of the dissolved oxygen content on corrosion of the ferritic–martensitic steel P92 in supercritical water, Corros. Sci. 56 (2012)

123–128.

[106] M.P. Phaniraj, D.-I. Kim, Y.W. Cho, Effect of grain boundary characteristics on the oxidation behavior of ferritic stainless steel, Corros. Sci. 53 (2011) 4124–4130.

[107] L. Tan, X. Ren, T.R. Allen, Corrosion behavior of 9–12% Cr ferritic–martensitic steels in supercritical water, Corros. Sci. 52 (2010) 1520–1528.

[108] M. Inoue, T. Kaito, S. Ohtsuka, Research and development of oxide dispersion strengthened ferritic steels for sodium cooled fast breeder reactor fuels, Mater. Issues Gener. IV Syst. (2008) 311–325.

[109] H. Je, A. Kimura, Stress corrosion cracking susceptibility of oxide dispersion strengthened ferritic steel in supercritical pressurized water dissolved with different hydrogen and oxygen contents, Corros. Sci. 78 (2014) 193–199.

[110] H. Hu, Z. Zhou, M. Li, L. Zhang, M. Wang, S. Li, et al., Study of the corrosion behavior of a 18Cr-oxide dispersion strengthened steel in supercritical water, Corros. Sci. 65 (2012) 209–213.

[111] J. Isselin, R. Kasada, A. Kimura, Corrosion behaviour of 16%Cr–4%Al and 16%Cr ODS ferritic steels under different metallurgical conditions in a supercritical water environment, Corros. Sci. 52 (2010) 3266–3270.

[112] L. Tan, K. Sridharan, T.R. Allen, Altering Corrosion Response via Grain Boundary Engineering, Mater. Sci. Forum. 595-598 (2008) 409–418.

[113] X. Peng, J. Yan, Y. Zhou, F. Wang, Effect of grain refinement on the resistance of 304 stainless steel to breakaway oxidation in wet air, Acta Mater. 53 (2005) 5079–5088.

[114] X. Ren, K. Sridharan, T.R. Allen, Effect of grain refinement on corrosion of ferritic-martensitic steels in supercritical water environment, Mater. Corros. 61 (2010) 748–755.

[115] M. Nezakat, H. Akhiani, M. Hoseini, J. Szpunar, Effect of thermo-mechanical processing on texture evolution in austenitic stainless steel 316L, Mater. Charact. 98 (2014) 10–17.

[116] S. Al-Shahrani, T.J. Marrow, Effect of Surface Finish on Fatigue of Stainless Steels, in: 12th Int. Conf. Fract., Ottawa, 2009.

[117] S. Uran, B. Veal, M. Grimsditch, J. Pearson, A. Berger, Effect of Surface Roughness on Oxidation: Changes in Scale Thickness, Composition, and Residual Stress, Oxid. Met. 54 (2000) 73–85.

[118] P. Shewmon, Diffusion in solids, 1990.

[119] G.E. Totten, M.A.H. Howes, Steel Heat Treatment Handbook, Marcel Dekker, Inc., New York, 1997.

[120] L. Tan, Y. Yang, T.R. Allen, Oxidation behavior of iron-based alloy HCM12A exposed in supercritical water, Corros. Sci. 48 (2006) 3123–3138.

[121] T. Allen, G. Was, Grain boundary engineering and radiation resistance of GFR candidate metallic materials, 2006.

[122] H. Akhiani, M. Nezakat, S. Penttilä, J. Szpunar, The oxidation resistance of thermo-mechanically processed Incoloy 800HT in supercritical water, J. Supercrit. Fluids. 101 (2015) 150–160.

[123] J. Pelleg, L.Z. Zevin, S. Lungo, N. Croitoru, Reactive-sputter-deposited TiN films on glass substrates, Thin Solid Films. 197 (1991) 117–128.

[124] U.C. Oh, J.H. Je, Effects of strain energy on the preferred orientation of TiN thin films, J. Appl. Phys. 74 (1993) 1692.

[125] L. Hultman, Low-energy (~100 eV) ion irradiation during growth of TiN deposited by reactive magnetron sputtering: Effects of ion flux on film microstructure, J. Vac. Sci. Technol. A Vacuum, Surfaces, Film. 9 (1991) 434.

[126] P.R. Seré, J.D. Culcasi, C.I. Elsner, A.R. Di Sarli, Relationship between texture and corrosion resistance in hot-dip galvanized steel sheets, Surf. Coatings Technol. 122 (1999) 143–149.

[127] S. Suwas, N. Gurao, Crystallographic texture in Materials, J. Indian Inst. Sci. 88 (2012) 151–177.

[128] M. Hatherly, W.B. Hutchinson, An introduction to textures in metals, Institution of Metallurgists, 1979.

[129] J. Hirsch, K. Lücke, Mechanism of deformation and development of rolling textures in polycrystalline f.c.c. metals—II. Simulation and interpretation of experiments on the basis of Taylor-type theories, Acta Metall. (1988).

[130] J. Hirsch, K. Lücke, M. Hatherly, Mechanism of deformation and development of rolling textures in polycrystalline fcc Metals—III. The influence of slip inhomogeneities and twinning, Acta Metall. 36 (1988) 2905–2927.

[131] M.P. Groover, Introduction to Manufacturing Processes, Wiley, 2011.

[132] M.P. Groover, Fundamentals of Modern Manufacturing: Materials, Processes, and Systems, 5th ed., Wiley, 2012.

[133] G.E. Dieter, Mechanical metallurgy, McGraw-Hill, New York, 1976.

[134] N.P. Gurao, S. Sethuraman, S. Suwas, Effect of strain path change on the evolution of texture and microstructure during rolling of copper and nickel, Mater. Sci. Eng. A. 528 (2011) 7739–7750.

[135] R. Garg, N. Gurao, Evolution of texture and grain boundary microstructure in two-phase (α+ β) brass during recrystallization, Philos. Mag. 91 (2011) 4089–4108.

[136] H. Akhiani, M. Nezakat, A. Sonboli, J. Szpunar, The origin of annealing texture in a cold-rolled Incoloy 800H/HT after different strain paths, Mater. Sci. Eng. A. 619 (2014) 334–344.

[137] H. Akhiani, M. Nezakat, M. Sanayei, J. Szpunar, The effect of thermo-mechanical processing on grain boundary character distribution in Incoloy 800H/HT, Mater. Sci. Eng. A. 626 (2015) 51–60.

[138] H. Akhiani, M. Nezakat, A. Sonboli, J. Szpunar, The origin of annealing texture in a cold-rolled Incoloy 800H/HT after different strain paths, Mater. Sci. Eng. A. 619 (2014) 334–344.

[139] M.R. Toroghinejad, F. Ashrafizadeh, A. Najafizadeh, A.O. Humphreys, D. Liu, J.J. Jonas, Effect of rolling temperature on the deformation and recrystallization textures of warm-rolled steels, Metall. Mater. Trans. A. 34 (2003) 1163–1174.

[140] H.P. Yang, F. Zhang, Y.H. Sha, X. Zhu, L. Zuo, Effects of Rolling Temperature on Through-Thickness Deformation and Recrystallization Textures in Heavily Rolled Silicon Steel, in: Adv. Mater. Res., 2013: pp. 1729–1733.

[141] R. Abbaschian, R.E. Reed-Hill, Physical Metallurgy Principles, 4th ed., Cengage Learning, 2009.

[142] H.F.G. de Abreu, S.S. de Carvalho, P. de Lima Neto, R.P. dos Santos, V.N. Freire, P.M. de O. Silva, et al., Deformation induced martensite in an AISI 301LN stainless steel: characterization and influence on pitting corrosion resistance, Mater. Res. 10 (2007) 359–366.

[143] V. Tsakiris, D.V. Edmonds, Martensite and deformation twinning in austenitic steels, Mater. Sci. Eng. A. 273-275 (1999) 430–436.

[144] B. Ravi Kumar, R. Singh, B. Mahato, P.K. De, N.R. Bandyopadhyay, D.K. Bhattacharya, Effect of texture on corrosion behavior of AISI 304L stainless steel, Mater. Charact. 54 (2005) 141–147.

[145] D.F. Torgerson, B.A. Shalaby, S. Pang, CANDU technology for Generation III+ and IV reactors, Nucl. Eng. Des. 236 (2006) 1565–1572.

[146] R.B. Duffey, CANDU and Generation IV System, in: 14th Pacific Basin Nucl. Conf., Honolulu, USA, 2004: pp. 273–277.

[147] R. Duffey, I. Pioro, Supercritical water-cooled nuclear reactors: review and status, in: Nucl. Mater. React., 2005.

[148] M. Yetisir, W. Diamond, L.K.H. Leung, D. Martin, R. Duffey, Conceptual mechanical design for a pressure-tube type supercritical water-cooled reactor, in: 5th Int. Sym. SCWR, 2011.

[149] G.S. Was, S. Teysseyre, Challenges and recent progress in corrosion and stress corrosion cracking of alloys for supercritical water reactor core components, in: T.R. Allen, P.J. King, L. Nelson (Eds.), 12th Environ. Degrad. Conf. Mater. Nucl. Power Syst. - Water React., Warrendale, USA, n.d.: pp. 1343–1357.

[150] Y. Jiao, J. Kish, W. Zheng, D. Guzonas, Intergranular Corrosion Resistance of Thermally-Treated Type 310S Stainless Steel, in: 7th Int. Symp. Supercrit. Water-Cooled React., Helsinki, Finland, n.d.: pp. 331–345.

[151] D. Guzonas, R. Novotny, Supercritical water-cooled reactor materials – Summary of research and open issues, Prog. Nucl. Energy. 77 (2014) 361–372.

[152] M. Nezakat, H. Akhiani, S. Penttilä, J. Szpunar, Oxidation behavior of austenitic stainless steel 316L and 310S in air and supercritical water, J. Nucl. Eng. Radiat. Sci. (2015).

[153] L. Tan, T.R. Allen, J.T. Busby, Grain boundary engineering for structure materials of nuclear reactors, J. Nucl. Mater. 441 (2013) 661–666.

[154] L. Tan, K. Sridharan, T.R. Allen, The effect of grain boundary engineering on the oxidation behavior of INCOLOY alloy 800H in supercritical water, J. Nucl. Mater. 348 (2006) 263–271.

[155] H. Akhiani, M. Nezakat, J.A. Szpunar, Grain Boundary Engineering in Incoloy 800H / HT via Thermo-Mechanical Processing, (2014).

[156] M. Halvarsson, J.E. Tang, H. Asteman, J.-E. Svensson, L.-G. Johansson, Microstructural investigation of the breakdown of the protective oxide scale on a 304 steel in the presence of oxygen and water vapour at 600ºC, Corros. Sci. 48 (2006) 2014–2035.

[157] M. Nezakat, H. Akhiani, S. Penttilä, S.M. Sabet, J. Szpunar, Characterization of the oxide film on stainless steel 316L exposed to supercritical water environment, Corros. Sci. (2015).

APPENDIX

A.1. COPYRIGHT PERMISSION FOR CHAPTER 4

Dear Mr. Nezakat:

It is our pleasure to grant you permission **to use all or any part of** the ASME paper "Oxidation Behavior of Austenitic Stainless Steel 316L and 310S in Air and Supercritical Water," by Majid Nezakat; Hamed Akhiani; Sami Penttilä; Jerzy Szpunar, ASME J of Nuclear Rad Sci. 2016; 2(2), cited in your letter for inclusion in a PHD Thesis as one chapter entitled AUSTENITIC STAINLESS STEELS FOR FUTURE NUCLEAR FUEL CLADDINGS to be published by University of Saskatchewan

Permission is granted for the specific use as stated herein and does not permit further use of the materials without proper authorization. Proper attribution must be made to the author(s) of the materials. **Please note**: if any or all of the figures and/or Tables are of another source, permission should be granted from that outside source or include the reference of the original source. ASME does not grant permission for outside source material that may be referenced in the ASME works.

As is customary, we request that you ensure full acknowledgment of this material, the author(s), source and ASME as original publisher. Acknowledgment must be retained on all pages printed and distributed.

Many thanks for your interest in ASME publications.

Sincerely,

Beth Darchi
Publishing Administrator
ASME
2 Park Avenue, 6th Floor
New York, NY 10016-5990
Tel 1.212.591.7700
darchib@asme.org

A.2. COPYRIGHT PERMISSION FOR CHAPTER 5

ELSEVIER LICENSE

TERMS AND CONDITIONS

Oct 13, 2015

This is a License Agreement between Majid Nezakat ("You") and Elsevier ("Elsevier") provided by Copyright Clearance Center ("CCC"). The license consists of your order details, the terms and conditions provided by Elsevier, and the payment terms and conditions.

All payments must be made in full to CCC. For payment instructions, please see information listed at the bottom of this form.

Supplier	Elsevier Limited The Boulevard,Langford Lane Kidlington,Oxford,OX5 1GB,UK
Registered Company Number	1982084
Customer name	Majid Nezakat
Customer address	University of Saskatchewan Saskatoon, SK S7N 5A9
License number	3726901119250
License date	Oct 13, 2015
Licensed content publisher	Elsevier
Licensed content publication	Materials Characterization

Licensed content title	Effect of thermo-mechanical processing on texture evolution in austenitic stainless steel 316L
Licensed content author	Majid Nezakat,Hamed Akhiani,Majid Hoseini,Jerzy Szpunar
Licensed content date	December 2014
Licensed content volume number	98
Licensed content issue number	n/a
Number of pages	8
Start Page	10
End Page	17
Type of Use	reuse in a thesis/dissertation
Intended publisher of new work	other
Portion	full article
Format	both print and electronic
Are you the author of this Elsevier article?	Yes
Will you be translating?	No
Title of your thesis/dissertation	AUSTENITIC STAINLESS STEELS FOR FUTURE NUCLEAR FUEL CLADDINGS
Expected completion date	Dec 2015
Estimated size (number of pages)	200

Elsevier VAT number	GB 494 6272 12
Permissions price	0.00 CAD
VAT/Local Sales Tax	0.00 CAD / 0.00 GBP
Total	0.00 CAD

Terms and Conditions

INTRODUCTION

1. The publisher for this copyrighted material is Elsevier. By clicking "accept" in connection with completing this licensing transaction, you agree that the following terms and conditions apply to this transaction (along with the Billing and Payment terms and conditions established by Copyright Clearance Center, Inc. ("CCC"), at the time that you opened your Rightslink account and that are available at any time athttp://myaccount.copyright.com).

GENERAL TERMS

2. Elsevier hereby grants you permission to reproduce the aforementioned material subject to the terms and conditions indicated.

3. Acknowledgement: If any part of the material to be used (for example, figures) has appeared in our publication with credit or acknowledgement to another source, permission must also be sought from that source. If such permission is not obtained then that material may not be included in your publication/copies. Suitable acknowledgement to the source must be made, either as a footnote or in a reference list at the end of your publication, as follows:

"Reprinted from Publication title, Vol /edition number, Author(s), Title of article / title of chapter, Pages No., Copyright (Year), with permission from Elsevier [OR APPLICABLE SOCIETY COPYRIGHT OWNER]." Also Lancet special credit - "Reprinted from The Lancet, Vol. number, Author(s), Title of article, Pages No., Copyright (Year), with permission from Elsevier."

4. Reproduction of this material is confined to the purpose and/or media for which permission is hereby given.

5. Altering/Modifying Material: Not Permitted. However figures and illustrations may be altered/adapted minimally to serve your work. Any other abbreviations, additions, deletions and/or any other alterations shall be made only with prior written authorization of Elsevier Ltd. (Please contact Elsevier at permissions@elsevier.com)

6. If the permission fee for the requested use of our material is waived in this instance, please be advised that your future requests for Elsevier materials may attract a fee.

7. Reservation of Rights: Publisher reserves all rights not specifically granted in the combination of (i) the license details provided by you and accepted in the course of this licensing transaction, (ii) these terms and conditions and (iii) CCC's Billing and Payment terms and conditions.

8. License Contingent Upon Payment: While you may exercise the rights licensed immediately upon issuance of the license at the end of the licensing process for the transaction, provided that you have disclosed complete and accurate details of your proposed use, no license is finally effective unless and until full payment is received from you (either by publisher or by CCC) as provided in CCC's Billing and Payment terms and conditions. If full payment is not received on a timely basis, then any license preliminarily granted shall be deemed automatically revoked and shall be void as if never granted. Further, in the event that you breach any of these terms and conditions or any of CCC's Billing and Payment terms and conditions, the license is automatically revoked and shall be void as if never granted. Use of materials as described in a revoked license, as well as any use of the materials beyond the scope of an unrevoked license, may constitute copyright infringement and publisher reserves the right to take any and all action to protect its copyright in the materials.

9. Warranties: Publisher makes no representations or warranties with respect to the licensed material.

10. Indemnity: You hereby indemnify and agree to hold harmless publisher and CCC, and their respective officers, directors, employees and agents, from and against any and all claims arising out of your use of the licensed material other than as specifically authorized pursuant to this license.

11. No Transfer of License: This license is personal to you and may not be sublicensed, assigned, or transferred by you to any other person without publisher's written permission.

12. No Amendment Except in Writing: This license may not be amended except in a writing signed by both parties (or, in the case of publisher, by CCC on publisher's behalf).

13. Objection to Contrary Terms: Publisher hereby objects to any terms contained in any purchase order, acknowledgment, check endorsement or other writing prepared by you, which terms are inconsistent with these terms and conditions or CCC's Billing and Payment terms and conditions. These terms and conditions, together with CCC's Billing and Payment terms and conditions (which are incorporated herein), comprise the entire agreement between you and publisher (and CCC) concerning this licensing transaction. In the event of any conflict between your obligations established by these terms and conditions and those established by CCC's Billing and Payment terms and conditions, these terms and conditions shall control.

14. Revocation: Elsevier or Copyright Clearance Center may deny the permissions described in this License at their sole discretion, for any reason or no reason, with a full refund payable to you. Notice of such denial will be made using the contact information provided by you. Failure to receive such notice will not alter or invalidate the denial. In no event will Elsevier or Copyright Clearance Center be responsible or liable for any costs, expenses or damage incurred by you as a result of a denial of your permission request, other than a refund of the amount(s) paid by you to Elsevier and/or Copyright Clearance Center for denied permissions.

LIMITED LICENSE

The following terms and conditions apply only to specific license types:

15. **Translation**: This permission is granted for non-exclusive world **English** rights only unless your license was granted for translation rights. If you licensed translation rights you may only translate this content into the languages you requested. A professional translator must perform all translations and reproduce the content word for word preserving the integrity of the article.

16. **Posting licensed content on any Website**: The following terms and conditions apply as follows: Licensing material from an Elsevier journal: All content posted to the web

site must maintain the copyright information line on the bottom of each image; A hyper-text must be included to the Homepage of the journal from which you are licensing athttp://www.sciencedirect.com/science/journal/xxxxx or the Elsevier homepage for books athttp://www.elsevier.com; Central Storage: This license does not include permission for a scanned version of the material to be stored in a central repository such as that provided by Heron/XanEdu.

Licensing material from an Elsevier book: A hyper-text link must be included to the Elsevier homepage at http://www.elsevier.com . All content posted to the web site must maintain the copyright information line on the bottom of each image.

Posting licensed content on Electronic reserve: In addition to the above the following clauses are applicable: The web site must be password-protected and made available only to bona fide students registered on a relevant course. This permission is granted for 1 year only. You may obtain a new license for future website posting.

17. **For journal authors:** the following clauses are applicable in addition to the above:

Preprints:

A preprint is an author's own write-up of research results and analysis, it has not been peer-reviewed, nor has it had any other value added to it by a publisher (such as formatting, copyright, technical enhancement etc.).

Authors can share their preprints anywhere at any time. Preprints should not be added to or enhanced in any way in order to appear more like, or to substitute for, the final versions of articles however authors can update their preprints on arXiv or RePEc with their Accepted Author Manuscript (see below).

If accepted for publication, we encourage authors to link from the preprint to their formal publication via its DOI. Millions of researchers have access to the formal publications on ScienceDirect, and so links will help users to find, access, cite and use the best available version. Please note that Cell Press, The Lancet and some society-owned have different preprint policies. Information on these policies is available on the journal homepage.

Accepted Author Manuscripts: An accepted author manuscript is the manuscript of an article that has been accepted for publication and which typically includes author-incorporated changes suggested during submission, peer review and editor-author communications.

Authors can share their accepted author manuscript:

- - immediately
    - via their non-commercial person homepage or blog
    - by updating a preprint in arXiv or RePEc with the accepted manuscript
    - via their research institute or institutional repository for internal institutional uses or as part of an invitation-only research collaboration work-group
    - directly by providing copies to their students or to research collaborators for their personal use
    - for private scholarly sharing as part of an invitation-only work group on commercial sites with which Elsevier has an agreement
- - after the embargo period
    - via non-commercial hosting platforms such as their institutional repository
    - via commercial sites with which Elsevier has an agreement

In all cases accepted manuscripts should:

- - link to the formal publication via its DOI
- - bear a CC-BY-NC-ND license - this is easy to do
- - if aggregated with other manuscripts, for example in a repository or other site, be shared in alignment with our hosting policy not be added to or enhanced in any way to appear more like, or to substitute for, the published journal article.

Published journal article (JPA): A published journal article (PJA) is the definitive final record of published research that appears or will appear in the journal and embodies all value-adding publishing activities including peer review co-ordination, copy-editing, formatting, (if relevant) pagination and online enrichment.

Policies for sharing publishing journal articles differ for subscription and gold open access articles:

Subscription Articles: If you are an author, please share a link to your article rather than the full-text. Millions of researchers have access to the formal publications on ScienceDirect, and so links will help your users to find, access, cite, and use the best available version.

Theses and dissertations which contain embedded PJAs as part of the formal submission can be posted publicly by the awarding institution with DOI links back to the formal publications on ScienceDirect.

If you are affiliated with a library that subscribes to ScienceDirect you have additional private sharing rights for others' research accessed under that agreement. This includes use for classroom teaching and internal training at the institution (including use in course packs and courseware programs), and inclusion of the article for grant funding purposes.

Gold Open Access Articles: May be shared according to the author-selected end-user license and should contain a CrossMark logo, the end user license, and a DOI link to the formal publication on ScienceDirect.

Please refer to Elsevier's posting policy for further information.

18. **For book authors** the following clauses are applicable in addition to the above: Authors are permitted to place a brief summary of their work online only. You are not allowed to download and post the published electronic version of your chapter, nor may you scan the printed edition to create an electronic version. **Posting to a repository:** Authors are permitted to post a summary of their chapter only in their institution's repository.

19. **Thesis/Dissertation**: If your license is for use in a thesis/dissertation your thesis may be submitted to your institution in either print or electronic form. Should your thesis be published commercially, please reapply for permission. These requirements include permission for the Library and Archives of Canada to supply single copies, on demand, of the complete thesis and include permission for Proquest/UMI to supply single copies, on demand, of the complete thesis. Should your thesis be published commercially, please reapply for permission. Theses and dissertations which contain embedded PJAs as part of the formal submission can be posted publicly by the awarding institution with DOI links back to the formal publications on ScienceDirect.

changes were made and the licensor is not represented as endorsing the use made of the work. Further, any new works must be made available on the same conditions. The full details of the license are available at http://creativecommons.org/licenses/by-nc-sa/4.0.

CC BY NC ND: The CC BY-NC-ND license allows users to copy and distribute the Article, provided this is not done for commercial purposes and further does not permit distribution of the Article if it is changed or edited in any way, and provided the user gives appropriate credit (with a link to the formal publication through the relevant DOI), provides a link to the license, and that the licensor is not represented as endorsing the use made of the work. The full details of the license are available at http://creativecommons.org/licenses/by-nc-nd/4.0. Any commercial reuse of Open Access articles published with a CC BY NC SA or CC BY NC ND license requires permission from Elsevier and will be subject to a fee.

Commercial reuse includes:

- - Associating advertising with the full text of the Article
- - Charging fees for document delivery or access
- - Article aggregation
- - Systematic distribution via e-mail lists or share buttons

Posting or linking by commercial companies for use by customers of those companies.

20. **Other Conditions**:

v1.8

Questions? customercare@copyright.com or +1-855-239-3415 (toll free in the US) or +1-978-646-2777.

A.3. COPYRIGHT PERMISSION FOR CHAPTER 6

ELSEVIER LICENSE

TERMS AND CONDITIONS

Oct 13, 2015

This is a License Agreement between Majid Nezakat ("You") and Elsevier ("Elsevier") provided by Copyright Clearance Center ("CCC"). The license consists of your order details, the terms and conditions provided by Elsevier, and the payment terms and conditions.

All payments must be made in full to CCC. For payment instructions, please see information listed at the bottom of this form.

Supplier	Elsevier Limited The Boulevard,Langford Lane Kidlington,Oxford,OX5 1GB,UK
Registered Company Number	1982084
Customer name	Majid Nezakat
Customer address	University of Saskatchewan Saskatoon, SK S7N 5A9
License number	3726900819818
License date	Oct 13, 2015
Licensed content publisher	Elsevier
Licensed content publication	Corrosion Science

Licensed content title	Effect of thermo-mechanical processing on oxidation of austenitic stainless steel 316L in supercritical water
Licensed content author	Majid Nezakat,Hamed Akhiani,Sami Penttilä,Seyed Morteza Sabet,Jerzy Szpunar
Licensed content date	May 2015
Licensed content volume number	94
Licensed content issue number	n/a
Number of pages	10
Start Page	197
End Page	206
Type of Use	reuse in a thesis/dissertation
Portion	full article
Format	both print and electronic
Are you the author of this Elsevier article?	Yes
Will you be translating?	No
Title of your thesis/dissertation	AUSTENITIC STAINLESS STEELS FOR FUTURE NUCLEAR FUEL CLADDINGS
Expected completion date	Dec 2015
Estimated size (number of pages)	200
Elsevier VAT number	GB 494 6272 12
Permissions price	0.00 CAD

VAT/Local Sales Tax	0.00 CAD / 0.00 GBP
Total	0.00 CAD

Terms and Conditions

INTRODUCTION

1. The publisher for this copyrighted material is Elsevier. By clicking "accept" in connection with completing this licensing transaction, you agree that the following terms and conditions apply to this transaction (along with the Billing and Payment terms and conditions established by Copyright Clearance Center, Inc. ("CCC"), at the time that you opened your Rightslink account and that are available at any time athttp://myaccount.copyright.com).

GENERAL TERMS

2. Elsevier hereby grants you permission to reproduce the aforementioned material subject to the terms and conditions indicated.

3. Acknowledgement: If any part of the material to be used (for example, figures) has appeared in our publication with credit or acknowledgement to another source, permission must also be sought from that source. If such permission is not obtained then that material may not be included in your publication/copies. Suitable acknowledgement to the source must be made, either as a footnote or in a reference list at the end of your publication, as follows:

"Reprinted from Publication title, Vol /edition number, Author(s), Title of article / title of chapter, Pages No., Copyright (Year), with permission from Elsevier [OR APPLICABLE SOCIETY COPYRIGHT OWNER]." Also Lancet special credit - "Reprinted from The Lancet, Vol. number, Author(s), Title of article, Pages No., Copyright (Year), with permission from Elsevier."

4. Reproduction of this material is confined to the purpose and/or media for which permission is hereby given.

5. Altering/Modifying Material: Not Permitted. However figures and illustrations may be altered/adapted minimally to serve your work. Any other abbreviations, additions, deletions and/or any other alterations shall be made only with prior written authorization of Elsevier Ltd. (Please contact Elsevier at permissions@elsevier.com)

6. If the permission fee for the requested use of our material is waived in this instance, please be advised that your future requests for Elsevier materials may attract a fee.

7. Reservation of Rights: Publisher reserves all rights not specifically granted in the combination of (i) the license details provided by you and accepted in the course of this licensing transaction, (ii) these terms and conditions and (iii) CCC's Billing and Payment terms and conditions.

8. License Contingent Upon Payment: While you may exercise the rights licensed immediately upon issuance of the license at the end of the licensing process for the transaction, provided that you have disclosed complete and accurate details of your proposed use, no license is finally effective unless and until full payment is received from you (either by publisher or by CCC) as provided in CCC's Billing and Payment terms and conditions. If full payment is not received on a timely basis, then any license preliminarily granted shall be deemed automatically revoked and shall be void as if never granted. Further, in the event that you breach any of these terms and conditions or any of CCC's Billing and Payment terms and conditions, the license is automatically revoked and shall be void as if never granted. Use of materials as described in a revoked license, as well as any use of the materials beyond the scope of an unrevoked license, may constitute copyright infringement and publisher reserves the right to take any and all action to protect its copyright in the materials.

9. Warranties: Publisher makes no representations or warranties with respect to the licensed material.

10. Indemnity: You hereby indemnify and agree to hold harmless publisher and CCC, and their respective officers, directors, employees and agents, from and against any and all claims arising out of your use of the licensed material other than as specifically authorized pursuant to this license.

11. No Transfer of License: This license is personal to you and may not be sublicensed, assigned, or transferred by you to any other person without publisher's written permission.

12. No Amendment Except in Writing: This license may not be amended except in a writing signed by both parties (or, in the case of publisher, by CCC on publisher's behalf).

13. Objection to Contrary Terms: Publisher hereby objects to any terms contained in any purchase order, acknowledgment, check endorsement or other writing prepared by you, which terms are inconsistent with these terms and conditions or CCC's Billing and Payment terms and conditions. These terms and conditions, together with CCC's Billing and Payment terms and conditions (which are incorporated herein), comprise the entire agreement between you and publisher (and CCC) concerning this licensing transaction. In the event of any conflict between your obligations established by these terms and conditions and those established by CCC's Billing and Payment terms and conditions, these terms and conditions shall control.

14. Revocation: Elsevier or Copyright Clearance Center may deny the permissions described in this License at their sole discretion, for any reason or no reason, with a full refund payable to you. Notice of such denial will be made using the contact information provided by you. Failure to receive such notice will not alter or invalidate the denial. In no event will Elsevier or Copyright Clearance Center be responsible or liable for any costs, expenses or damage incurred by you as a result of a denial of your permission request, other than a refund of the amount(s) paid by you to Elsevier and/or Copyright Clearance Center for denied permissions.

LIMITED LICENSE

The following terms and conditions apply only to specific license types:

15. **Translation**: This permission is granted for non-exclusive world **English** rights only unless your license was granted for translation rights. If you licensed translation rights you may only translate this content into the languages you requested. A professional translator must perform all translations and reproduce the content word for word preserving the integrity of the article.

16. **Posting licensed content on any Website**: The following terms and conditions apply as follows: Licensing material from an Elsevier journal: All content posted to the web site must maintain the copyright information line on the bottom of each image; A hyper-text must be included to the Homepage of the journal from which you are licensing at http://www.sciencedirect.com/science/journal/xxxxx or the Elsevier homepage for books at http://www.elsevier.com; Central Storage: This license does not include permission for a

scanned version of the material to be stored in a central repository such as that provided by Heron/XanEdu.

Licensing material from an Elsevier book: A hyper-text link must be included to the Elsevier homepage at http://www.elsevier.com . All content posted to the web site must maintain the copyright information line on the bottom of each image.

Posting licensed content on Electronic reserve: In addition to the above the following clauses are applicable: The web site must be password-protected and made available only to bona fide students registered on a relevant course. This permission is granted for 1 year only. You may obtain a new license for future website posting.

17. **For journal authors:** the following clauses are applicable in addition to the above:

Preprints:

A preprint is an author's own write-up of research results and analysis, it has not been peer-reviewed, nor has it had any other value added to it by a publisher (such as formatting, copyright, technical enhancement etc.).

Authors can share their preprints anywhere at any time. Preprints should not be added to or enhanced in any way in order to appear more like, or to substitute for, the final versions of articles however authors can update their preprints on arXiv or RePEc with their Accepted Author Manuscript (see below).

If accepted for publication, we encourage authors to link from the preprint to their formal publication via its DOI. Millions of researchers have access to the formal publications on ScienceDirect, and so links will help users to find, access, cite and use the best available version. Please note that Cell Press, The Lancet and some society-owned have different preprint policies. Information on these policies is available on the journal homepage.

Accepted Author Manuscripts: An accepted author manuscript is the manuscript of an article that has been accepted for publication and which typically includes author-incorporated changes suggested during submission, peer review and editor-author communications.

Authors can share their accepted author manuscript:

- - immediately
    - via their non-commercial person homepage or blog
    - by updating a preprint in arXiv or RePEc with the accepted manuscript
    - via their research institute or institutional repository for internal institutional uses or as part of an invitation-only research collaboration work-group
    - directly by providing copies to their students or to research collaborators for their personal use
    - for private scholarly sharing as part of an invitation-only work group on commercial sites with which Elsevier has an agreement
- - after the embargo period
    - via non-commercial hosting platforms such as their institutional repository
    - via commercial sites with which Elsevier has an agreement

In all cases accepted manuscripts should:

- - link to the formal publication via its DOI
- - bear a CC-BY-NC-ND license - this is easy to do
- - if aggregated with other manuscripts, for example in a repository or other site, be shared in alignment with our hosting policy not be added to or enhanced in any way to appear more like, or to substitute for, the published journal article.

Published journal article (JPA): A published journal article (PJA) is the definitive final record of published research that appears or will appear in the journal and embodies all value-adding publishing activities including peer review co-ordination, copy-editing, formatting, (if relevant) pagination and online enrichment.

Policies for sharing publishing journal articles differ for subscription and gold open access articles:

Subscription Articles: If you are an author, please share a link to your article rather than the full-text. Millions of researchers have access to the formal publications on ScienceDirect, and so links will help your users to find, access, cite, and use the best available version.

Theses and dissertations which contain embedded PJAs as part of the formal submission can be posted publicly by the awarding institution with DOI links back to the formal publications on ScienceDirect.

If you are affiliated with a library that subscribes to ScienceDirect you have additional private sharing rights for others' research accessed under that agreement. This includes use for classroom teaching and internal training at the institution (including use in course packs and courseware programs), and inclusion of the article for grant funding purposes.

Gold Open Access Articles: May be shared according to the author-selected end-user license and should contain a CrossMark logo, the end user license, and a DOI link to the formal publication on ScienceDirect.

Please refer to Elsevier's posting policy for further information.

18. **For book authors** the following clauses are applicable in addition to the above: Authors are permitted to place a brief summary of their work online only. You are not allowed to download and post the published electronic version of your chapter, nor may you scan the printed edition to create an electronic version. **Posting to a repository:** Authors are permitted to post a summary of their chapter only in their institution's repository.

19. **Thesis/Dissertation**: If your license is for use in a thesis/dissertation your thesis may be submitted to your institution in either print or electronic form. Should your thesis be published commercially, please reapply for permission. These requirements include permission for the Library and Archives of Canada to supply single copies, on demand, of the complete thesis and include permission for Proquest/UMI to supply single copies, on demand, of the complete thesis. Should your thesis be published commercially, please reapply for permission. Theses and dissertations which contain embedded PJAs as part of the formal submission can be posted publicly by the awarding institution with DOI links back to the formal publications on ScienceDirect.

Elsevier Open Access Terms and Conditions

You can publish open access with Elsevier in hundreds of open access journals or in nearly 2000 established subscription journals that support open access publishing.